Crystallisation Kinetics and Optical Properties of $Ge_2Sb_2Te_5$

Gerard Ruitenberg

St Cross College, Oxford
Department of Materials, University of Oxford



A thesis submitted for the degree of
Doctor of Philosophy
in the University of Oxford

Trinity Term 2001



Abstract

Crystallisation Kinetics and Optical Properties of $Ge_2Sb_2Te_5$

Gerard Ruitenberg

St Cross College, Oxford
Department of Materials, University of Oxford
A thesis submitted for the degree of Doctor of Philosophy in the University of Oxford
Trinity Term 2001

This thesis reports on the work carried out by the author on the crystallisation kinetics and optical properties of thin amorphous $Ge_2Sb_2Te_5$ films. This study is prompted by the application of these films in optical phase change recording media. The work is partly theoretical and partly experimental in nature.

Starting from the general nucleation and growth theory, it was shown that the Johnson-Mehl-Avrami-Kolmogorov (JMAK) equations are equally valid under linear heating conditions as under isothermal annealing conditions. All peak shift methods for determining the JMAK parameters were shown to be equivalent and valid within the JMAK framework. The crystallisation kinetics of amorphous $Ge_2Sb_2Te_5$ films were investigated under isothermal annealing conditions. Crystallisation was found to be preceded by a temperature dependent incubation time. The JMAK parameters were determined and found to be in good agreement with the nucleation and growth parameters, which were determined independently.

The optical properties of many materials can be described by three parameters: the plasma energy, E_p, an effective transition energy, Δ, and a damping constant, Γ. A theoretical model was developed that aims to calculate these parameters from the co-ordination of nearest neighbours in the structure. The model was found to work for a simplified silicon Hamiltonian and it is described how the model could be extended to include more realistic systems. E_p, Δ and Γ were determined before and after crystallisation of amorphous $Ge_2Sb_2Te_5$ films. From the numerical values of these parameters, it was concluded that the change in the reflectivity upon crystallisation is primarily due to the change in Δ. The change in the co-ordination of nearest neighbours upon crystallisation was investigated. The topological co-ordination was found to be very similar in both phases. The change in the optical properties is thought to be due to the change in chemical order of the nearest neighbours.

Acknowledgements

First of all, I would like to thank Prof. Laurens Katgerman for effectively getting me into this university. I will *never* forget.

I am grateful to the Engineering and Physical Sciences Research Council (EPSRC) for giving me a scholarship that enabled me to do a D.Phil. here in Oxford.

Regarding my project, I would like to thank my supervisor, Dr. Amanda Petford-Long, for her guidance, support and general willingness to help me. Also, I would like to thank:
My second supervisor, Prof. Peter Dobson, for guiding my experimental optics work; Prof. David Pettifor, who helped me with the four level recursion model; Prof. David Cockayne for teaching me how to get radial distribution functions; Dr. Evgueni Tsymbal for his calculation of the absorption spectrum in Fig. 6.5; Ron Doole for his patience in teaching me how to operate an electron microscope; Dr. Rafal Dunin-Borkowski for conducting the EELS experiments and for helping me, together with Dr. Will McBride, to obtain my electron diffraction patterns; Dr. Marcus Ormston for his help with the X-ray reflectometer; Prof. Carmen Afonso for helping me make my samples; Philips Research Laboratories for providing me with a second set of samples; Dr. Geoff Grime and Dr. István Rajta for helping with the PIXE analysis of my films; Dr. Erik Woldt and Prof. Lok Lew Yan Voon who, presumably out of a genuine interest in my research, spent days answering my e-mails without any apparent gain on their part.

On a more personal note, I would like to thank all the people of the Magnetic Materials Group who have made my stay in the group pleasurable. In particular Mike Fenn, the walking dictionary/thesaurus, and Marcus Ormston ("Women... they're so complex... and yet so simple...") for being my friends and for not being the type of scientist/engineer that I had almost come to accept as a rule. Then Vasyl Kravets ("Sugar in Ukraine sweeter than in England"), who treated me as a lost son when I visited him in Kiev. And Evgueni, with whom I had many a pint of Burton and beef and mustard flavoured crisps.

Finally, I would like to thank all the people at St Cross College who gave me the most colourful social life that I have experienced so far. In particular, I would like to thank Julia Atkinson and James Rudman of the kitchen staff for their kindness and for feeding me nice fresh food for four years; Jim Williamson, my friend and senior sponsor, still in charge of my moral decline; Diarmaid MacCulloch, for altogether being such a remarkable person; Judith Ledger for taking my rent and battels off me with love and care; Suzy Hodge, for being my duckling, love-munchkin; kissums! And finally Dorothee Bruns, Barry Derham, Anne Haour, Michel Kenzelmann, Susy Bantick, Katiana Finnis, Hugh Roberts, Sabrina Inowlocki and Amol Kahlon, who I hope to have befriended for life.

Table of Contents

Abstract ii

Acknowledgements iii

Chapter I Introduction 1.1

1.1 Project Aims 1.1

1.2 Optical Phase Change Media 1.1

1.2.1 Principle of operation of CDs, CD-R's and CD-RWs 1.2

1.2.2 Compatibility of optical media 1.3

1.2.3 Criteria for a good phase change material 1.4

1.2.4 Disc structure of a modern CD-RW disc 1.5

1.3 Development of CD-RW media 1.7

1.4 Thesis Outline 1.11

References 1.13

Chapter II Film Growth and Characterisation Techniques 2.1

2.1 Introduction 2.1

2.2 Sputter deposition 2.2

2.3 Proton Induced X-ray Emission (PIXE) Spectroscopy 2.4

2.4 Grazing Incidence X-ray Reflectivity (GIXR) 2.6

2.4.1 Introduction 2.6

2.4.2 Theory 2.7

2.4.3 How to obtain density, film thickness and roughness 2.10

2.5 Transmission Electron Microscopy (TEM) 2.12

2.5.1 Introduction 2.12

2.5.2 Basic principle of a TEM 2.12

2.5.3 Diffraction 2.14

2.5.4 Imaging 2.15

2.5.5 *In-situ* annealing 2.16

2.5.6 Electron energy loss spectroscopy (EELS) 2.17

2.5.7 Determining the radial distribution function (RDF) 2.17

2.5.8 Sample preparation 2.18

2.6 The IR-VIS-UV Spectrophotometer 2.18

2.6.1 Introduction 2.18

2.6.2 Instrumental set up 2.19

2.6.3 How R and T are calculated 2.20

2.7 Ellipsometry 2.22

2.7.1 Introduction 2.22

2.7.2 Theory 2.22

2.7.3 The ellipsometer; measuring Δ and Ψ 2.23

2.7.4 Calculating the optical constants from Δ and Ψ 2.26

References 2.28

Chapter III Johnson-Mehl-Avrami-Kolmogorov Theory **3.1**

3.1 Introduction 3.1

3.2 The JMAK Equation in Integral Form 3.2

3.2.1 Nucleation and growth 3.2

3.2.2 The extended volume 3.3

3.2.3 Relation between real and extended volume 3.4

3.3 The Isothermal JMAK Equations 3.6

3.3.1 Four special cases 3.6

3.3.2 The isothermal JMAK parameters 3.9

3.3.3 Determining the isothermal JMAK parameters from experiment 3.11

3.3.4 The isothermal JMAK reaction rate equation 3.11

3.4 The Linear Heating JMAK Equations 3.12

3.4.1 Novel derivation of the linear heating JMAK equation 3.12

3.4.2 The linear heating JMAK reaction rate equation 3.16

3.4.3 Justification for using peak shift methods 3.18

3.4.4 Determining the linear heating JMAK parameters from experiment 3.20

3.5 Two Important Assumptions 3.21

3.5.1 Assuming the thermal energy is small compared to activation energies 3.21

3.5.2 The hard impingement approximation 3.22

3.6 The Incubation Time 3.22

3.7 The Average Grain Size 3.23

3.8 Summary 3.23

References 3.26

Chapter IV *In*-situ TEM Crystallisation Experiments 4.1

4.1 Introduction 4.1

4.2 Experimental methods for determining the crystallised fraction 4.3

4.2.1 Reflectivity etc. 4.4

4.2.2 Calorimetry 4.4

4.2.3 *In-situ* TEM 4.5

4.3 Experimental details 4.6

4.4 Results 4.8

4.5 Discussion 4.15

4.6 Summary and conclusions 4.20

References 4.22

Chapter V Optics Theory - Background 5.1

5.1 Introduction 5.1

5.2 Fundamental Optics 5.1

5.2.1 Maxwell's equations and the material relations 5.2

5.2.2 Including absorption 5.3

5.2.3 The Kramers-Kronig relations and Sum Rules 5.5

5.3 Classical Derivation of the Lorentz Expression 5.7

5.3.1 Plasma oscillations 5.7

5.3.2 The dielectric function of a free electron gas 5.9

5.3.3 The dielectric function for bound electrons 5.10

5.3.4 Including absorption 5.10

5.3.5 The electron energy loss function 5.12

5.3.6 The absorption spectrum in the limit $\Gamma \rightarrow 0$ 5.13

5.4 Quantum mechanical derivation of the Lorentz expression 5.15

5.4.1 The atomic orbitals of an isolated free atom 5.15

5.4.2 The band structure of a solid 5.17

5.4.3 Derivation of the Lorentz expression 5.21

5.4.4 The absorption spectrum of the linear chain 5.23

5.5 Phillips' Spectroscopic Theory 5.27

5.5.1 Phillips' theory 5.27

5.5.2 Including amorphous materials 5.29

References 5.31

Chapter VI Relating the Absorption Spectrum to the Local Structure 6.1

6.1 Introduction 6.1

6.2 One Effective Lorentz Oscillator 6.1

6.2.1 Conserving the moment μ_1 6.2

6.2.2 Conserving the moment μ_{-1} 6.3

6.2.3 Conserving the moment μ_0 6.4

6.2.4 Constant momentum matrix elements 6.6

6.2.5 Example: the linear chain 6.6

6.3 A simplified silicon Hamiltonian 6.8

6.4 The four-level recursion model 6.12

6.4.1 The density of states 6.13

6.4.2 Recursion coefficients 6.14

6.4.3 A symmetric four-level approximation 6.16

6.4.4 Calculating the recursion coefficients 6.17

6.5 Discussion and conclusions 6.22

References 6.27

Chapter VII Determining the Optical Properties of $Ge_2Sb_2Te_5$ 7.1

7.1 Introduction 7.1

7.2 Determining the film composition (PIXE) 7.2

7.3 Measuring film thickness and density (GIXR) 7.3

7.4 Determining the optical constants n and k 7.6

7.4.1 Reflection, refraction and transmission 7.7

7.4.2 Measuring R_t, R_t' and T_t 7.12

7.4.3 Calculating n and k from R_f, T_f and $R_{a,f}$ 7.15

7.4.4 Calculating n and k from R_f and T_f only 7.17

7.4.5 Obtaining n and k from R_t, R_t' and T_t 7.19

7.4.6 Recap of the iteration procedure 7.20

7.4.7 Spectrometry results for n and k 7.22

7.4.8 Ellipsometry results for n and k 7.23

7.4.9 Comparison with n and k from the literature 7.24

7.5 Determining the plasma energy 7.26

7.6 Fitting Δ and Γ for both phases to the absorption spectra 7.27

7.7 Summary and conclusions 7.30

References 7.32

Chapter VIII Determining the local structure of $Ge_2Sb_2Te_5$ **8.1**

8.1 Introduction 8.1

8.2 Obtaining the radial distribution functions from experiment 8.2

8.2.1 Sample preparation 8.2

8.2.2 Measuring the diffraction patterns 8.3

8.2.3 Obtaining the scattered intensity *vs.* reciprocal space distance 8.3

8.2.4 Calibrating the reciprocal space distance 8.4

8.2.5 Calculating the radial distribution function 8.8

8.3 Determining the nearest neighbour coordination 8.12

8.3.1 The NaCl-type crystalline phase 8.12

8.3.2 The amorphous phase 8.16

8.3.3 The hexagonal crystalline phase 8.19

8.4 Discussion and conclusions 8.23

References 8.28

Chapter IX Conclusions and Suggestions for Further Work 9.1

9.1 Introduction 9.1

9.2 Conclusions 9.1

9.3 Suggestions for further work 9.6

CHAPTER I

Introduction

1.1 Project Aims

The basic idea behind this project was to try and understand the physics of rewritable compact discs (CD-RWs). The development of CD-RWs has been largely empirical and suitable materials for the "active layer", the critical component in a rewritable CD, have been found by trial and error. When the physics of phase change materials is understood, it would be possible to predict which materials are suitable as a phase change material.

The aim of this project was a) to investigate the crystallisation kinetics of thin $Ge_2Sb_2Te_5$ films and b) to measure the atomic structure and the optical properties of this material before and after crystallisation and develop a simple quantum mechanical model that quantitatively relates the change in structure to the change in the optical properties, in particular reflectivity. It was decided to work on $Ge_2Sb_2Te_5$ because it is a material that is widely investigated and has been shown to be suitable as a phase change material.

1.2 Optical Phase Change Media

In this section, a brief explanation is given of how rewritable CDs work, how they relate to other optical storage media and how their development came along. This should illustrate the technological relevance of the research presented in the following chapters.

1.2.1 Principle of operation of CDs, CD-Rs and CD-RWs

On any type of compact disc (CD), digital information is contained in a string of bits that spirals from the inside of the disc to the outside [1]. The information is read by focusing a laser onto the bits, letting it run along the track and measuring the intensity of the reflected beam. As the reflectivity of the bits differs from the background, the information is detected.

During manufacturing of a conventional CD, dips are impressed in the polycarbonate (PC) layer. An aluminium reflective layer is then sputtered on top of the PC layer, conserving the dips. These dips reflect light more diffusely than the flat background. Some of this diffusely reflected light will not be reflected in the direction of the detector, which therefore picks up a lower signal when the beam passes a bit; the bit will effectively look dark.

On a recordable CD (CD-R), the active layer is made of an organic dye [2]. Information is written onto the dye using a focused laser beam that illuminates the dye and makes it opaque, much like the way photographic paper works. As the dye then looks dark at the position of the bit, it can be read as a conventional CD, using the same laser but now at an intensity low enough not to change the dye. As this process is irreversible, a CD-R can, in principle, be erased but not rewritten.

A rewritable CD (CD-RW), on the other hand, can be erased and/or rewritten. The active layer of phase change media is made of a chalcogenide alloy (e.g. In-Sb-Te doped with Ag

[3] or Ge-Sb-Te [4]) which has a crystalline atomic structure when the CD is blank. To write a bit of information on the CD, a focused laser is used to locally melt the alloy and change its thermodynamic phase from a solid crystalline one to a non-crystalline, or *amorphous*, liquid. When the laser is turned off, the melt then cools down to room temperature in a time too short for crystallisation to occur and the amorphous state of the material is frozen in. To erase the bit, the same laser can be used to heat the material to a temperature below the melting point for a time long enough to let the material crystallise. As the amorphous phase has a lower reflectivity than the crystalline phase, the bit can be read using the same laser at even lower intensity so that neither writing nor erasing occurs at the same time.

The terminology used above applies to compact discs used for audio applications. In computer jargon, compact discs are called CD-ROMs, for "read only memory"; recordable compact discs are called CD-R/ROM or (more correctly, as ROM specifically implies non-recordable and non rewritable) WORM, for "write once, read many" and rewritable compact discs CD-RW/ROM.

1.2.2 Compatibility of optical media

In principle, all of the above media can be made compatible. At present, however, CD-RW players/recorders can write CD-Rs and read CD-Rs and CDs, CD-R players/recorders can read CDs and CD players can read CD-Rs, but neither CD-R players/recorders nor CD players can read CD-RW discs. This is because the difference in reflectivity between an amorphous bit and its crystalline background requires a more sensitive detection system than the ones in CD-R and CD players. This incompatibility is obviously a tremendous drawback and will need to be resolved for the CD-RW format to become popular.

Compact discs for audio and computer use are sometimes not compatible. This is really an incompatibility of the code used to store the information and has nothing to do with the underlying principles of the recording medium as described in subsection 1.2.1.

Finally, there are audio discs on the market for professional and consumer use, respectively. The difference is that, for copyright reasons, CD-Rs and CD-RWs for consumer use can *not* be used to make a copy of a copy, while the professional ones can. Compact discs for consumer and professional use do not use different principles for recording.

1.2.3 Criteria for a good phase change material [5]

The most important criteria for a suitable optical phase change material are:

1) Good readability. The difference in the reflectivity between the amorphous and crystalline phase, the so-called *optical contrast*, should be as high as possible.

2) Good recordability; a) the material should be a good glass former and b) no crystallisation should occur when the melt cools down after the laser is switched off.

3) Fast erasing. When the amorphous bit is heated to a temperature below the melting point, crystallisation should be fast.

4) Long lifetime. Once the amorphous bits are written, they should be stable and not crystallise spontaneously at room temperature.

5) Many rewrite cycles. It is desirable to have a CD that you can rewrite many times, for which it is necessary to have a completely reversible phase transition.

6) High information density. To increase the information density, the bit size needs to be reduced. The bit size is determined by the size to which the laser spot can be focused. This, in turn, is given by the diffraction limit, and in practice limited by the wavelength of the laser light.

Some of these criteria impose conflicting conditions on the phase change material. Points 3) and 4) require the crystallisation kinetics to be such that crystallisation is fast enough at the "erasing temperature" to achieve acceptable erasing times, but slow enough at room temperature to assure data stability. It will be shown later that points 1) and 6) impose conflicting conditions on the optical properties of the phase change material. This illustrates the importance of quantitative knowledge of the optical properties and the crystallisation kinetics of the phase change material.

1.2.4 Disc structure of a CD-RW disc

The active layer (typically 25 nm thick) is only one of the many layers in a CD-RW disc. A schematic cross section of a modern disc structure is drawn in Fig. 1.1 [6-9].

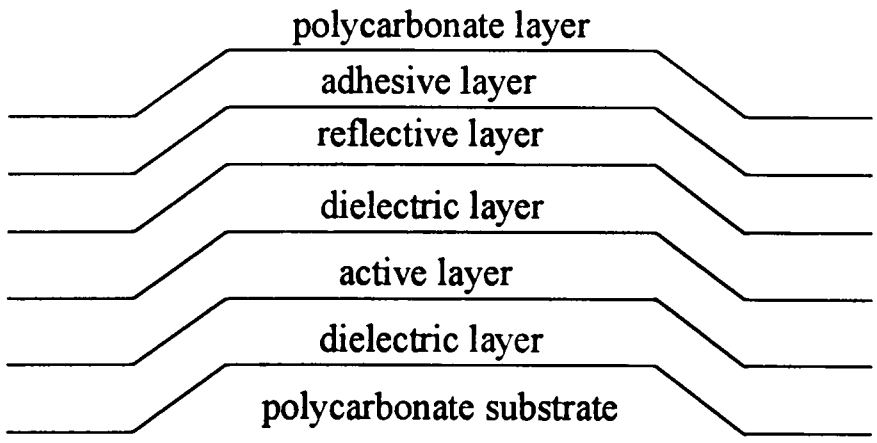


Figure 1.1 Schematic representation of the disc structure of a modern phase change medium; the laser shines on the disc from the bottom [6-9].

The bottom layer is a pre-grooved polycarbonate (PC) substrate layer, on which all the other layers are deposited. The grooves define the track on which the information is written. The PC layers are very thick (typically 1 mm for the bottom layer and 0.1 mm for the top layer) compared to the thickness of the other layers (typically 10 - 100 nm) and give the CD its mechanical stability.

The active layer is sandwiched between two dielectric layers (typically 50 nm for the top layer and 100 nm for the bottom layer), made of SiO_2, Si_3N_4, ZnS or a combination of these [5]. These layers contain the liquid bits of the active layer during writing and protect it against oxidation, and also prevent the formation of holes in the active layer that otherwise occur after many write-erase cycles. The dielectric layers also act as heat sinks and protect the PC layers against thermal degradation. Their third main function is that they act as a "seeding layer", allowing crystallites to form at the active layer–dielectric layer interfaces. As the active layer is thin (typically 25 nm), interface processes are important and the properties of the seeding layer can greatly influence the crystallisation kinetics by changing the energy barrier for the formation of nuclei at the interfaces. Finally, they determine the cooling rate of the active layer [5].

The reflective layer (typically 100 nm think) is made of an aluminium alloy and reflects the laser light that is transmitted by the active layer back into the detector, increasing the signal. The adhesive layer improves the adhesion between the reflective layer and the top PC layer. Information about the manufacturer of the disc etc. can be printed onto the top PC layer.

In this study, however, only the properties of the active layer, including the active layer–dielectric layer interfaces, are investigated. In particular, the kinetics of the amorphous to crystalline phase transition is studied, as well as the corresponding change in optical reflectivity.

1.3 Development of CD-RW media

The start of the development of optical recording media is marked by the discovery of the laser in 1960 [10]. The principle of optical recording was first demonstrated in 1972 at the Philips Research Laboratories; it then took until 1982 until the first (Philips®) CD player became commercially available. In 1991 the first commercial (Panasonic®) CD-RW player/recorder was introduced.

Phase change media were invented back in 1968 by S.R. Ovshinsky [11]. He showed that a $Ge_{10}Te_{48}As_{30}Si_{12}$ thin film could locally be switched between an amorphous and a crystalline phase. The amorphous phase is highly resistive while the crystalline phase is conductive; the information was read by locally measuring the electrical resistance of the material. The first *optical* phase change medium was introduced two years later by Feinleib *et al.* [12]. They showed that a region of a $Ge_{15}Sb_2Te_{81}S_2$ alloy film with a 3 μm diameter could locally be switched between an amorphous and a crystalline phase using a focused 515 nm Ar laser. The writing and erasing times were of the order of 10 μs. A "sharp change in optical transmission or reflection" is claimed to have been observed, but no results are presented. Feinleib *et al.* did not comment on any of the other points mentioned in section 1.2.3 regarding the suitability of $Ge_{10}Te_{48}As_{30}Si_{12}$ as a phase change medium. The authors present a model that attributes the high crystallisation speed to the introduction of excess carriers by the photon flux (i.e. not just the resulting rise in temperature) but no experimental data to support the model are included.

In principle, it is possible to store information either by writing amorphous bits on a crystalline background or by writing crystalline bits on an amorphous background. The latter

principle was investigated by Gravesteijn *et al.* [13]. They found that it was feasible to write crystalline bits on an amorphous background. However, re-amorphising this bit caused too much crystallisation *around* the bit (where the material is heated below the melting point but above the crystallisation temperature) to use this method for rewritable CDs. The method could still be used for write once media [14], but organic dyes turned out to be more suitable candidates because of their low production cost [15] and very high optical contrast [16]. Writing amorphous bits on a crystalline background thus remains the only option for phase change media at present.

The as-deposited state of the active layer, however, is usually amorphous. In order to be able to write melt-quenched amorphous bits on a crystalline background, this as-deposited amorphous film needs to be crystallised first. This is done with a focused laser and this process is known as "initialisation". The structure and physical properties of amorphous materials are generally dependent on the method by which the amorphous phase is produced and on its state of relaxation [17-20]. We may therefore expect that the crystallisation kinetics of the as-deposited amorphous film during initialisation may differ from the crystallisation kinetics of the melt-quenched bit during the erase process. This was indeed found to be the case for Ge [21], Sb-Ge [22], Sn-Te-Se [23], $Ge_{22}Sb_{25}Te_{54}$ [24] and $Ge_2Sb_2Te_5$ [25] amorphous films; the laser-quenched amorphous state crystallises much faster. The difference is mainly due to the presence of small crystalline atomic clusters in the laser-quenched amorphous state, known as embryos [26], which initiate the crystallisation process. Park *et al.* showed that it is possible to "prime" the as-deposited amorphous $Ge_2Sb_2Te_5$ state, i.e. to introduce these embryos by a suitable annealing treatment with a laser, so that the annealed amorphous state has similar crystallisation properties as the laser-quenched amorphous state [25].

Recently, a disc structure has been proposed that does not require initialisation [27-29]. A 7 nm [27] thin Sb "crystallisation assist layer" is deposited before the active layer, a V doped Ag-In-Sb-Te alloy. Sb is the fastest crystallising metal known [30] and under the right conditions can be made to crystallise during sputtering [27]. The crystalline Sb layer then facilitates nucleation of the active layer, allowing it to crystallise under conditions that would not lead to crystallisation if the Sb layer were absent. Thus, a crystalline active layer is effectively deposited, making the initialisation process redundant.

If it takes a 10 μs laser pulse to erase a bit, as it did for the first optical phase change medium, it would take over ten hours to erase a complete 650 MB CD. Thus, there was a great incentive to find materials with shorter crystallisation times and by the mid to late 80s, a number of materials had been found that could be crystallised by laser pulses in the ns regime: In-Se (200 ns) [31], Sb_2Se (200 ns) [32], GeTe (50 ns) [33], $Ge_2Sb_2Te_5$ (50 ns) [34], $Ge_1Sb_2Te_4$ (40 ns) [34], In-Sb-Te (15 ns) [35]. These pulse times correspond to pulses of a laser focused to typically 1μm, at a power of the order of 10 mW for films with a thickness of typically 20 nm. Pulse times in the ns regime are sufficiently short to make the materials suitable candidates for commercial phase change media. Sb-rich alloys have even shorter erase times; amorphous Ge_9Sb_{91} films can be crystallised with laser pulses in the picosecond regime [36]. However, not all of the above materials show a large enough change in reflectivity upon crystallisation. Ge_9Sb_{91}, for example, has an optical contrast of about 4 %, which is detectable but not high enough to make the material a likely candidates for commercial phase change media. Optical contrasts of 24 % [37] and 30 % [38] have been reported for GeTe, 17 % [39] and 19 % [40] for $Ge_1Sb_2Te_4$ and 15 % for $Ge_2Sb_2Te_5$ [39].

In addition, not all of the fast crystallising materials have a low enough crystallisation speed at room temperature to guarantee a long lifetime for the CD-RW. Taking this restriction into account, the main candidates that remain are Ge-Sb-Te alloys [39] and Ag-In-Sb-Te alloys [41]. The latter have been widely used in commercially available CD-RWs. The main disadvantage of these alloys is that their crystallisation kinetics are such that it takes about 36 minutes [42] to erase a standard 74 minute CD-RW. As this is a very long time, interest remains in finding a phase change material that crystallises faster during erasing, whilst the amorphous phase is stable at room temperature. The crystallisation of amorphous alloys is a nucleation and growth process; nuclei of crystalline material are formed and grow until they touch and the crystallisation process comes to an end. Sometimes, nucleation is found to occur only after a certain *incubation time*. Crystallisation is said to be "nucleation dominated" when nucleation is the rate determining factor of crystallisation, and growth dominated when growth is the rate determining factor. In general, both processes are important so that both the nucleation and growth parameters play a decisive role in determining whether or not a certain material is suitable as a phase change medium.

The problem of the long erase times can be partially circumvented by using the direct-over-write (DOW) technique. An amorphous bit can be written on a phase change film by melting the material with a laser and letting it cool down, regardless of whether the material was crystalline or amorphous before heating started. Around the bit, the material will be heated to a temperature below the melting point, but above the crystallisation temperature. Thus, a crystalline ring will be formed around the amorphous bit, again regardless of the phase of the film before the bit was written. This effect is called the "self sharpening effect" [43], and it allows writing on a CD-RW without the need for a separate erase process, which considerably reduces the time it takes to rewrite a disk. Note, however, that during the

writing it is still necessary to erase the spaces between the new bits. Thus, the recording speed is now limited by the crystallisation kinetics rather than by the time it takes to locally melt the phase change material. The disc structure described in section 1.2.4 was found to give rise to a cooling rate in the melt of the order of 10^{10} K/s [6]. This is high enough to assure that most chalcogenide alloys discussed don't crystallise when cooling down from the melt.

The transition between the amorphous and crystalline states is reversible in principle. The number of write/erase cycles, however, is limited by thermal degradation of the PC layers and oxidation of the active layer, the rate of which depends on the gas permeability of the layers around the active layer. Using a disc structure similar to the one described in section 1.2.4, numbers of write/erase cycles of the order of 10^5 or more were achieved for a number of chalcogenide materials, e.g. As-Te [44], In-Sb-Te [45] and Ge-Sb-Te alloys [46].

To achieve the information density of a conventional CD (650 MB on a 12 cm diameter disc), the size of the bit must be close to 1 μm in diameter. Due to the diffraction limit, the point to which a laser beam can be focused cannot be smaller than approximately $1.22\lambda/NA$, where λ is the wavelength of the light and NA is the numerical aperture. With improvement of the optics of the laser, the numerical aperture has been increased to 0.4. Thus, a laser wavelength of 800 nm or less can nowadays fulfil the minimum requirement for the information density. The main outstanding task in the development of phase change media is thus to find a material that crystallises faster than the present phase change materials in use, is stable at room temperature and has the required optical contrast.

1.4 Thesis Outline

Chapter I gives an introduction to this thesis. It outlines the aims of the project, explains the technological background that motivated this research and gives a description of this thesis. Chapter II describes the experimental techniques that were used to grow and characterise the samples. Chapters III and IV are concerned with crystallisation kinetics. In chapter III, a formal and general presentation of the Johnson-Mehl-Avrami-Kolmogorov equation under isothermal and linear heating conditions is given. This forms the basis for understanding the data from the *in-situ* crystallisation experiments described in chapter IV. Chapters V-VIII aim to lay the basis for understanding quantitatively how the change in the atomic structure that occurs during crystallisation relates to the observed change in optical reflectivity. Chapter V outlines the theoretical optics background needed for chapters VI and VII. Chapter VI describes how the optical properties of the $Ge_2Sb_2Te_5$ films were obtained before and after crystallisation. In chapter VII, the quantum mechanical theory that links the absorption spectrum to the local atomic structure of a material is developed. Chapter VIII describes how the radial distribution function (RDF) of $Ge_2Sb_2Te_5$ was obtained experimentally before and after crystallisation. The RDF contains information about the local atomic co-ordination. This structural information is to be used as input for the model discussed in Chapter VI to calculate the absorption spectrum. Finally, conclusions and suggestions for further work are presented in chapter IX.

References

[1] S. W. Ng, *IEEE Comp. Soc. Press* **1** (1991) p. 100.

[2] H. Oba, M. Abe, M. Umehara, T. Sato, Y. Ueda and M. Kunikane,

Dig. Techn. Pap. Opt. Soc. Am. (1985) p. 86.

[3] Y. Ide, M. Harigaya, Y. Kageyama and H. Iwasaki, *Ricoh Techn. Rep.* **22** (1996).

[4] K. Nishiuchi, N. Akahira, E. Ohno and N. Yamada, *Jpn. J. Appl. Phys.* **31** (1992) p. 653.

[5] M. Libera and M. Chen, *MRS Bulletin,* April (1990) p. 40.

[6] T. Ohta, K. Inoue, M. Uchida, K. Yoshioka, T. Akiyama, S. Furukawa, K. Nagata and

S. Nakamura, *Jpn. J. Appl. Phys.* **28** (1989) p. 123.

[7] H. Iwasaki, Y. Ide, M. Harigaya, Y. Kageyama and I. Fujimura,

Jpn. J. Appl. Phys. **31** (1992) p. 461.

[8] T. Yoshida, N. Akahira, S. Ohara, K. Nisiuchi and S. Ohara,

Jpn. J. Appl. Phys. **31** (1992) p. 476.

[9] T. Ohta, N. Akahira, S. Ohara and I. Satoh, *Optoel.- Dev. and Techn.* **10** (1995) p. 361.

[10] T.H. Maiman, *Nature*, vol. **187** (1960) p. 493.

[11] S.R. Ovshinsky, *Phys.Rev. Lett.* **21** nr. 20 (1968) p. 1450.

[12] J. Feinleib, J. de Neufville, S.C. Moss and S.R. Ovshinsky,

Appl. Phys. Lett. **18** nr. 6 (1971) p. 254.

[13] D.J. Gravesteijn, C.J. van der Poel, P.M.L.O. Scholte and C.M.J. van Uijen,

Philips Tech. Rev. **44** no. 8/9/10 (1989) p.250.

[14] D.J. Gravesteijn, H.M. van Tongeren-HM, M. Sens, T. Bertens and C.J. van der Poel,

Appl. Opt. **26** nr. 22 (1987) p. 4772.

[15] E. Hamada, Y. Shin and T. Ishiguro, *Proc. SPIE - Int. Soc. Opt. Eng.* **1078** (1989) p. 80.

[16] W. Schild, *Funkschau* **2** (1989) p. 43.

[17] W.C. Sinke, S. Roorda and F.W. Saris, *J. Mat. Sci.* **6** (1988) p. 1201.

[18] M.G. Grimaldi, P. Baeri and M.A. Malvezzi, *Phys. Rev. B* **44** (1991) p. 1546.

[19] S. Coffa, J.M. Poate, D.C. Jacobson and A. Polman, *Appl. Phys. Lett.* **58** (1991) p. 2916.

[20] L. Pusztai, J. Sietsma and B.J. Thijsse, *Phil. Mag. B* **71** (1995) p. 383.

[21] F. Vega, R. Serna, C.N. Afonso, D. Bermejo and G. Tejeda,

J. Appl. Phys. **75** (1994) p. 7287.

[22] M.C. Morilla, C.N. Afonso, A.K. Petford-Long and R.C. Doole,

Phil. Mag. A **73** (1996) p. 1237.

[23] M. Terao, T. Nishida, Y. Miyauchi, T. Kaku, S. Hirogome and Y. Sugita,

Jpn. J. Appl. Phys. **28** (1989) p. 804.

[24] P.K. Khulbe, E.M. Wright, T. Hurst and M. Mansuripur,

IEEE 2000 Opt. Data Storage, Conf. Dig. (2000) p. 212.

[25] J. Park, M.R. Kim, W.S. Choi, H. Seo and C. Yeon, *Jpn. J. Appl. Phys.* **38** (1999),

p. 4775.

[26] P.K. Khulbe, E.M. Wright and M. Mansuripur, *J. Appl. Phys.* **88** (2000) p. 3926.

[27] J. Tominaga, T. Kikukawa, M. Takahashi, T. Kato and T. Aoi,

Jpn. J. Appl. Phys. **36** (1997) p. 3598.

[28] S. Ogawa, K. Takeguchi and I. Morimoto

Proc. SPIE, Int. Soc. Opt. Eng **3401** (1998) p. 244.

[29] S. Ogawa, K. Takeguchi and I. Morimoto

Proc. SPIE, Int. Soc. Opt. Eng **3401** (1998) p. 272.

[30] F. Jiang and M. Okuda, *Jpn. J. Appl. Phys.* **28** (1989) p. 293.

[31] M. Terao, T. Nishida, Y. Miyauchi, S. Hirogome, T. Kaku and N. Ohta

Proc. SPIE, Int. Soc. Opt. Eng. **695** (1986) p. 105.

[32] R. Barton, C.R. Davis, K. Rubin and G. Lim, *Appl. Phys. Lett.* **48** no. 19 (1986) p. 1255.

[33] M. Chen, K.A. Rubin and R. W. Barton, *Appl. Phys. Lett.* **49** (1986) p. 502.

[34] N. Yamada, E. Ohno, N. Akahira, K. Nishiuchi, K. Nagata and M. Takao

Jap. J. Appl. Phys. **26** supp. 26-4 (1987) p. 61.

[35] D.J. Gravesteijn, *Appl. Opt.* **27** no. 4 (1988) p. 736.

[36] J. Solís, C.N. Afonso, J.F. Trulli and M.C. Morilla,

J. Appl. Phys. **75** no. 12 (1994) p. 7788.

[37] Y. Nakayoshi, Y. Kanemitsu, Y. Masumoto and Y. Maeda,

Jpn. J. Appl. Phys. **31** (1991) p. 471.

[38] M. Libera, *Polycrystalline Thin Films-Structure, Texture, Properties and Applications,*

ed. M. Parker, *Mat. Res. Soc. Symp. Proc.* **V343** (1994).

[39] N. Yamada, E. Ohno, K. Nishiuchi and N. Akahira

J. Appl. Phys. **69** no. 5 (1991) p. 2849.

[40] Z. L. Mao, H. Chen, A. Jung, *J. J. Appl. Phys.* **78** (1995) p. 2338.

[41] H. Iwasaki, M. Harigaya, Nonoyama, Y. Kageyama, M. Takahashi, K. Yamada,

H. Deguchi and Y. Ide, *J. Appl. Phys.* **32B** (1993) p. 5241.

[42] S. Beavis and C. Barrie, *The Guardian* Thursday 4 December (1997) p. 21.

[43] T. Yoshida, N. Akahira, S. Ohara, K. Nishiuchi and T. Ishida

Jpn. J. Appl. Phys. **31** (1992) p. 476.

[44] P.C. Clemens, *Appl. Opt. Lett.* **22** (1983) p. 3165.

[45] Y. Sato, Y. Maeda, H.Andoh, I.Ikuta, M. Nagai, N. Tsuboi, H. Minemura and

M. Ishigaki, *Proc. Soc. Photo-Opt. Instr. Eng.* **1078** (1989) p. 11.

[46] T. Ohta, M. Uchida, K. Yoshioka, S. Furukawa and K. Kotera,

Proc. Soc. Photo-Opt. Instr. Eng., Techn. Digest Ser. **1** (1989) p.14.

CHAPTER II

Film Growth and Characterisation Techniques

2.1 Introduction

In this chapter, the techniques used to grow and characterise the $Ge_2Sb_2Te_5$ films are discussed. The samples used for the crystallisation experiments were grown using radio frequency (RF) sputter deposition at the Philips Research Laboratories in Eindhoven, The Netherlands, while the samples used for the optical experiments were grown using direct current (DC) sputter deposition at the Instituto de Óptica "Daza de Valdés" (CSIC) in Madrid, Spain. Both techniques are described in section 2.2.

The composition of the optical samples was checked using proton induced X-ray emission spectroscopy (PIXE); this technique is described in section 2.3.

The film thickness of the samples was obtained from grazing incidence X-ray reflectivity (GIXR) measurements; the principles of this technique can be found in section 2.4.

All information on the crystallisation kinetics, the plasma energy and the radial distribution function (RDF) was obtained using transmission electron microscopy (TEM) and the details of this technique can be found in section 2.5.

Section 2.6 describes the spectrophotometer used to determine the optical properties of the $Ge_2Sb_2Te_5$ films from the near infra-red (IR) to the ultra-violet (UV) region.

2.2 Sputter deposition [1, 2]

Thin films for optical phase change media are normally grown using DC or RF sputtering. A simple sputtering kit consists of two parallel plates in a sputtering chamber filled with an inert gas, usually argon, at a pressure of typically 10^{-4} to 10^{-6} bar. The plates are connected to a power supply and effectively act as a large capacitor. One of the plates is the sputtering target and is made of the material to be deposited and, in the case of DC sputtering, is connected to the negative electrode of the power supply. One or several substrates are located in front of the positive electrode. By applying a high voltage between the two plates, a plasma discharge is set up. The plasma discharge is initiated by electrons emitted from the negative electrode. These electrons are accelerated towards the positive electrode, impact on the gas atoms and ionise them. The electrons that are produced repeat the process and avalanche ionisation produces the plasma. This way of producing a plasma is called diode discharge. The positive ions that are created are accelerated towards the target material. On impact, they "sputter" atoms from the target material which is then deposited onto all internal surfaces, including the substrate. Fig. 2.1 shows a picture of a DC diode discharge sputtering system.

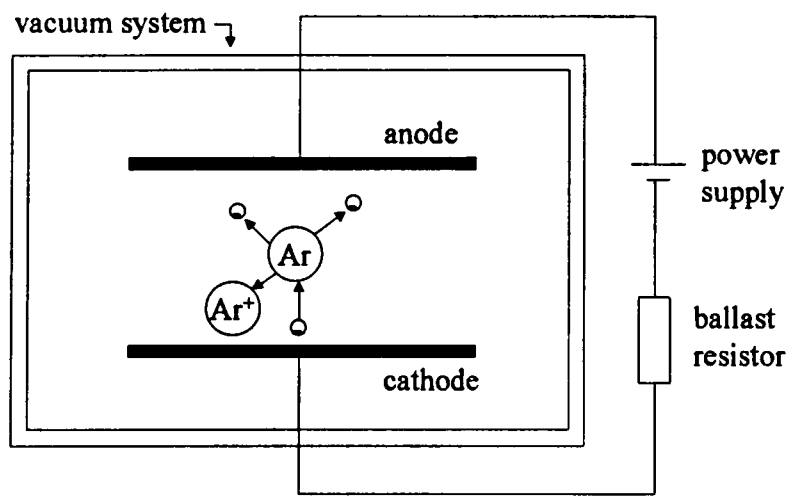


Figure 2.1 Schematic representation of a DC diode discharge sputtering system.

The main disadvantage of DC sputter deposition is that it requires the sputter target to be conducting. If the sputter target is an insulator, the positive ions from the plasma would still be accelerated towards the target, but are not neutralised by the electrons from the metal backing of the target as they cannot move through the insulator. Thus, a positive charge builds up on the surface of the target and the ion bombardment comes to a halt. To remedy this problem [3], an AC voltage is applied to the target. During part of the cycle, the voltage of the target is negative compared to the plasma voltage and the plasma ions are accelerated towards the target to contribute to sputtering. Charge then builds up on the surface of the target, but this charge is neutralised during the remainder of the cycle when the voltage of the target is positive compared to the plasma voltage and electrons travel from the plasma to the target. The average target voltage is kept lower than the plasma voltage such that, during one cycle, the target voltage is negative compared to the plasma voltage for most of the time. This is because the mobility of the electrons is higher than that of the ions; the neutralisation step can therefore take less time. This also ensures that the target is bombarded with ions, rather than the substrate. The frequency of the AC voltage should be at least 10 MHz, otherwise the positive charge build-up on the target reduces the impact energy of the ions too much, and it should be lower than 100 MHz, to give the ions enough time to reach the target. In practice, an RF frequency of 13.56 MHz is used internationally, to avoid interference with communication applications.

The deposition rate is mainly determined by the target current (i.e. the current between the target and the substrate) [4]; the higher the target current, the higher the deposition rate. Increasing the substrate bias slightly decreases the deposition rate. Increasing the pressure reduces the mean free path of the sputtered atoms and therefore also reduces the sputtering rate, but this is also a minor effect.

Alloys can be fabricated using a single target of the desired composition or by using multiple targets (co-sputtering). In the latter case, the voltage of the sputtering targets can be adjusted separately to control the sputtering rates of the individual targets so that the composition of the sample can be varied.

2.3 Proton Induced X-ray Emission Spectroscopy

Proton induced X-ray emission (PIXE) [5] is an energy dispersive spectroscopic technique used for quantitative elemental analysis. It can be used to detect sodium and any element higher in the periodic table, with detection limits [6] of typically 10 ppm. PIXE analysis is non-destructive, does not require sample preparation and can be used for solids, liquids and gases alike.

In a typical PIXE instrument [7], negatively charged hydrogen atoms, generated in an ion-source, are introduced into an accelerator, where they are accelerated by an electric field to a kinetic energy of typically 2-3 MeV. The ion beam is then split into an electron beam and a proton beam by applying an electric field perpendicular to the velocity of the ion beam. The electron beam is discarded and the proton beam used to irradiate the sample whose composition is to be determined. A schematic picture of the PIXE instrument used in this work is shown in Fig. 2.2.

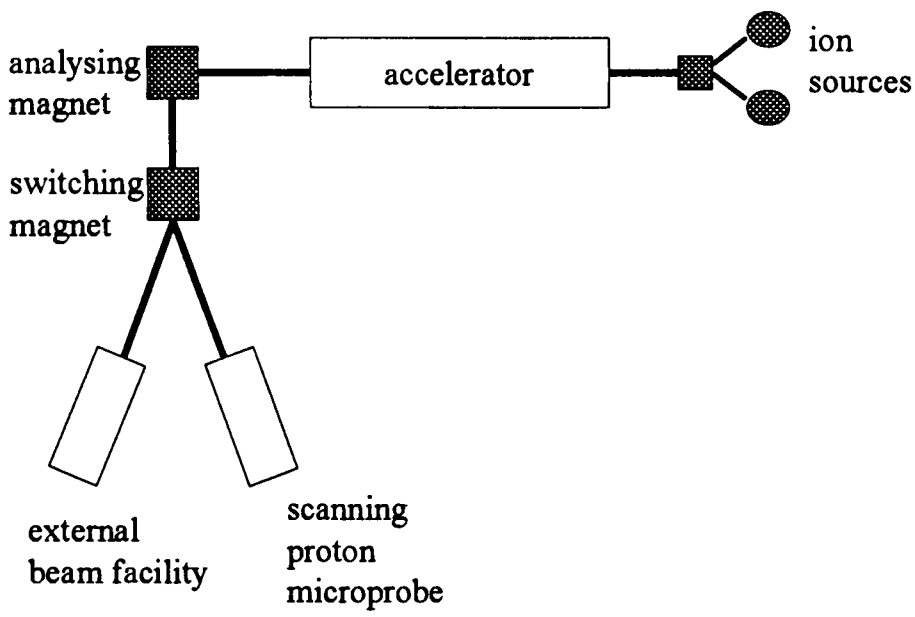


Figure 2.2 Schematic representation of the PIXE instrument used in this work.

Some of these protons knock electrons out of the inner atomic shells of the atoms in the sample. Subsequently, an electron from an outer shell will fall into the inner shell vacancy to minimise the atom's energy. As this happens, an X-ray photon, with an energy equal to the energy difference between the outer and inner shell, is emitted. The energy levels of the inner shells are of the order of 10 keV; their precise energy is determined by the charge of the nucleus, and hence is element specific. The energy levels of the outer electrons are of the order of 10 eV and their precise energy is a function of the atomic structure as well as the charge of the nucleus. Thus, by measuring the intensity of the emitted X-rays as a function of their photon energy in the 10 keV range, element specific information is essentially obtained. The result of such a measurement is called a PIXE spectrum. In order to obtain the chemical composition of the sample, PIXE spectra of elemental materials are recorded as a reference. The peaks in a sample PIXE spectrum identify the elements present in the sample. The area under a particular set of peaks is a measure of the concentration of the element in question. Fig. 2.3 shows a PIXE spectrum of $Ge_2Sb_2Te_5$.

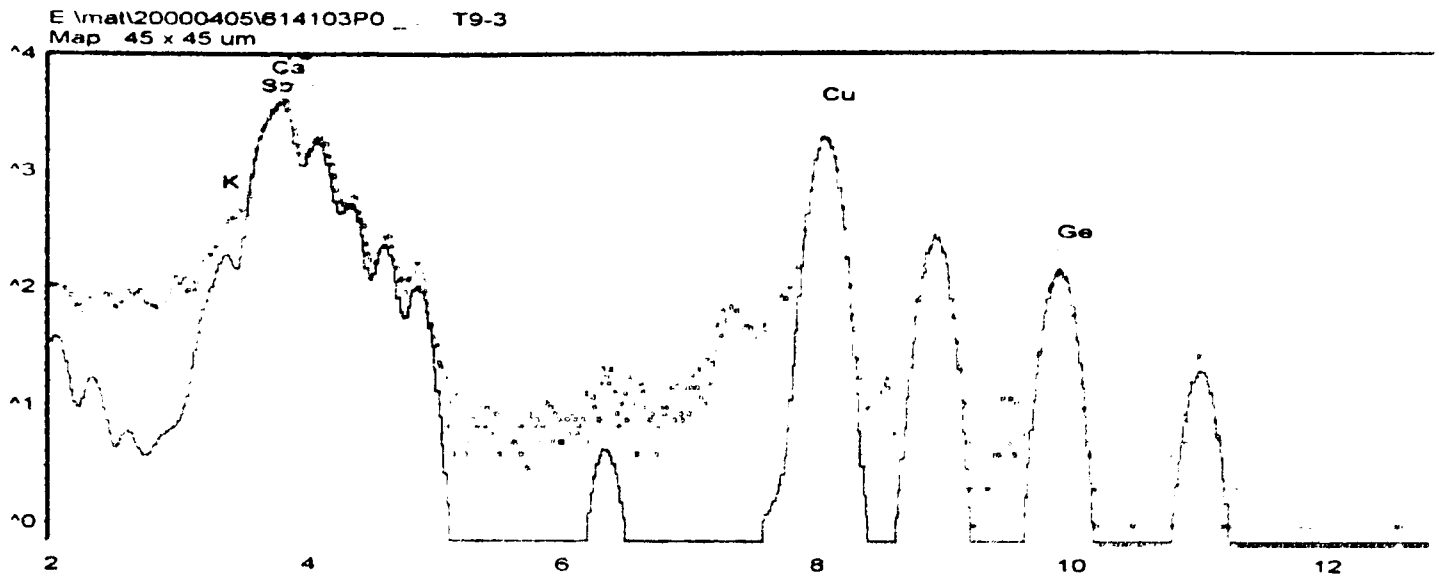


Figure 2.3 Example of a PIXE spectrum of $Ge_2Sb_2Te_5$.

2.4 Grazing Incidence X-ray Reflectometry

2.4.1 Introduction

Grazing incidence X-ray reflectometry (GIXR) [8, 9] is a non-destructive technique that can be used to determine the density and thickness of a thin film and the interfacial roughness of the air/sample and sample/substrate interfaces.

A GIXR apparatus measures the reflectivity of an X-ray beam, that is almost parallel to the surface of the sample, as a function of the angle of incidence to a sample. Fig. 2.4 shows a typical set-up in a GIXR instrument, in a "theta – two theta" alignment.

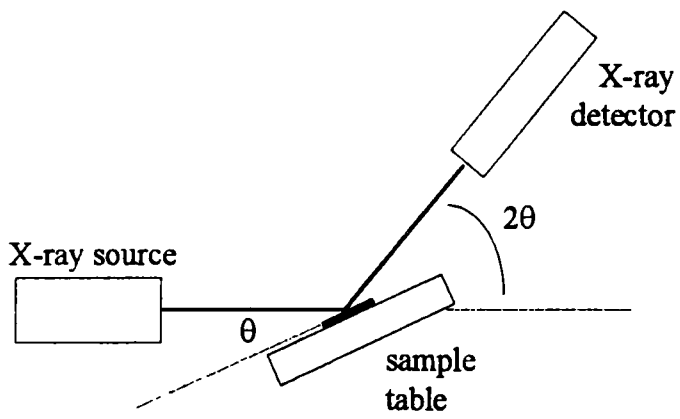


Figure 2.4 The theta – two theta alignment of the sample, X-ray source and detector in the BEDE scientific grazing incidence X-ray reflectometer.

A GIXR scan starts with the X-ray source, sample table and the X-ray detector aligned. The angle between the incident beam and the sample surface is then gradually increased (by keeping the source stationary, tilting the table and adjusting the detector position, when a theta – two theta alignment is used) to 2 -3 degrees and the reflectivity recorded by the detector.

The instrument used in this study was a BEDE Scientific grazing incidence X-ray reflectometer. It uses copper K_α radiation, which has a wavelength of 0.154 nm. Seen head-on, the X-ray beam is 8 mm wide and 40 μm high (but note that because of the small angle of incidence, the illuminated area is almost square). The incident angle is scanned over a range of 0.00 - 0.04 radians or from zero to just over two degrees.

2.4.2 Theory

In this section, we explain why a reflectivity trace of a thin film on a thick substrate looks the way it does and how it is affected by roughness of the interfaces.

First consider the simple case of a semi-infinite solid with no air/sample interface roughness. In the X-ray regime it can be assumed that the refractive index of air is equal to one, while the refractive index of the solid is almost one. From elementary optics, when the angle of incidence, θ (see Fig. 2.4) is very close to zero, total external reflection occurs and the incident beam is entirely reflected by the air/sample interface. However, above a certain critical angle, θ_c, which is determined by the electron density of the sample material, the incident beam is partly reflected by the air/sample interface and partly *refracted* into the sample. From this point, the reflectivity tails off as θ^{-4}, according to standard Fresnel theory,

while the intensity of the refracted beam increases accordingly. The resulting reflectivity trace is shown in Fig. 2.5; it is referred to as the "background trace". Note that the electron density is the only parameter of the sample material needed to describe this background trace.

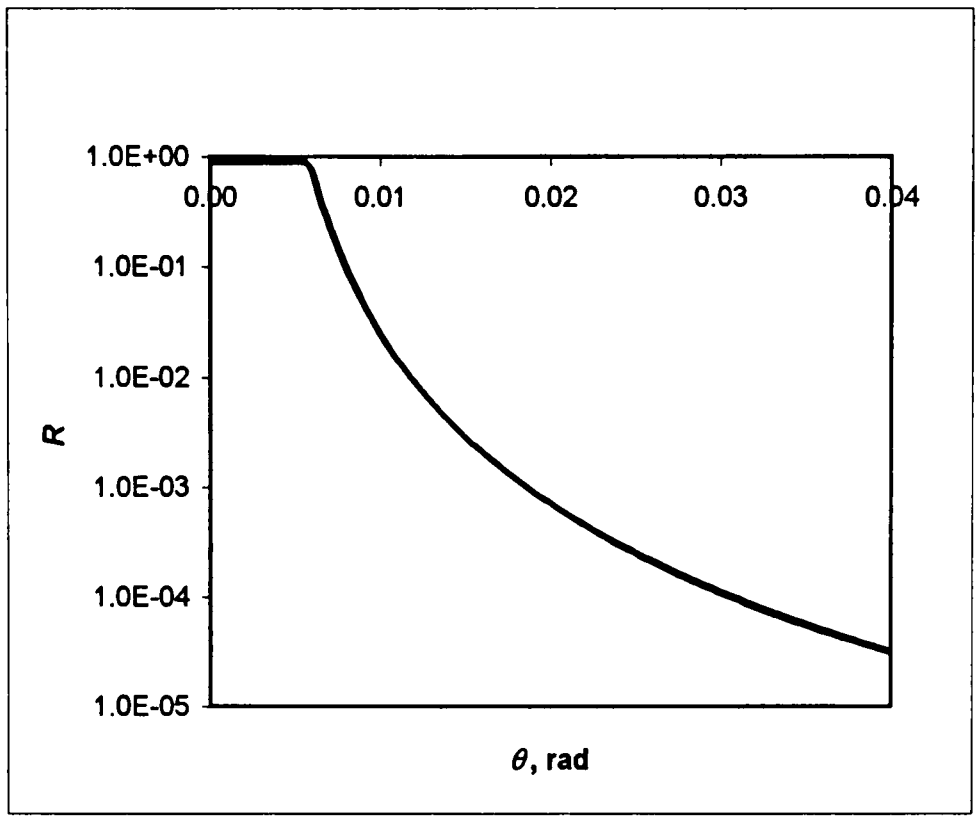


Figure 2.5 Background GIXR reflectivity trace, due to reflection of the air/sample interface only.

Now consider a thin film on a thick substrate, with no air/sample or sample/substrate roughness. In this case, the beam that is refracted into the sample material will hit the sample/substrate interface, part of it will again be reflected back and then refracted from the sample/air interface in the direction of the detector. As this beam travels further than light that is directly reflected towards the detector from the air/sample interface, its phase is different and the two beams interfere. During the scan of angle, the path difference changes and the interference will be alternately constructive and destructive, giving rise to an oscillation on top of the background trace, known as Kiessig [10] fringes. Kiessig showed

that when the refractive index of the sample is larger than that of the substrate, the m^{th} maximum in the reflectivity trace occurs at an angle

$$\theta_m = \sqrt{\left(\frac{\lambda}{2t_f}m\right)^2 + \theta_c^2}\,, \tag{2.1a}$$

where λ is the wavelength of the X-ray radiation and t_f is the thickness of the sample (after film thickness). When the sample has a lower refractive index than the film, the fringes are at

$$\theta_m = \sqrt{\left(\frac{\lambda}{2t_f}(m+\tfrac{1}{2})\right)^2 + \theta_c^2} \tag{2.1b}$$

Fig. 2.6 shows a typical reflectivity trace for a thin film.

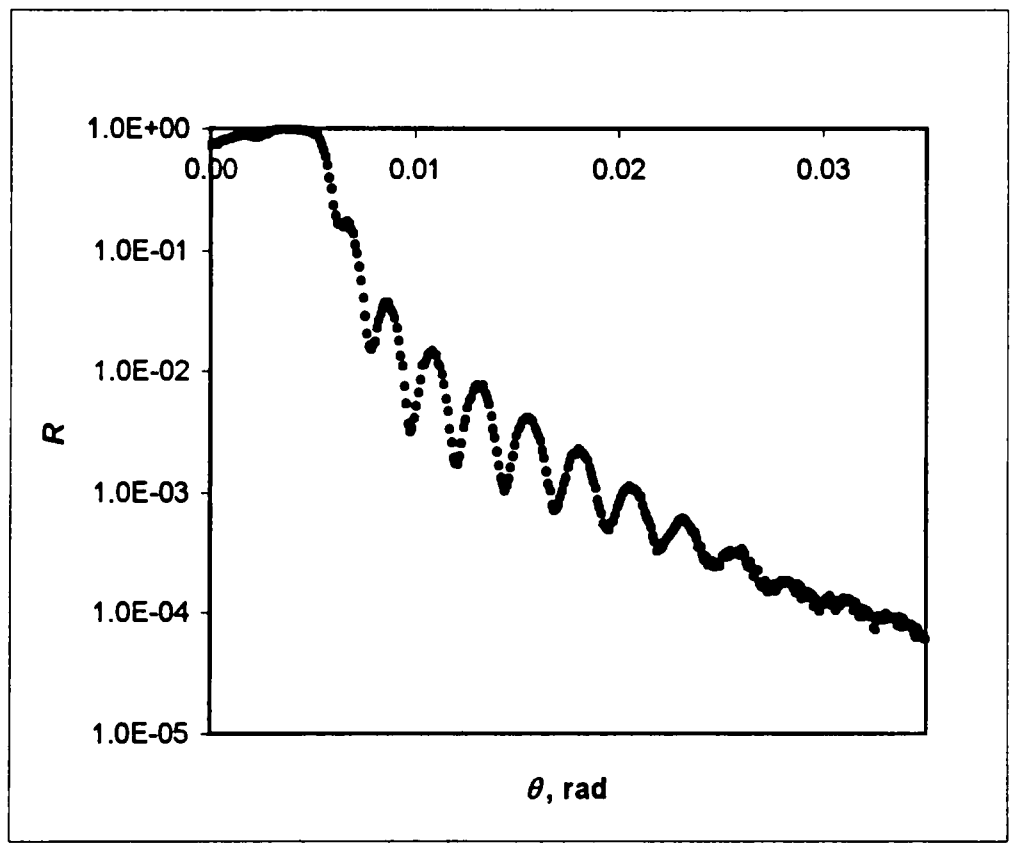


Figure 2.6 Typical GIXR reflectivity trace for a thin film sample.

The theory presented so far does not quite describe experimental reflectivity traces. This is because only specular reflection has been considered and possible roughness of the air/sample and sample/substrate interfaces has been neglected. Imagine a cross-section of an interface, which can be considered as oscillating about a flat, ideal imaginary interface. The root-mean-square (RMS) value of this oscillation is called the RMS roughness. Parratt [11]

has shown how to incorporate the effect of the RMS roughness into the theory that describes the reflectivity traces. Including the roughness of both the air/sample and the sample/-substrate interfaces broadens the Kiessig fringes and causes a sharper fall in reflectivity above the critical angle. However, the RMS roughness of the air/sample interface has a stronger influence on the tail of the trace and the sample/substrate interfaces causes more damping of the Kiessig fringes.

It is noted that the RMS roughness is a measure of the *amplitude* of the oscillation we discussed earlier, but does not contain any information about the *period* of the oscillation, or the *length scale* of the roughness. This length scale can be of the order of the sample size, in which case the "roughness" is more like a macroscopic variation in the sample thickness; it can be of the order of the atomic separation, in which case the "roughness" is rather an interdiffusion of the two layers in question. The RMS roughness in both cases can be the same. The two extreme cases are illustrated in Fig. 2.7.

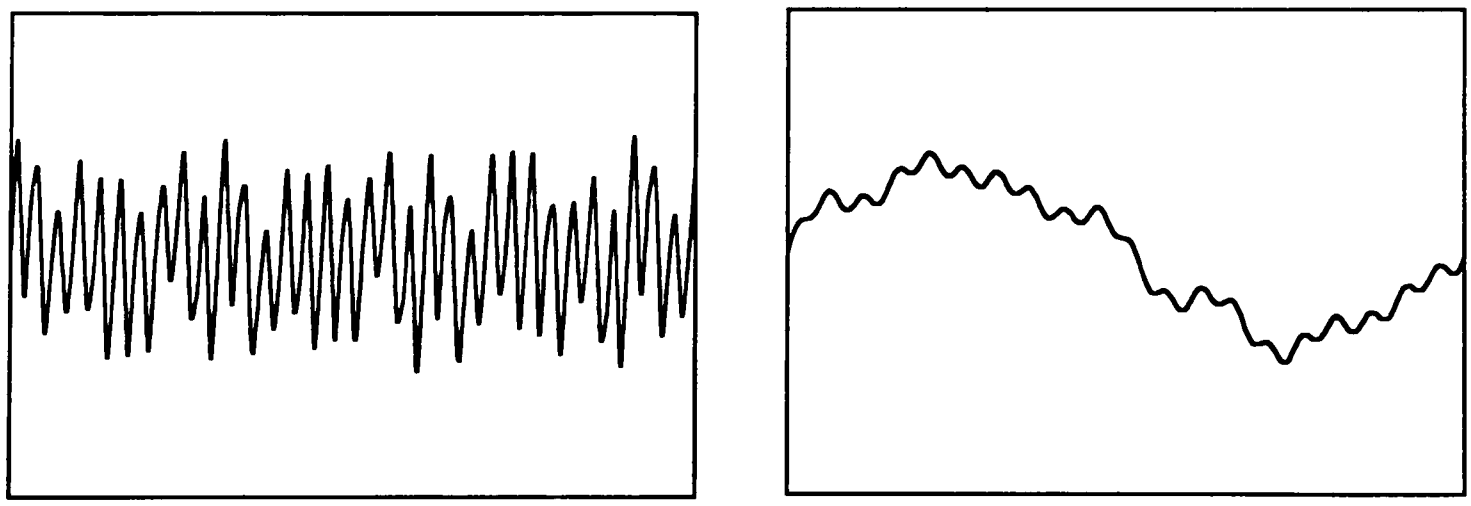


Figure 2.7 Example of two different interfaces that have the same RMS roughness.

2.4.3 How to obtain density, film thickness and roughness

The Bede Scientific GIXR reflectometer comes with a software package that simulates GIXR reflectivity traces, using the theory described in the previous section. Knowing the composition of the sample and the composition and density of the substrate, the simulated trace can be fitted to an experimental trace using the mass density of the sample (which gives the electron density, since the composition is known), the film thickness and the RMS roughness of the air/sample and sample/substrate interfaces as fit parameters.

The fitting procedure described above is rather time consuming as it is necessary to change the input parameters manually after each simulation and find the best fit by trail and error. It is much easier to obtain the thickness of the film from an experimental reflectivity trace by measuring the positions of the maxima in the Kiessig fringes and make a plot of θ_m^2 vs. either m^2 or $(m+\frac{1}{2})^2$, depending on the value for the refractive indices of sample and substrate. Eq (2.1) shows that this gives a straight line with slope $(\lambda / 2t_f)^2$. As the wavelength of the X-rays is known, the film thickness can be obtained from the slope.

To speed up the iteration procedure further, the critical angle can be measured from an experimental reflectivity trace, then the mass density can be calculated from it and can be used as the first input for the iteration. There is still a need for iteration because the critical angle cannot be determined with arbitrary accuracy from a reflectivity trace as the trace is smoothed due to instrumental limitations. These limitations are accounted for in the simulation, so that a more accurate critical angle can be determined using the iteration procedure described above. Having found the thickness and the critical angle, finding the roughness of the air/sample and sample/substrate interfaces by iteration is now much easier as the number of independent fit parameters has been reduced to two.

The position of the Kiessig fringes can be determined accurately. The error in the film thickness, determined from a *series* of those Kiessig fringes, is therefore small; typically less than 5 %. The critical angle is less pronounced than the Kiessig fringes and can therefore not be determined with the same accuracy. The resulting uncertainty in the calculated density is typically less than 10 %. The error in the RMS roughness of the interfaces can be substantially larger.

2.5 Transmission Electron Microscopy (TEM)

2.5.1 Introduction

A transmission electron microscope (TEM) can be used in imaging mode, to record images of thin films, or in diffraction mode, to obtain average structural information about the sample material. Depending on the instrument and its settings, the resolution in imaging mode can be anything up to 0.12 nm (atomic resolution). The technique is destructive in the sense that it requires the preparation of a TEM specimen from the sample, but does not destroy the sample. TEM specimens need to have a thickness of the order of a few tens of nm, approximately. A TEM can be used to study several physical processes *in-situ*, e.g. reaction with a gas in the column, structural changes upon heating or the effect of the presence of a magnetic field, etc.

2.5.2 Basic principle of a TEM [12]

A TEM uses an electron source to illuminate the sample. A tungsten filament, LaB_6 filament or a field emission gun (FEG) can be used as an electron source. The electrons are accelerated by an electric field to a kinetic energy of typically 0.2 - 1.0 MeV. To obtain a beam with a well-defined direction, an aperture is placed in front of the source. The electron beam is then sent down the evacuated "column" of the TEM. Inside the column, sets of coils

are used to create magnetic fields. Due to the Lorentz force acting upon the electrons, the direction of propagation of the electron beam can be changed. The coils can thus be used to focus the electron beam and are therefore referred to as lenses, after the analogy with an optical microscope. The first sets of lenses, two condenser lenses and the upper objective lens, are used to form a parallel beam that illuminates the sample, which is inserted into the column. The pre-specimen lenses are shown in Fig. 2.8.

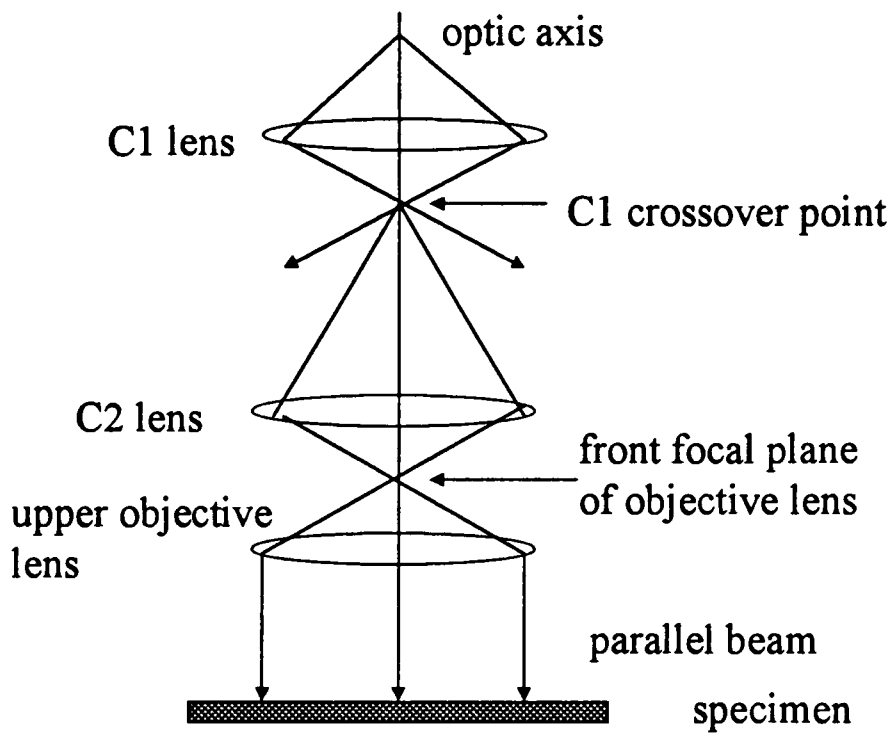


Figure 2.8 Ray-diagram of the for the pre-specimen electron optics in a TEM. C1 and C2 are the first and second condenser lenses, respectively.

The electron beam then passes through the sample and is then focused by the (lower) objective lens, an intermediate lens and a projector lens to produce either a diffraction pattern or an image of the sample on a fluorescent screen. This is further discussed in the next two sections. The screen can be lifted and the beam projected onto photographic film or a video camera to record the data.

2.5.3 Diffraction

The electron waves which exit from the sample consist of a forward scattered wave that travels along the optic axis of the microscope and of waves that are scattered over a small angle with respect to the optic axis. The objective lens focuses the forward scattered beam to a point on the optic axis in its back focal plane; as illustrated in the ray diagram in Fig. 2.9.

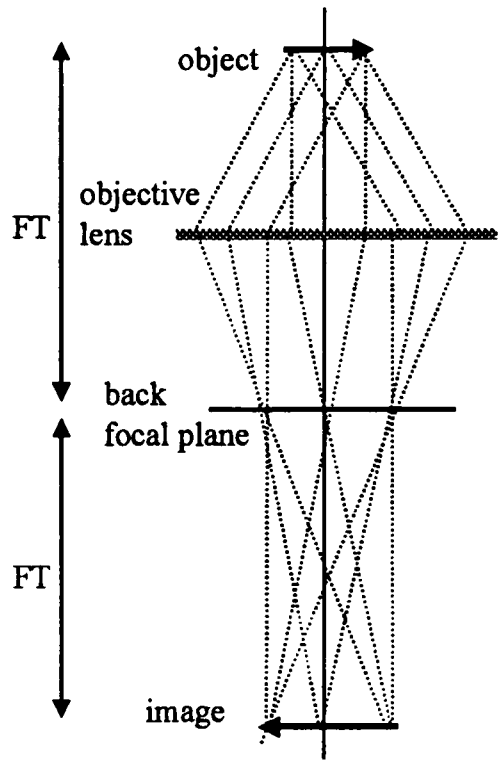


Figure 2.9 Ray diagram representing the formation of a diffraction pattern in the back focal plane and of an inverted, enlarged image.

Waves that are scattered from any point in the sample into a certain direction are also focused in the back focal plane, at a distance from the optical axis which is given by Bragg's law [13]

$$2d \sin\theta = n\lambda . \qquad (2.2)$$

The intensity distribution of the electron waves in the back focal plane forms a Fraunhofer diffraction pattern. Mathematically, the amplitude of the waves in the back focal plane is given by the Fourier transform of the amplitude of the waves that exit the sample. Physically, this means that the information about the sample contained in the waves is presented not in real space but in *reciprocal space*. As a consequence, the structural information contained in

the diffraction pattern is *non-local*; it is information about the *average* configuration of the atoms in the sample. This electron diffraction pattern can be projected onto the fluorescent screen by adjusting the strength of the intermediate lens. A post-specimen ray diagram of the electron beam in diffraction mode is shown in Fig. 2.10.

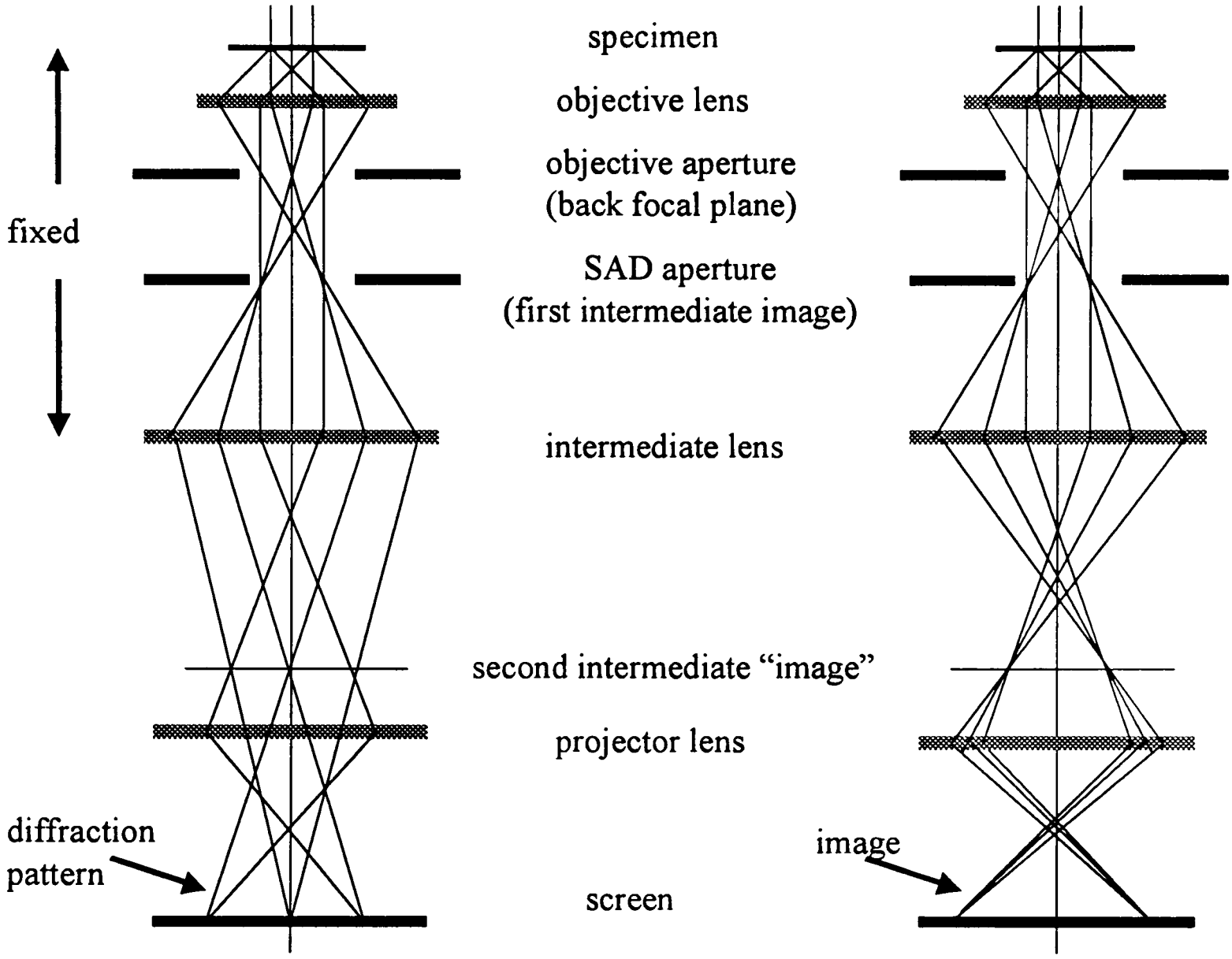


Figure 2.10 Ray diagram of the electron beams in a TEM in diffraction mode (left) and imaging mode (right).

2.5.4 Imaging

After the rays pass through the back focal plane of the objective lens, rays that are scattered from the same point of the specimen in different directions are brought together to focus in what is called the image plane. As can be seen from Fig. 2.10, the image is an inverted,

magnified reproduction of the object. Mathematically, this means that the amplitude of the waves in the image plane is re-created from the amplitude of the waves in the back focal plane by taking the inverse Fourier transform.

But what causes image contrast in a TEM image? There are two main types of image contrast; phase contrast [14] and amplitude contrast. The latter is sub-divided into bright field and dark field contrast [12]. Bright field contrast is obtained by putting an aperture in the back focal plane that lets through the undiffracted beam, but none of the other beams. As diffraction occurs from features in the structure, these features will appear in dark contrast against a bright featureless background [15]. Dark field contrast is obtained by letting through only one of the diffracted beams. Therefore, a dark field image will look like the "negative" image of the bright field image in that the features will now look bright compared to the dark featureless background. Phase contrast imaging was not used in this study.

2.5.5 *In-situ* annealing

The TEM sample holder that was used for the crystallisation experiments was fitted with a heating coil located in a furnace around the sample and a thermocouple, located inside the coil. In this way, the sample could be heated inside the TEM while changes to the image or diffraction pattern were followed in real time. The heating current was manually controlled and the temperature indicated digitally on a screen. The observed changes in the structure during heating were monitored by recording the image on video tape. A video recorder was used, which recorded a video frame every 40 ms. Each of the individual frames has a time code so that by analysing the frames, the speed of the observed changes in the structure could be quantified.

2.5.6 Electron energy loss spectroscopy (EELS) [12, 16]

A TEM can be used to measure the EELS [17, 18] spectrum of the sample. The electron beam is focused to a small probe on the sample. The transmitted beam is now not used to obtain a diffraction pattern or an image, but the energy spectrum of the beam is analysed. This is done by passing the beam through a "magnetic prism", which disperses the beam in terms of its electron energy. The resulting spectrum is then focused onto a detector to count the number of electrons with a certain energy.

If all scattering that occurs in the sample were elastic, the energy loss spectrum would consist of a peak at zero position (the energy loss is zero by definition if scattering is elastic) with a width corresponding to the spread in the accelerating voltage. However, when inelastic scattering occurs, the EELS spectrum will show structure at higher energy as well. In the range of 0 - 50 eV, the energy loss is a result of the interaction of the electron beam with the valence electrons in the material. In particular, it shows a large peak around 15 - 20 eV, depending on the density of the valence electrons, that corresponds to the excitation energy of a plasmon. A plasmon is a collective oscillation of the valence electrons and will be discussed in more detail in section 5.3.1. EELS was used to measure the plasma energy, i.e. the position of the plasmon peak. At higher energy loss, absorption peaks corresponding to the excitation of inner electron shells are observed, but EELS spectra were not measured in this energy regime in this work. A TEM equipped with a field emission gun (FEG) is used to perform EELS experiments, as this gives a zero loss peak with a width of a few eV only.

2.5.7 Determining the radial distribution function (RDF)

Electron diffraction experiments were performed on a JEOL 3000F FEGTEM. The diffraction patterns were recorded using a charge coupled device (CCD) camera and saved as

a Digital Micrograph file. The data were then transferred to SEMPER, an image processing software package. From these diffraction patterns, the radial distribution function is calculated; the details of this procedure are described in chapter VIII.

2.5.8 Sample preparation

The $Ge_2Sb_2Te_5$ films used for the TEM experiments had a thickness of approximately 25 nm, which, for this material, is thin enough to allow transmission of a 300 - 400 keV electron beam. Therefore, there was no need to thin the samples. The films were sputter-deposited on carbon-coated mica. The carbon layer, approximately 30 nm thick, has the function of a "release layer" and enables the film to be separated from the mica. To do that, the sample is first cut into small squares, typically 4 mm^2, using a razor blade. These squares are then picked up with a pair of tweezers and carefully submerged, substrate side down, into distilled water contained in a small "floating dish". If this is done at a slight angle, the surface tension between the water and the film will pull the film, together with the release layer, off the mica, leaving the film floating on the water and the mica submerged. The film is then picked up on a copper TEM grid and carefully dried by touching the bottom of the grid with a piece of paper, which absorbs the water between the film and the grid so that the film ends up making good contact with the grid bars. This ensures good heat conduction from the grid bars to the sample, which is essential for the *in-situ* heating experiments. The carbon release layer of the samples used for the RDF experiments was removed by plasma cleaning for 5 minutes with a Fischione 1020 plasma cleaner.

2.6 The IR-VIS-UV spectrophotometer

2.6.1 Introduction

An IR-VIS-UV spectrophotometer (often simply referred to as a "spectrometer") can be used to measure the reflectivity and the transmittivity of a material from the infra red (IR) through the visible (VIS) to the ultra violet (UV) range of the optical spectrum.

The instrument used in this study was a Perkin-Elmer Lambda 19 (PE λ-19) IR-VIS-UV spectrophotometer, which operates in the wavelength range of 200 - 2000 nm, at a wavelength resolution of 0.2 nm. How this instrument works is described in the next section.

2.6.2 Instrumental set-up

The Perkin-Elmer λ-19 spectrophotometer essentially consists of [19]: 1) a light source that emits light in a broad spectral range, 2) a diffraction grating (monochromator) that disperses the light according to wavelength, producing a spectrum of light, 3) a slit to select a particular wavelength from this spectrum, 4) a sample compartment where the light is reflected/transmitted by the sample into 5) the detector.

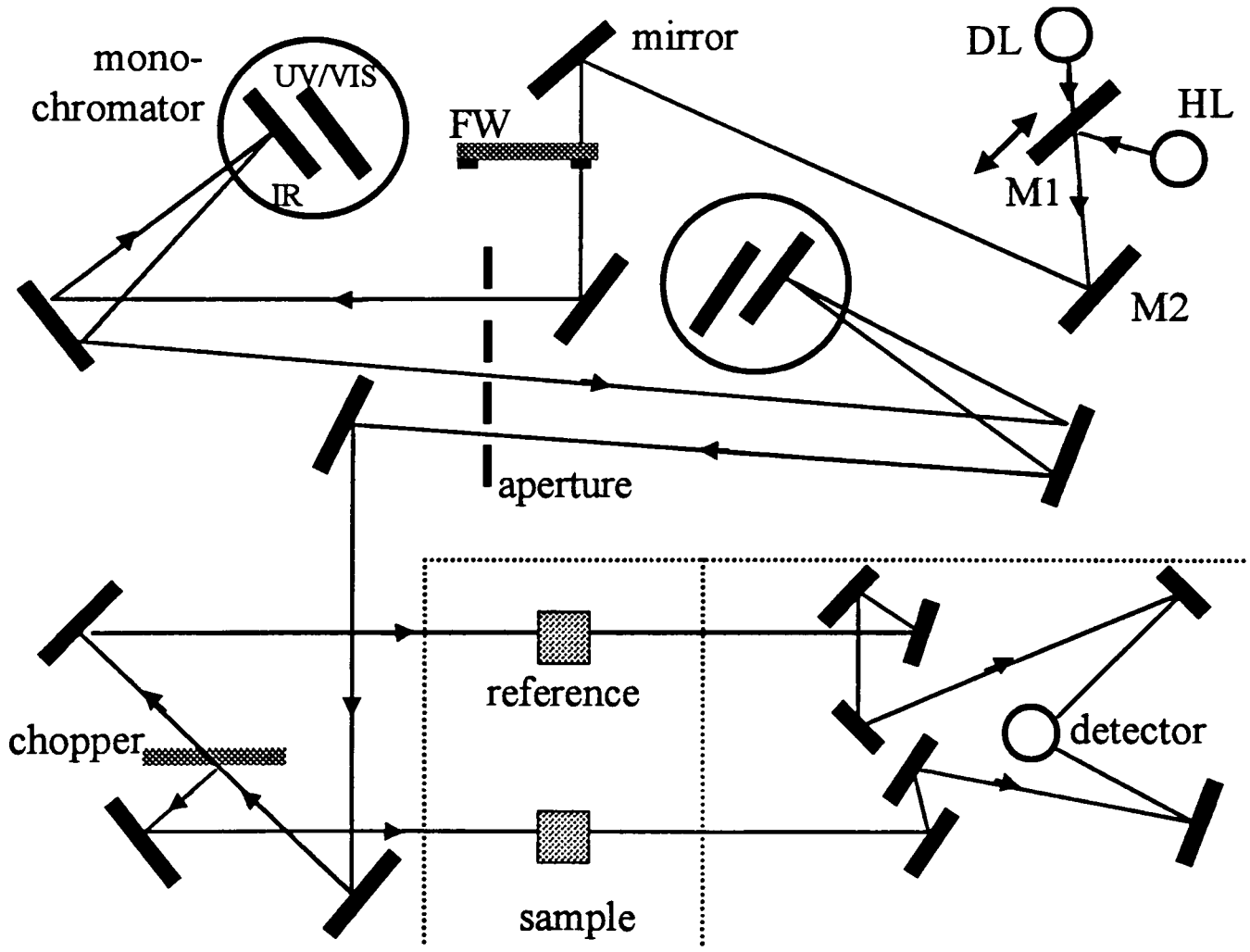


Figure 2.11 Schematic representation of the Perkin-Elmer λ-19 spectrometer.

Fig. 2.11 shows a schematic of the optical system of the Perkin-Elmer Lambda 19 spectrophotometer. To cover the broad range of wavelengths, two light sources are used; a halogen lamp (HL) covering 200 - 320 nm and a deuterium lamp (DL) covering 320 - 2000 nm. The halogen lamp is selected when the source mirror (M1) blocks the light from the deuterium lamp and reflects the light of the halogen lamp onto mirror M2. When the source mirror is removed, the light from the deuterium lamp is reflected by M2 while the light from the halogen lamp misses the mirror completely. The source change is automatic. Depending on the wavelength being produced, the beam is then pre-filtered by one of the optical filters on the filter wheel (FW) assembly. To achieve the small wavelength resolution, the light then passes two (identical) monochromators. Each of these consists of two diffraction gratings; one for the NIR range and one for the UV-VIS range. Now that the desired wavelength is selected, the beam is split by a chopper. The chopper consists of a rotating disc with four segments on it; a mirror, reflecting the beam through the sample; an absorbing segment, allowing the detector to measure the dark signal; a window segment, creating a reference beam and a second absorbing segment. Both beams are then directed into the same detector. Two detectors are also used; a PbS detector covers 200 - 860 nm and a photo multiplier covers the 860 - 2000 nm range. The detector change is automatic.

2.6.3 How R and T are calculated

The PE λ-19 is connected to a PC, which calculates either the reflectivity or the transmittivity of the sample from the detector output, as a function of wavelength.

In transmission mode, the transmittivity of the sample is simply given by

$$T = \frac{I_S - I_D}{I_R - I_D} \qquad (2.2)$$

I_S and I_R are the intensities of the sample beam and the reference beam, respectively, and I_D is the dark signal. Note that the reference beam *passes through* the window of the chopper and is reflected into the detector by *five* mirrors while the sample beam is *reflected* by the chopper and then reflected into the detector by *four* mirrors. This set-up is used because no mirror reflects *all* the incoming light so that both beams must pass the same number of mirrors, otherwise eq (2.2) does not yield $T = 1$ even if the sample were to transmit all the incoming light.

In reflectivity mode, things are a little bit more complicated. A "reflectivity attachment", consisting of two additional mirrors, is used to reflect the beam onto the sample and back into the detector. As there are now two extra reflectors in the path of the sample beam, a reference run is needed to correct for the fact that the reflectivity of the prism used in the reflectivity attachment is not unity. In the reference run, an Al mirror is used, which is assumed to have a reflectivity of 1. Thus, the *reference run* produces

$$R_{ref} = \frac{I_{Al} - I_D}{I_R - I_D}, \qquad (2.3)$$

while the *sample run* yields

$$R_S = \frac{I_S - I_D}{I_R - I_D}, \qquad (2.4)$$

from which the reflectivity of the sample can be calculated:

$$R = R_S \cdot \frac{R_{Al}}{R_{ref}}, \qquad (2.5)$$

where R_{Al} is the reflectivity of aluminium, which was looked up in the literature.

The systematic error in the reflectivity is approximately 10 % (as always, this is a *relative* error; if the result of a measurement of the reflectivity is 50 %, this means the real value probably lies between 45 % and 55 %).

2.7 Ellipsometry

2.7.1 Introduction

Ellipsometry [20] is a technique that can be used to determine the optical constants of a material. There are spectroscopic ellipsometers on the market, but the equipment used in this study used a monochromatic light source; a red laser with wavelength 633 nm.

2.7.2 Theory

To understand how ellipsometry [21] works, some fundamental aspects of light [22, 23] need to be reviewed. A light wave propagating in a certain direction consists of an electric field vector and a magnetic field vector, which are both perpendicular to the direction of propagation; i.e. light is a transverse electromagnetic (EM) wave. To understand ellipsometry, only the electric field vector needs to be considered. The magnitude, A, of this electric field vector as a function of position, x, and time, t, is

$$A = A_0 \sin\left(-\frac{2\pi}{\lambda}(x - vt) + \delta\right) \qquad (2.6)$$

where A_o is the amplitude of the electric field, λ is the wavelength of the light, v its velocity and δ is an arbitrary phase factor. The electric field vector can point in any direction perpendicular to the direction of propagation.

When the electric field vectors of the light waves in a beam have no preferred orientation, the light is referred to as *unpolarised*. Light sources generally emit unpolarised light. When

the field vectors of the light waves in a beam all lie in a single plane, the light is referred to as *linearly polarised* because the field vectors seem to lie on one line when looked at along the direction of propagation. Now consider two linearly polarised waves, with the same amplitude, that are in phase, with perpendicular polarisation directions. The sum of two such waves is again a linearly polarised wave, with the polarisation direction at an angle of 45° to the original beams. If the amplitude of the original waves were not the same, the resultant wave would still be linearly polarised, but not at 45° to the original beams. If the two original beams would be out of phase, the field vector of the resultant beam would rotate around the direction of propagation. In the case that this phase difference is 90°, the field vector, when looked at along the direction of propagation, appears to rotate around a circle. This type of light is referred to as *circularly polarised.* It is easy to see that when the phase difference is not 0° or 90°, the field vector will rotate along an ellipse. This type of light is referred to as *elliptically polarised.*

2.7.3 The ellipsometer; measuring Δ and Ψ

In an ellipsometry experiment, the "ellipsometry parameters" Δ and Ψ (not to be confused with the effective transition energy Δ and the wave function Ψ that appear in chapter V) are measured, from which the optical constants can be calculated. Fig. 2.12 shows a conceptual schematic of an ellipsometer. The light source, in this case a red laser, produces polarised light of wavelength 633 nm. The light is passed through a polariser, reflected off the sample, then passed through a quarter wave plate (rotatable along the beam axis) and a second polariser (also rotatable along the beam axis) which is called the analyser. The intensity of the light that passes through this set-up is measured by a photo multiplier.

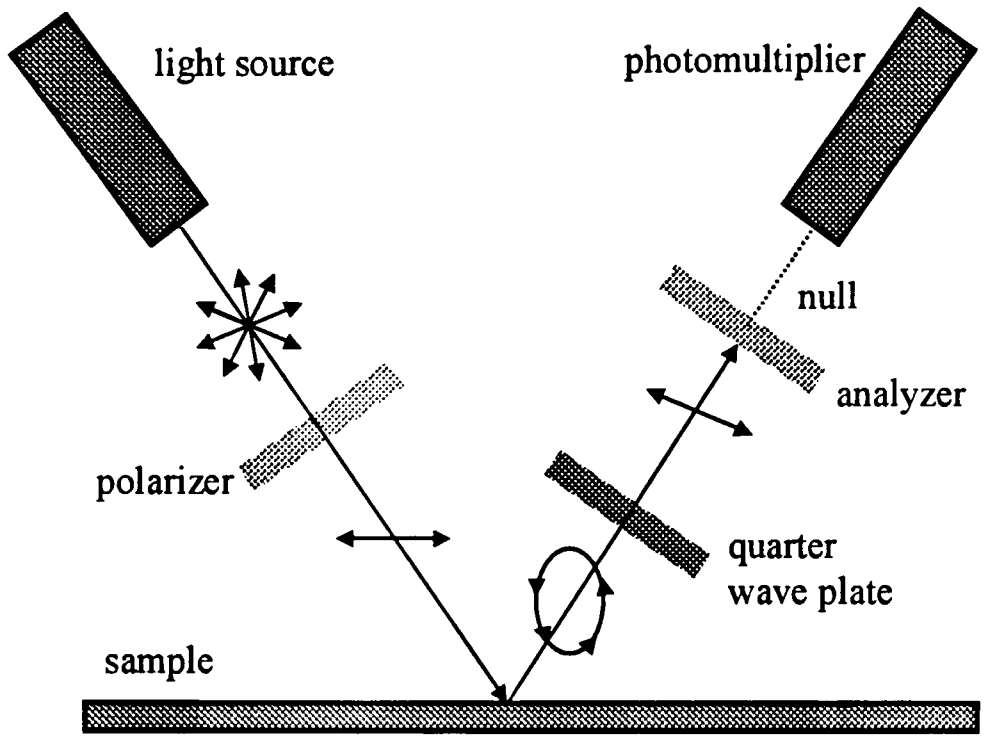


Figure 2.12 Schematic diagram of an ellipsometer set-up.

Assume first that the polarisation angle of the incident beam is 45°, so that the incident light contains an equal amount of s- and p-polarised light. Upon reflection from the sample, both components experience a phase shift. δ_i and δ_r are defined as the phase differences between the s and p polarised components of the incident and reflected waves. Their difference, Δ, is defined as

$$\Delta \equiv \delta_i - \delta_r . \qquad (2.7)$$

Thus, Δ is the phase difference that occurs upon reflection; it ranges from 0° to 360°. As a result of this change in phase, the reflected light will generally be elliptically polarised. Fig. 2.13 shows the polarisation of the reflected beam as a function of Δ.

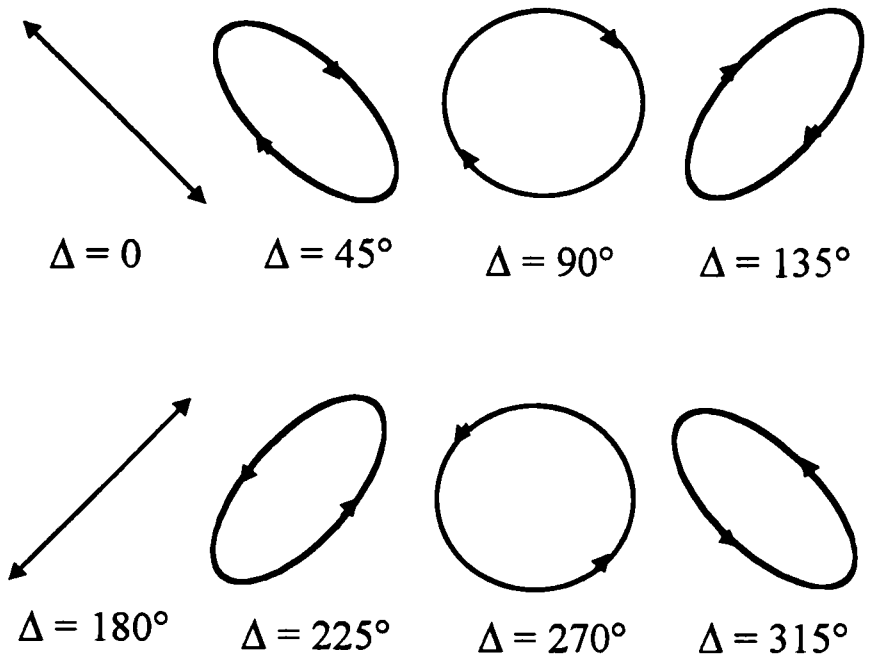


Figure 2.13 Polarisation of the reflected beam as a function of Delta.

When properly orientated, the quarter wave plate changes the polarisation from elliptical to linear, without changing the polarisation direction (i.e. the orientation of the linearly polarised light coincides with the axis of the ellipse). The correct orientation is found by rotating the quarter wave plate so as to optimise the signal of the photo multiplier. Finally, the analyser is rotated to minimise the signal of the photo multiplier. The relative angular displacement between the two polarisers is equal to Δ.

In general, the reflectivity, defined as the ratio of the intensities of the reflected and incoming beams, depends on the polarisation direction of the incoming light. We define Ψ through

$$\tan \Psi \equiv \sqrt{\frac{R^p}{R^s}} . \qquad (2.8)$$

where R^p and R^s are the reflectivities for s- and p-polarised light, respectively. These reflectivities can be measured by rotating the polariser to obtain p- or s- polarised incident

light, respectively, and measuring the intensity in the reflected beam with the photo multiplier. Hence, Ψ is obtained through eq (2.8).

2.7.4 Calculating the optical constants from Δ and Ψ

All optical properties of a material can be described in terms of the complex refractive index:

$$\tilde{n} = n + ik\,, \qquad (2.9)$$

where n is the refractive index as it appears in Snell's law and k is the absorption coefficient. n and k are usually referred to as "the optical constants"; they are *constant* in the sense that they are materials properties, but they generally are a *function* of the wavelength of the incident light.

As Δ and Ψ are optical properties, they can be expressed in terms of n and k of the film, assuming that the film thickness and the optical properties of the substrate are known. In the present studies, the optical properties of the substrate are taken from the literature, whilst the film thickness is accurately determined in an independent measurement (see section 7.3). Conversely, the optical constants can be obtained by measuring Δ and Ψ and determining the values of n and k that give the experimentally determined values of Δ and Ψ. This is done graphically, using so-called Δ/Ψ trajectories. These are curves in the Δ - Ψ plane of either constant n or constant k. The optical constants are found iteratively as follows:

1) guess a value for k

2) use the first Δ - Ψ trajectory to find the corresponding n

3) with this value of n, use the second Δ - Ψ trajectory to find a first approximation for k etc.

The iteration is stopped when the optical constants no longer change significantly with each iteration. In practice, this procedure converges in only a few iterations. The accuracy of the values for n and k determined in this way for a typical error in the film thickness (see section

7.3), is estimated to be a few percent only. An example of a Δ - Ψ trajectory for k is given in Fig. 2.14.

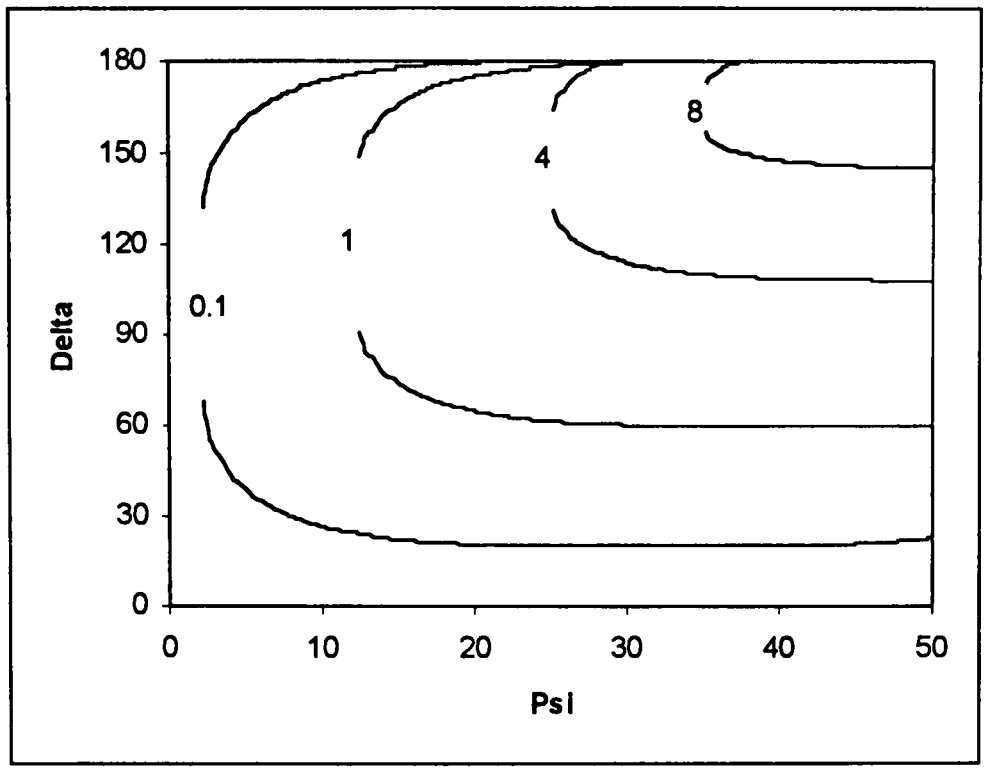


Figure 2.14 Example of a Delta - Psi diagram for the absorption coefficient, showing the contours $k = 0.1$, $k = 1$, $k = 4$, $k = 8$ and $k = 0.1$.

References

[1] J.L Vossen and W. Kern (ed.) in *Thin Film Processes*,

Academic Press, London (1991) p. 19.

[2] E.D. McClanahan and N. Laegreid in *Sputtering by Particle Bombardment III*,

R. Behrisch and K. Wittmaack (ed.), Springer Varlag, Berlin, Chapter VII (1991).

[3] G.S. Anderson, Wm. N. Mayer and G.K. Wehner,

J. Appl. Phys. **33** nr. 10 (1962) p. 2991.

[4] P.J. Kelley and R.D. Arnell, *Surface Coatings and Technology* 86/87 (1996) p. 425.

[5] S.A.E. Johansson, J.L. Campbell and K.G. Malmqvist (Ed.), *Particle-Induced X-Ray Emission Spectroscopy (PIXE)*, John Wiley & Sons, New York (1995).

[6] http://www.supernet.net/~pixe/pixe.html

Copyright © 1997 by PIXE Analytical Laboratories, Tallahassee, Florida, USA

[7] http://users.ox.ac.uk/~spm1/pixe.htm

Oxford University, Oxford, United Kingdom

[8] D.K. Bowen and M. Worthington, *Adv. X-Ray Anal.* **36** (1993) p. 171.

[9] K. Stoev and K. Sakurai, *The Rigaku Journal* **14** nr. 2 (1997) p. 22.

[10] L.G. Kiessig, Ann. Phys. **10** (1931) pp. 715 and 769.

[11] L. Parratt, Phys. Rev. **95** (1954) p. 359.

[12] D.B. Williams and C.B. Carter, *Transmission Electron Microscopy*,

Plenum Press, New York (1996).

[13] C. Kittel, *Introduction to Solid State Physics* 6th ed., John Wiley & Sons, Inc. (1986).

[14] O. Scherzer, *J. Appl. Phys.* **20** (1949) p. 20.

[15] P.B. Hirsh, A. Howie, R.B. Nicholson, D.W. Pashley and M.J. Whelan,

Electron Microscopy of Thin Crystals, Butterworths (1965).

[16] R.F. Egerton, *Electron Energy-Loss Spectroscopy in the Electron Microscope* 2nd Ed., Plenum Press, New York (1996).

[17] J. Hillier and R.F. Baker, *J. Appl. Phys.* **15** (1944) p. 663.

[18] http://interface.phy.uic.edu/research/techniques/eels.html

[19] *Perkin-Elmer Lambda 19 UV/VIS/NIR Spectrometer Instrument Manual*, Bodenseewerk Perkin-Elmer GmbH, Ueberlingen (1993).

[20] H. G. Tompkins, *A User's Guide to Ellipsometry*, Academic Press Limited, London (1993).

[21] R.M.A. Azzam and N.M. Bashara, *Ellipsometry and Polarised Light*, North Holland Publishing Co., Amsterdam (1977).

[22] G.S. Monk, *Light*, Dover, New York (1963).

[23] M. Born and E. Wolf, *Fundamentals of Optics*, Pergamon Press, New York (1969).

CHAPTER III

Johnson-Mehl-Avrami-Kolmogorov Kinetics

3.1 Introduction

The crystallisation of the amorphous bits of information in a phase-change medium, is governed by the nucleation and growth of crystallites in the amorphous matrix. The transformation rate as a function of temperature is of crucial importance to the stability of the bits at the temperature of operation and to the time it takes to erase a bit during laser heating. In this chapter, the theory of nucleation and growth kinetics is described in detail in order to be able to interpret the experimental results presented in the next chapter.

Johnson-Mehl-Avrami-Kolmogorov (JMAK) transformation kinetics describe the extent to which a material is transformed during a certain phase transformation, as a function of temperature and time. This information is contained in the JMAK parameters, which are constant with respect to time and temperature. Crystallisation of amorphous materials and other solid state phase transformations are examples of transformations that are described by JMAK kinetics. The equations that describe the JMAK kinetics were first derived for transformations under isothermal heating conditions [1–4]. Efforts have also been made to derive the JMAK equations under linear heating conditions [5–8]. The main interest for the linear heating JMAK equations lies in the fact that linear heating experiments are much

faster than isothermal experiments, so that it takes less time to determine the JMAK parameters from a linear heating experiment. Also, isothermal experiments have the drawback that the sample needs to be heated to the desired temperature in a time that is much smaller than the transformation time. However, it is not obvious how the parameters determined from isothermal and linear heating experiments are related. This problem is treated in this chapter, following a rather formal approach.

First, the *integral* form of the JMAK equations, which does *not* depend on the temperature-time path, is presented. Then, the JMAK equations are derived for constant temperature and under linear heating conditions. Several ways of determining the JMAK parameters are discussed and the relation between the isothermal and the linear heating JMAK parameters is rigorously derived.

3.2 The JMAK equations in integral form

Around 1940, various authors (see e.g. [1–3]) independently developed a description of isothermal transformation reactions based on nucleation and growth. Some four decades later, several authors [5–7] used this isothermal theory as a starting point for describing the transformation kinetics under non-isothermal annealing conditions. As this procedure is conceptually wrong (but sometimes does yield numerically correct JMAK parameters), the JMAK equation is here presented first in a general integral form. The isothermal and linear heating JMAK equations are then derived by integrating along the corresponding temperature – time path.

3.2.1 Nucleation and growth [9]

Consider a system of volume V that undergoes the phase transformation $\alpha \rightarrow \beta$. The volume of the transformed region is V^{β}, the volume of the untransformed region is V^{α} and $V = V^{\alpha}$

+ V^{β}. The volume fraction of transformed material is V^{β}/V.

Consider a nucleus formed at time $t = \tau$. After time τ, the size of the nucleus increases continuously according to

$$v = v(t, \tau) \qquad \text{for} \quad t \geq \tau \tag{3.1}$$

and $$v = 0 \qquad \text{for} \quad t < \tau \tag{3.2}$$

where v is the volume of a region of phase β originating at time $t = \tau$. Suppose that between times τ and $(\tau + \mathrm{d}\tau)$ a certain number of nuclei are formed in the untransformed region with volume V^{α}. This number is $IV^{\alpha}\mathrm{d}\tau$ and defines the nucleation rate I at time τ.

During the initial stages of the transformation, when $V^{\beta} << V^{\alpha}$, the nuclei are widely spaced and the interference of neighbouring nuclei is negligible. Under these conditions, the transformed volume at time t resulting from regions nucleated between τ and $(\tau + \mathrm{d}\tau)$ is

$$dV^{\beta} = v(t, \tau) I(\tau) V^{\alpha} d\tau \,. \tag{3.3}$$

Since V^{α} is effectively constant during this stage of the transformation and equal to V, the total volume transformed at time t is

$$V^{\beta} = V \int_{\tau=0}^{t} v(t, \tau) I(\tau) d\tau \,. \tag{3.4}$$

3.2.2 The extended volume

Eq (3.4) is valid only during the initial stages of the transformation. To include the later stages of the transformation, the fact that growth slows down because transformed regions will eventually impinge (growth stops) and because the untransformed region becomes smaller (fewer nuclei can form), should be included. The problem is purely geometrical. During the time $\mathrm{d}\tau$ when $IV^{\alpha}\mathrm{d}\tau$ new transformed regions are nucleated, it may also be considered that $IV^{\beta}\mathrm{d}\tau$ regions would have nucleated in the transformed portion of the system,

had not transformation previously occurred there. Avrami described these as phantom nuclei and went on to define an "extended" volume of transformed material, V_e^{β}, by the relation

$$V_e^{\beta} = (V^{\alpha} + V^{\beta}) \int_{\tau=0}^{t} v(t,\tau) I(\tau) \mathrm{d}\tau \,. \qquad (3.5)$$

V_e^{β} differs from the actual volume of transformed material in two ways. Firstly, phantom regions, regions that nucleated in already transformed material, have been included. Secondly, all regions have been treated as though they continued growing, irrespective of other regions. The extended volume may be larger than the real volume of the system, V, because some elements of the transformed volume are counted twice, others three times and so on. The significance of V_e^{β} is that it is simply related to the kinetic laws of growth, which may be separated from the geometrical problem of impingement. So now the relation between V_e^{β} and V^{β} has to be found.

3.2.3 Relation between real and extended volume

Consider any small random region, of which a fraction $1 - (V^{\beta}/V)$ remains untransformed at time t. During a further time $\mathrm{d}t$, the extended volume of β in the region will increase by $\mathrm{d}V_e^{\beta}$, and the true volume by $\mathrm{d}V^{\beta}$. Of the new elements of volume which make up $\mathrm{d}V_e^{\beta}$, a fraction $1 - (V^{\beta}/V)$ on average will lie in already transformed material. This result clearly follows only if $\mathrm{d}V_e^{\beta}$ can be treated as a completely random volume element and it is for this reason that phantom nuclei have been included in the definition of $\mathrm{d}V_e^{\beta}$.

The above arguments are based on the assumption that nucleation is random, in the sense that if the system is divided into small equal volume elements, the probability of forming a nucleus in unit time is the same for all these elements. The treatment does not preclude the possibility that nuclei form preferentially at certain sites in the β phase, but as developed

here, it may be applied to experimental observations when the sampled volume contains several such sites.

The relation between V^β and V_e^β is now written in the form

$$\mathrm{d}V^\beta = \left(1-(V^\beta/V)\right)\mathrm{d}V_e^\beta \tag{3.6}$$

or $$-V\frac{\mathrm{d}\left(1-(V^\beta/V)\right)}{1-(V^\beta/V)} = \mathrm{d}V_e^\beta \tag{3.7}$$

which can be integrated to give

$$V^\beta/V = 1-\exp(-V_e^\beta/V)\,. \tag{3.8}$$

Defining, for convenience of notation,

$$x \equiv V^\beta/V \tag{3.9}$$

and $$x_e \equiv V_e^\beta/V\,, \tag{3.10}$$

the volume fraction of transformed material, x, can be written

$$x(t) = 1-\exp(-x_e(t)) \tag{3.11}$$

with $$x_e(t) = \int_{\tau=0}^{t} v(t,\tau)I(\tau)\mathrm{d}\tau\,. \tag{3.12}$$

Note that eq (3.4) is effectively given by the first term in the expansion of the right hand side of eq (3.11), so that the two expressions become equivalent as $t \to 0$ in accordance with the assumptions made in deriving eq (3.11). From the second term in the expansion it can be deduced that in order to have $x \approx x_e$ to one percent accuracy, x_e must be smaller than 0.14, i.e. before 14 % by volume of the material has transformed.

Assuming isotropic growth in b dimensions, the nuclei formed at time τ will have a volume

$$v(t,\tau) = g\left[R(t,\tau)\right]^b \tag{3.13}$$

where g is a geometrical factor of order unity and R is the radius of the particle. For a certain growth rate $G(t)$, the particle radius will increase as

$$R(t,\tau) = \int_{\theta=\tau}^{t} G(\theta)\mathrm{d}\theta \tag{3.14}$$

where θ is a dummy parameter of dimension time, that runs from the moment the nucleus is formed, τ, until t, the time after the beginning of the annealing experiment.

3.3 The Isothermal JMAK Equations

The isothermal JMAK equations are

$$x(t) = 1 - \exp(-kt^n) \tag{3.15}$$

$$k(T) = k_0 \exp\left(-\frac{\Delta H}{k_B T}\right) \tag{3.16}$$

where k_B is the Boltzmann constant and n, ΔH and k_0 are the JMAK parameters. n is often called the *transformation index* or *Avrami exponent*, ΔH is usually referred to as the "activation energy" and k_0 simply as the pre-exponential constant of the *rate factor*, k. Thus, eqs (3.15) and (3.16) describe the volume fraction of material transformed as a function of time t and temperature T in terms of three materials constants. These equations can be derived for a number of distinct cases of nucleation and growth. Four of these cases are presented in this section. The relation between the JMAK parameters and the nucleation and growth parameters is given for the cases considered. It is explained how to obtain the JMAK parameters from experiment. Finally, the isothermal JMAK reaction rate equation is derived.

3.3.1 Four special cases [10]

Case 1: Fixed number of nuclei and constant growth rate.

Assume that at the start of the transformation a fixed number, N, of nuclei is present per unit volume and no nuclei are formed during the transformation. Mathematically, this is the same as saying that the nucleation rate, I, is equal to

$$I(\tau) = N\delta(\tau) \tag{3.16}$$

where $\delta(\tau)$ is the Dirac delta function (see Appendix IIIA for the properties of the delta function), so that N nuclei are created at $\tau = 0$ with none created at subsequent time. If the growth of the particles is *interface controlled* (i.e. determined by what happens at the interface between the two phases only) the growth rate, G, is constant with respect to time. Assuming an Arrhenian temperature dependence, so that

$$G = G_0 \exp\left(-\frac{E_g}{k_B T}\right) \tag{3.17}$$

where E_g is the activation energy for growth and G_0 is a constant. Putting eq (3.17) into Eq (3.14), it can be seen that

$$R(t,\tau) = (t-\tau)G \tag{3.18}$$

as G is not a function of time. Putting eq (3.18) into eq (3.13) gives

$$v(t,\tau) = g(t-\tau)^b G^b . \tag{3.19}$$

Putting this and eq (3.16) into eq (3.12) yields

$$x_e(t) = gNG_0^b \exp\left(-\frac{bE_g}{k_B T}\right)t^b \tag{3.20}$$

by the properties of the delta function and from eq (3.17).

Comparing eqs (3.11) and (3.12) to eqs (3.15) and (3.16), yields the isothermal JMAK equation as well as expressions for the JMAK parameters:

$$n = b \qquad \Delta H = bE_g, \qquad k_0 = (g/n)NG_0^b, \tag{3.21}$$

for this particular case.

Case 2: Constant nucleation and growth rates.

Assume the nucleation rate is independent of time and follows an Arrhenian temperature dependence:

$$I = I_0 \exp\left(-\frac{E_n}{k_b T}\right) \tag{3.22}$$

where E_n is the activation energy for nucleation and I_0 is a constant.

Following the same steps as for the last case, it can be shown that

$$n = 1 + b \qquad \Delta H = E_n + bE_g, \qquad k_0 = (g/n) I_0 G_0^{\,b}, \tag{3.23}$$

for this case.

Case 3: Fixed number of nuclei and parabolic growth rate

When the chemical composition of the parent and product phases is not the same, growth of the interface needs to be accompanied by diffusion of atoms to and away from the interface. As growth progresses, a concentration gradient will build up and atoms need to diffuse over increasingly large distances, which slows down the growth process. Growth is then said to be *diffusion controlled* and the growth rate is equal to

$$G(t) \equiv \frac{dR}{dt} = \frac{D}{R(t)} \tag{3.24}$$

where D is the diffusion coefficient, which is assumed to depend on temperature according to

$$D = D_0 \exp\left(-\frac{E_d}{k_B T}\right). \tag{3.25}$$

Separating the R and t variables in eq (3.24) gives

$$RdR = Ddt \tag{3.26}$$

which can be integrated from 0 to R and τ to t on each side, respectively, to give

$$\frac{1}{2}R^2 = (t-\tau)D, \qquad (3.27)$$

which is essentially $R(t,\tau)$. The rest of the derivation is analogous to the previous cases and the JMAK parameters are then

$$n = b/2 \qquad \Delta H = (b/2)E_g, \qquad k_0 = (g/n)N D_0^{b/2}, \qquad (3.28)$$

for this case.

Case 4: Constant nucleation rate and parabolic growth rate

The derivation of this case follows from cases 1 and 3 and gives for the JMAK parameters

$$n = 1 + (b/2), \quad \Delta H = E_n + (b/2)E_g, \quad k_0 = (g/n)I_0 D_0^{b/2}. \qquad (3.29)$$

Note: it was assumed that the temperature dependence of the nucleation and growth rate is Arrhenian. This is true if the kinetics of the nucleation and growth processes follow Boltzmann statistics. The Boltzmann factor $\exp\left(-\frac{\Delta E}{k_B T}\right)$ then corresponds to the *fraction* of atoms that have a thermal energy larger than the energy barrier ΔE. But this is only true if this fraction is *small*, that is if $k_B T << \Delta E$. Thus, eqs (3.15) and (3.16) only hold if

$$\Delta E_n >> k_B T \qquad (3.30)$$

and $$\Delta E_g >> k_B T\,. \qquad (3.31)$$

These equations will be needed in deriving the linear heating equations, but it is emphasised that the restrictions apply equally under isothermal conditions.

3.3.2 The isothermal JMAK parameters

Ranganathan *et al.* [10] suggested combining the four cases discussed above by writing the Avrami exponent as

$$n = a + bc\,. \tag{3.32}$$

The *nucleation index*, a, is 0 when no nuclei are formed during the transformation and 1 when the nucleation rate is constant. In fact, it can be shown [11] that eq (3.32) holds for any $a > 0$ when the time dependence of the *number* of nuclei is proportional to t^a:

$$N(t) \propto t^a\,, \tag{3.33a}$$

or $$I(t) = I_o t^{a-1} \exp\left(-\frac{E_n}{k_B T}\right) \tag{3.33b}$$

for the nucleation *rate* with an Arrhenian temperature dependence. Thus, for $0 < a < 1$, the nucleation rate decreases with time and $a > 1$ when the nucleation rate increases with time. The *morphology index*, b, which indicates in how many dimensions the nuclei grow (i.e. b is 1 when they grow as needles, 2 when they grow as discs and 3 when they form spheres) and a *growth index*, c, which is 1 for interface-controlled growth and 1/2 for diffusion-controlled growth.

The effective activation energy can then be written as

$$\Delta H = E_n + bcE_g\,. \tag{3.34}$$

From eqs (3.32) and (3.34), it can be seen that $\Delta H/n$ is a weighted average of the activation energy for nucleation and the activation energy for growth.

The pre exponential factor of the rate constant is given by

$$k_0 = \frac{g}{n} I_o G_o^{bc} \tag{3.35a}$$

or $$\ln(k_0) \approx \ln I_o + bc \ln G_o\,, \tag{3.35b}$$

as g/n is of the order unity. As the main contribution to pre-exponential factors like I_o and G_o is an attempt frequency, $k_o^{1/n}$ can be thought of as an *effective attempt frequency*.

3.3.3 Determining the isothermal JMAK parameters from experiment

Eq (3.15) can be rearranged to give

$$\ln(-\ln(1-x)) = \ln k + n \ln t \,. \tag{3.36}$$

If $x(t)$ is known from an isothermal annealing experiment at a temperature T_1, the left hand side of this equation can be plotted as a function of $\ln t$. If the transformation obeys JMAK kinetics, this yields a straight line with slope n. From the intercept with the ordinate, $k(T_1)$ can be determined.

Eq (3.16) can be written as

$$\ln k(T) = \ln k_0 - \frac{\Delta H}{k_B T} \,. \tag{3.37}$$

Thus, if $x(t)$ is known at a series of temperatures, $k(T)$ can be determined for each of these temperatures. Plotting $\ln k$ versus $1/k_B T$, a straight line is obtained with slope $-\Delta H$. The pre-factor k_0 can be obtained from the intercept with the ordinate.

3.3.4 The isothermal JMAK rate equation

The isothermal transformation rate can easily be determined by differentiating Eq (3.15) with respect to time

$$\frac{dx}{dt}(t) = nkt^{n-1} \exp(-kt^n) \,. \tag{3.38}$$

Because of the explicit relation between x and t, given by eq (3.15), the transformation rate can be expressed as a function of x

$$\frac{dx}{dt}(x) = nk^{\frac{1}{n}}(1-x)\left[-\ln(1-x)\right]^{1-\frac{1}{n}} \,. \tag{3.39}$$

This equation is usually referred to as the JMAK reaction rate equation. Eq (3.39) is of experimental importance because the reaction rate is proportional to the latent heat released per unit time during the transformation. As this heat flow can be measured in a calorimetry experiment, the JMAK parameters can be determined using eq (8.39).

3.4 The Linear Heating JMAK Equations

The linear heating JMAK equations were first derived by Woldt [8] for a number of nucleation modes and interface controlled growth. His approach is mathematically rather laborious and uses the exponential integral function to evaluate eqs (3.16) and (3.12). Here, a simpler route shall be followed, essentially by using eqs (3.30) and (3.31) to simplify integration earlier than Woldt does. In addition, the linear heating JMAK equation for diffusion controlled growth is derived for the first time in this work.

3.4.1 Novel derivation of the linear heating JMAK equation

The linear heating JMAK equations can be written as

$$x(t) = 1 - \exp(-k' t^{2n}) \tag{3.40}$$

with $$k'(\varphi, T) = k_0' \varphi^n \exp\left(-\frac{\Delta H}{k_B T}\right) \tag{3.41}$$

where φ is the heating rate, i.e.

$$T = \varphi t\,, \tag{3.42}$$

n and ΔH are given by eqs (3.32) and (3.34) and k_0' is a constant.

Comparing the isothermal and linear heating JMAK equations, it can be seen that that

1) the Avrami exponent differs by a factor two;

2) the rate factor in the linear heating case, $k'(\varphi,T)$, *implicitly* depends on time through $T = \varphi t$ and *explicitly* depends on the heating rate through the φ^n term.

Even though the Avrami exponents have been derived under isothermal [10] and linear heating [8] conditions, the fact that the results only differ by a factor of two seems to have gone unnoticed and the fact stated in this work for the first time.

Case 1: Constant nucleation rate, interface-controlled growth

For this case, the radius of the particle is obtained by putting the growth rate of eq (3.17) into Eq (3.14) under the linear heating condition defined by eq (3.42)

$$R(t,\tau) = G_o \int_{\tau}^{t} \exp\left(-\frac{1}{\alpha\theta}\right) \mathrm{d}\theta\,, \tag{3.43}$$

where $\alpha \equiv k_B\varphi/E_g$ is defined for convenience and θ is a dummy parameter in time.

Substituting $\xi = 1/\theta$ gives

$$R(t,\tau) = G_o \int_{1/\tau}^{1/t} -\xi^{-2} \exp\left(-\frac{\xi}{\alpha}\right) \mathrm{d}\xi\,. \tag{3.44}$$

Now, if it is assumed that, as ξ runs from $1/\tau$ to $1/t$, the $\exp(-\xi/\alpha)$ term varies much more quickly than the ξ^{-2} term, this gives

$$R(t,\tau) \approx G_o \xi^{-2} \int_{1/\tau}^{1/t} -\exp\left(-\frac{\xi}{\alpha}\right) \mathrm{d}\xi$$

$$= \left(\frac{G_o}{\alpha}\right)^c [f(t) - f(\tau)]^c \tag{3.45}$$

with $c = 1$, where it has been written for convenience

$$f(t) \equiv (\alpha t)^2 \exp\left(-\frac{1}{\alpha t}\right). \tag{3.46}$$

Putting eqs (3.13) and (3.45) into (3.12) gives

$$x_e(t) = \frac{C_o}{\alpha^{bc}} \int_0^t \left[f(t) - f(\tau)\right]^{bc} \exp\left(-\frac{\varepsilon}{\alpha\tau}\right) \mathrm{d}\tau \,, \tag{3.47}$$

where $C_0 \equiv gI_0 G_0^{bc}$ (3.48)

and $\varepsilon \equiv E_n / E_g$ (3.49)

have been defined for convenience. The power term $\left[f(t) - f(\tau)\right]^{bc}$ in eq (3.47) can be expanded as a binomial series and the integral evaluated analytically. This is done in Appendix IIIB and gives

$$x_e(t) = k'_o \, \varphi^{1+bc} t^{2(1+bc)} \exp\left(-\frac{E_n + bcE_g}{k_B \varphi t}\right) \tag{3.50}$$

with $k_0^{'} = gI_0^a G_0^{bc} C_1 \left(\frac{k_B}{E_g}\right)^{1+bc}$ (3.51)

where $C_1(bc, \varepsilon) = \sum_{j=0}^{\infty} \binom{bc}{j} \frac{(-1)^j}{j+\varepsilon}$ (3.52)

Putting eq (3.50) back into eq (3.11) and using eqs (3.32) and (3.34) finally leads to eqs (3.40) and (3.41) for $a = 1$ and $c = 1$, completing the derivation of the linear heating JMAK equations for a constant nucleation rate and interface-controlled growth.

Eq (3.52) is the most general and concise expression for C_1, but it does not give much physical insight in how C_1 depends on bc and ε. For the cases considered, i.e. one- , two- or three-dimensional interface-controlled growth, bc can take the values 1, 2 or 3. For integer values of bc, the series terminates when $j = bc$; the binomial coefficients are then equal to zero when $j > bc$. Evaluating the summation gives

$$C_1(1, \varepsilon) = \frac{1}{\varepsilon + \varepsilon^2} \,. \tag{3.53}$$

$$C_1(2,\varepsilon) = \frac{2}{2\varepsilon + 3\varepsilon^2 + \varepsilon^3} \tag{3.54}$$

$$C_1(3,\varepsilon) = \frac{6}{6\varepsilon + 11\varepsilon^2 + 6\varepsilon^3 + \varepsilon^4} \tag{3.55}$$

These equations show that C_1 is a smooth, decreasing function of ε ($=E_n/E_g$) it is of the order unity when ε ranges from 0.5 to 2. Note that $C(bc,1) = (1+bc)^{-1}$.

Eqs (3.50) to (3.52) are identical to Woldt's result.

Case 2: Constant nucleation rate and diffusion-controlled growth

The derivation of the particle radius as a function of time is similar to the corresponding isothermal case and yields

$$R(t,\tau) = \left(2\frac{D_0}{\alpha}\right)^c [f(t) - f(\tau)]^c, \tag{3.56}$$

where $c = 0.5$ and $f(t)$ is given by eq (3.46). The rest of the derivation is analogous to that of the last case and leads to Eq (3.50) but with $c = 0.5$. k_0' is given by eq (3.51), but with G_0, the pre-exponential constant of the growth rate, replaced with $2D_0$, the pre-exponential constant of the diffusion coefficient.

However, as now $c = 0.5$, bc can take the non-integer values $bc = 0.5$ and $bc = 1.5$, for which the series in eq (3.52) does not terminate. Fortunately, it converges very quickly. Fig. 3.1 shows that taking the first five terms in eq (3.52) gives values for $C_1(0.5,\varepsilon)$ and $C_1(1.5,\varepsilon)$ that compare very well with solutions obtained by numerically solving the integral in eq (3.47) for $bc = 0.5$ and $bc = 1.5$.

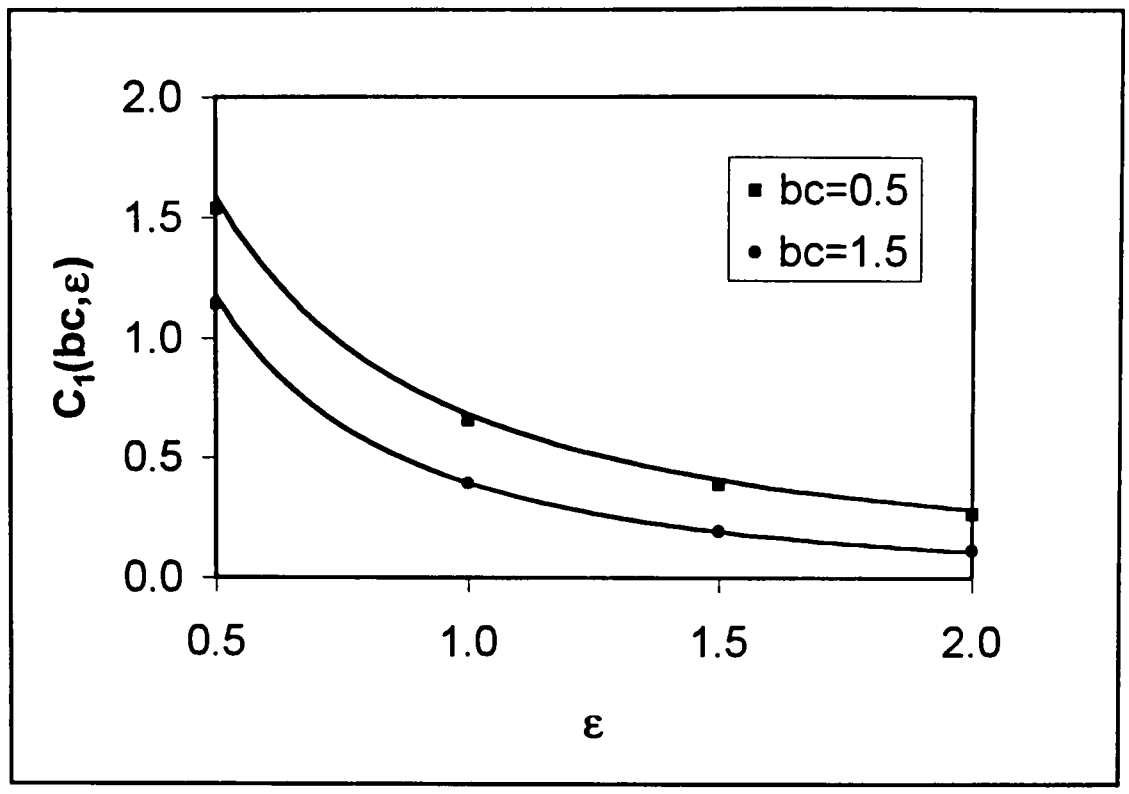


Figure 3.1 Comparison of $C_1(bc,\varepsilon)$ for two non-integer values for bc, obtained by truncating the summation in eq (3.52) after the first five terms (full line) and by accurate numerical integration of eq (3.47).

The derivation of the linear heating JMAK equations, eqs (3.40) and (3.41), for diffusion-controlled growth, is now complete. This is the first proof that the linear heating JMAK equations, eqs (3.40) and (3.41), are also valid for diffusion controlled growth, just as in the isothermal case.

3.4.2 The linear heating reaction rate equation

As for the isothermal case, the linear heating JMAK transformation rate equation can be calculated by differentiating eq (3.40) with respect to time. In the limit $\Delta H/2n >> k_BT$ (which is hardly restrictive, as already $E_n >> k_BT$ and $E_g >> k_BT$) this gives

$$\frac{\mathrm{d}x}{\mathrm{d}t}(x) = \frac{\Delta H}{k_B \varphi}(k')^{1/n}(1-x)(-\ln(1-x))^{(n-1)/n}. \qquad (3.57)$$

Thus, unlike $x(t)$, $\mathrm{d}x/\mathrm{d}t$ has the same form for both the isothermal and the linear heating case, apart from the different pre-factors: $nk_o^{1/n}$ for eq (3.39) and $(k'_o)^{1/n}\Delta H / k_B$ for eq (3.57)

(note that the heating rate drops out) and for the fact that Eq (3.57) has an *implicit* time dependence through the temperature dependence of the rate factor, eq (3.16). The linear heating reaction rate equation was derived before by Woldt [8], but his expression has an *explicit* time dependence, as well as depending on time through $x(t)$ and $T(t)$. Although the two expressions are formally equivalent, only eq (3.57) brings out the resemblance with the isothermal reaction rate equation, eq (3.39). The resemblance between the two rate equations is brought out here for the first time.

Eq (3.57) is a very important result; there has been a lot of speculation in the literature on the correct form of the non-isothermal transformation rate equation. eq (3.39) is often assumed to be valid for any temperature-time path; this is *not* generally correct as this equation is obtained from the *isothermal* JMAK equation. Henderson has argued that "*if it can be shown that the transformation rate depends only on the state variables of fraction transformed and temperature, and not on the thermal history*" [6], then eq (3.39) is also valid for non-isothermal transformations. In a later article [7], Henderson argues that, in general, the transformation rate *does* depend on the thermal history, and that eq (3.39) is only valid for non-isothermal reactions for certain special cases, namely site-saturated nucleation, a zero nucleation rate and isokinetic transformations (i.e. transformation for which $E_n = E_g$). It thus follows that eqs (3.39) and (3.57) should both describe the transformation rate under linear heating conditions, when $\varepsilon = E_n/E_g = 1$. Therefore, the pre-factors of eqs (3.39) and (3.57) should be the same. It shall be verified that this is indeed so, taking a constant nucleation rate ($a = 1$) as an example. The ratio of the pre-factors is in that case

$$\frac{\Delta H}{n k_B}\left(\frac{k'_o}{k_o}\right)^{1/n} . \qquad (3.58)$$

This ratio should be equal to one for $E_n = E_g = \Delta H/n$. With eqs (3.35) and (3.51), this gives

$$\frac{\Delta H}{nk_B}\left(nC_1(bc,1)\right)^{1/n}\left(\frac{nk_B}{\Delta H}\right)^{(1+bc)/n} \qquad (3.59)$$

which is indeed equal to one, as $C_1(bc,1) = (1+bc)^{-1} = n^{-1}$ for the case considered. Thus, it has been shown here, for the first time, that Henderson's approach is consistent with the more rigorous approach of solving eq (3.12) under linear heating conditions. However, this does *not* mean that the isothermal reaction rate equation may be used for other non-isothermal annealing conditions.

3.4.3 Justification for using peak shift methods

The temperature at which the reaction rate has a maximum, T_p, is a function of the heating rate, φ. Methods for determining the JMAK parameters from a measurement of $T_p(\varphi)$ are known as *peak shift methods*. Assuming the isothermal reaction rate equation is valid under linear heating conditions, Henderson [6] showed how peak shift methods may be used to determine the JMAK parameters. As it was shown in this work that Henderson's assumption is correct (see section 3.4.2), his justification for using peak shift methods has also been shown to be valid. However, there are two reasons for giving a new derivation for these methods. Firstly, justifying peak shift methods becomes much simpler now that eqs (3.39) and (3.40) have been derived in addition to eq (3.57). Secondly, it can now be pointed out that the justification is valid as long as eqs (3.30) and (3.31) hold and that no additional assumptions need to be made.

During the transformation, after most of the nuclei have formed and the particles grow, the transformation rate goes through a maximum, before impingement of the particles of the transformed phase brings the process to an end. This peak in dx/dt occurs when $d^2x/dt^2 = 0$.

The temperature at which this peak occurs is denoted T_p. Taking the second derivative of eq (3.40) with respect to time and setting it to zero gives

$$x_e(T_p) \approx 1. \qquad (3.60)$$

if it is assumed that $\Delta H/2n >> k_B T$, which is barely restrictive as it was already assumed that the activation energies for both nucleation and growth are much larger than the thermal energy. This means that under linear heating conditions, the extended volume is equal to the real volume of the system at the peak in the transformation rate. This is mostly a numerical coincidence; it can easily be shown that under *isothermal* conditions $x_e(T_p) = (n - 1)/n$. Nonetheless, $x_e = 1$ has some physical significance, as, during the transformation, the transformation rate is decreased by impingement and impingement becomes important when the extended volume approaches the real volume.

The true importance of eq (3.60) lies in the fact that the fraction crystallised at the peak in the transformation rate is equal to $x(T_p) = 1-e^{-1} = 0.63$, *regardless of the heating rate*. This fact lies at the heart of all peak shift methods. From eqs (3.11), (3.40), (3.41) and eq (3.60), it follows that

$$k'_o \left(\frac{T_p^2}{\varphi}\right)^n \exp\left(-\frac{\Delta H}{k_B T_p}\right) = 1. \qquad (3.61)$$

Thus the temperature at which the maximum in the transformation rate occurs is a function of the heating rate: T_p increases as a function of φ. Hence, by measuring T_p for different heating rates, ΔH and k'_o can be obtained from eq (3.61). To do so, the logarithm is taken at both sides of eq (3.60) to give

$$\ln\left(\frac{\varphi}{T_p^2}\right) = \tfrac{1}{n} \ln k'_o - \frac{\Delta H}{n k_B T_p}. \qquad (3.62)$$

Having measured $T_p(\varphi)$, $\ln(\varphi/T_p^2)$ can be plotted against $1/T_p$; this should give a straight line with slope $\Delta H/nk_B$ that intercepts the vertical axis at $(1/n)\ln k'_o$. Such a plot is called a "Kissinger plot" and this method for obtaining $\Delta H/n$ is called "Kissinger analysis" after the person who first derived eq (3.62), be it for a completely different kind of rate equation [12]. This completes our novel derivation that justifies Kissinger analysis.

Kissinger analysis is not the only type of peak shift method. It can be shown from eq (3.61) that plots of $\ln(\varphi/T_p)$ vs. $1/T_p$ or simply $\ln(\varphi)$ vs. $1/T_p$ will also give a straight line with the same slope and intersect as eq (3.62), provided eqs (3.30) and (3.31) hold. As the validity of the linear heating JMAK equations is already based on the assumption that eqs (3.30) and (3.31) hold, it is now clear, again for the first time, that the three peak shift methods are formally equivalent within the JMAK framework.

3.4.4 Determining the linear heating JMAK parameters from experiment

ΔH can be determined from a measurement of the fraction transformed, $x(t)$, or of the transformation rate, dx/dt. Eqs (3.39) and (3.40) can be rewritten as

$$\ln(-\ln(1-x)) = \ln\left(\frac{k'_o}{\varphi^n}\right) + 2n\ln T - \frac{\Delta H}{k_B T}. \qquad (3.63)$$

Taking the derivative with respect to $1/T$ gives

$$\frac{d\ln(-\ln(1-x))}{d(1/T)} = -2nT - \frac{\Delta H}{k_B} \approx -\frac{\Delta H}{k_B}, \qquad (3.64)$$

where again $\Delta H/2n >> k_B T$ has been used. Hence, plotting $\ln(-\ln(1-x))$ vs. $1/T$ gives a straight line with slope $-\Delta H/k_B$ that intercepts the vertical axis at $\ln(k'_o/\varphi^n)$.

Starting from eq (3.57), it can be shown that

$$\frac{\mathrm{d}\ln(\mathrm{d}x/\mathrm{d}t)}{\mathrm{d}(1/T)} \approx -\frac{\Delta H}{k_B}\left(1 - x_e(t)\right). \qquad (3.65)$$

Hence, plotting ln(dx/dt) vs. $1/T$ gives a curve with a slope equal to $-\Delta H/k_B$ in the limit $t \rightarrow 0$. This result contradicts Henderson's result [6]; he concludes that a plot of ln(dx/dt) versus $1/T$ should give a straight line with a slope approximately equal to $-\Delta H/nk_B$ (and not $-\Delta H/k_B$). In Appendix IIIC, it is explained where Henderson's derivation goes wrong.

Having obtained values for $\Delta H/n$ and ΔH, the transformation index, n, can be calculated. Knowing n, the effective attempt frequency under linear heating conditions, k'_o, is obtained from the intercept with the vertical axis in our Kissinger plot or, alternatively, from the constant in eq (3.64).

3.5 Two Important Assumptions

In deriving the isothermal and linear heating JMAK equations, two important assumptions have been made; how restricting these are shall now be discussed.

3.5.1 Assuming the thermal energy is small compared to activation energies

First consider a linear heating experiment. For practical reasons, heating is started at a temperature at which the parent phase is kinetically stable, i.e. when the nucleation and growth rates are effectively zero. Thus, at the start of the heating experiment the thermal energy is always negligible compared to the activation energies. On the other hand, if heating is continued long enough, eqs (3.30) and (3.31) will eventually be violated. The question is whether or not the transformation is effectively over by then. Woldt showed that solving the integral form of the JMAK equation numerically *without* using eqs (3.30) and (3.31) compares very well to the analytical expression for $x(t)$ derived in section 3.4.1, for a few typical values of the activation energies for nucleation (E_n = 0.5 - 1.0 eV) and growth (E_n =

0.5 - 1.0 eV). This suggest that eqs (3.30) and (3.31) generally hold, as smaller activation energies would lead to faster transformations so that the transformation will effectively be completed at a lower temperature.

3.5.2 The hard impingement approximation

The derivations of the isothermal and linear heating JMAK equations for diffusion-controlled growth are based on the assumption that the growth rate is given by eq (3.24). In the context of nucleation and growth kinetics, this approximation is called the "hard impingement approximation". It ignores the fact that growth will slow down before the particles physically touch, because the untransformed regions saturate with the element(s) that diffuses away from the interface. Hence, the approximation can only be expected to hold for small x. However, it has been shown that, under linear heating conditions, the peak in the transformation rate occurs at $x = 0.63$, which is not small. Hence, Kissinger analysis will only give an approximate value for the $\Delta H/n$ that determines the initial stages of the transformation. Similarly, eq (3.63) will give a curve, with slope equal to $-\Delta H/k_B$, only for small x. The difference between the slope of eq (3.63) at $x = 0$ and at $x = 0.63$ gives a qualitative idea of the inaccuracy of Kissinger analysis. For a more quantitative treatment, eqs (3.11) to (3.13) should be solved for diffusion-controlled growth with soft impingement.

3.6 The incubation time

When an incubation time, τ, precedes the crystallisation process, its temperature dependence is given by [9, 13]

$$\tau = \tau_o \exp\left(\frac{\Delta H / n}{k_B T}\right), \qquad (3.66)$$

where $\tau_o = \frac{8}{p}\left(k_o^{-\frac{1}{n}}\right)\frac{\gamma\beta^{4/3}}{H^2}k_B T\left(1-\frac{T}{T_m}\right)^{-2}$; (3.67)

p is the probability of an atom to move in the direction of the interphase boundary, γ is the specific interface energy, β is the atomic number density, H is the heat of fusion and T_m is the melting point. Note that, when nuclei are not immediately formed at the start of the anneal, the time variable in the JMAK kinetics starts at the end of the incubation time, and not at the beginning of the anneal.

3.7 The average grain size

Back in 1937, Kolmogorov derived an expression for the total *number* of grains formed during the transformation, in terms of the nucleation and growth parameters [4]. In appendix D, it is shown how it follows from Kolmogorov's expression that the average *grain size* in the transformed phase, ρ, is equal to

$$\rho = \rho_o \exp\left(-\frac{\Delta H'}{k_B T}\right), \quad (3.68)$$

where ρ_o is a constant and $\Delta H'$ is given by

$$\Delta H' = \frac{ac}{a+bc}\left[E_g - (E_n / a)\right] \quad (3.69)$$

for the nucleation rate given by eq (3.22). Note that, unlike ΔH, $\Delta H'$ can be negative; its sign will be the same as the sign of $E_g - (E_n/a)$. As a consequence, the average grain size *increases* with increasing isothermal annealing temperature when $E_g > E_n/a$, while it *decreases* otherwise. The temperature dependence of the grain size is calculated in terms of the nucleation and growth parameters for the first time in this work.

3.8 Summary

The *isothermal* JMAK equations are

$$x(t) = 1 - \exp(-kt^n) \tag{3.70}$$

with $$k(T) = k_0 \exp\left(-\frac{\Delta H}{k_B T}\right). \tag{3.71}$$

They describe the volume fraction, x, of transformed material as a function of time, t, at a constant temperature, T.

The *linear heating* JMAK equations are

$$x(t) = 1 - \exp(-k' t^{2n}) \tag{3.72}$$

with $$k'(\varphi, T) = k_0' \varphi^n \exp\left(-\frac{\Delta H}{k_B T}\right) \tag{3.73}$$

where φ is the heating rate, i.e. $T = \varphi t$.

The isothermal JMAK parameters are n, ΔH, and k_0; the linear heating JMAK parameters are $2n$, ΔH and k_0'. In both cases, n and ΔH are related to the nucleation and growth parameters through eqs (3.32) to (3.34). The pre-exponential of the rate constant does not transfer.

The method for obtaining the JMAK parameters from experiment is described in sections 3.3.3 and 3.4.4 for isothermal and linear heating experiments, respectively.

The average grain size, ρ, depends on temperature according to

$$\rho = \rho_o \exp\left(-\frac{\Delta H'}{k_B T}\right), \tag{3.74}$$

where ρ_o is a constant and $\Delta H'$ is given by eq (3.69).

When an incubation time, τ, precedes the transformation, its temperature dependence is

$$\tau = \tau_o \exp\left(\frac{\Delta H / n}{k_B T}\right), \tag{3.75}$$

where τ_o is given by eq (3.67).

References

[1] W.A. Johnson, R.F. Mehl, *Trans. Am. Inst. Min. (Metall.) Engs.* **135** (1939) p. 416.

[2] M. Avrami, *J. Phys. Chem.* **7** (1939) p. 1103, *J. Phys. Chem.* **8** (1940) p. 212,
J. Phys. Chem. **9** (1941) p. 177.

[3] A.N. Kolmogorov, *Ivz. Akad. Nauk. SSSR, Ser. Mat.* **3** (1937) p. 335 (in Russian).

[4] A.N. Shiryayev (ed.), *Selected Works of A.N. Kolmogorov*, Vol. II
Kluwer Academic Publishers, Dordrecht (1992) (in English).

[5] E.A. Marseglia, *J. Non-Cryst. Sol.* **41** (1980) p. 31.

[6] D.W. Henderson, *J. Non-Cryst. Sol.* **30** (1979) p. 301.

[7] D.W. Henderson, *J. Thermal Ana.* **15** (1979) p. 325.

[8] E. Woldt, *J. Phys. Chem. Sol.* Vol. **53** Nr. 4, (1992) p. 521.

[9] J.W. Christian, *The Theory of Transformations in Metals and Alloys*, Part I
Pergamon Press, Oxford (1975).

[10] S. Ranganathan and M. von Heimendahl, *J. Mat. Sci.* **16** (1981) p. 2401.

[11] P.G. Boswell, *J. Mat. Sci.* **15** (1980) p. 1939.

[12] H.E. Kissinger, *Anal. Chem.* **29** (1957) p. 32.

[13] V. Weidenhof, I. Friedrich, S. Ziegler and M. Wuttig, *J. Appl. Phys.* **89** (2001) p. 3168.

CHAPTER IV

In-situ TEM Crystallisation Experiments

4.1 Introduction

In this chapter, the crystallisation kinetics of a thin $Ge_2Sb_2Te_5$ film, sandwiched between two Si_3N_4 dielectric layers, is investigated. Thin $Ge_2Sb_2Te_5$ films are currently used as optical phase change rewritable storage media [1], because this material has the required optical contrast, stability of the amorphous phase at room temperature and can be crystallised by laser pulses of 50 ns [2]. However, interest remains in finding phase change materials with shorter crystallisation times. For this reason, it is interesting to understand the details of the crystallisation kinetics of phase change materials.

It was found by Mao *et al.*[3] that when amorphous $Ge_1Sb_2Te_4$ films are heated at a constant heating rate in the range of 0.2 – 0.5 K/s, they crystallise into a NaCl-type crystalline phase, at a temperature that lies in the range of 400 – 440 K, depending on the heating rate. Increasing the temperature further induces a transformation from the NaCl-type cubic crystalline phase to a hexagonal phase. A change in the reflectivity of 15 % - 20 % for the amorphous to crystalline transition is reported while no appreciable change in the reflectivity was found for the crystal to crystal phase transition. González-Hernández *et al.* [4] also investigated phase transitions in Ge-Sb-Te alloys with compositions along the

$GeTe$-Sb_2Te_3 pseudo-binary line, *viz.* $Ge_1Sb_4Te_7$, $Ge_1Sb_2Te_4$ and $Ge_2Sb_2Te_5$; they found that when annealed at approximately 470 K, these amorphous Ge-Sb-Te films crystallised into the NaCl-type structure, whilst annealing at higher temperatures induced a transformation into a rhombohedral phase. The fact that crystallisation does not occur at the same temperature is most likely due to the fact that González-Hernández *et al.* did an isothermal anneal and probably heated the samples to 470 K at a much higher rate than 0.5 K/s. The second crystalline phase of $Ge_2Sb_2Te_5$ was examined in detail using electron diffraction by Petrov *et al.* [5], who found the structure to be hexagonal, but report the presence of rhombohedral-like symmetry in the electron diffraction pattern., which probably misled González-Hernández *et al.* As the crystalline to crystalline phase change is not accompanied by a change in the optical reflectivity, it is not of practical importance in the context of phase change media and no reports on the transformation kinetics of this phase transition are found in the literature. The remainder of this chapter will focus on the amorphous to NaCl-type crystalline phase transition in $Ge_2Sb_2Te_5$.

The crystallisation kinetics of amorphous $Ge_2Sb_2Te_5$ have been investigated by a number of authors, using a variety of techniques. Yamada *et al.* [2] used differential scanning calorimetry (DSC) on electron beam evaporated bulk samples to determine the effective activation energy using Kissinger analysis. Oshima [6] investigated 30 nm thin films, deposited by RF sputtering and sandwiched between two dielectric seeding layers of various compositions (SiO_2, Si_3N_4, Ta_2O_5, ZnS and ZnS-SiO_2), using the optical transmittance of the samples to monitor their fraction transformed in a linear heating experiment. Trappe *et al.* [7] heated melt-quenched $Ge_2Sb_2Te_5$ with a laser and used the optical reflectance to monitor the fraction crystallised. Jeong *et al.* [8] deposited 200 nm films using direct current (DC) magnetron sputtering and performed DSC as well as *in-situ*

TEM experiments. Friedrich *et al.* [9] determined the effective activation energy from Kissinger analysis of DC sputtered films, measuring the electrical resistance to monitor the fraction crystallised. Finally, Weidenhof *et al.* [10] investigated 85 nm DC sputtered films, crystallised with a laser, using the optical reflectance to measure the fraction crystallised. The studies mentioned above interpret the crystallisation kinetics in terms of the Johnson-Mehl-Avrami-Kolmogorov (JMAK) transformation kinetics and are mainly focused at determining the JMAK parameters, which describe the volume fraction of crystallised material as a function of temperature and time.

The JMAK parameters, however, do not unveil the mechanisms of nucleation and growth that underlie the phase transition. Detailed knowledge of where and how fast the nuclei form, how they grow and at what speed is essential for understanding how the crystallisation properties may be improved. The work described in this chapter aims at making a complete study of the nucleation and growth parameters of thin $Ge_2Sb_2Te_5$ films, in addition to determining the JMAK parameters for their crystallisation. Transmission electron microscopy (TEM) with *in-situ* heating offers the possibility to do this, as individual nuclei can be seen to form and grow in real time, allowing all the nucleation and growth parameters to be determined independently.

4.2 Experimental methods for determining the crystallised fraction

There are three different ways to measure the volume fraction of crystallised material, x, during an annealing experiment. They will be briefly discussed here, to point out their advantages and limitations. All three methods have been used in studying the crystallisation kinetics of amorphous $Ge_2Sb_2Te_5$.

4.2.1 Reflectivity etc.

Perhaps the easiest method of determining the fraction crystallised is by measuring a physical property (e.g. optical reflectivity or transmittivity, electrical resistivity, density etc.) that changes upon crystallisation, as a function of time during the annealing experiment. Taking the optical reflectivity, R, as an example, it is then assumed that, at any point in the transformation, the reflectivity of the sample is given by

$$R = (1-x)R_A + xR_X\,, \qquad (4.1)$$

where R_A and R_X are the reflectivities of the amorphous and crystalline state, respectively. In other words, the reflectivity of the sample is assumed to be equal to the average of the amorphous and crystalline values, weighted by the volume of the amorphous and crystalline regions, respectively. Eq (4.1) can be rewritten as

$$x(t) = \frac{R(t) - R_A}{R_X - R_A}, \qquad (4.2)$$

so that a measurement of $R(t)$ gives the fraction crystallised as a function of time. It is important to realise, however, that eq (4.2) is only valid when the parameter in question changes linearly with x. That this is not always the case is best illustrated using a measurement of the electrical resistivity as an example. Assume the resistivity of the crystalline phase is lower than that of the amorphous phase. From the moment the crystallites start to touch, the current will preferentially flow through the crystalline material, so that the resistivity of the material is closer to that of the crystalline phase than would be expected from the crystalline volume fraction.

4.2.2 Calorimetry

The driving force for the crystallisation process is the fact that the crystalline phase has a lower energy than the amorphous phase. During crystallisation, the difference in energy

between the two phases is released in the form of heat. Thus, it may be assumed that the heat *flow* from the sample, dH/dt, is proportional to the rate of change of x:

$$\frac{\mathrm{d}x}{\mathrm{d}t} = C\frac{\mathrm{d}H}{\mathrm{d}t}. \qquad (4.3)$$

This is known as the Borchard assumption [11, 12]. This expression may then be integrated to yield the fraction crystallised as a function of time:

$$x(t) = C\int_0^t \frac{\mathrm{d}H}{\mathrm{d}t}\mathrm{d}t \qquad (4.4)$$

The proportionality constant, C, follows from the normalisation condition

$\int_0^{t_f} (\mathrm{d}x/\mathrm{d}t)\mathrm{d}t = 1$, where t_f is the time at which the transformation is effectively completed.

The heat flow from a crystallising sample can be determined using calorimetric methods such as differential scanning calorimetry (DSC) or differential thermal analysis (DTA). Thus, the transformation rate, dx/dt, is obtained as a function of time in such a calorimetric experiment. The transformation rate can be numerically integrated to yield $x(t)$.

4.2.3 *In-situ* TEM

In-situ TEM offers the possibility to directly observe the nucleation and growth of the individual crystallites in real time. For the electrons to pass through the sample and form an image on the screen, the sample needs to be thin (typically 5–50 nm). The surfaces of the sample, however, may affect the nucleation process as surface atoms may form crystalline clusters more easily than atoms surrounded by the amorphous bulk. This makes *in-situ* TEM less suitable for studying bulk crystallisation, but it makes it a very good technique for studying crystallisation in samples that have thin film applications, as is the case for the active layer in phase change media. To determine the volume fraction of transformed

material, x, the fraction of the screen that is seen to be covered by crystallites is measured and taken to be equal to x. This ignores the fact that the TEM image is a two dimensional *projection* of the film. This approach overestimates the contribution to x of crysallites smaller than the film thickness, as the amorphous material between these crystallites and the film surfaces is effectively counted as crystalline material. This effect is small when the crystallites grow out to a diameter that is large compared to the film thickness. Another potential problem with using *in-situ* TEM is that irradiation of the sample by the electron beam can cause local heating of the material or otherwise influence the crystallisation kinetics. Finally, the crystallised fraction is a macroscopic quantity that cannot be studied on too small a scale; the sampled volume must be large enough to give a statistically good representation of the crystallisation process. If the sampled volume is not large enough, the crystallisation parameters measured would depend on where the sampled volume is chosen. In practice, the latter is not the case as long as the sample volume contains at least ten nuclei.

4.3 Experimental Details

Amorphous $Ge_2Sb_2Te_5$ films, 25 nm thick, were grown using RF sputtering from a single target of the required composition. The film was sandwiched between two dielectric Si_3N_4 layers, approximately 2 nm thick. The stack was grown on carbon-coated mica substrates. Small pieces were cut and the stacks were floated off the substrate onto de-ionised water and picked up on 200 mesh copper TEM grids.

The samples were observed during *in-situ* heating in a JEOL 4000EX TEM. The column vacuum in the microscope was approximately 6×10^{-10} bar. The TEM sample holder was fitted with a furnace placed around the specimen position and a thermocouple was mounted

in the sample holder to measure the temperature of the sample. The uncertainty in the temperature is estimated at ±10 K. The samples were heated to the desired (constant) annealing temperature at a rate of approximately 5 K/s. Annealing temperatures between 413 K and 450 K were chosen; lower temperatures lead to impractically long experiments while at higher temperatures, crystallisation starts during heating. The beam conditions were chosen to minimise heating of the sample under the electron beam. The influence of the beam on the crystallisation process was investigated by crystallising the film to about $x = 0.5$ and comparing the regions that crystallised under the beam with regions that were not irradiated during crystallisation; no difference was observed.

Crystallisation was followed in bright field imaging mode on a TV monitor and recorded on video tape. A magnification of 3.0×10^5 on the screen was chosen; this magnification was high enough to clearly see individual crystallites nucleate and grow, while it was low enough so that the image contained a large number of nuclei, thereby ensuring that the crystallisation process visible on the screen gave a representative picture of the process across the film. The spatial resolution on the screen was about 10 nm, and the time resolution of the video recording system was 40 ms. For each annealing temperature, a number of frames throughout the crystallisation process were analysed. The crystallites can be observed as they either have darker or brighter contrast than the amorphous film and as each frame carries a time code, the time evolution of the crystallisation process can be followed. Fig. 4.1 shows a typical example of how a $Ge_2Sb_2Te_5$ crystallite can be seen to grow in an *in-situ* TEM experiment.

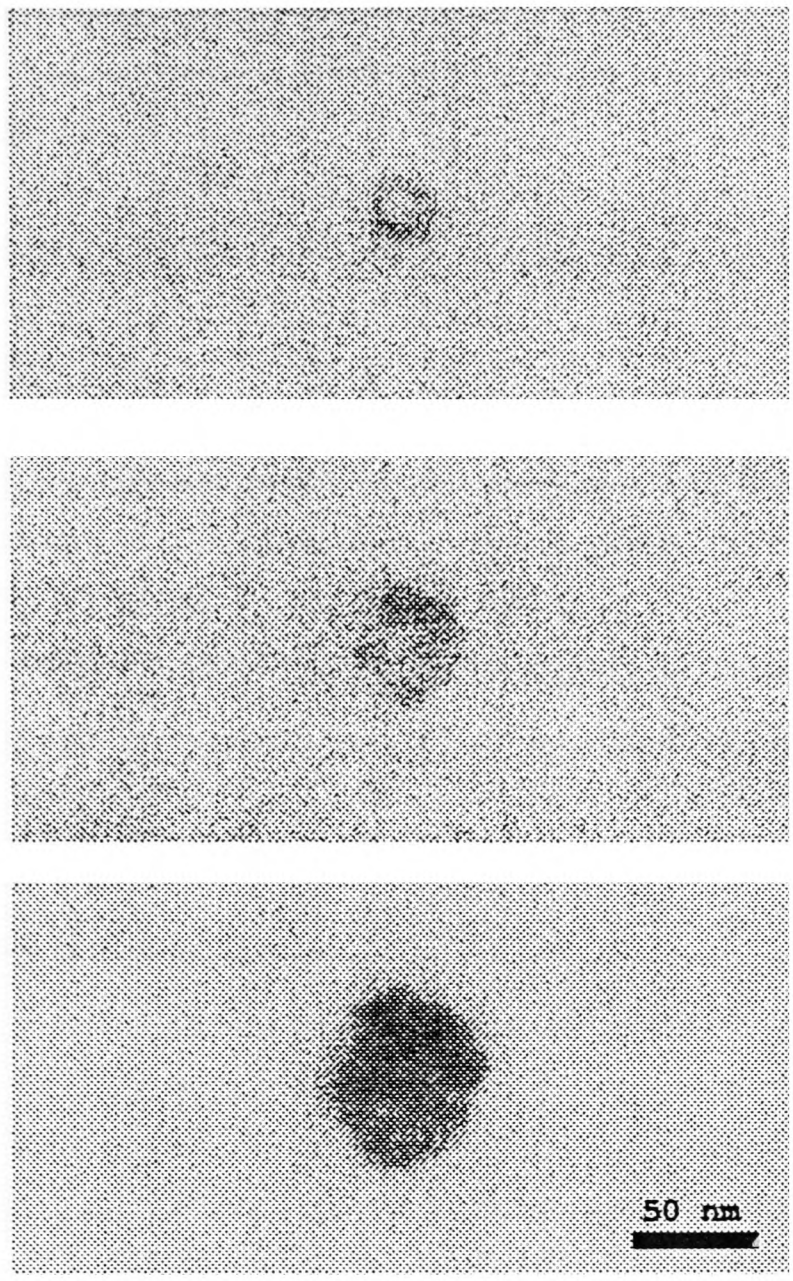


Figure 4.1 TEM image of a $Ge_2Sb_2Te_5$ crystallite in an amorphous matrix during an isothermal anneal at 435 K after 90, 98 and 105 seconds, respectively.

4.4 Results

The start of the crystallisation process was found to be preceded by a temperature-dependent incubation time, defined as the time between the first video frame at which the isothermal temperature is reached and the first frame at which a nucleus is observed. The nucleation times are plotted in an Arrhenius plot in Fig. 4.2 yielding $\Delta H/n = 1.8 \pm 0.5$ eV and $\ln(\tau_o) = -45 \pm 13$.

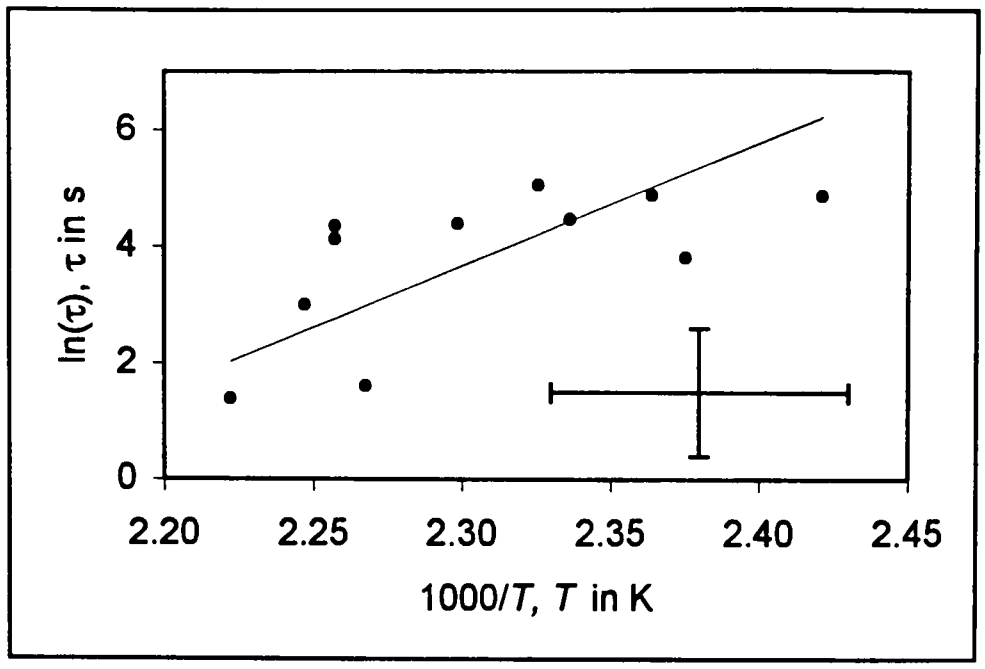


Figure 4.2 Arrhenius plot of the temperature dependence of the incubation time.

From eqs (3.66) and (3.67) it follows that:

$$\frac{\partial \ln \tau}{\partial (1/T)} = \frac{\Delta H}{n k_B} - T - 2\frac{T^2}{T_m - T}. \qquad (4.5)$$

As the annealing temperatures are all around $T = 430$ K and the melting point of $Ge_2Sb_2Te_5$ is $T_m = 889$ K [2], both T and $2T^2/(T_m - T)$ are much smaller than $(\Delta H / nk_B)$, which is of the order of 10^4. This justifies the use of an Arrhenius plot for obtaining $\Delta H/n$ and $\ln(\tau_o)$.

For each isothermal anneal, the fraction crystallised is determined as a function of time by measuring the fraction of the screen covered by crystallites for each of a number of frames throughout the crystallisation process. From eq (3.15), it can be seen that plotting $\ln(-\ln(1-x))$ vs. $\ln(t)$ gives a straight line with slope n and intercept $\ln(k)$. Fig. 4.3 shows such a plot for $T = 435$ K.

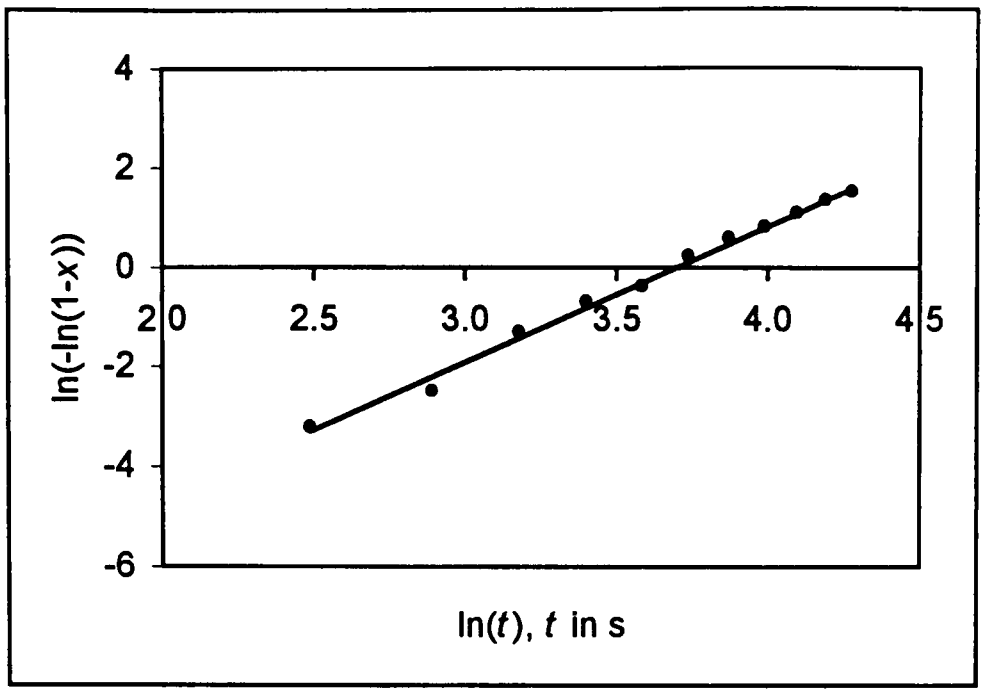


Figure 4.3 Plot of ln(–ln(1–x)) vs. ln(t) at an annealing temperature of 435 K.

This procedure was repeated for each annealing experiment. The values of n obtained at each temperature were then averaged to give $n = 3.4 \pm 0.9$, where the error is determined from the standard deviation of all the values of n. From eq (3.16), it can be seen that plotting ln (k) as a function of reciprocal temperature gives a straight line; ΔH is determined by the slope, while the intercept gives ln(k_o). Fig. 4.4 shows a plot of ln (k) vs. 1000/T. The activation energy is found to be $\Delta H = 7.8 \pm 2.0$ eV, whilst the intercept gives ln (k_o) = 200 ± 50.

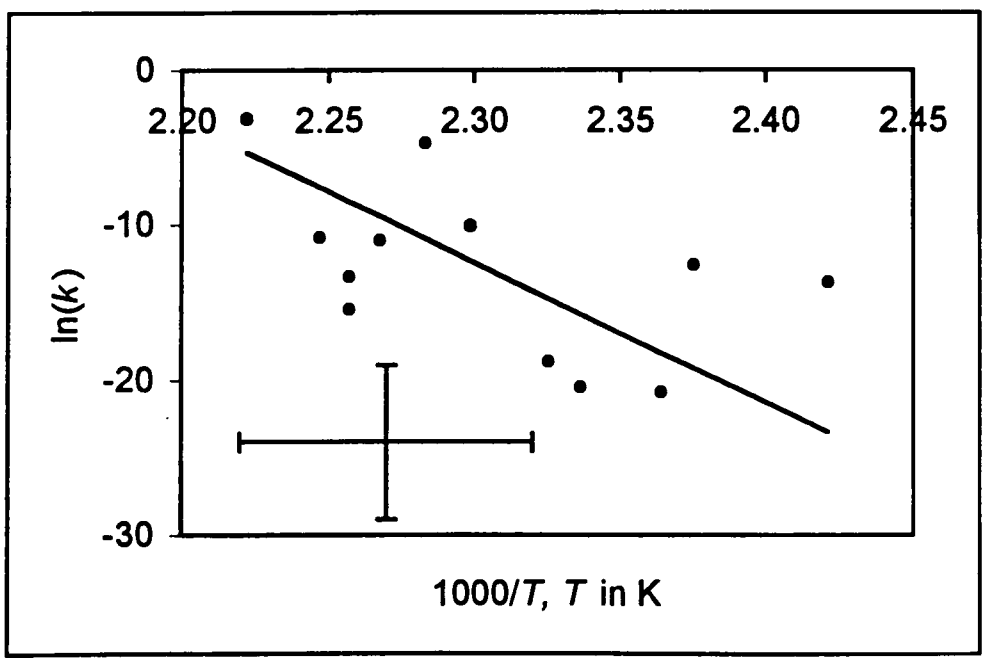


Figure 4.4 Arrhenius plot of the temperature dependence of the rate constant, k.

The nucleation rate per unit volume, I, was determined by counting the number of crystalline nuclei on the screen, N, as a function of time, and then calculating the nucleation rate per unit volume using

$$I = \frac{1}{V}\frac{\mathrm{d}N/\mathrm{d}t}{1-x}, \qquad (4.6)$$

where $V = 1.3 \times 10^{-20}$ m^3 is the volume observed (i.e. the area on the screen times the film thickness); the $(1 - x)$ term takes into account the fact that nuclei are formed in the untransformed area only.

The nucleation index, a, was determined from eq (3.33), by first calculating a_i from two consecutive frames

$$a_i = \frac{\partial \ln N_i}{\partial \ln t_i} \approx \frac{\ln N_{i+1} - \ln N_i}{\ln t_{i+1} - \ln t_i} \qquad (4.7)$$

and then averaging over all the frames:

$$a = \frac{\sum_i (1-x_i)a_i}{\sum_i (1-x_i)}. \qquad (4.8)$$

The $(1 - x)$ weighting term was used because the contribution of nucleation to the crystallisation process decreases as the transformation proceeds. The nucleation index was determined for each anneal and the results were averaged to give $a = 2.8 \pm 0.6$, which indicates that the nucleation *rate*, I, increases with time as $t^{1.8}$, as $I \equiv dN/dt \propto t^{a-1}$ from eq (3.33).

Having obtained the nucleation index, $\ln(I t^{1-a})$ can be plotted as a function of reciprocal temperature: the result is shown in Fig. 4.5. From eq (3.33b), it can be seen that the slope of

such a plot is related to E_n, while the intercept equals $\ln(I_o)$. The plot yields $E_n = 4.7 \pm 1.1$ and $\ln(I_o) = 166 \pm 43$.

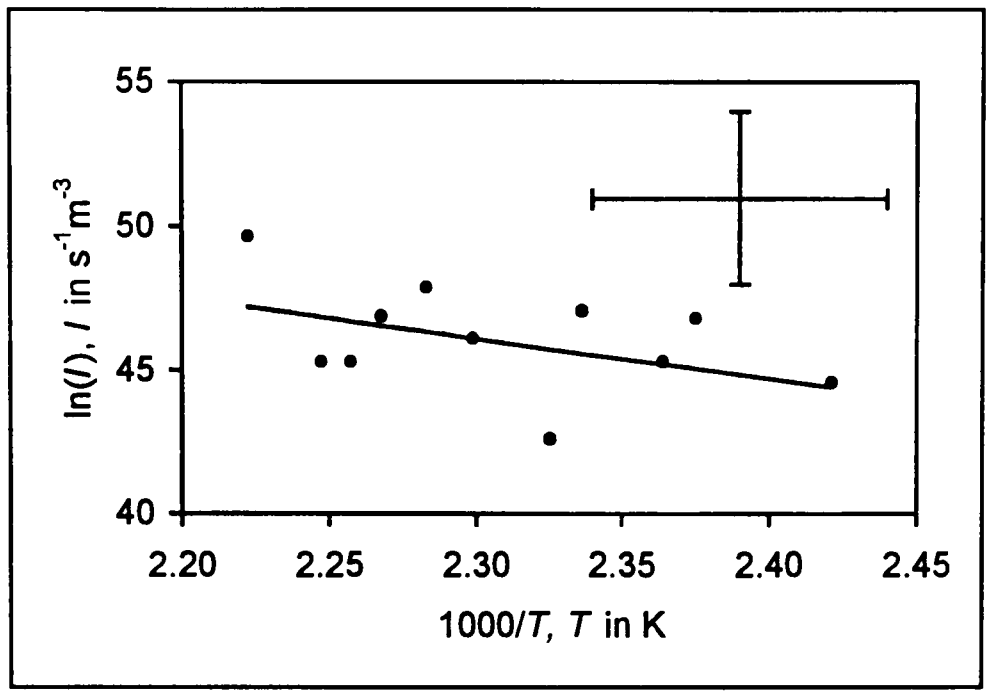


Figure 4.5 Arrhenius plot of the temperature dependence of the nucleation rate, I.

As the crystallites grow out to a radius much larger than the film thickness, their shape is disc-like; the dimensionality of their growth is therefore taken to be $b = 2$.

The crystallites were found to have a constant growth rate, so that $c = 1$. The increase of the radius with time (the interface velocity) was measured for a number of crystallites at each annealing temperature and averaged. This procedure was repeated at each temperature; the results are plotted in an Arrhenius plot in Fig. 4.6. The slope corresponds to an activation energy for growth of $E_g = 1.6 \pm 0.6$ eV and the intercept is at $\ln(G_o) = 43 \pm 25$, with G_o in $\mathrm{m\,s^{-1}}$.

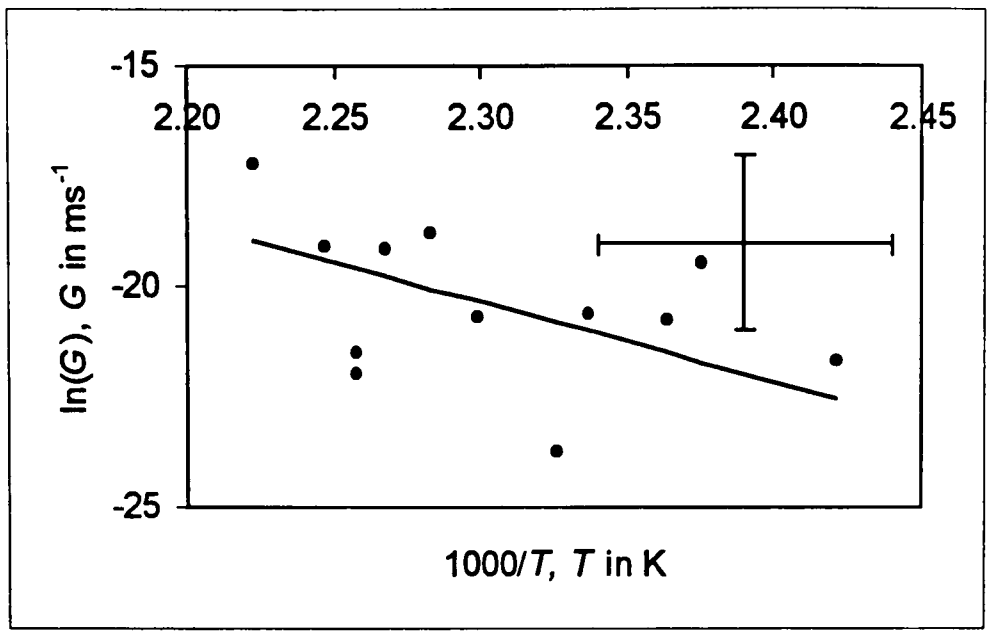


Figure 4.6 Arrhenius plot of the temperature dependence of the growth rate, G.

The average grain size was determined as a function of temperature directly from the TEM images; the result is plotted as an Arrhenius plot in Fig. 4.7. The slope corresponds to $\Delta H' = -0.2 \pm 0.7$ eV and the intercept is $\ln(\rho_o) = -15 \pm 20$, with ρ_o in m.

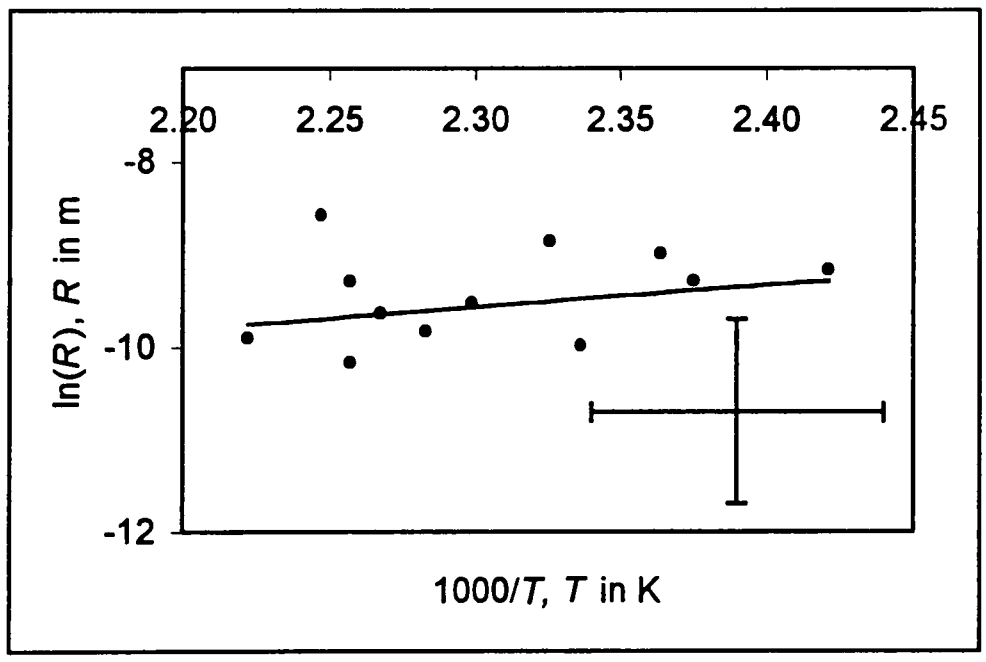


Figure 4.7 Arrhenius plot of the temperature dependence of the average grain size.

The contrast between the centre of the crystallites and the amorphous background was measured as a function of particle radius for a large number of particles at different

temperatures. The intensities were scaled to the intensity at the maximum particle radius; the result is plotted in Fig. 4.8.

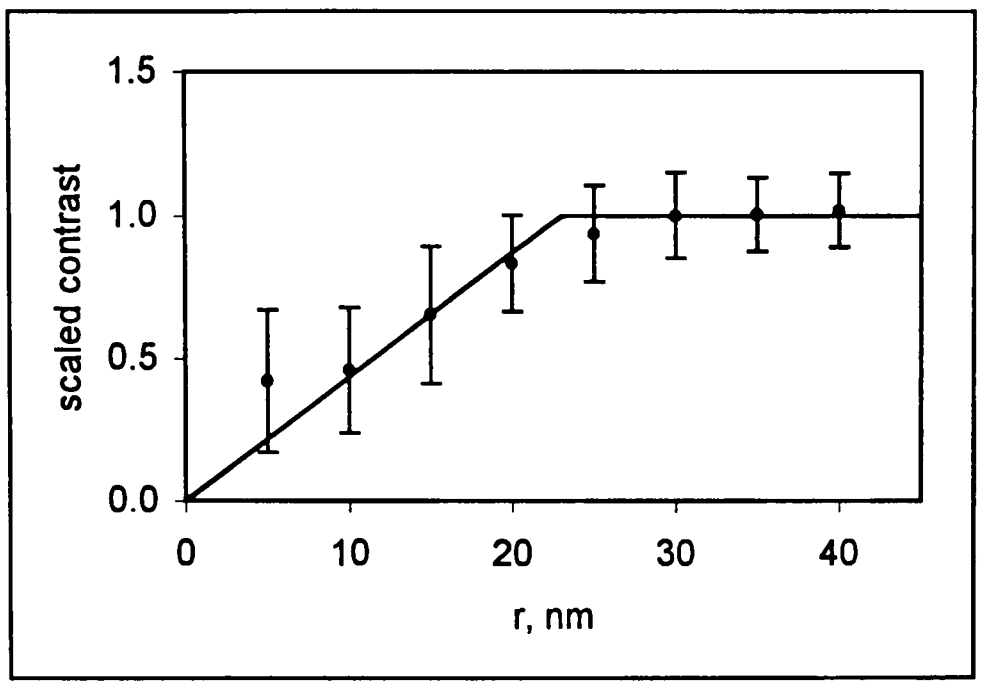


Figure 4.8 Scaled contrast of the centre of a crystallite as a function of its radius, *r*.

The data were fitted to the trend line shown, using the cross-over point between linear increase and saturation as a fit parameter. The cross-over point was found to be at 23 nm, just below the film thickness. This suggests that the nuclei originate at the interface of the $Ge_2Sb_2Te_5$ layer with the dielectric layers, as in that case, the contrast of the centre of the crystallite is expected to increase linearly until the particle radius equals the film thickness and then to remain constant thereafter. In the case of bulk nucleation, a less pronounced change is expected, at *half* the film thickness.

The values of all the determined parameters are summarised in Table 4.1.

Table 4.1 Summary of the values of the parameters determined for the $Ge_2Sb_2Te_5$ samples analysed.

JMAK parameters; eqs (3.32), (3.34), (3.35b) $n = 4.3 \pm 0.9$ $\Delta H = 7.8 \pm 2.0$ eV $\ln(k_o) = 200 \pm 50$
Nucleation parameters; eq (3.33) $a = 2.8 \pm 0.6$ $E_n = 4.7 \pm 1.1$ eV $\ln(I_o) = 166 \pm 43$
Growth parameters; eq (3.17), sec. 3.3.2 $b = 2$; $c = 1$ $E_g = 1.6 \pm 0.6$ eV $\ln(G_o) = 43 \pm 25$
T- dependence of τ*;* eqs (3.75) $\Delta H/n = 1.8 \pm 0.5$ eV $\ln(\tau_o) = -45 \pm 13$
T- dependence of ρ*;* eqs (3.74) $\Delta H = -0.2 \pm 0.7$ eV $\ln(\rho_o) = -15 \pm 20$

4.5 Discussion

The crystallisation kinetics of amorphous $Ge_2Sb_2Te_5$ films, sandwiched between two dielectric layers, was investigated under isothermal conditions. The reaction was found to have a temperature dependent incubation time, as first observed for In-Te alloy films by Sugiyama *et al.* [13]. The activation energy determined from the temperature dependence

of the incubation time, $\Delta H/n = 1.8 \pm 0.5$ eV, agrees with the value reported by Weidenhof *et al.* [10], $\Delta H/n = 1.9$ eV. The pre exponential constant also agrees with the value of $\ln(\tau_o) = -47$ reported by Weidenhof *et al*, but this is hardly surprising, as the error in $\ln(\tau_o)$ is very large. The latter is due to the fact that $\Delta H/n >> k_B T$ ($k_B T \approx 0.03$ eV around $T = 400$ K) for the temperature range that is experimentally accessible, so that small changes in the slope of the trend line in a Arrhenius plot result in large changes in the intercept, $\ln(\tau_o)$, and thus in a very large error in τ_o. This makes it practically impossible to verify if eq (3.67) correctly describes the experimental data. The much smaller uncertainty in the activation energy confirms the Arrhenian temperature dependence of the incubation time in the investigated temperature interval, as predicted by eq (3.66). The value found for $\Delta H/n$ agrees with the values for ΔH and n quoted in Table 4.1. This means that, as predicted by eqs (3.70) and (3.71) and by eq (3.75), both the incubation time and the time scale on which the nucleation and growth process occurs, indeed depend on temperature through the *same* activation energy, $\Delta H/n$.

Accounting for this incubation time, the transformation kinetics were analysed within the JMAK framework. The JMAK parameters and the "activation energy" that determines the temperature dependence of the average grain size, $\Delta H'$, were determined. In addition, the nucleation and growth parameters were determined independently. This makes it possible to experimentally verify the validity of eqs (3.32), (3.34), (3.35b) and (3.69); this is done in Table 4.2.

Table 4.2 Comparison of the JMAK parameters and $\Delta H'$ determined directly (first entry) and from the nucleation and growth parameters (second entry), respectively.

Avrami exponent; eq (3.32)
$n = 3.4 \pm 0.9$
$a + bc = 4.8 \pm 0.6$
Effective activation energy; eq (3.34)
$\Delta H = 7.8 \pm 2.0$ eV
$E_n + bcE_g = 7.9 \pm 1.6$ eV
pre-exponential constant; eq (3.35b)
$\ln(k_o) = 200 \pm 50$
$\ln(I_o) + bc \ln(G_o) = 250 \pm 70$
T- dependence of ρ*;* eq (3.69)
$\Delta H' = -0.2 \pm 0.7$ eV
$\frac{ac}{a+bc}\left[E_g - (E_n / a)\right] = -0.1 \pm 0.8$ eV

From Table 4.2, it can be seen that the values of the parameters n, ΔH, $\ln(k_o)$ and $\Delta H'$, determined from $x(t)$ and the temperature dependence of the grain size, agree with the values calculated from the nucleation and growth parameters, within experimental error. This provides experimental support for the validity of eqs (3.32), (3.34), (3.35b) and (3.69), confirming that the microscopic nucleation and growth processes indeed determine the macroscopic fraction transformed in the way that the JMAK theory predicts it should occur. The expression for the Avrami exponent in terms of the nucleation and growth parameters is well documented by Christian [14], while Von Heimendahl *et al.* [15] experimentally verified the expression for the effective activation energy. Eqs (3.35b) and (3.69), however, have not yet been tested experimentally, to the knowledge of the author. As both methods for obtaining the JMAK parameters quoted in Table 4.2 should give the same answer, the

two entries may be averaged to arrive at their most accurate values: $n = 4.1 \pm 0.5$; $\Delta H/n = 2.0 \pm 0.4$ eV and $\ln(k_o) = 220 \pm 40$. The value of $\Delta H/n$ is quoted instead of ΔH, as some authors only quote the activation energy determined using Kissinger analysis, which gives $\Delta H/n$, not ΔH [16, 17].

Whether crystalline nuclei are formed throughout the bulk of the as-deposited amorphous $Ge_2Sb_2Te_5$ layer or rather at the interfaces with the dielectric media was investigated for the first time. Nucleation was found to occur predominantly at the interfaces between the active layer and the dielectric layers. This agrees with the findings of Henderson *et al.* [18], who found that As_2Se_3, also a chalcogenide glass, has propensity for surface nucleation. By investigating partially crystallised As_2Se_3 powder samples with an optical microscope, they found that nuclei only formed at the surfaces of the particles. Thus, the nucleation behaviour is expected to be governed by the structure of the interfaces between the dielectric layers and the active layer. Using different materials for the dielectric layers is therefore expected to change the nucleation parameters and therewith the JMAK parameters. This agrees with the fact that Oshima [6] found different values for the JMAK parameters n and $\Delta H/n$, depending on the dielectric layer material used; $n = 1.0$ and $\Delta H/n = 3.0$ eV for SiO_2; $n = 1.8$ and $\Delta H/n = 2.5$ eV for Si_3N_4; $n = 1.5$ and $\Delta H/n = 2.4$ eV for Ta_2O_5; $n = 3.0$ and $\Delta H/n = 2.9$ eV for ZnS; $n = 3.2$ and $\Delta H/n = 2.6$ eV for ZnS-SiO_2 and finally $n = 1.5$ and $\Delta H/n = 2.2$ eV for a single $Ge_2Sb_2Te_5$ layer without any dielectric layers. From the scatter in the data points in Oshima's Kissinger plots, the error in the activation energy is estimated to be about 0.3 eV, so that $\Delta H/n = 2.5 \pm 0.3$ eV found for the films with a Si_3N_4 seeding layer agrees with $\Delta H/n = 2.0 \pm 0.4$ eV found in the present work. The latter is also consistent with the values $\Delta H/n = 2.2$ eV (Yamada *et al.* [2]), $\Delta H/n = 2.0$ eV (Trappe *et al.* [7]), $\Delta H/n = 2.2 \pm 0.1$ eV (Friedrich *et al.* [9]) and $\Delta H/n = 2.0 \pm 0.2$ eV (Weidenhof *et al.*

[10]). Jeong *et al.* [8] find that the crystallisation of their films occurs in two stages; the first stage having $\Delta H/n = 2.3$ eV and the second $\Delta H/n = 2.0$ eV. Thus, the values for $\Delta H/n$ reported in the literature show little variation and an average of just over 2 eV.

The values reported for the Avrami exponent, n, on the other hand, are not so consistent. Jeong *et al.* find a value for n in the range 3.6–5.8 for the first stage of the transformation and n in the range 1.0–1.3 for the second stage. The fact that they find that the transformation occurs in two stages might be due to the fact that they used a very thick film. This poses no geometrical restrictions on the growth of the crystallites, so that we expect spherically shaped crystallites, i.e. $b = 3$, who's growth is still interface-controlled: $c = 1$. Using eq (3.32), this gives $a = 1.7 \pm 1.1$ for the nucleation index, which agrees with the value $a = 2.8 \pm 0.6$ quoted in Table 1. The first stage ends when the crystallites that formed at the interface touch. The very small values found for the Avrami exponent during the second stage suggests that bulk nucleation is negligible. If there is no nucleation in the second stage, then $a = 0$ and $E_n = 0$ [15], whilst the crystallites now grow out in one dimension, along the normal of the film: $b = 1$. Putting these values into eq (3.32) gives $n = 1$, which lies in the range of the values for the Avrami index found by the authors.

Weidenhof *et al.* report $n = 2.6 \pm 0.1$. The value found for n, however, strongly depends on how one accounts for an incubation time. Fig. 3 (a) in reference [10] shows that if the incubation time is not accounted for, plotting $\ln(-\ln(1-x))$ vs. $\ln(t)$ gives a curve with a slope varying around 1.5 at the beginning of the experiment (x between 0.2 and 8 %) to become constant and equal to 5.8 for the remaining part (x between 8 and 99 %). Thus, ignoring the data corresponding to $x < 8$ % would yield $n = 5.8$. To account for the incubation time, τ, the authors rescale the time to $t' \equiv t - \tau$, where τ is chosen to coincide

with the moment the slope of the plot effectively becomes constant (i.e. at $x = 8$ % for the case considered). They then plot $\ln(-\ln(1-x))$ vs. $\ln(t')$ and obtain a straight line with slope $n = 2.5$. Although this procedure of finding the incubation times is very clear, the incubation time, by definition, is the time that passes before the first nuclei are formed and this is obviously long before 8 % of the material has crystallised. The criterion used to obtain the incubation times in Fig. 4.1, *viz.* equating τ to the time the first nucleus is seen to appear, seems more appropriate as it is based on the direct observation of a nucleus. As one visible nucleus on the screen corresponds to a fraction crystallised of about $x \approx 0.5$ %, i.e. much smaller than 8 %, the incubation times in the present work will be shorter. This squares with the fact that the most accurate estimate for the Avrami index, $n = 4.1 \pm 0.5$, lies between 2.5 and 5.8. The low value for the Avrami index, $n = 1.8$, found by Oshima for the crystallisation of a 30 nm thick RF sputtered $Ge_2Sb_2Te_5$ film sandwiched between Si_3N_4 layers, does not agree with the present work. The reason for this is unclear. It may be that, unlike DC sputtering, RF sputtering does not produce a completely amorphous $Ge_2Sb_2Te_5$ film. If that were the case, nucleation is no longer required during crystallisation (i.e. $a = 0$) and an Avrami exponent of 2 would be expected. Weidenhof *et al.* are the only authors to report a value for the pre-exponential constant and found, using the notation of eqs (3.70) and (3.71), $\frac{1}{n}\ln(k_o) = 51$. This compares well with $\frac{1}{n}\ln(k_o) = 53 \pm 12$ found in this work.

4.6 Summary and conclusions

The isothermal crystallisation kinetics of thin $Ge_2Sb_2Te_5$ films, sandwiched between Si_3N_4 dielectric layers, were studied in detail using *in-situ* TEM. An incubation time was found to precede the crystallisation, in accordance with the literature. The JMAK parameters and the individual nucleation and growth parameters were determined. The relationship between the JMAK parameters and the nucleation and growth parameters was tested and found to

hold. As a best estimate of the JMAK parameters, we found $\Delta H/n = 2.0 \pm 0.4$ eV; $n = 4.1 \pm 0.5$ and $\ln(k_o) = 220 \pm 40$. These values are in good agreement with most of the literature. Nucleation was found to occur at the interface with the dielectric layers. The average grain size did not show appreciable temperate dependence in the investigated temperature range.

References

[1] J. Tominaga, T. Kikukawa, M. Takahashi, T. Kato and T. Aoi,

Jpn. J. Appl. Phys. **36** (1997) p. 3598.

[2] N. Yamada, E. Ohno, K. Nishiuchi and N. Akahira, *J. Appl. Phys.* **69** (1991) p. 2849.

[3] Z.L. Mao, H. Chen, Ai-lien Jung, *J. Appl. Phys.***78** nr 4 (1995) p. 2338.

[4] J. González-Hernández, E. López-Cruz, M. Yáñez-Limón, D. Strand, B.B. Chao and

S.R. Ovshinsky, *Sol. State Comm.* **95** nr. 9 (1995) p. 593.

[5] I.I. Petrov, R.M. Imamov and Z.G. Pinsker, *Sov. Phys. - Cryst.* **13** (1968) p. 339.

[6] N. Oshima, *J. Appl. Phys.* **79** (1996) p. 8357.

[7] C. Trappe, B. Bechevet, S. Facsko and H. Kurz, *Jpn. J. Appl. Phys.* **37** (1998) p. 2114.

[8] T.H. Jeong, M.R. Kim and H. Seo, *J. Appl. Phys.* **86** (1999) p. 774.

[9] I. Friedrich, V. Weidenhof, W. Njoroge, P. Franz and M. Wuttig,

J. Appl. Phys. **87** (2000) p. 4130.

[10] V. Weidenhof, I. Friedrich, S. Ziegler and M. Wuttig, *J. Appl. Phys.* **89**(2001) p. 3168.

[11] H.J. Borchard and F. Daniels, *J. Am. Chem. Soc.* **78** (1957) p. 41.

[12] H.J. Borchard, *J. Inorg. Nucl. Chem.* **12** (1960) p. 252.

[13] Y. Sugiyama, R. Chiba, S. Fujimori and N. Funakoshi,

J. Non-Cryst. Sol. **122** (1990) p. 83.

[14] J.W. Christian, *The Theory of Transformations in Metals and Alloys, Part I.*

Pergamon Press, Oxford (1975).

[15] M. von Heimendahl and G. Kuglstatter, *J. Mat. Sci.* **16** (1981) p. 2405.

[16] D.W. Henderson, *J. Non-Cryst. Sol.* **30** (1979) p. 301.

[17] E. Woldt, *J. Phys. Chem. Sol.* **53** (1992) p. 521.

[18] D.W. Henderson and D.G. Ast, *J. Non-Cryst. Sol.* **64** (1984) p. 43.

CHAPTER V

Optics Theory - Background

5.1 Introduction

In this chapter, the theoretical background for the next two chapters is presented. The relationship between the optical constants, which determine all optical properties of a material, and the complex dielectric function is derived. It is shown how the real part of the complex dielectric function can be calculated from the *absorption spectrum*, the imaginary part of the dielectric function (and *vice versa*). The Lorentz expression for the dielectric function is derived classically and shown to be consistent with the absorption spectrum of a quantum solid. Phillips' empirical spectroscopic theory, which relates the local atomic structure to the static (i.e. at zero photon energy) limit of the dielectric function, is presented.

5.2 Fundamental Optics

In this section, light is described as a transverse electromagnetic (EM) wave with angular frequency ω and wave vector $\boldsymbol{k}$. Due to wave-particle duality, however, light can also be represented as a photon, a particle with energy E and momentum $\boldsymbol{p}$, given by

$$E = \hbar\omega \,. \tag{5.1a}$$

and

$$\boldsymbol{p} = \hbar\boldsymbol{k} \,. \tag{5.1b}$$

The latter representation will become useful in section 5.4, when the electronic response of a material is treated quantum mechanically.

5.2.1 Maxwell's equations and the material relations

An electromagnetic field is represented by the electric field vector, $\mathcal{E}$, and the magnetic field vector, $\boldsymbol{H}$. To describe the effect of these fields on material objects, it is necessary to introduce the electric current density, $\boldsymbol{j}$, the polarisation, $\boldsymbol{P}$, and the magnetic induction, $\boldsymbol{B}$ [1].These five basic quantities are connected through *Maxwell's equations*:

$$curl\, \boldsymbol{H} - \left(\varepsilon_o \dot{\mathcal{E}} + \dot{\boldsymbol{P}}\right) = \boldsymbol{j} \qquad (5.2a)$$

$$curl\, \mathcal{E} + \dot{\boldsymbol{B}} = 0 \qquad (5.2b)$$

$$div\left(\varepsilon_o \mathcal{E}\right) = \rho \qquad (5.2c)$$

$$div\, \boldsymbol{B} = 0 \qquad (5.2d)$$

where ρ is the electric charge density and a dot above a symbol denotes the time derivative. The materials properties that describe the response of the material to the EM field are defined through the *materials relations*:

$$\boldsymbol{j} = \sigma \mathcal{E} \qquad (5.3a)$$

$$\boldsymbol{P} = \varepsilon_o (\varepsilon - 1)\, \mathcal{E} \qquad (5.3b)$$

$$\boldsymbol{B} = \mu \boldsymbol{H}\,. \qquad (5.3c)$$

These relations define the specific conductivity, σ, the dielectric function, ε, and the magnetic permeability, μ. When the material does not respond to the EM field, no current or polarisation is induced (i.e. $\sigma = 0$ and $\varepsilon = 1$), and the induction equals the magnetic field (i.e. $\mu = 1$). The field vectors $\mathcal{E}$ and $\boldsymbol{H}$ are related by means of simultaneous differential equations. By substituting the materials relations into the Maxwell equations, separate

differential equations for $\mathcal{E}$ and $\boldsymbol{H}$ can be derived. For a *homogeneous* medium, it can be shown that this gives for the electric field vector [1]

$$\nabla^2 \mathcal{E} - \frac{\varepsilon\mu}{c^2}\ddot{\mathcal{E}} = 0\,. \tag{5.4}$$

Eq (5.4) is a standard wave equation which is satisfied by the plane wave

$$\mathcal{E} = \mathcal{E}_o \exp[i(\boldsymbol{k}x - \omega t)], \tag{5.5}$$

where ω is the angular frequency of the oscillation and $\boldsymbol{k}$ is the wave vector. The velocity of the wave is

$$v = \frac{x}{t} = \frac{\omega}{|\boldsymbol{k}|}. \tag{5.6}$$

Putting eq (5.5) into eq (5.4) gives

$$-\omega^2 \mathcal{E} + \frac{\varepsilon\mu}{c^2}\boldsymbol{k}^2 \mathcal{E} = 0, \tag{5.7}$$

From eqs (5.6) and (5.7) it thus follows that the velocity of the plane wave is equal to

$$v = \frac{c}{\sqrt{\varepsilon\mu}}. \tag{5.8}$$

The *refractive index*, n, of a material is defined as the ratio of the velocities of light in vacuum and in the material in question, i.e.

$$n \equiv \frac{c}{v}. \tag{5.9}$$

Comparing eqs (5.8) and (5.9) gives

$$n = \sqrt{\varepsilon\mu}\,, \tag{5.10}$$

which is known as *Maxwell's formula*.

5.2.2 Including absorption

Thus far, it is assumed that the EM wave passes through the medium without being attenuated; absorption by the material is ignored. It can be shown that including absorption gives rise to a damping term in the wave equation for $\mathcal{E}$ [1]:

$$\nabla^2 \mathcal{E} - \frac{\varepsilon\mu}{c^2}\ddot{\mathcal{E}} - \frac{4\pi\mu\sigma}{c^2}\dot{\mathcal{E}} = 0. \tag{5.11}$$

The solution to this differential equation can be written in a form analogous to eq (5.5) by introducing a *complex* wave vector, $\tilde{k}$:

$$\mathcal{E} = \mathcal{E}_o \exp[i(\tilde{k}\, x - \omega t)]. \tag{5.12}$$

As $\dot{\mathcal{E}} = -i\omega\mathcal{E}$, eq (5.11) may be rewritten as

$$\nabla^2 \mathcal{E} - \frac{\mu}{c^2}\left(\varepsilon + i\frac{4\pi\sigma}{\omega}\right)\dot{\mathcal{E}} = 0. \tag{5.13}$$

To retain the analogy with the non-absorbing case, a complex dielectric function is defined

$$\tilde{\varepsilon} \equiv \varepsilon + i\frac{4\pi\sigma}{\omega}, \tag{5.14}$$

which is often written as

$$\tilde{\varepsilon} \equiv \varepsilon_1 + i\varepsilon_2. \tag{5.15}$$

Substituting eq (5.12) and (5.14) into (5.13) gives

$$\tilde{k} = \frac{\omega}{c}\sqrt{\tilde{\varepsilon}\mu}, \tag{5.16}$$

which defines the complex wave vector in eq (5.12). Similarly, absorption calls for a complex refractive index

$$\tilde{n} = \sqrt{\tilde{\varepsilon}\mu}. \tag{5.17}$$

As strongly magnetic materials are not of interest to this study, $\mu \approx 1$, so that

$$\tilde{n} = \sqrt{\tilde{\varepsilon}}. \tag{5.18}$$

The complex refractive index is usually written as

$$\tilde{n} = n + ik, \tag{5.19}$$

where n is the refractive index and k is called the *absorption coefficient*. Equating the real and imaginary parts of eq (5.18) gives

$$n = \left[\tfrac{1}{2}\sqrt{\varepsilon_1^2 + \varepsilon_2^2} + \tfrac{1}{2}\varepsilon_1\right]^{\frac{1}{2}} \tag{5.20a}$$

and $$k = \left[\tfrac{1}{2}\sqrt{\varepsilon_1^2 + \varepsilon_2^2} - \tfrac{1}{2}\varepsilon_1\right]^{\frac{1}{2}}. \tag{5.20b}$$

Inverting these equations to express the real and imaginary parts of the dielectric function in terms of the optical constants gives the simpler relations

$$\varepsilon_1 = n^2 - k^2 \tag{5.20c}$$

and $$\varepsilon_2 = 2nk\,. \tag{5.20d}$$

From eq (5.12), it can be seen that the square intensity of the EM wave is given by

$$|\mathcal{E}|^2 = |\mathcal{E}_o|^2 \exp\left(-2x\,\mathrm{Im}[\tilde{k}]\right). \tag{5.21}$$

Using eqs (5.16), (5.17) and (5.19), this can be rewritten as

$$|\mathcal{E}|^2 = |\mathcal{E}_o|^2 \exp\left(-2\frac{\omega}{c}kx\right). \tag{5.22}$$

Thus, as the wave travels through an absorbing medium, its intensity decreases at a rate given by the absorption coefficient, k. The energy density of the electric component of the EM wave, w_e, can be shown to be related to the square intensity through [1]

$$w_e = \frac{1}{2}\varepsilon_o\, n^2\, |\mathcal{E}|^2. \tag{5.23}$$

n and k are often referred to as the *optical constants*, as they are materials constants. In general, however, like ε_1 and ε_2, they are functions of ω, the frequency of the EM wave.

5.2.3 The Kramers-Kronig relations and Sum Rules

The material relation eq (5.3b) describes the polarisation induced by the electric field. The proportionality "constant" in such a relation is called a *linear response function*. It can be shown [2] that for *any* complex response function, its real and imaginary parts are related throught the Kramers-Kronig relations. For the dielectric response function, $[\tilde{\varepsilon}(E)-1]$, the Kramers-Kronig relations take the form

$$\varepsilon_1(E) = 1 + \frac{2}{\pi}\mathscr{P}\int_0^\infty \frac{E'\varepsilon_2(E')}{(E')^2 - E^2}\,\mathrm{d}E' \qquad (5.24a)$$

and $$\varepsilon_2(E) = \frac{2}{\pi}E\mathscr{P}\int_0^\infty \frac{\varepsilon_1(E')-1}{(E')^2 - E^2}\,\mathrm{d}E', \qquad (5.24b)$$

where $\mathscr{P}$ denotes "principal integral" and means the singularity at $E = E'$ is to be ignored. Note that E is the photon energy while E' is a dummy parameter of unit energy. Eqs (5.24) state that if the absorption spectrum, ε_2, is known over the entire range of photon energy E, then the real part of the dielectric function can be calculated, and vice versa.

There is an infinite number of integral relations between the real and imaginary parts of the dielectric function (or refractive index), known as *sum rules*. They can be derived from the Kramers-Kronig relations and the high-energy limit, $E >> E_p$, of the dielectric function:

$$\varepsilon_1(E) = 1 - \left(\frac{E_p}{E}\right)^2 + O(E^{-3}) \qquad (5.25a)$$

and $$\varepsilon_2(E) \le O(E^{-3}), \qquad (5.25b)$$

where E_p is the *plasma energy* (to be discussed in section 5.3), which is approximately 15 – 20 eV, and O is the order symbol. Eqs (5.25) can be shown to be a rigorous result [2]. Taking the limit $E \to \infty$ in eq (5.24a) and comparing with eq (5.25a) gives

$$\int_0^\infty E'\varepsilon_2(E')\mathrm{d}E' = \frac{\pi}{2}E_p^2, \qquad (5.26)$$

which is known as the *f* sum rule. Taking $E \to 0$ in eq (5.24a) gives the static limit sum rule

$$\varepsilon_1(0) = 1 + \frac{2}{\pi}\int_0^\infty \frac{\varepsilon_2(E)}{E}\,\mathrm{d}E\,. \qquad (5.27)$$

This result will be important in relating the static optical properties, as treated in Phillips' spectroscopic theory (see section 5.5), to the model for the absorption spectrum, to be developed in the next chapter. A large number of sum rules for the optical constants can be found in [3]. Sum rules can be used as a self-consistence check for experimentally determined values for the optical constants. From a theoretical point of view, they can be used to test model dielectric functions. In fact, an approximate dielectric function is considered virtuous if it obeys the Kramers-Kronig relations and therefore the sum rules.

5.3 Classical Derivation of the Lorentz Expression

In this section, the functional form of the dependence of the dielectric function on the photon energy is derived for a material with a classical response to the EM field. The result will be used later in section 5.6.

5.3.1 Plasma oscillations

Consider a lattice of ions held together by a free electron gas [4]. Plasma oscillations are collective longitudinal oscillations of the electrons in a free electron gas. These oscillations constitute a polarisation wave which sets up planes of alternately positive and negative charge, as shown in Fig. 5.1.

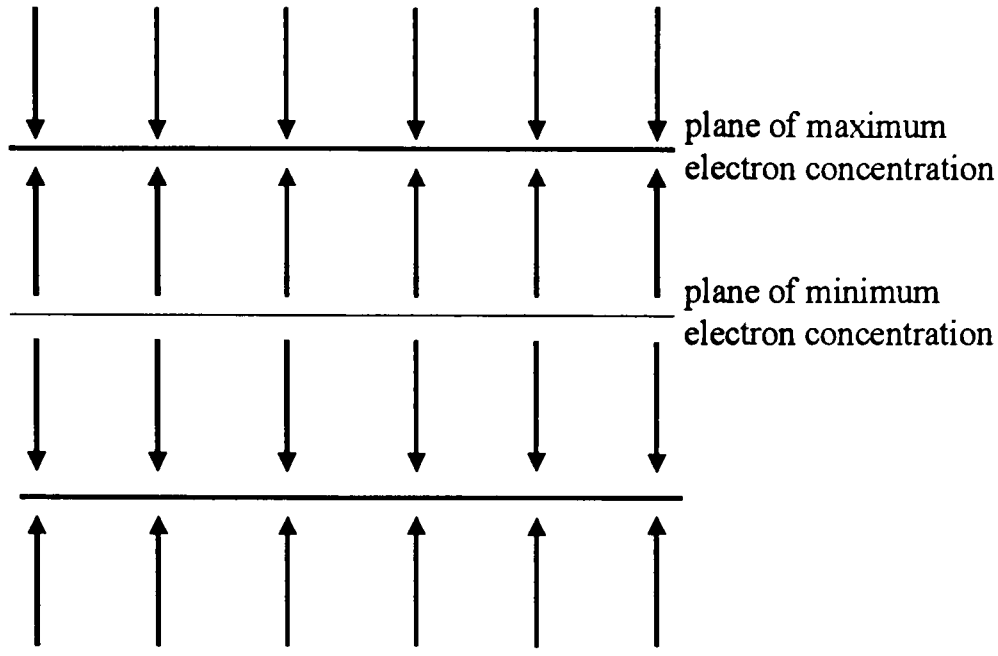


Figure 5.1 Schematic representation of the planes of minimum and maximum electron concentration set up by a plasma oscillation.

By the geometry of the planes, this creates a depolarisation field

$$\mathcal{E} = -\frac{\boldsymbol{P}}{\varepsilon_o}. \tag{5.28}$$

The displacement of an electron with charge $-e$ by distance x creates a dipole moment

$$\boldsymbol{p} = -e\boldsymbol{x}. \tag{5.29}$$

Thus, the polarisation , i.e. the dipole moment per unit volume, is equal to

$$\boldsymbol{P} = \frac{N}{V}\boldsymbol{p} = -\frac{N}{V}e\boldsymbol{x}. \tag{5.30}$$

Putting eq (5.30) into eq (5.28) gives

$$\mathcal{E} = \frac{N}{V}\frac{e}{\varepsilon_o}x \tag{5.31}$$

for the polarisation field. Each electron in the gas feels a force $-e\mathcal{E}$ as a result of this field so that, according to Newton's second law of motion:

$$m_e\ddot{\boldsymbol{x}} = -\frac{N}{V}\frac{e}{\varepsilon_o}\boldsymbol{x}, \tag{5.32}$$

where m_e is the mass of the electron. Eq (5.32) may be written as

$$\ddot{x} + \omega_p^2 x = 0, \tag{5.33}$$

which is a standard wave equation, suggesting the plasma oscillation has frequency

$$\omega_p \equiv \sqrt{\frac{N}{V}\frac{e^2}{\varepsilon_o m_e}}, \tag{5.34}$$

known as the *plasma frequency*. Plasma oscillations can be triggered by an EM field or by passing an electron through the plasma. This will be accompanied by an energy loss equal to

$$E_p = \hbar\omega_p, \tag{5.35}$$

or an integral multiple of E_p. Thus, the plasma frequency can be determined from the energy loss spectrum of an electron beam or an EM field.

5.3.2 The dielectric function of a free electron gas [5]

In the presence of an EM field, $\mathcal{E}$, the equation of motion for the electron is

$$m_e \ddot{x} = -e\mathcal{E}. \tag{5.36}$$

Assuming x has an harmonic time dependence, it follows that

$$-m_e\omega^2 x = -e\mathcal{E}, \tag{5.37}$$

where ω is the angular frequency of the oscillating electron. Thus, the displacement of the electron is related to the field through

$$x = \frac{e}{m_e\omega^2}\mathcal{E}. \tag{5.38}$$

With eqs (5.29) and (5.30), this gives for the polarisation

$$P = -\frac{N}{V}\frac{e^2}{m_e\omega^2}\mathcal{E}. \tag{5.39}$$

Comparing eqs (5.3b) and (5.39) finally gives

$$\varepsilon(E) = 1 - \frac{E_p^2}{E^2}, \qquad (5.40)$$

where the definition of the plasma frequency, eqs (5.1a) and (5.35) have been used.

5.3.3 The dielectric function for bound electrons [5]

The simplest way of treating bound rather than free electrons is by assuming that the electrons are sitting in a *parabolic* potential:

$$V = C\,x^2, \qquad (5.41)$$

The electrons then experience a force – dV/dx in addition to the force of the EM field, so that the equation of motion becomes

$$m_e \ddot{\boldsymbol{x}} = -e\,\mathcal{E} - 2C\boldsymbol{x}\,. \qquad (5.42)$$

Solving this equation of motion as was done for eq (5.36) gives

$$\varepsilon(E) = 1 + \frac{E_p^2}{\Delta^2 - E^2}, \qquad (5.43)$$

where Δ can be shown to be given by

$$\Delta \equiv \hbar\sqrt{2C / m_e}\;; \qquad (5.44)$$

the $\sqrt{2C / m_e}$ term is the *eigen frequency* of the electron, which performs a harmonic oscillation, rocking back and forth in its parabolic potential. Δ can thus be thought of as the *resonance energy* of the system, because when the photon energy, E, equals Δ, the frequency of the EM field is equal to the eigen frequency of the electron. Note that eq (5.43) has a singularity at $E = \Delta$; the dielectric response is well defined everywhere except at the resonance energy itself. Also note that eq (5.43) is real; in other words: absorption is not included.

5.3.4 Including absorption

The singularity in eq (5.43) can be remedied by including a damping term in the equation of motion:

$$m_e \ddot{x} = -e\mathcal{E} - 2Cx - \gamma \dot{x} . \qquad (5.45)$$

where γ, the constant of proportionality between the damping force and the velocity of the electron is called the damping constant. Eq (5.45) leads to the dielectric function

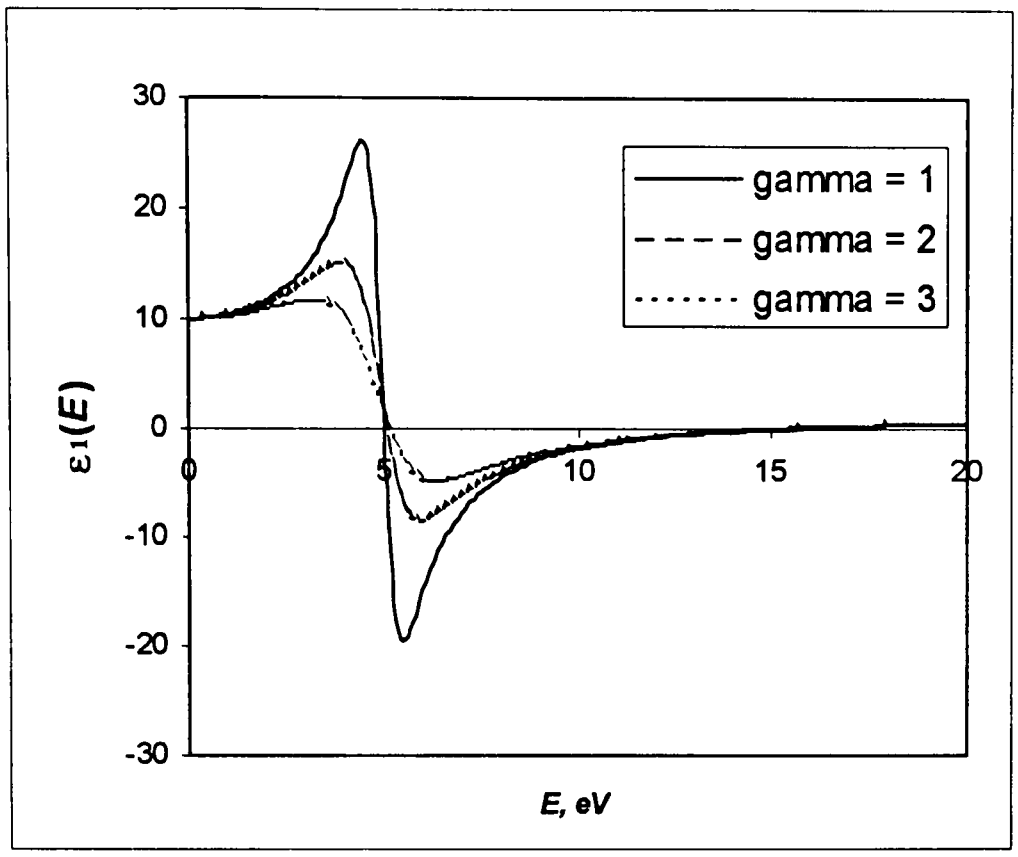
$$\tilde{\varepsilon}(E) = 1 + \frac{E_p^2}{\Delta^2 - E^2 - i\Gamma E} \qquad (5.46)$$

where Γ is defined by the damping constant: $\Gamma \equiv \hbar\gamma / m_e$. Thus, the damping term has removed the singularity in the real part of the dielectric function and has introduced an imaginary part. Eq (5.46) is called the *Lorentz expression* for the dielectric function; it describes the dielectric response of a damped harmonic oscillator to an EM field. Multiplying both the numerator and the denominator of the fraction by the complex conjugate of the denominator and comparing with eq (5.15) yields

$$\varepsilon_1(E) = 1 + E_p^2 \frac{\Delta^2 - E^2}{(\Delta^2 - E^2)^2 + (\Gamma E)^2} \qquad (5.47a)$$

and $$\varepsilon_2(E) = E_p^2 \frac{(\Gamma E)}{(\Delta^2 - E^2)^2 + (\Gamma E)^2} . \qquad (5.47b)$$

Fig. 5.2 a) shows a plot of the real part of the dielectric function, ε_1, for various values of Γ. Fig. 5.2 b) shows a plot of the imaginary part, indicating that $\varepsilon_2(E)$ takes the form of a *peak around* Δ, with *width approximately equal to* Γ.



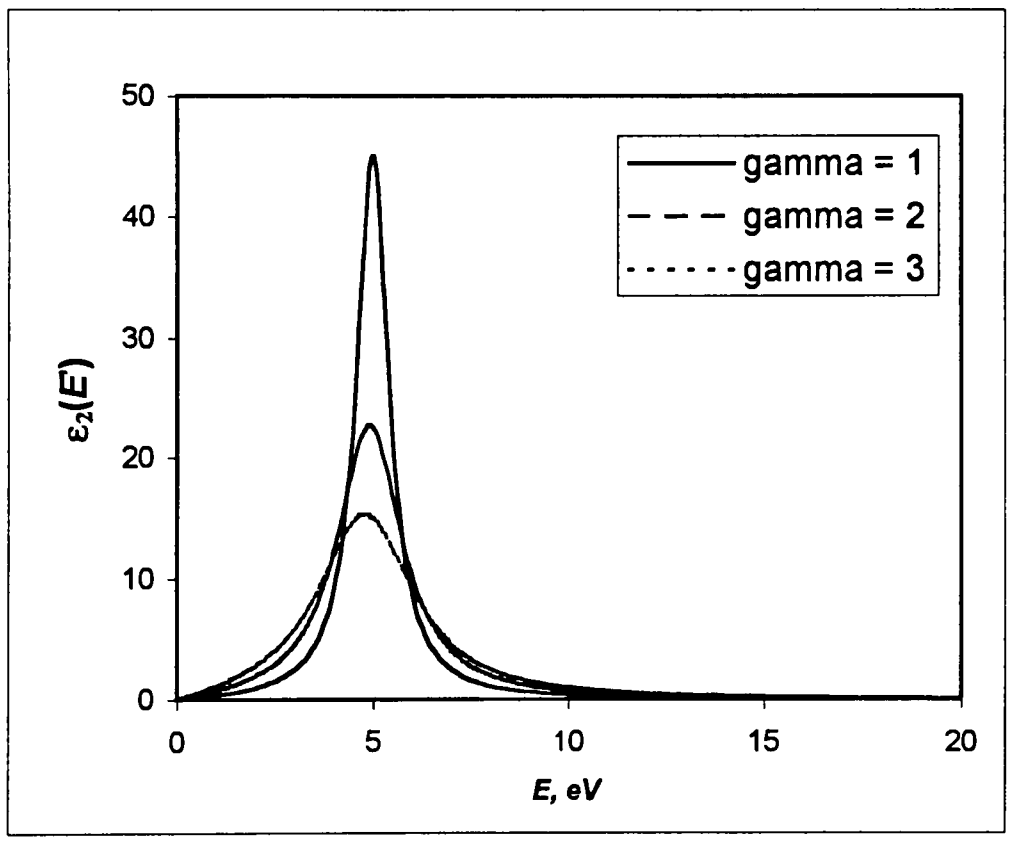


Figure 5.2 Plot of the real and imaginary parts of the dielectric function in eq (5.47) for $E_p = 15$ eV, $\Delta = 5$ eV and different values for the damping constant, Γ.

5.3.5 The electron energy loss function

The electron energy loss function (or simply loss function) is defined as

$$-\mathrm{Im}[\tilde{\varepsilon}^{-1}] = -\mathrm{Im}\left[\frac{1}{\varepsilon_1 + i\varepsilon_2}\right] = \frac{\varepsilon_2}{\varepsilon_1^2 + \varepsilon_2^2}, \qquad (5.48)$$

and is thus a renormalised absorption spectrum. The loss function for the damped harmonic oscillator, eq (5.46), is thus

$$-\mathrm{Im}[\tilde{\varepsilon}^{-1}] = -\mathrm{Im}\left[\frac{1}{1+E_p^2/(\Delta^2 - E^2 - i\Gamma E)}\right]$$

$$= E_p^2 \frac{\Gamma E}{(E_p^2 + \Delta^2 - E^2)^2 + (\Gamma E)^2}, \qquad (5.49)$$

which is very similar to the functional form of the absorption spectrum in eq (5.47b). Whilst the absorption spectrum consists of a peak around Δ, the loss function consists of a peak around $\sqrt{E_p^2 + \Delta^2}$, both with the same width Γ. As $E_p^2 >> \Delta^2$, the peak in the loss function is close to the plasma energy.

5.3.6 The absorption spectrum in the limit $\Gamma \to 0$

Letting Γ approach zero in eq (5.47b) yields

$$\varepsilon_2(E) = E_p^2 \frac{(\Gamma E)}{(\Delta^2 - E^2)^2}, \qquad (5.50)$$

which is zero *unless* $E = \Delta$. In the latter case, the limit is

$$\varepsilon_2(E) = E_p^2 \lim_{\Gamma \to 0} \frac{1}{\Gamma E}, \qquad (5.51)$$

which is infinite. Thus, in the limit of $\Gamma \to 0$, the absorption peak has infinite height and zero width. The surface under the peak follows from

$$\int_0^\infty \lim_{\Gamma \to 0} \varepsilon_2(E)\mathrm{d}E = E_p^2 \int_0^\infty \lim_{\Gamma \to 0} \frac{1/(\Gamma E)}{1+[(\Delta+E)(\Delta-E)/\Gamma E]^2}\mathrm{d}E$$

$$= E_p^2 \frac{1}{2\Delta} \lim_{\Gamma' \to 0} \int_0^\infty \frac{1/\Gamma'}{1+[(\Delta-E)/\Gamma']^2}\mathrm{d}E \qquad (5.52)$$

$$= E_p^2 \frac{\pi}{2\Delta}$$

In the second step the substitution $\Gamma' \equiv \Gamma / 2$ is made and E is replaced by Δ to simplify the expression as much as possible without affecting the singularity. This may be done because in the limit $\Gamma \to 0$, $\varepsilon_2(E) = 0$ unless $E = \Delta$. The third step follows as the surface under a Lorentzian is equal to π, independent of Γ. Thus, in the limit $\Gamma \to 0$, the absorption peak becomes

$$\varepsilon_2(E) = E_p^2 \frac{\pi}{2\Delta} \delta(E - \Delta). \tag{5.53}$$

When each electron is allowed to have a different eigen frequency $\Delta E_j / \hbar$ and Γ_j, the absorption spectrum is equal to

$$\varepsilon_2(E) = \frac{\pi}{2} E_p^2 \sum_j \frac{f_j}{\Delta E_j} \delta(E - \Delta E_j). \tag{5.54}$$

where f_j is the *oscillator strength*, the fraction of electrons with eigen frequency $\Delta E_j / \hbar$. In the next section, eq (5.54) will be derived quantum mechanically, proving that the functional form of the imaginary part of the dielectric function is the same for the classical and quantum mechanical case. The main reason why eq (5.54) was derived here classically first is because in the next chapter, the quantum mechanical absorption spectrum will be modeled to eq (5.47b). Knowing that eq (5.54a) is the *real* part of the dielectric function of which eq (5.54b) is the imaginary part, eq (5.54a) thus gives an analytic expression for the quantum mechanical model for the dielectric function.

5.4 Quantum Mechanical Derivation of the Lorentz Expression

In the previous section, the electrons were treated as particles, sitting in a parabolic potential. The dielectric response was calculated by solving the classical equation of motion in the presence of an EM field. In reality, however, electrons are not classical particles sitting in a parabolic potential. Rather, they are quantum mechanical particles whose properties are determined by their wave function Ψ. The wave function is found by solving the *Schrödinger equation*

$$\hat{H}\Psi = E\Psi \tag{5.55}$$

where $\hat{H}$ is the total energy operator, the *Hamiltonian*, and E is the energy of the particle described by Ψ. The solutions of eq (5.55) are eigen functions; operating upon them with the Hamiltonian leaves the eigen functions unchanged, apart from a proportionality constant, E. For an electron moving in a potential $V(\boldsymbol{r})$, the Hamiltonian is equal to

$$\hat{H} = -\frac{\hbar^2}{2m_e}\nabla^2 + V(\boldsymbol{r}). \tag{5.56}$$

5.4.1 The atomic orbitals of an isolated free atom

An electron in an isolated free atom feels a spherically symmetric potential $V(\boldsymbol{r})$ due to the nucleus and the effective potential of the other electrons [6]. Solving the Schrödinger equation for this case yields eigen functions

$$\Psi_{nlm}(\boldsymbol{r}) = R_{nl}(r)Y_{lm}(\theta,\varphi), \tag{5.57}$$

where $\boldsymbol{r}$, θ and φ are spherical polar coordinates. The *orbitals*, as these eigen functions are known as, are characterised by three quantum numbers:

the principal quantum number: $n = 1, 2, 3, \ldots$

the orbital quantum number: $l = 0, 1, 2, \ldots, n-1$

and the magnetic quantum number $m = 0, \pm 1, \pm 2, \ldots, \pm l$.

The energy of the orbitals is proportional to $-1/n^2$; the angular momentum of the orbital is given by $\hbar\sqrt{l(l+1)}$, whilst m gives the component of the angular momentum in a particular direction. States with orbital quantum numbers $l = 0$, 1 are called s and p orbitals, respectively, and the orbitals are labelled 1s ($n = 1$, $l = 0$), 2s ($n = 2$, $l = 0$), $2p_x$ ($n = 2$, $l = 1$, $m = 1$), $2p_y$ ($n = 2$, $l = 1$, $m = -1$), $2p_z$ ($n = 2$, $l = 1$, $m = 0$), 3s, etc.

The orbitals are orthonormal:

$$\int \Psi^*_{nlm}(\boldsymbol{r})\Psi_{n'l'm'}(\boldsymbol{r})\mathrm{d}\boldsymbol{r} = \begin{cases} 0 & \text{for } n \neq n', l \neq l' \text{ or } m \neq m' \\ 1 & \text{for } n = n', l = l' \text{ and } m = m' \end{cases}, \qquad (5.58)$$

Each of the states can be occupied by two electrons only, according to the Pauli exclusion principle. The first three radial functions are given by

$$R_{1s}(r) = 2\exp(-r), \qquad (5.59a)$$

$$R_{2s}(r) = \tfrac{1}{\sqrt{2}}(1-\tfrac{1}{2}r)\exp(-r/2), \qquad (5.59b)$$

and $$R_{2p}(r) = \tfrac{1}{\sqrt{24}} r\exp(-r/2). \qquad (5.59c)$$

Note that the R_1 state falls off faster with distance than the R_2 states. The functions Y_{0m}, corresponding to the s-orbitals, can be shown to have no angular dependence. The states with non-zero angular momentum, however, are not spherically symmetric. For the s and p_z orbitals, for example, it can be shown that

$$Y_{00} = \tfrac{1}{\sqrt{4\pi}} \qquad (5.60a)$$

and $$Y_{10} = \sqrt{\tfrac{3}{4\pi}}\cos\theta. \qquad (5.60b)$$

Note that the p orbital is negative for $\theta > \pi/2$, i.e. for $z = r\cos\theta < 0$. The intercept of the s and p_z orbitals with the y-z plane are shown in Fig. 5.3.

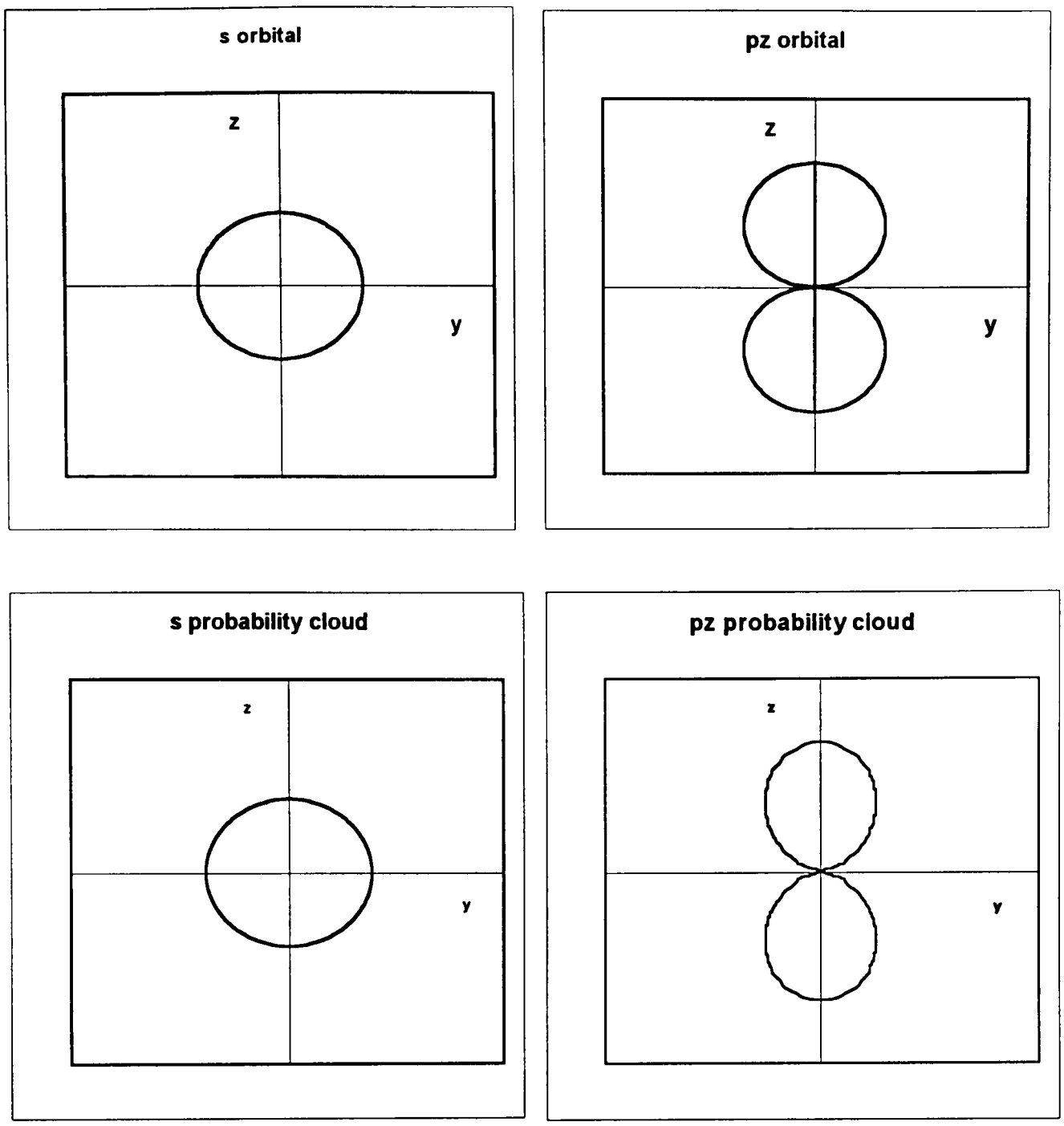


Figure 5.3 Intercept of the s and p_z orbitals with the x-y plane and their corresponding probability clouds.

The p_x and p_y orbitals have the same shape as p_z, but lie along the x and y axes, respectively. The probability clouds are given by $|Y|^2$; they are also shown in Fig. 5.3.

5.4.2 The band structure of a solid

When atoms are brought together to form a solid, the outer electrons (valence electrons) become detached from the ion cores and are allowed to move through the solid [7]. Valence electrons feel a potential

$$V(\boldsymbol{r}) = \sum_j V_j(\boldsymbol{r}_j), \tag{5.61}$$

where V_j is the potential due to ion core j at position $\boldsymbol{r}_j$. The electron eigenvalues are obtained by looking for wave functions that are linear combinations of the atomic valence orbitals:

$$\Psi = \sum_{\alpha,j} c_{\alpha,j}\psi_{\alpha,j}\,, \tag{5.62}$$

where $\psi_{\alpha,j}$ denotes orbital α on atom j. As the atomic orbitals are known, the remaining task is to calculate the coefficients $c_{\alpha,j}$.

As an illustration, the simplest case of an atomic structure shall be considered first; a monatomic linear chain of single atoms, with one valence s orbital on each atom. According to Bloch's theorem, the wave function for this case can be written as

$$\Psi = \frac{1}{\sqrt{N}}\sum_{j=1}^{N} e^{ikja}\psi_j \tag{5.63}$$

where N is the number of electrons, ψ_j is the s orbital on atom j, a is the periodicity of the chain and k the wave vector of the electron. Putting eq (5.63) into eq (5.55) gives

$$\frac{1}{\sqrt{N}}\sum_j e^{i(kja)}\hat{H}\psi_j = \frac{1}{\sqrt{N}}\sum_j e^{i(kja)}E\psi_j\,. \tag{5.64}$$

Multiplying from the left by $e^{-i(kpa)}\psi_p^*$ and integrating over $\boldsymbol{r}$ gives

$$\sum_j e^{i[k(j-p)a]}\int \psi_p^*\hat{H}\psi_j\,\mathrm{d}\boldsymbol{r} = \sum_j e^{i[k(j-p)a]}E\int \psi_p^*\psi_j\,\mathrm{d}\boldsymbol{r}$$

$$= E\int \psi_p^*\psi_j\,\mathrm{d}\boldsymbol{r} = E\,, \tag{5.65}$$

if it is assumed that the overlap between the s orbitals may be ignored. With the *on-site energy* of the orbital equal to

$$E_s = \int \psi_j^*\hat{H}\psi_j\,\mathrm{d}\boldsymbol{r} \tag{5.66}$$

and including only *hopping integrals* between s states on nearest neighbours

$$(ss\sigma) = \int \psi_j^* \hat{H} \psi_{j+1} \mathrm{d}\boldsymbol{r}\,, \tag{5.67}$$

it follows from eq (5.65) that

$$E = E_s + (e^{i(ka)} + e^{-i(ka)})(ss\sigma) = E_s + 2(ss\sigma)\cos(ka)\,. \tag{5.68}$$

The relation between the energy, E, and the wave vector, k, is known as the *band structure*. For the simple case considered, $E(k)$ is a single band, drawn in Fig. 5.4.

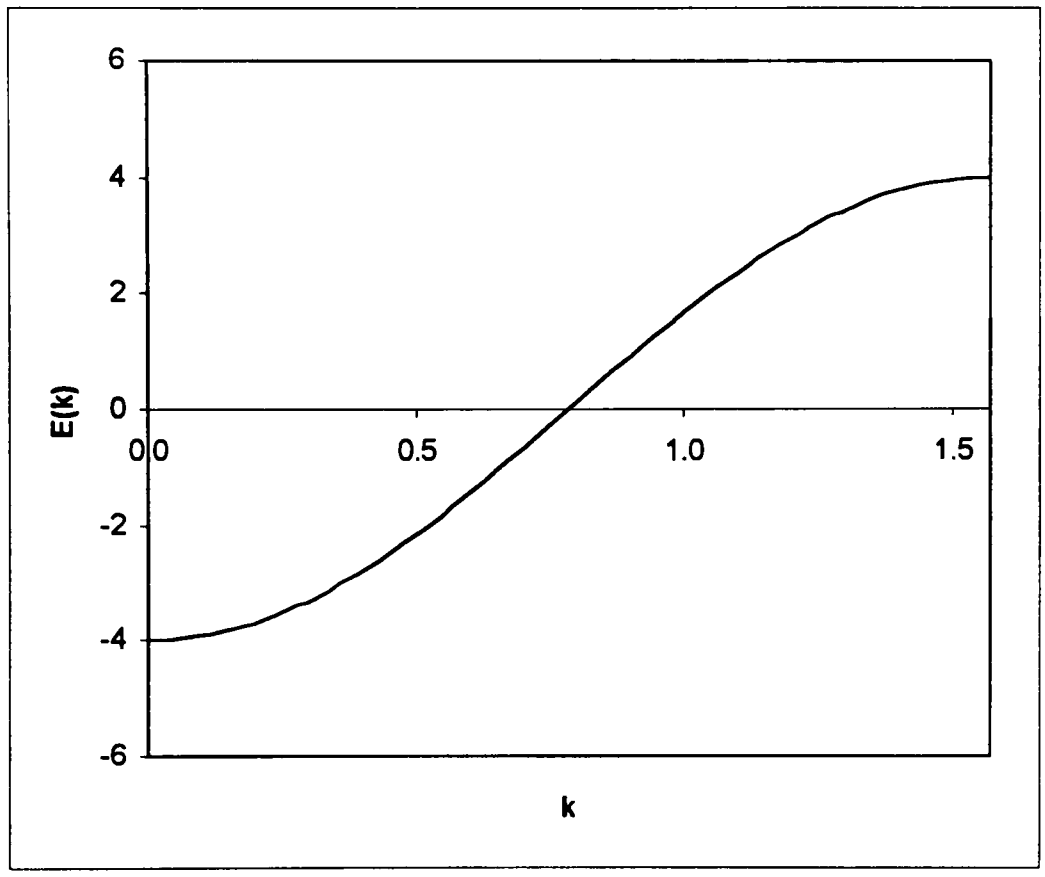


Figure 5.4 Plot of eq (5.68), the band structure of the monatomic linear chain, plotted for $0 < k < \pi/a$, with $a = 2$, $E_s = 0$ and (ssσ)= – 2 eV.

Now, consider a linear chain consisting of *two* alternating types of atom, -A-B-A-B-A- etc, with one s orbital and on-site energies E_A and E_B, respectively ($E_A < E_B$), and nearest neighbour hopping integral (ssσ). The wave function now becomes

$$\Psi = \frac{1}{\sqrt{N}} \sum_j e^{i(k2aj)} [c_A \psi_{A,j} + c_B \psi_{B,j}]\,, \tag{5.69}$$

as there are two atoms in the unit cell and the periodicity is $2a$. Putting eq (5.69) into eq (5.55), multiplying from the left by $\psi_{A,o}$ and integrating over $\boldsymbol{r}$ now gives

$$(E_A - E)c_A + (ss\sigma)(1 + e^{-i(k2a)})c_B = 0 \qquad (5.70a)$$

whilst multiplying with $\psi_{B,o}$ and integrating gives

$$(ss\sigma)(e^{i(k2a)} + 1)c_A + (E_B - E)c_B = 0. \qquad (5.70b)$$

These two equations can be written in matrix form as

$$\begin{bmatrix} E_A - E & (ss\sigma)(1 + e^{-i(k2a)}) \\ (ss\sigma)(1 + e^{i(k2a)}) & E_B - E \end{bmatrix} \begin{bmatrix} c_A \\ c_B \end{bmatrix} = 0. \qquad (5.71)$$

The solutions follow from equating the determinant to zero:

$$(E_A - E)(E_B - E) - (ss\sigma)^2(1 + e^{-i(k2a)})(1 + e^{i(k2a)}) = 0 \qquad (5.72)$$

which is a quadratic equation in E with solutions

$$E^{\pm} = E_{AB} \pm \sqrt{\delta^2 + 4(ss\sigma)^2 \cos^2(ka)}, \qquad (5.73)$$

where $E_{AB} \equiv (E_A + E_B)/2$ and $\delta \equiv (E_A - E_B)/2$. Eq (5.73) is plotted in Fig. 5.5. The presence of *two* orbitals in the unit cell has given rise to two energy bands. In general, the number of orbitals in the unit cell equals the number of energy bands.

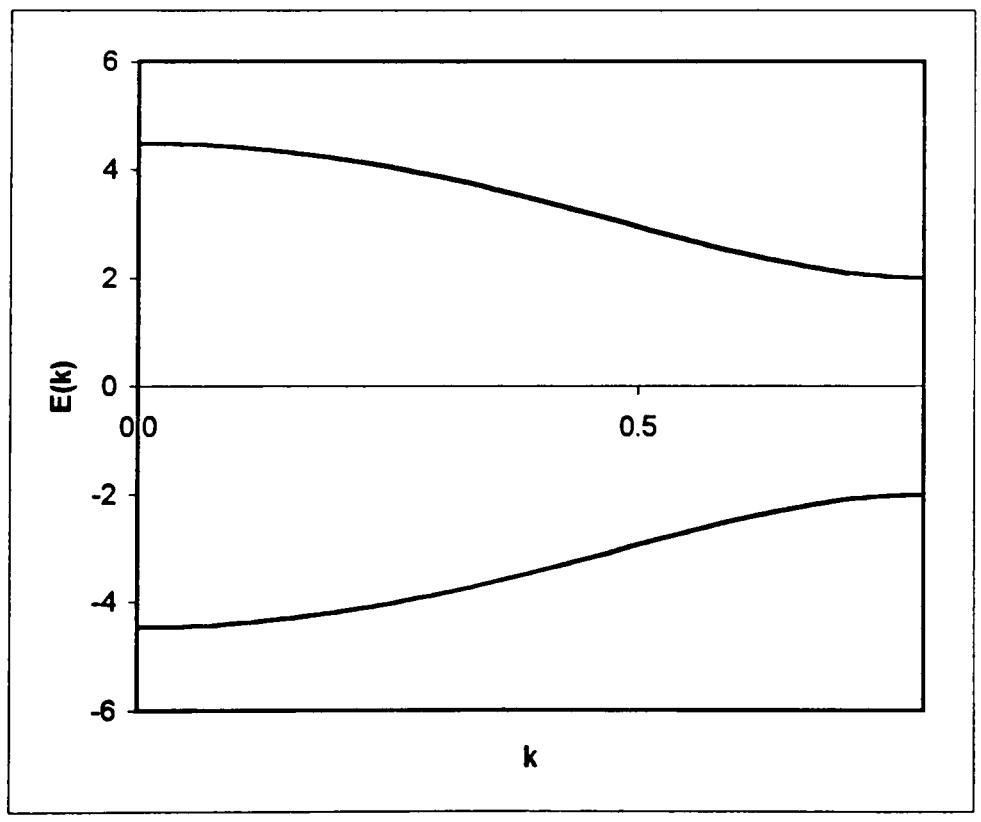


Figure 5.5 Plot of eq (5.73), the band structure of the -A-B-A-B-A- linear chain, plotted for $0 < k < \pi/2a$, with $a = 2$, $E_{AB} = 0$, $\delta = 2$ eV and (ssσ)= – 2 eV.

The optical response of a material can be calculated from the band structure. How this is done is treated in the next section, using the bands in Fig. 5.5 as an example.

5.4.3 Derivation of the Lorentz expression

In the presence of an EM field, the Hamiltonian for the electron can be written as [8]

$$\hat{H} = \hat{H}_o + \hat{H}_{er}, \tag{5.74}$$

where $\hat{H}_o$ is the Hamiltonian for the unperturbed system treated in the previous section and $\hat{H}_{er}$ is the electron-radiation interaction Hamiltonian. As $\hat{H}_{er}$ is small compared to $\hat{H}_o$, the band structure corresponding to $\hat{H}$ can be approximated by the unperturbed band structure. Consider the EM field as a flux of photons of energy $E = \hbar\omega$. These photons can excite an electron in a valence band state to an unoccupied state in the conduction band, absorbing the photon. It is this quantum mechanical process that gives rise to the absorption in a material. Conservation of energy requires that the transition energy $\Delta E \equiv E_c - E_v$ equals the photon energy:

$$\Delta E \equiv E. \tag{5.75}$$

The transition probability per unit time, $\mathscr{T}$, is given by Fermi' s Golden Rule:

$$\mathscr{T} = \frac{2\pi}{\hbar}\sum_i |<c|\hat{H}_{er}|v>|_i^2 \delta(E - \Delta E_i), \tag{5.76}$$

where $\delta(E)$ is the delta function and Dirac notation is used for convenience:

$$|<c|\hat{H}_{er}|v>|^2 \equiv |\int \psi_c^* \hat{H}_{er} \psi_v \mathrm{d}\boldsymbol{r}|^2. \tag{5.77}$$

As $|c>$ and $|v>$ are Bloch waves, they have a well defined wave vector, k. In that case, $\hat{H}_{er}$ is conveniently expressed in terms of the momentum operator, $\hat{\boldsymbol{p}}$:

$$\hat{H}_{er} = \frac{e}{m_e c} \boldsymbol{A} \cdot \hat{\boldsymbol{p}}, \tag{5.78}$$

where $\hat{p} = -i\hbar\nabla$ (5.79)

and A is the vector potential of the electric field, related to the electric field vector through

$$\frac{\partial A}{\partial t} = -c\,\mathcal{E} \tag{5.80}$$

and $$A = -\frac{\mathcal{E}}{2q}\exp[i(qr - \omega t)], \tag{5.81}$$

where q is the wave vector of the photon. Putting eq (5.78) and (5.81) into eq (5.77) gives

$$|<c|\hat{H}_{er}|v>|^2 = \left(\frac{e}{m_e\omega}\right)^2 |\tfrac{1}{2}\mathcal{E}|^2 |<c|\underline{e}\,\hat{p}|v>|^2, \tag{5.82}$$

where the dispersion relation for photons, $\omega = cq$, is used and $\underline{e}$ is a unit vector in the direction of A. Thus, the transition probability per unit time is

$$\mathcal{T} = \frac{2\pi}{\hbar}\left(\frac{e}{m_e\omega}\right)^2 |\tfrac{1}{2}\mathcal{E}|^2 \sum_i |<c|\underline{e}\,\hat{p}|v>|_i^2\, \delta(E - \Delta E_i)\ . \tag{5.83}$$

The *power loss* of the $\mathcal{E}$ field per unit volume due to the absorption thus becomes

$$\text{power loss} = \mathcal{T}\frac{\Delta E}{V}. \tag{5.84}$$

The power loss can also be expressed in terms of the energy density of the field, w_e

$$\text{power loss} = -\frac{\mathrm{d}w_e}{\mathrm{d}t} = -\frac{\mathrm{d}w_e}{\mathrm{d}x}v. \tag{5.85}$$

Using eqs (5.9), (5.22) and (5.23) then gives

$$\text{power loss} = \tfrac{1}{2}\varepsilon_o\omega\varepsilon_2\,|\mathcal{E}|^2, \tag{5.86}$$

where the relation $\varepsilon_2 = 2nk$ has been used, which easily follows from eq (5.18). Equating eqs (5.84) and (5.86), then gives, with eq (5.83):

$$\varepsilon_2(E) = \frac{\pi e^2\hbar^2}{\varepsilon_o m_e^2 E^2}\sum_i |<c|\underline{e}\,\hat{p}|v>|_i^2\, \delta(E - \Delta E_i)\ . \tag{5.87}$$

Using the fact that this equals zero unless $E = \Delta E_i$ and the definition of the plasma energy, eqs (5.50), (5.34) and (5.35), the absorption spectrum becomes

$$\varepsilon_2(E) = \frac{\pi}{2} E_p^2 \sum_j \frac{f_j}{\Delta E_j} \delta(E - \Delta E_j), \tag{5.88}$$

which has the same functional form as the classical case , eq (5.54), but with

$$f_i \equiv \frac{2|<c|\underline{e}\,\hat{\boldsymbol{p}}|v>|_i^2}{N_v m_e \Delta E_i} \tag{5.89}$$

for the oscillator strength.

5.4.4 The absorption spectrum of the linear chain

The oscillator strength is usually calculated by assuming that the momentum matrix elements in eq (5.89) are constant. However, when $|c>$ and $|v>$ are known Bloch functions, the oscillator strength can be calculated exactly from the tight binding Hamiltonian [9], using the relation

$$\hat{\boldsymbol{p}}(k) = \frac{m_e}{\hbar} \nabla_k \hat{\boldsymbol{H}}(k). \tag{5.90}$$

For the monatomic linear chain described in section 5.4.1, the Hamiltonian is

$$\hat{\boldsymbol{H}}(k) = \begin{bmatrix} E_A & (ss\sigma)(1+e^{-i(k2a)}) \\ (ss\sigma)(1+e^{i(k2a)}) & E_B \end{bmatrix}, \tag{5.91}$$

so that the momentum operator becomes

$$\hat{\boldsymbol{p}}(k) = \frac{m_e}{\hbar} \begin{bmatrix} 0 & -i2a(ss\sigma)e^{-i(k2a)} \\ i2a(ss\sigma)e^{i(k2a)} & 0 \end{bmatrix}. \tag{5.92}$$

The momentum matrix element corresponding to the transition from a valence state to a conduction state is then given by [9]

$$\hat{p}_{cv}(k) \equiv <c|\hat{\boldsymbol{p}}(k)|v> = \frac{m_e}{\hbar} \left[\sum_{\alpha,\alpha'} (c_\alpha^-)^* c_{\alpha'}^+ \nabla_k \hat{\boldsymbol{H}}_{\alpha\alpha'}(k) \right]$$

$$= \frac{m_e}{\hbar}\left[(c_A^-)^* c_B^+ (-i2a(ss\sigma)e^{-i(k2a)}) + (c_B^-)^* c_A^+ (i2a(ss\sigma)e^{i(k2a)})\right]. \quad (5.93)$$

Knowing the eigenvalues $E^{\pm}$ from eq (5.73), the coefficients $c_A^{\pm}$ and $c_B^{\pm}$ follow from the first equation in the secular determinant in eq (5.71):

$$(E_A - E^{\pm})c_A^{\pm} + (ss\sigma)(1 + e^{-i(k2a)})c_B^{\pm} = 0 \quad (5.94)$$

and the normalisation condition for the eigenvector

$$|c_A^{\pm}|^2 + |c_B^{\pm}|^2 = 1. \quad (5.95)$$

By inspection of eqs (5.94) and (5.95), the solutions can be seen to be

$$c_A^{\pm} = -\frac{(ss\sigma)(1 + e^{-i(k2a)})}{\sqrt{|E_A - E^{\pm}|^2 + |(ss\sigma)(1 + e^{-i(k2a)})|^2}} \quad (5.96a)$$

and $$c_B^{\pm} = \frac{E_A - E^{\pm}}{\sqrt{|E_A - E^{\pm}|^2 + |(ss\sigma)(1 + e^{-i(k2a)})|^2}}. \quad (5.96b)$$

Substituting these solutions into eq (5.93) and following through some algebra gives

$$|\hat{p}_{cv}(k)|^2 = |\hat{p}_{cv}(0)|^2 \frac{\delta^2 + 4(ss\sigma)^2 \cos^4(ka)}{\delta^2 + 4(ss\sigma)^2 \cos^2(ka)} \quad (5.97a)$$

where $$|\hat{p}_{cv}(0)|^2 = 4\frac{m_e^2}{\hbar^2} a^2 (ss\sigma)^2, \quad (5.97b)$$

and it was defined earlier that $\delta \equiv (E_A - E_B)/2$. Thus, the momentum matrix element is not constant, but depends on k through eq (5.97a). Fig. 5.6 shows that the momentum matrix element has maxima at the centre and the edge of the Brillouin zone.

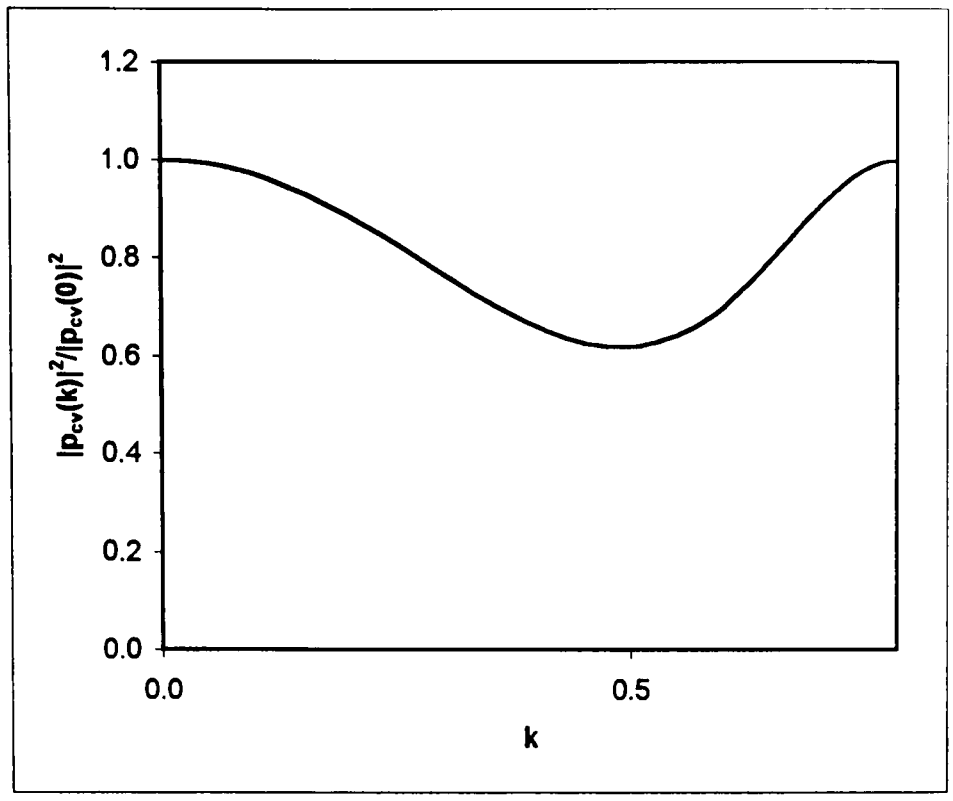


Figure 5.6 Plot of eq (5.97a), showing the dependence of the momentum matrix element on the wave vector for transitions from the valence band to the conduction band in Fig. 5.5.

Also, at the centre and the band edges, $\partial E(k)/\partial k = 0$, so that there are many transitions with a transition energy close to $\Delta E_1 = 2\delta$ and $\Delta E_2 = 2\sqrt{\delta^2 + 4(ss\sigma)^2}$. These two effects give rise to peaks in the absorption spectrum at ΔE_1 and ΔE_2. The oscillator strength for the linear chain follows by putting eq (5.97) into eq (5.89), where the transition energy, $\Delta E(k)$ follows from eq (5.73):

$$\Delta E(k) = 2\sqrt{\delta^2 + 4(ss\sigma)^2 \cos^2(ka)} \qquad (5.98)$$

Fig. 5.7 shows the absorption spectrum for the linear chain (obtained by making a partition of k to get a finite sum in eq (5.89), and then introducing a small peak broadening to smooth the curve).

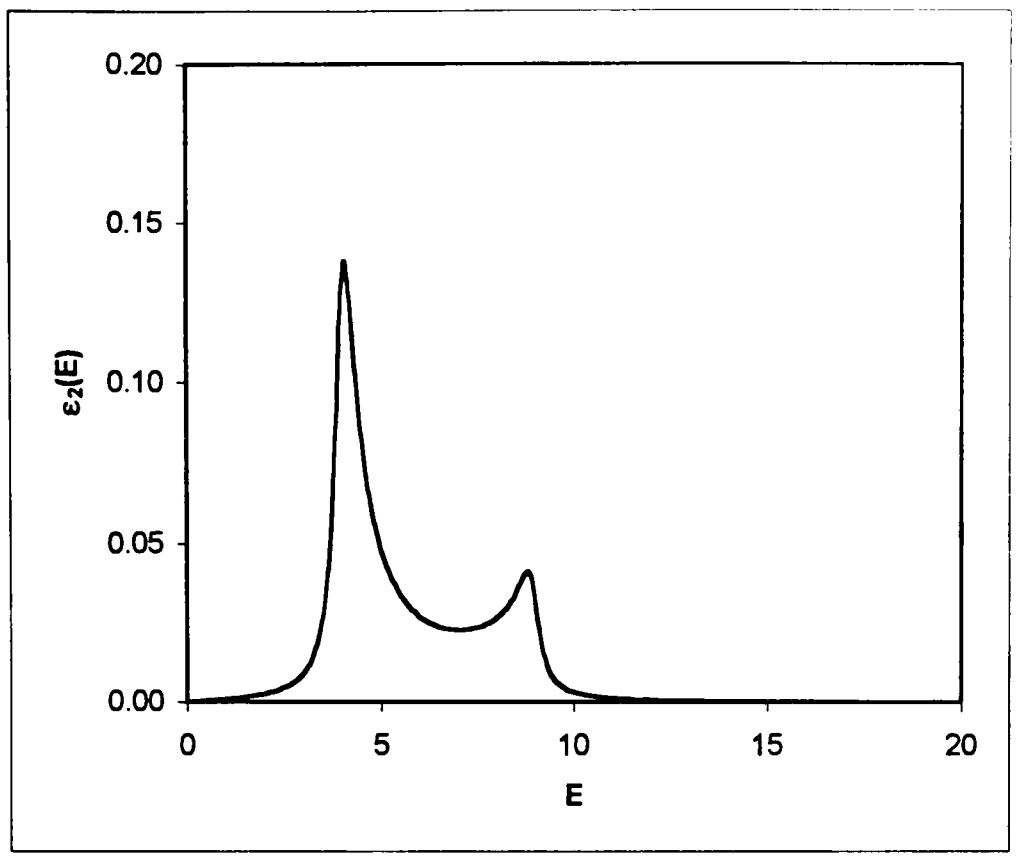


Figure 5.7 Absorption spectrum of the linear chain; the peaks correspond to the transitions at $k = 0$ and $k = \pi/2a$ in Figs. 5.5 and 5.6.

The first peak corresponds to transitions around $k = \pi/2a$. As $k = 2\pi/\lambda$, these electronic eigen states have wavelength $\lambda = 4a$. Eq (5.73) shows that $\Psi^-(\frac{\pi}{2a})$ has eigenvalue E_A, which means that $\Psi^-(\frac{\pi}{2a})$ has maxima on the A atoms and goes through zero on the B atoms, so that the corresponding charge density $|\Psi^-(\frac{\pi}{2a})|^2$ piles up charge on the A atoms. Similarly, $|\Psi^+(\frac{\pi}{2a})|^2$ piles up charge on the B atoms. Thus, the peak in the absorption spectrum at ΔE_1 is due to a transition from a state that piles up charge on the A atoms to a state that piles up charge on the B atoms. The second peak is due to transitions around $k = 0$, or, since the Brillouin zone has period π/a, at $k = \pi/a$, so that the electronic eigen states have wavelength $\lambda = 2a$. The eigen state with energy $E^-(\frac{\pi}{a}) = E_{AB} - \sqrt{\delta^2 + 4(ss\sigma)^2}$ is the state of lowest energy, the *bonding state*, and piles up charge *between* the positive ions, giving rise to the bonding. The eigen state with energy $E^+(\frac{\pi}{a}) = E_{AB} + \sqrt{\delta^2 + 4(ss\sigma)^2}$ is the anti-

bonding state. Thus, the peak at ΔE_2 is due to the transition from the bonding to the anti-bonding state. The peaks in the absorption spectrum can thus be seen to arise from transitions between the bonding and anti-bonding states of the purely *ionic* bond (ΔE_1) and the most covalent bond (ΔE_2). This ties in well with the Phillips' spectroscopic theory treated in the next section.

5.5 Phillips' Spectroscopic Theory

Phillips' spectroscopic theory [10, 11] is an empirical theory that relates the short-range atomic structure of crystalline semiconductors to the static dielectric function, $\varepsilon_1(0)$, i.e. the real part of the dielectric function in the limit of zero photon energy. It was generalised by Brodsky and Stiles [12] to include amorphous semiconductors. They used the theory to calculate the static dielectric function of amorphous GeTe from the crystalline value and the changes in the local structure, thus relating the cptical contrast at zero photon energy to the changes in the local structure upon crystallisation. Phillips' spectroscopic theory is briefly reviewed in this section.

5.5.1 Phillips' theory

When the absorption spectrum of a semiconductor consists of a single peak at energy $E = \Delta$ and zero width, the static limit of the dielectric function is given by

$$\varepsilon_1(0) = 1 + \left(\frac{E_p}{\Delta}\right)^2 . \qquad (5.99)$$

This result was first derived by Penn by calculating the dielectric response of a nearly free electron gas [13]. The result follows more directly by taking the limits $\Gamma \to 0$ and then $E \to$

0 in eq (5.47). The reflectivity of bulk material is $R = [(1-\tilde{n})/(1+\tilde{n})]^2$, so that, as $\varepsilon_2(0) = 0$, it follows from eqs (5.20) that

$$R(0) = \left[\frac{1-\sqrt{\varepsilon_1(0)}}{1+\sqrt{\varepsilon_1(0)}}\right]^2. \qquad (5.100)$$

Inverting eq (5.100) gives

$$\varepsilon_1(0) = \left[\frac{1+\sqrt{R(0)}}{1-\sqrt{R(0)}}\right]^2, \qquad (5.101)$$

so that Δ can be determined experimentally from the plasma energy and $R(0)$, by using eqs (5.99) and (5.101). Phillips then assumed that Δ has a covalent component ΔE_{cov} and an ionic component ΔE_{ion}, related through

$$\Delta^2 = \Delta E_{\text{cov}}^2 + \Delta E_{ion}^2. \qquad (5.102)$$

For monatomic materials ($\Delta E_{ion} = 0$), he then found that ΔE_{cov} varies with the nearest neighbour distance, d, as

$$\Delta E_{\text{cov}} = \alpha d^{-\frac{5}{2}}, \qquad (5.103)$$

where α is a constant, independent of the specific element. Knowing α, ΔE_{ion} is obtained for a non-monatomic material from d and Δ, using eqs (5.102) and (5.103). These ionic components of Δ are then found to closely fit

$$\Delta E_{ion} = b\left(\frac{z_1}{r_1} - \frac{z_2}{r_2}\right)\exp\left(-k_{TF}\frac{r_1+r_2}{2}\right), \qquad (5.104)$$

where b is a fit parameter of order unity; z_1 and z_2 are the number of valence electrons of atoms 1 and 2, r_1 and r_2 are their covalent radii and k_{TF} is the Thomas-Fermi screening factor

$$k_{TF}^2 = \frac{4m_e e^2}{\hbar^2}\left(\frac{3N_v}{\pi V}\right)^{\frac{1}{3}}, \qquad (5.105)$$

where N_v/V is the number density of valence electrons.

5.5.2 Including amorphous materials

Brodsky and Stiles essentially assume that the formulae above are valid for amorphous (A) as well as crystalline (X) semiconductors so that, from eq (5.99), it follows

$$\frac{\varepsilon_1^A(0)-1}{\varepsilon_1^X(0)-1}=\left(\frac{E_p^A}{E_p^X}\right)^2\left(\frac{\Delta^X}{\Delta^A}\right)^2, \tag{5.106}$$

which, using eqs (5.34) and (5.102) gives

$$\frac{\varepsilon_1^A(0)-1}{\varepsilon_1^X(0)-1}=\frac{\rho^A}{\rho^X}\frac{(\Delta E_{\text{cov}}^X)^2+(\Delta E_{ion}^X)^2}{(\Delta E_{\text{cov}}^A)^2+(\Delta E_{ion}^A)^2}, \tag{5.107}$$

where ρ is the mass density of the solid, proportional to the number density of valence electrons. ΔE_{cov}^A is found from eq (5.103):

$$\frac{\Delta E_{\text{cov}}^A}{\Delta E_{\text{cov}}^X}=\left(\frac{d^X}{d^A}\right)^{\frac{5}{2}}, \tag{5.108}$$

and ΔE_{ion}^A from eq (5.104):

$$\frac{\Delta E_{ion}^A}{\Delta E_{ion}^X}=\frac{d^X}{d^A}\frac{\exp(-\frac{1}{2}d^A k_{TF}^A)}{\exp(-\frac{1}{2}d^X k_{TF}^X)}, \tag{5.109}$$

if it is assumed that the covalent radii are proportional to the nearest neighbour distances; k_{TF}^A is found from

$$\frac{k_{TF}^A}{k_{TF}^X}=\left(\frac{\rho^A}{\rho^X}\right)^{\frac{1}{6}}. \tag{5.110}$$

Thus, from the experimentally determined values for $\varepsilon_1^X(0)$, d^X, ρ^X and the atomic radii and valencies, Phillips' empirical relations yield Δ^X, ΔE_{cov}^X, ΔE_{ion}^X and k_{TF}^X. Knowing these values and measuring ρ^A and d^A, Brodsky and Stiles' scaling relations yield k_{TF}^A, ΔE_{ion}^A, ΔE_{cov}^A, Δ^A, and, finally, $\varepsilon_1^A(0)$. Following this procedure, Brodsky and Stiles used the

experimental value $\varepsilon_1^X(0) = 36$ to predict $\varepsilon_1^A(0) = 14$ [12] from the change in the structure; this compares quite well with $\varepsilon_1^A(0) = 11$ found experimentally. From eq (5.100), it can be seen that this "predicts" for the optical contrast $\Delta R(0)$ = 18 %, while $\Delta R(0)$ = 22 % is found experimentally. Although the agreement is satisfactory, it is noted that an experimentally determined value for $R^X(0)$ was used to calculate $\varepsilon_1^X(0)$, so that the optical contrast is not calculated using structural information only.

Phillips' theory provides a useful link between the local structure and the optical contrast in the static limit. However, in practice the static limit is of little use as lasers used in data storage applications have photons with energies close to Δ, not close to zero. In the next chapter, it is shown how the introduction of only one additional parameter leads to a model dielectric function that describes the dielectric response of a semiconductor as a function of *arbitrary* photon energy, E.

References

[1] M. Born and E. Wolf, *Principles of Optics*, 3rd ed., Pergamon Press, Oxford (1965).

[2] G.D. Mahan, *Many-Particle Physics*, 2nd ed., Plenum Press, New York (1990).

[3] D.Y. Smith, *Handbook of Optical Constants of Solids*, Academic Press (1985).

[4] C. Kittel, *Introduction to Solid State Physics*, 6th ed., Wiley & Sons, New York (1986).

[5] H. Ibach and H. Lüth, *Solid State Physics*, 3rd ed., Springer Verlag, Berlin (1990).

[6] D.G. Pettifor, *Bonding and Structure of Molecules and Solids*, Oxford University Press (1995).

[7] A. P. Sutton, *Electronic Structure of Materials*, Oxford University Press, Oxford (1993).

[8] P.Y. Yu and M. Cardona, *Fundamentals of Semiconductors*, 2nd ed., Springer Verlag, Berlin (1999).

[9] L.C. Lew Yan Voon and L.R. Ram-Mohan, *Phys. Rev. B* **47** (1993) p. 15500.

[10] J.C. Phillips, *Phys. Rev. Lett.* **19** (1967) p. 415.

[11] J.A. Van Vechten, *Phys. Rev.* **182** (1969) p. 391.

[12] M. H. Brodsky and P.J. Stiles, *Phys. Rev. Lett.* **25** (1970) p. 798.

[13] D. Penn, *Phys. Rev.* **128** (1962) p. 2063.

CHAPTER VI

Relating the Absorption Spectrum to the Local Structure

6.1 Introduction

The aim of this chapter is to describe the absorption peak in terms of its position, Δ (i.e. the effective transition energy) and width, Γ (i.e. the width of the spectrum of absorption peaks) and relate these parameters to the local atomic structure. Firstly, it will be shown how Δ and Γ can be calculated from a spectrum of delta function peaks. Secondly, it will be shown how the absorption spectrum can be approximated by a small number of peaks, related to the local atomic structure, taking Si as an example. Both these two steps represent original work. The resulting model dielectric function is valid for arbitrary photon energy and its static limit puts Phillips' empirical theory on a tight-binding footing, which has not been done previously.

6.2 One Effective Lorentz Oscillator

In section 5.4, the absorption spectrum of a solid was derived to be

$$\varepsilon_2(E) = \frac{\pi}{2} E_p^2 \sum_j \frac{f_j}{\Delta E_j} \delta(E - \Delta E_j) . \qquad (6.1)$$

In practice, this collection of delta peaks merges into one effective absorption peak with relatively well defined position and width. If this is the case, the dielectric function in eq (6.1) can be approximated by

$$\varepsilon_2(E) = E_p^2 \frac{\Gamma E}{(\Delta^2 - E^2)^2 + (\Gamma E)^2}, \qquad (6.2)$$

which has the functional form of the Lorentz expression for the classical damped harmonic oscillator, eq (5.47). Thus, the task is to find expressions for Γ and Δ in terms of f_i and ΔE_i that best describe eq (6.2). This can be done by requiring that the moments μ_n of the absorption spectrum, defined by

$$\mu_n \equiv \int_0^\infty E^n \varepsilon_2(E) \mathrm{d}E, \qquad (6.3)$$

be conserved. Obviously, in the hypothetical case that eq (6.1) can be described *exactly* by eq (6.2), it is possible to preserve *all* the (infinite) moments in eq (6.3). However, when the absorption spectrum of eq (6.1) takes the shape of a peak with a fairly well defined position and width, it is possible to conserve no more than *three* moments, as there are three free fitting parameters in eq (6.2), *viz.* E_p, Δ and Γ. Thus, conserving three moments gives three parameters in three unknowns, which can be solved exactly. So which three moments must be chosen to be conserved? The most obvious moments to try and conserve are μ_1 and μ_{-1}, because not only are the corresponding integrals (see eq (6.3)) known *exactly* from the sum rules in section 5.2.3, but these sum rules arose from physical restrictions. From eq (6.3) it can be seen that the moment μ_0 is the *surface under the absorption peak*, which shall be chosen as the third and final moment to be conserved.

6.2.1 Conserving the moment μ_1

In section 5.2.3 it was shown that the imaginary part of the dielectric function must obey the sum rule

$$\int_0^\infty E\varepsilon_2(E)\mathrm{d}E = \frac{\pi}{2} E_p^2, \qquad (6.4)$$

which is the first moment of the absorption spectrum. The Lorentz expression for the classical harmonic oscillator, eq (5.47), can be easily shown to obey the Kramers-Kronig relations (see section 5.2.3). It also has the correct high energy limit of eq (5.25), so that eq (6.2) obeys this sum rule. Putting eq (6.1) into eq (6.4) gives

$$\mu_1 = \frac{\pi}{2} E_p^2 \sum_i \int_0^\infty E \frac{f_i}{\Delta E_i} \delta(E - \Delta E_i) dE = \frac{\pi}{2} E_p^2 \sum_i f_i \,. \tag{6.5}$$

Thus, to preserve the first moment, eqs (6.4) and (6.5) must be equal so that

$$\sum_i f_i = 1, \tag{6.6}$$

just as for the classical oscillator strength. As the quantum mechanical oscillator strength is not a fraction, eq (6.6) is not at all obvious. Eq (6.6) can also be found by putting eq (6.1) into the first Kramers-Kronig relation, eq (5.24a), to obtain

$$\varepsilon_1(E) = 1 + E_p^2 \sum_i f_i \frac{\Delta E_i^2 - E^2}{(\Delta E_i^2 - E^2)^2 + (\Gamma E)^2} \tag{6.7}$$

and equate this to the high-energy limit of

$$\varepsilon_1(E) = 1 + E_p^2 \frac{\Delta^2 - E^2}{(\Delta^2 - E^2)^2 + (\Gamma E)^2}, \tag{6.8}$$

which is the real part of the dielectric function that corresponds to eq (6.2), given previously in eq (5.47a). Thus, conserving the first moment of $\varepsilon_2(E)$ also makes sure that the *high-energy limit* of $\varepsilon_1(E)$ remains exact.

6.2.2 Conserving the moment μ_{-1}

The static limit sum rule, eq (5.27), also derived in section 5.2.3, can be written as

$$\int_0^\infty \frac{\varepsilon_2(E)}{E} dE = \frac{\pi}{2}[\varepsilon_1(0) - 1]. \tag{6.9}$$

Eq. (6.9) states that in order to preserve the moment μ_{-1}, the static limit of $\varepsilon_1(E)$ must be conserved. Equating eqs (6.8) and (6.9) in the limit $E \to 0$ gives

$$\Delta^{-2} = \sum_i f_i \Delta E_i^{-2}, \tag{6.10}$$

which defines the Δ from Penn's result in eq (5.98). Thus, by conserving the moment μ_{-1}, the *zero-energy limit* of the dielectric function also remains exact.

6.2.3 Conserving the moment μ_0

The moment μ_0, the surface under the absorption peak for eq (6.1) is equal to

$$\mu_0 = \frac{\pi}{2} E_p^2 \sum_i \int_0^\infty \frac{f_i}{\Delta E_i} \delta(E - \Delta E_i) dE = \frac{\pi}{2} E_p^2 \sum_i \frac{f_i}{\Delta E_i}. \tag{6.11}$$

However, eq (6.2) cannot be integrated analytically. To remedy this eq (6.2) is approximated by a double Lorentzian

$$\varepsilon_2(E) = E_p^2 \frac{1}{2\Delta} \left[\frac{\Gamma/2}{(E-\Delta)^2 + (\Gamma/2)^2} - \frac{\Gamma/2}{(E+\Delta)^2 + (\Gamma/2)^2} \right]. \tag{6.12}$$

The second (negative) peak at $E = -\Delta$ makes sure that $\varepsilon_2(0) = 0$ and causes $\varepsilon_2(E)$ to fall off as E^{-3}, in accordance with the high energy limit of eq (5.25); Γ is the FWHM width. Eq (6.12) *can* be integrated analytically:

$$\mu_0 = E_p^2 \frac{1}{2\Delta} \int_0^\infty \frac{2/\Gamma}{1+[2(E-\Delta)/\Gamma]^2} - \frac{2/\Gamma}{1+[2(E+\Delta)/\Gamma]^2} dE$$

$$= E_p^2 \frac{1}{2\Delta} \left[\tan^{-1}\left(\frac{E-\Delta}{\Gamma/2}\right) - \tan^{-1}\left(\frac{E+\Delta}{\Gamma/2}\right) \right]_0^\infty$$

$$= E_p^2 \frac{1}{\Delta} \tan^{-1}\left(\frac{2\Delta}{\Gamma}\right). \tag{6.13}$$

Equating eqs (6.11) and (6.13) yields

$$\Gamma = \frac{2\Delta}{\tan[\frac{\pi}{2}\sum_i f_i(\Delta/\Delta E_i)]}. \qquad (6.14)$$

Now, as the envelope of the absorption spectrum in eq (6.1) becomes narrower, $\Delta E_i \to \Delta$ for all i, so that $\varphi \equiv \frac{\pi}{2}\sum_i f_i(\Delta/\Delta E_i) \to \frac{\pi}{2}$, $\tan\varphi \to \infty$ and $\Gamma \to 0$ (as one would expect; as the distribution in eq (6.1) collapses into one delta function peak, so should eq (6.2)). Thus, in the limit of $\Gamma \to 0$

$$\frac{1}{\tan\varphi} = \frac{\cos\varphi}{\sin\varphi} \approx \cos\varphi \approx \tfrac{\pi}{2} - \varphi\,, \qquad (6.15)$$

so that eq (6.14) becomes

$$\Gamma = \pi\Delta\left[1 - \sum_i f_i \frac{\Delta}{\Delta E_i}\right]. \qquad (6.16)$$

How well eq (6.16) preserves the moment μ_0 is illustrated in Fig. 6.1, where $\mu_0(\Gamma)$ from eq (6.13) is compared with numerically integrating the damped harmonic oscillator for various values of Γ.

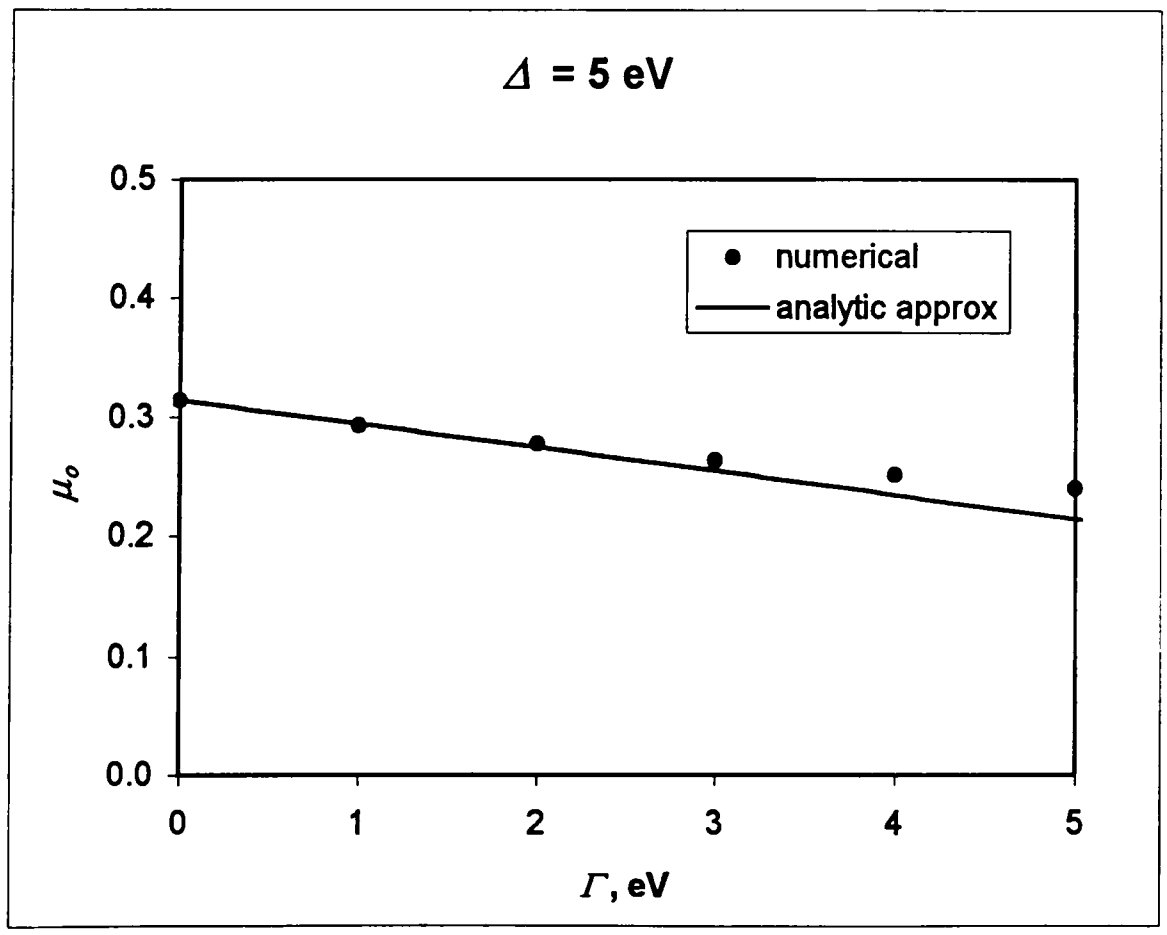


Figure 6.1 Plot of the surface under $\varepsilon_2(E)$, for E_p = 15 eV and Δ = 5 eV, as a function

of Γ obtained by numerically integrating eq (6.2) and from the analytic expression in eq (6.13), respectively.

Fig. 6.1 shows that the moment is indeed preserved very well, for values for $0 < \Gamma < \Delta$ (*c.f.* for Si: $\Gamma \approx 1$ eV and $\Delta \approx 4$ eV [1]). This means that the expression for the peak width given by eq (6.16) makes sure that the surface under the absorption peak in eq (6.2) is close to the surface under the absorption peak in eq (6.1).

6.2.4 Constant momentum matrix elements

The momentum matrix element of transition i are approximately constant [2], so that eq (5.89) shows that the oscillator strength f_i is proportional to

$$f_i' = \Delta E_i^{-1}. \qquad (6.17)$$

The constant of proportionality follows from eq (6.6), i.e.

$$f_i = \frac{f_i'}{\sum_i f_i'}. \qquad (6.18)$$

6.2.5 Example: the linear chain

The use of the single-peak model developed in the previous section is well illustrated by using the linear chain as an example. The peaks in the absorption spectrum are due to transitions from the bonding to the anti-bonding state of the purely ionic and most covalent bonds, respectively. For the arbitrary choice $\delta = (ss\sigma) = 2$ eV, this gives rise to peaks at

$$\Delta E_1 = 2\delta = 4.0 \text{ eV} \qquad \Delta E_2 = 2\sqrt{\delta^2 + 4(ss\sigma)^2} = 8.9 \text{ eV}$$

Assuming the momentum matrix elements are constant, these peaks have corresponding oscillator strengths proportional to

$$f_1' = \frac{1}{\Delta E_1} = 0.25 \qquad f_2' = \frac{1}{\Delta E_2} = 0.11$$

Putting all the weight of the absorption spectrum in these two peaks, eq (6.6) gives

$$f_1 = \frac{f_1'}{f_1' + f_2'} = 0.69 \qquad f_2 = \frac{f_2'}{f_1' + f_2'} = 0.31$$

Eq (6.10) then gives for the effective transition energy:

$$\Delta = [f_1 \Delta E_1^{-2} + f_2 \Delta E_2^{-2}]^{-\frac{1}{2}} = 4.6 \text{ eV} \tag{6.19}$$

and eq (6.16) gives for the peak width

$$\Gamma = \pi\Delta\left[1 - \left(f_1 \frac{\Delta}{\Delta E_1} + f_2 \frac{\Delta}{\Delta E_2}\right)\right] = 0.7 \text{ eV} \tag{6.20}$$

Putting these values for Δ and Γ into eq (6.2) finally yields the one effective Lorentz oscillator model for the absorption spectrum of the linear chain. Fig. 6.2 compares the model to the exact solution for $\varepsilon_2(E)$ as calculated in section 5.4.4.

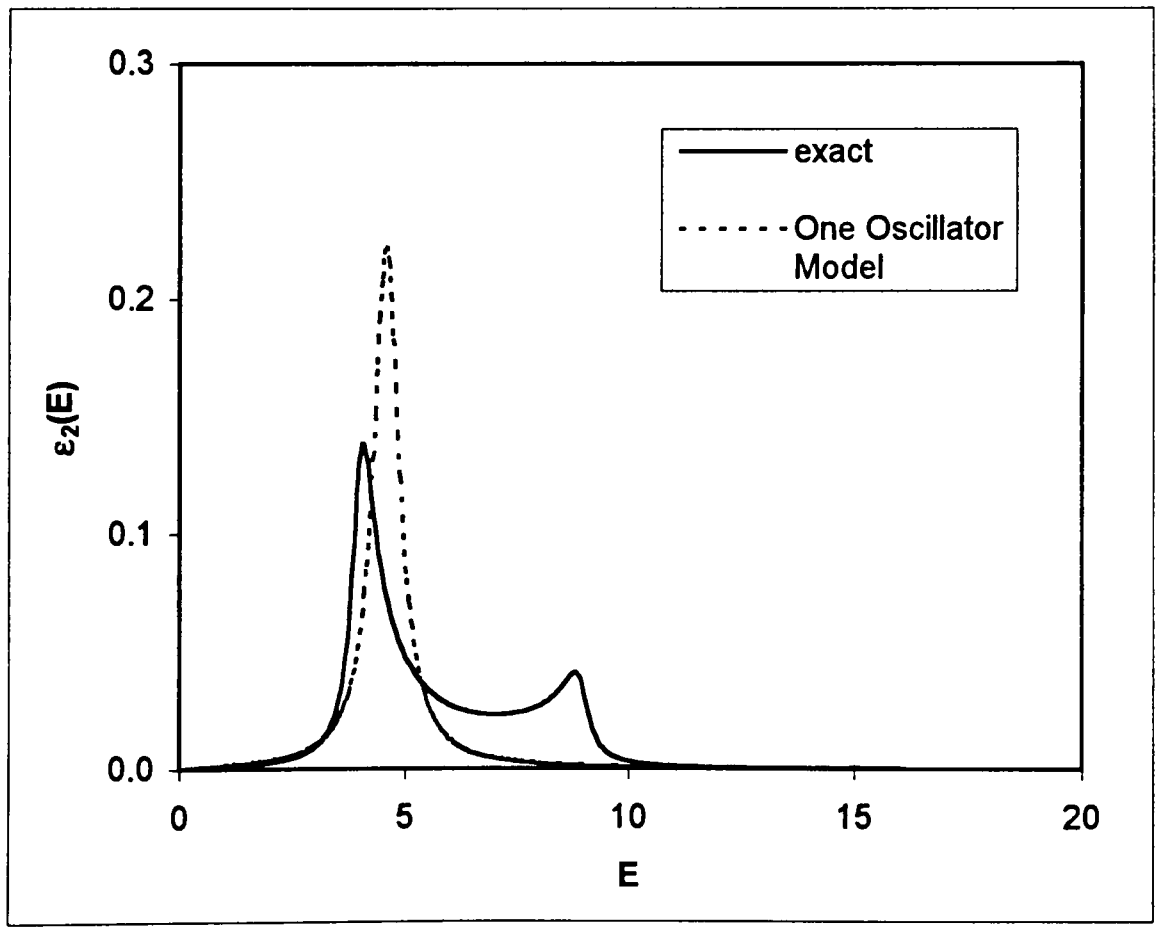


Figure 6.2 Comparison of the one effective oscillator model with the exact absorption spectrum for the linear chain model introduced in Chapter V.

The plot clearly shows that despite having replaced the infinite number of transitions due to the continuous bands as shown in Fig. 5.5 by only *one* effective transition, the fit is reasonable. The main reason why the fit is not excellent is because this simple linear chain model has an absorption spectrum consisting of two distinctive peaks. However, while the exact absorption spectrum is calculated by taking a huge number of transitions into account (larger than the number of states in the band structure, which is of the order of the number of atoms in the system!), the novel model presented here only needs *two* transition energies as input to give a fairly good description of the exact absorption spectrum.

Now that a model has been developed for calculating Δ and Γ from a number of peaks in the absorption spectrum, the rest of this chapter shall be devoted to calculating the position of these peaks in the absorption spectrum from the *local* atomic structure. Silicon is used as a test case because of its simple atomic structure.

6.3 A simplified silicon Hamiltonian

Crystalline silicon has the diamond structure. The unit cell of the diamond structure is given in Fig. 6.3. It can be thought of a two interpenetrating face centred cubic (FCC) lattices. One of the two FCC lattices is clearly visible in Fig. 6.3; the remaining four atoms shown belong to a second FCC lattice which is displaced along the (1,1,1) direction by 1/4 of the diagonal of the cube. The bonds of the atoms inside the unit cell with their nearest neighbours are indicated; all atoms have a four-fold nearest neighbour coordination and are said to be tetrahedrally coordinated as the nearest neighbours are located on the vertices of a regular tetrahedron.

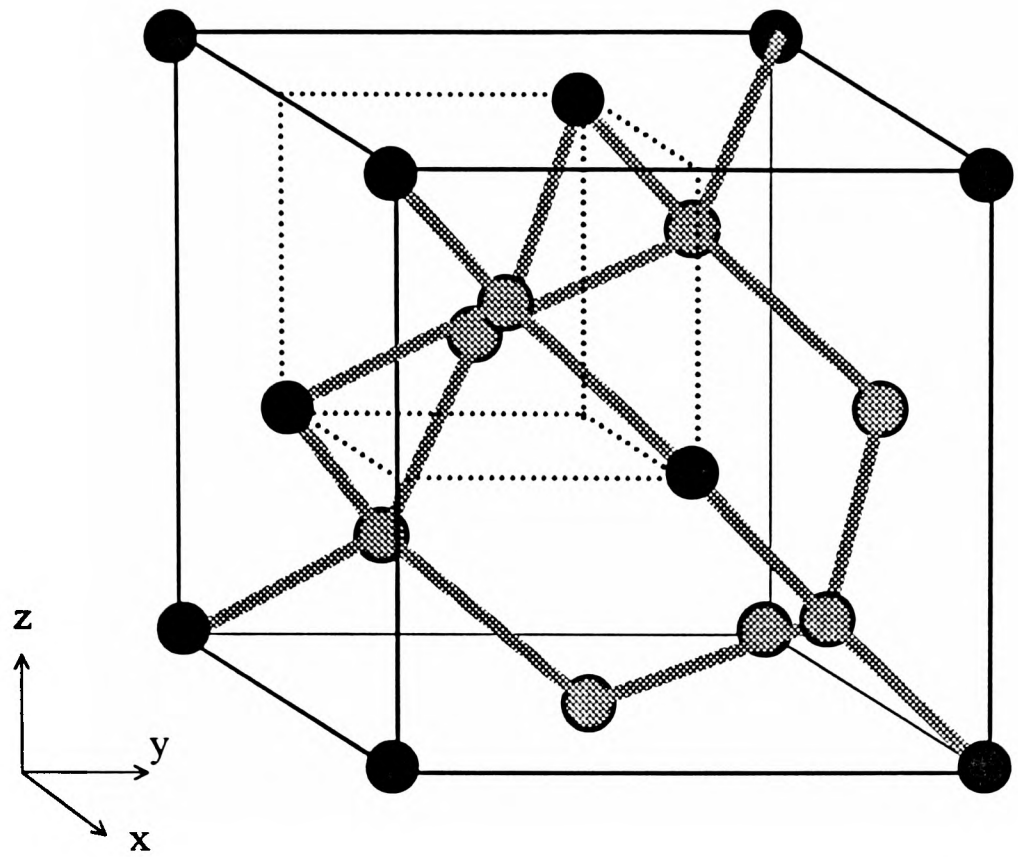


Figure 6.3 Unit cell of crystalline silicon. The atoms in the front, left and top faces of the cube are coloured black. The grey lines indicate nearest neighbour bonds.

The electronic configuration of a free silicon atom is [Ne] $3s^2 3p^2$ so that there are four outer shell electrons; two occupying an s state and two occupying p states. The 3s state and the three 3p states, $3p_x$, $3p_y$ and $3p_z$, will be used as an atomic basis set and will hereafter be referred to as $|s>$, $|x>$, $|y>$ and $|z>$. Consider two neighbouring Si atoms, labelled "1" and "2", each with a set of four atomic orbitals. The z-axis of the coordinate system is chosen along the bond direction. The electronic properties of Si can be described in terms of the on-site energies of the s orbital, $\varepsilon_s = <s_1|\hat{H}|s_1> = <s_2|\hat{H}|s_2>$, and of the p_x orbitals, $\varepsilon_p = <x_1|\hat{H}|x_1> = <x_2|\hat{H}|x_2>$, and similarly for the p_y and p_z orbitals, and the four fundamental hopping integrals $(ss\sigma) = <s_1|\hat{H}|s_2>$, $(sp\sigma) = <s_1|\hat{H}|z_2>$, $(pp\sigma) = <z_1|\hat{H}|z_2>$ and $(pp\pi) = <x_1|\hat{H}|x_2> = <y_1|\hat{H}|y_2>$. A schematic representation of these hopping integrals is shown in Fig. 6.4. The label "σ" indicates that the states in

question have no angular momentum about the bond axis whilst the label "π" is used when the angular momentum of the states is $m = \pm 1$.

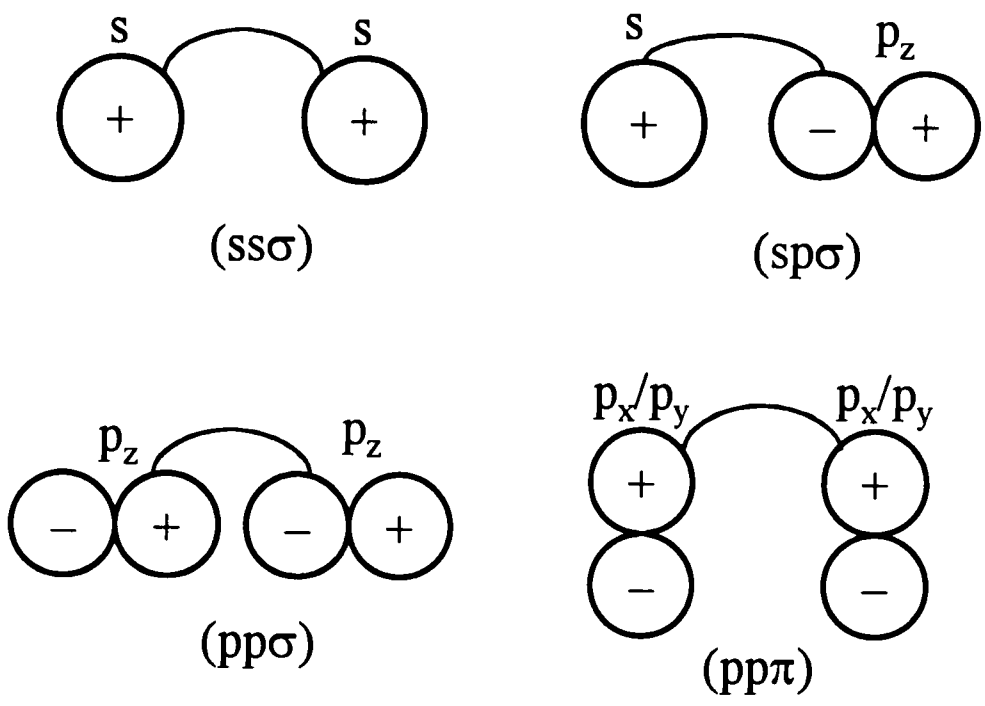


Figure 6.4 The fundamental hopping integrals (ssσ), (spσ), (ppσ) and (ppπ).

Electronic properties can be calculated in terms of these six parameters [4]; the on-site energies and the four hopping integrals. They can be found by fitting the result to experiment, using the six parameters as fit parameters. The widely used "Chadi parameterisation" [3] was obtained in this way and will be used as a starting point in this study: $\varepsilon_s = -5.25$, $\varepsilon_p = 1.20$, (ssσ) = −1.9375, (spσ) = 1.745, (ppσ) = 3.050 and (ppπ) = −1.075, all energies in eV.

The absorption spectrum for crystalline silicon can now be calculated from these six parameters in the same way as the absorption spectrum for the linear chain was calculated in section 6.2.5. In anticipation of the model developed in the next section, however, the following approximations are made first:

1) the on-site energies are set to zero: $\varepsilon_s = \varepsilon_p = 0$. As a consequence, the centre of weight of the s-like sates and the p-like states is both set to zero, to simplify the model.

2) the (ppπ) bonding is ignored: (ppπ) = 0. This also makes the maths easier and ignores an absorption peak due to transitions from the bonding to anti-bonding ppπ states.

3) (spσ) is taken as the geometric mean of the (ssσ) and (ppσ) hopping integrals:

$$(sp\sigma) = \sqrt{|(ss\sigma)|(pp\sigma)}, \tag{6.21}$$

to further reduce the number of parameters in the model. Only the positions of the peaks in the absorption spectrum are expected to be changed by this assumption.

Finally, the ratio between the (ppσ) and the (ssσ) hopping integrals,

$$p_\sigma \equiv \frac{(pp\sigma)}{|(ss\sigma)|}, \tag{6.22}$$

is allowed to vary by changing the value for (ssσ). This is not a simplifying assumption; by changing the value for p_σ, the strength of the (ppσ) bond relative to the (ssσ) bond is changed to see if the model developed in section 6.4 correctly describes the exact absorption spectrum for different values for p_σ.

The absorption spectra are now calculated [5] under these simplifying approximations and shown in Fig. 6.5 for p_σ = 1.5, 2.0 and 3.0, respectively.

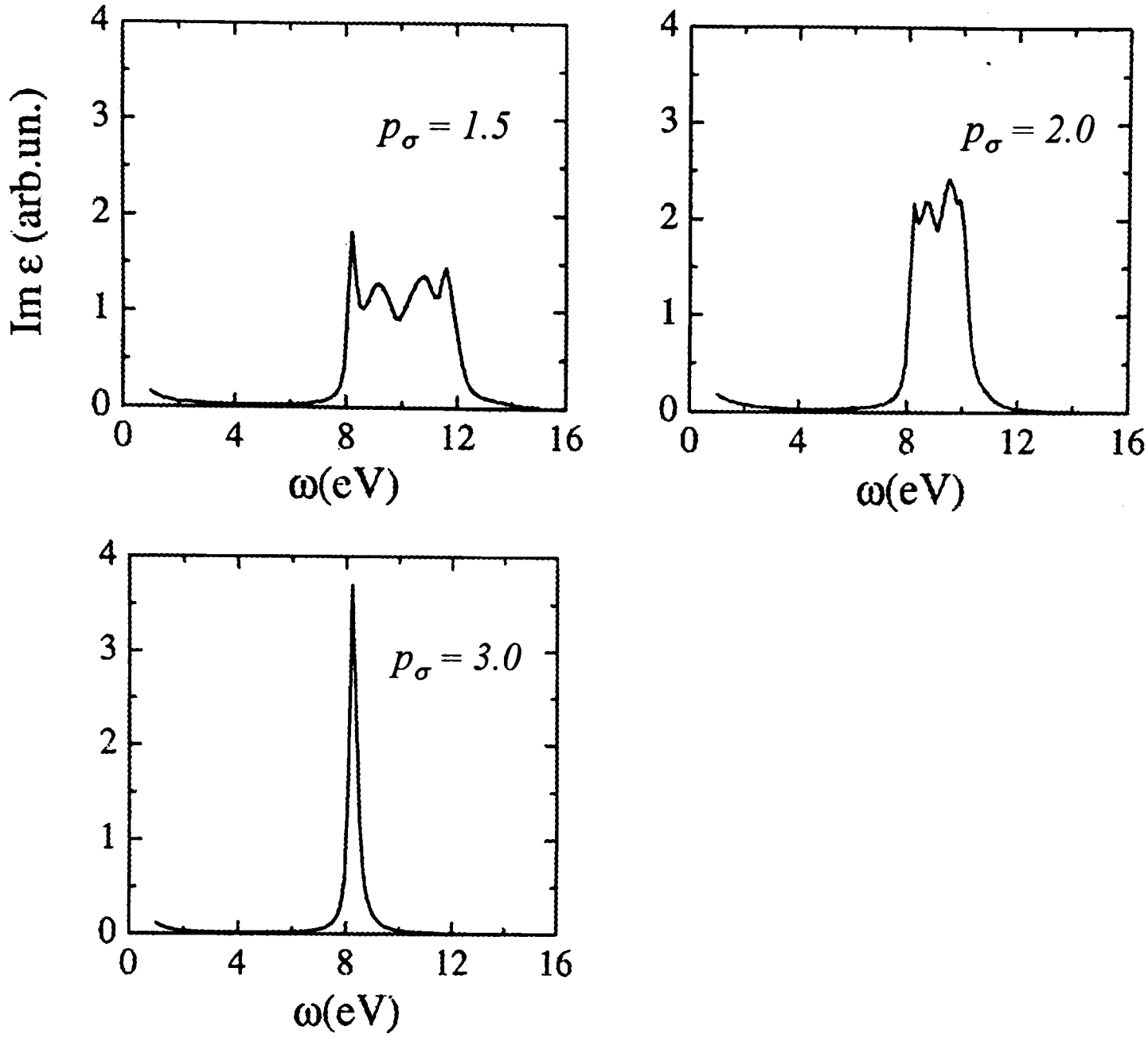


Figure 6.5 Plots of the absorption spectra for the Si Hamiltonian described in section 6.3, for $p_\sigma = 1.5$, 2.0 and 3.0, respectively [5].

It is emphasised that the absorption spectra are calculated using the translation symmetry of the crystal lattice; Bloch's theorem was used to calculate the band structure used to calculate the absorption spectrum. In the next section, a model will be developed for calculating the same absorption spectra from the local atomic coordination of the Si atoms.

6.4 The four-level recursion model

The model developed in this section is based on an approximate expression for the density of electronic states in terms of the recursion coefficients, which are calculated from the nearest neighbour coordination.

6.4.1 The density of states

Solving the Schrödinger equation,

$$\hat{H}\psi = E\psi\,, \tag{6.23}$$

gives a set of energy eigenvalues. The density of states (DOS), $\mathcal{N}(E)$, is the spectrum of these eigenvalues:

$$\mathcal{N}(E) = \sum_i \delta(E - E_i)\,, \tag{6.24}$$

where E_i is a solution of eq (6.23). Thus, the DOS at a given value of E is essentially the number of eigenvalues with energy E.

Apart from calculating the DOS directly by solving the Schrödinger equation, $\mathcal{N}(E)$ can be calculated from the Green's function of the Schrödinger equation, $G(E)$, which is defined by

$$G(E) \equiv \frac{1}{E - \hat{H}}\,. \tag{6.25}$$

For a localised wave function $\psi(r)$, the matrix element $G_{rr}(E)$ is defined as [6]

$$G_{rr}(E) \equiv \langle \psi(r) | \frac{1}{E - \hat{H}} | \psi(r) \rangle \tag{6.26}$$

$$= \frac{1}{E} \langle \psi(r) | \frac{1}{1 - (\hat{H}/E)} | \psi(r) \rangle = \frac{1}{E} \langle \psi(r) | 1 + (\hat{H}/E) - (\hat{H}/E)^2 + \cdots | \psi(r) \rangle$$

$$= \frac{1}{E} \sum_i \langle \psi(r) | 1 + (E_i/E) - (E_i/E)^2 + \cdots | \psi_i(r) \rangle = \sum_i \frac{< \psi_i(r) | \psi_i(r) >}{E - E_i}\,,$$

so that $G_{rr}(E)$ has poles where the Schrödinger equation has solutions. How eq (6.26) is linked to the DOS becomes clear by considering the expression

$$\mathrm{Im}[G_{rr}(E+i\eta)] = \sum_i <\psi_i(r)\,|\,\psi_i(r)> \mathrm{Im}[\frac{1}{E+i\eta-E_i}]$$

$$= -\sum_i <\psi_i(r)\,|\,\psi_i(r)> \frac{\eta}{(E-E_i)^2+\eta^2}. \qquad (6.27)$$

In the limit $\eta \to 0$, the Lorentzian in eq (6.27) turns into a delta function with surface π (*cf.* section 5.3.6) so that it follows from eqs (6.26) and (6.27) that [6]

$$\mathcal{N}_r(E) \equiv \sum_i <\psi_i(r)\,|\,\psi_i(r)> \delta(E-E_i)$$

$$= -\frac{1}{\pi}\lim_{\eta\to 0}\{\mathrm{Im}[G_{rr}(E+i\eta)]\}, \qquad (6.28)$$

where $\mathcal{N}_r(E)$ is the local density of states at position r. The total DOS, $\mathcal{N}(E)$, is then obtained by averaging over r.

The advantage of calculating the DOS using the Green's function instead of calculating it from the eigenvalues lies in the fact that the Green's function, unlike the eigenvalues, can be easily approximated using only a few parameters, the recursion coefficients. How this is done is shown in the next section.

6.4.2 Recursion coefficients

The Green function on an atom at $r = 0$, $G_{oo}(E)$, can be expanded as a continued fraction [6]:

$$G_{oo}(E) = \cfrac{1}{E-a_o-\cfrac{b_1^2}{E-a_1-\cfrac{b_2^2}{E-a_2-\cfrac{b_3^2}{E-a_3-\cdots}}}}, \qquad (6.29)$$

where the expansion coefficients a_i and b_i are known as the *recursion coefficients*. The first few recursion coefficients have a clear meaning in terms of the DOS. a_o is the *centre of*

weight of the DOS. This can be shown to be generally true, but is easily seen when $b_1 = 0$; the Green's function then becomes

$$G_{oo}(E) = \frac{1}{E - a_o}, \tag{6.29}$$

so that the DOS consists of a single delta function at $E = a_o$, i.e. the pole of the Green's function. The coefficient b_1 is related to the *width* of the DOS. This is true in general and can be shown easily in the case that all the other recursion coefficients are zero:

$$G_{oo}(E) = \frac{E}{E^2 - b_1^2} = \frac{1}{2}\left[\frac{1}{E - b_1} + \frac{1}{E + b_1}\right], \tag{6.30}$$

which gives rise to *two* delta functions in the DOS, a distance $2b_1$ apart. When $b_1 \neq 0$, $b_2 \neq 0$ but $a_o = a_1 = b_3 = 0$, it follows from eq (6.29) that

$$G_{oo}(E) = \frac{E^2 - b_2^2}{E[E^2 - (b_1^2 + b_2^2)]}, \tag{6.31}$$

which results in a DOS consisting of a symmetric spectrum of three delta function peaks; one at $E = 0$ and the other two at $E = \pm\sqrt{b_1^2 + b_2^2}$. As $b_2 \to 0$, eq (6.31) reduces to eq (6.30) and the spectrum is said to be completely *bimodal*, whilst as $b_1 \to 0$, it reduces to eq (6.29) and is completely *unimodal* so that (b_1/b_2) is a measure of how bimodal the spectrum is. For non-zero a_1, eq (6.31) becomes

$$G_{oo}(E) = \frac{E^2 - a_1 E - b_2^2}{E[E^2 - a_1 E - (b_1^2 + b_2^2)]} \tag{6.32}$$

which still has one pole at $E = 0$, but the other two poles are now at $E = \frac{1}{2}a_1$ $\pm\sqrt{(\frac{1}{2}a_1)^2 + (b_1^2 + b_2^2)}$. The corresponding DOS is no longer symmetric as the mid-point of the outer two delta functions is now centred at $\frac{1}{2}a_1$ while there is a delta function in-between them at zero energy. The DOS is *skewed* and a_1 is a measure of the extent of this skew.

6.4.3 A symmetric four-level approximation

The presence of a peak at $E = 0$ (at the Fermi energy, really, but this is set to zero) in an approximation for the DOS consisting of an *odd* number of peaks makes such a model unsuitable for describing materials with a bandgap; the model places a high density of states at the centre of the gap, where there should be none. A two-peak model for the DOS, on the other hand, predicts a bandgap as large as the width of the entire DOS, which is also unphysical. The simplest model that can be hoped to describe a material with a bandgap is therefore a symmetric four-level spectrum, i.e. $a_0 = a_1 = a_2 = a_3 = b_4 = 0$, whilst b_1, b_2 and b_3 are non-zero. Putting these values in eq (6.29) gives

$$G_{oo}(E) = \frac{E(E^2 - b_2^2 - b_3^2)}{E^4 - (b_1^2 + b_2^2 + b_3^2)E^2 + b_1^2 b_3^2}. \qquad (6.33)$$

Eq (6.33) can be written as

$$G_{oo}(E) = \frac{w_+}{E - E_+} + \frac{w_-}{E - E_-} + \frac{w_-}{E + E_-} + \frac{w_+}{E + E_+}, \qquad (6.34)$$

where the w's are the *residues* of the poles in the Green's function or the *weights* of the corresponding delta functions in the DOS. Equating the denominator in eq (6.33) to zero gives a quadratic equation in E^2 which can be solved to give

$$E_\pm = \left[\tfrac{1}{2}(b_1^2 + b_2^2 + b_3^2) \pm \tfrac{1}{2}\sqrt{(b_1^2 + b_2^2 + b_3^2)^2 - 4b_1^2 b_3^2}\right]^{\frac{1}{2}}$$

$$= \tfrac{1}{2}\sqrt{(b_1 + b_3)^2 + b_2^2} \pm \tfrac{1}{2}\sqrt{(b_1 - b_3)^2 + b_2^2}\,. \qquad (6.35)$$

By equating eqs (6.33) and (6.34), it is not so difficult to show that

$$w_\pm = \pm\frac{E_\pm^2 - (b_2^2 + b_3^2)}{2(E_+^2 - E_-^2)} = \frac{1}{4}\left[1 \pm \frac{b_1^2 - b_2^2 - b_3^2}{\sqrt{(b_1^2 + b_2^2 + b_3^2)^2 - 4b_1^2 b_3^2}}\right]. \qquad (6.36)$$

The two peaks at positive energy are centred around $\tfrac{1}{2}\sqrt{(b_1 + b_3)^2 + b_2^2}$ and separated by $\sqrt{(b_1 - b_3)^2 + b_2^2}$. Thus, the valence band, represented by the two peaks at negative energy,

is separated by $\sqrt{(b_1+b_3)^2+b_2^2}$ from the conduction band, represented by the two peaks at positive energy, whilst the width of both bands is equal to $\sqrt{(b_1-b_3)^2+b_2^2}$. As there are half as many electrons as there are states per atom (see section 6.3), half the number of states in the DOS will be occupied by electrons. To minimise energy, the states will be filled from lower energies upwards, thus occupying the complete valence band with electrons but not the conduction band. As absorption is the result of transitions from occupied states in the valence band to unoccupied states in the conduction band, the absorption spectrum will be centred at

$$\Delta = \sqrt{(b_1+b_3)^2+b_2^2} \qquad (6.37)$$

A *symmetric* four-peak DOS gives rise to *three* absorption peaks; one (with weight two) at Δ and two at $\Delta \pm \sqrt{(b_1-b_3)^2+b_2^2}$. The *full width* of the absorption spectrum is thus

$$\Gamma = 2\sqrt{(b_1-b_3)^2+b_2^2}\,. \qquad (6.38)$$

Accounting for the fact that the weights $w_\pm$ are not quite equal to 1/4 is expected to give a second order correction terms to eqs (6.37) and (6.38). Now that simple analytic expressions have been derived for the centre of weight and the width of the absorption spectrum in terms of the recursion coefficients, these will now be calculated from the local atomic structure.

6.4.4 Calculating the recursion coefficients

Instead of working with the s and p orbitals on neighbouring atoms, as in section 6.3, the σ-bonding *hybrids* [7]

$$|i\sigma>=\frac{1}{\sqrt{1+p_\sigma}}\left[|is>+\sqrt{p_\sigma}\,|iz>\right] \qquad (6.39a)$$

and

$$|j\sigma>=\frac{1}{\sqrt{1+p_\sigma}}\left[|js>-\sqrt{p_\sigma}\,|jz>\right] \qquad (6.39b)$$

may be used, where the z -axis is chosen along the bond direction. The reason for using these hybrids is that, due to the sign of the orbitals, the hybrids point in particular directions. The hybrid in eq (6.39a), for example, has a large positive lobe in the direction of the positive z-axis (the positive p-lobe and the positive s orbital add up) and a small negative lobe in the direction of the negative z-axis (due to the *negative* p-lobe being added to the positive s-lobe). When hybrid orbitals on adjacent atoms point *towards* each other, this gives rise to an increased overlap compared to the molecular orbitals (bonding hybrid). Overlap between hybrid orbitals that point away from each other, on the other hand, can be ignored (non-bonding hybrid). The p-content of this σ-bond is given by p_σ, defined in eq (6.22). A schematic representation of the two bonding hybrids in eq (6.39) is given in Fig. 6.6.

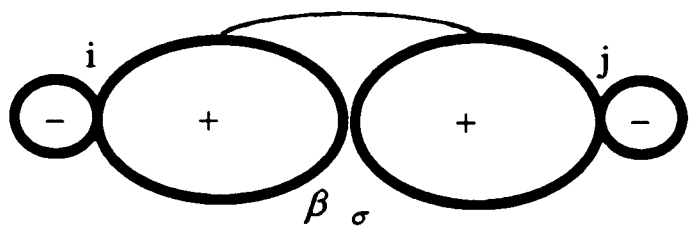


Figure 6.6 Schematic representation of sigma bonding orbitals on atoms i and j.

The hopping integral between these hybrid states is

$$h_\sigma \equiv < i\sigma \mid \hat{H} \mid j\sigma >$$

$$= \frac{-1}{1+p_\sigma}\left[\mid ss\sigma \mid +2\sqrt{p_\sigma}(sp\sigma) + p_\sigma (pp\sigma)\right]. \qquad (6.40)$$

Using the geometric mean approximation for (spσ), i.e. eq (6.21), this becomes

$$h_\sigma (R_{ij}) = -\frac{1+p_\sigma}{p_\sigma}(pp\sigma), \qquad (6.40)$$

where eq (6.22) has been used to eliminate |ssσ|. The overlap between this bonding hybrid and the equivalent bonding hybrid pointing from atom i to atom k, one of the other nearest neighbours, is equal to [8, 9]

$$g_\sigma(\theta_{ijk})h_\sigma(R_{ij}), \tag{6.42}$$

where the angular function, g_σ, is given by

$$g_\sigma(\theta) = \frac{p_\sigma}{1+p_\sigma}\left(\frac{1}{p_\sigma}+\cos(\theta)\right), \tag{6.43}$$

where θ is the bonding angle. It is easily shown that $\cos(\theta) = -1/3$ for the tetrahedral bond. Note that, as for the Chadi parameters, $p_\sigma = 1.57$ so that $g_\sigma = 0.18 << 1$. The recursion coefficients can be shown to be equal to [7]

$$\hat{b}_1^2 = 1+\Phi_{2\sigma} \tag{6.44a}$$

$$\hat{b}_2^2 = \frac{\Phi_{2\sigma}-\Phi_{2\sigma}^2+\Phi_{4\sigma}}{1+\Phi_{2\sigma}} \tag{6.44b}$$

and $$\hat{b}_3^2 = \frac{\hat{b}_2^2-(\hat{b}_1^2-1)+(\hat{b}_1^2-1)^2}{\hat{b}_1^2-1}, \tag{6.44c}$$

where the "hats" on the recursion coefficients indicate scaling by the σ bonding integral: $\hat{b}_i \equiv b_i / |h_\sigma(R_{ij})|$. The terms $\Phi_{2\sigma}$ and $\Phi_{4\sigma}$ include "hopping paths" of length two and length four, respectively, that start and end on atom i. For a monatomic material with $E_s = E_p = 0$, these terms are given by [7]:

$$\Phi_{2\sigma} = \sum_{k\neq i,j} g_\sigma^2(\theta_{jik})\hat{h}_\sigma^2(R_{ik}) = \sum_{k\neq i,j} g_\sigma^2(\theta_{jik}) \tag{6.45a}$$

and $$\Phi_{4\sigma} = \sum_{k\neq i,j} g_\sigma^2(\theta_{jik})\hat{h}_\sigma^4(R_{ik}) + \sum_{\substack{k,k'\neq i,j \\ k\neq k'}} g_\sigma(\theta_{jik})g_\sigma(\theta_{kik'})g_\sigma(\theta_{k'ij})\hat{h}_\sigma^2(R_{ik})\hat{h}_\sigma^2(R_{ik'})$$

$$= \sum_{k\neq i,j} g_\sigma^2(\theta_{jik}) + \sum_{\substack{k,k'\neq i,j \\ k\neq k'}} g_\sigma(\theta_{jik})g_\sigma(\theta_{kik'})g(\theta_{k'ij}), \tag{6.45b}$$

$\hat{h}_\sigma(R_{ik}) = h_\sigma(R_{ik})/h_\sigma(R_{ij}) = 1$ *etc.* as all four nearest neighbour σ bonds are equivalent in the diamond structure. Through the self-returning hopping paths of the electrons, the recursion coefficients (which determine the DOS through eq (6.28) and (6.29)), are

determined by the local co-ordination of the atoms. The contributions to $\Phi_{2\sigma}$ are pictured in Fig. 6.7 (a) and consist of hops from atom i to nearest neighbour k and back. As atom i has *three* nearest neighbours other than j, the sum yields $\Phi_{2\sigma} = 3g_\sigma^2$. The first term in eq (6.45b) is represented in Fig 6.7 (b) and also yields $3g_\sigma^2$. The second term is represented in Fig. 6.7 (c); as the first hop is out to one of the *three* nearest neighbours other than j and the second to one of the *two* nearest neighbours other than j or k, its contribution is $3 \cdot 2 \cdot g_\sigma^3 = 6g_\sigma^3$. The contributions due to hopping out to second nearest neighbours and back, as depicted in Fig. 6.7 (d), can be neglected for the σ bond [7]. These functions $\Phi_{2\sigma}$ and $\Phi_{4\sigma}$ depend on the local structure of the material through the self returning hopping paths of the sigma bond and thus provide the link between local atomic bonding and structure and the DOS.

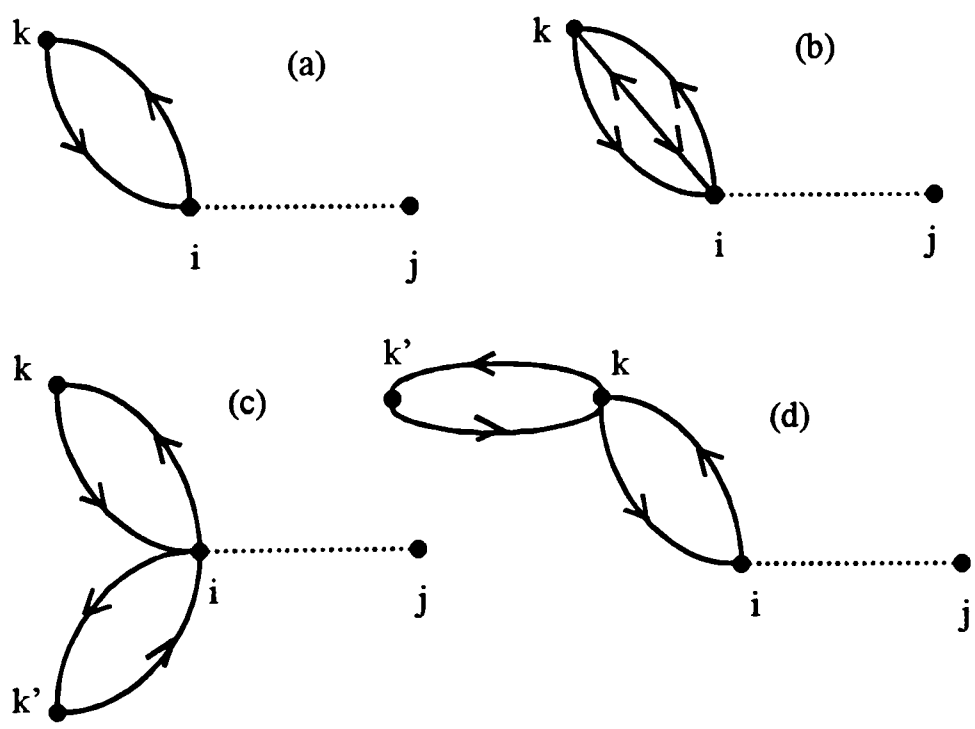


Figure 6.7 Hopping paths of length two (a), contributing to $\Phi_{2\sigma}$, and four (b), (c) and (d), contributing to $\Phi_{4\sigma}$.

As argued above, the nearest neighbour contributions of the σ bond give:

$$\Phi_{2\sigma} = 3g_\sigma^2 \qquad (6.46a)$$

and $\Phi_{4\sigma} = 3g_\sigma^2 + 6g_\sigma^3$. (6.46b)

Putting these values into eqs (6.40) gives, up to third order in g_σ

$$\hat{b}_1^2 = 1 + 3g_\sigma^2, \tag{6.47a}$$

$$\hat{b}_2^2 = 6g_\sigma^2 + \mathcal{O}(g_\sigma^3), \tag{6.47b}$$

and $$\hat{b}_3^2 = 1 + 2g_\sigma - 12g_\sigma^2 + \mathcal{O}(g_\sigma^3). \tag{6.47c}$$

Finally, substituting these expressions into eqs (6.37) and (6.38) gives to first order

$$\Delta = 2|h_\sigma| \tag{6.48a}$$

and $$\Gamma = 2g_\sigma |h_\sigma| \sqrt{6}. \tag{6.48b}$$

Thus, the centre of weight and the full width of the absorption spectrum have been calculated from the first nearest neighbour coordination and are expressed in terms of the nearest neighbour sigma hopping integral, h_σ, and the overlap between sigma states on the same atom, $g_\sigma h_\sigma$. The values for Δ and Γ, obtained from eqs (6.48), (6.40) and (6.43) are given in Table 6.1 for $p_\sigma = 1.5$, $p_\sigma = 2.0$ and $p_\sigma = 3.0$.

Table 6.1 Values for the angular function g_σ, the hopping integral h_σ, the centre of weight Δ, from eq (6.48a) and the width Γ, from eq (6.48b), of the absorption spectrum as a function of p_σ.

	$p_\sigma = 1.5$	$p_\sigma = 2.0$	$p_\sigma = 3.0$
g_σ	1/5	1/9	0
h_σ (eV)	–5.1	–4.6	–4.1
Δ (eV)	10.2	9.2	8.1
Γ (eV)	5.0	2.5	0

The values for the position, Δ, and the width, Γ, of the absorption spectrum corresponding to the simplified Si Hamiltonian have been calculated from the first nearest neighbour co-ordination. The values are to be compared with the exact result, shown in Fig. 6.5.

6.5 Discussion and conclusions

In section 6.2, a model absorption spectrum was presented to describe the optical response of a material in terms of three parameters: the plasma energy, E_p, the position of the absorption peak, Δ and the width of the absorption peak, Γ. By requiring that the moments μ_{-1}, μ_o and μ_1 of the model absorption spectrum must be equal to the corresponding moments of the exact absorption spectrum, analytic expressions were derived for Δ and Γ. From a purely mathematical point of view, there is no guarantee that this procedure yields a model absorption spectrum that even resembles the exact absorption spectrum, eq (6.1); the moments of a function are integrated properties and on their own contain very little information about the function itself. However, it is known empirically that eq (6.1) often resembles a peak with a fairly well defined position and width, which makes the procedure likely to produce a reasonable fit provided the moments are chosen correctly. From eq (6.3), it is clear that the higher the order of the moment, the more information it contains about the form of $\varepsilon_2(E)$ at *higher energy*, because the factor E^n acts as a weighting factor. However, as the model dielectric function falls off as E^{-3} at high photon energy, the highest order moment that can be calculated is μ_1, as moments of order two and higher *do not converge*. The integrand of μ_2, for example, is the product of E^2 with a function that falls off as E^{-3}, so that the integrand itself tails off as E^{-1}, causing the integral over E to be infinite. The delta functions in eq (6.1), on the other hand, have no tail so that the all moments of the exact absorption spectrum *do* converge. Thus, the largest moment that can be conserved is μ_1. In

section 6.2.1 it was found that preserving the moment μ_1 made the model dielectric function *exact* in the high energy limit, i.e. for $E >> \Delta$. In section 6.2.2 it was found that conserving the moment μ_{-1} made the model dielectric function *exact* in the static limit, i.e. at $E = 0$. The zeroth order moment is thus expected to give information about the behaviour of $\varepsilon_2(E)$ in the energy region not covered by the other two moments, i.e. the region around $E = \Delta$. Thus, the moments method, presented in this work for the first time, yields simple *analytical* expressions for the real and imaginary parts of the dielectric function, given in eqs (6.8) and (6.2), respectively, by effectively fitting eq (6.2) to the exact absorption spectrum, given in eq (6.1). The fit parameters, Δ and Γ, are also given *analytically*, by eqs (6.10) and (6.16), respectively, expressed in terms of the oscillator strengths and the transition energies of the exact absorption spectrum.

The simple analytical model for the dielectric function described above is of little use when the exact absorption spectrum is accurately known; the main use of the model comes in when only the main features of absorption peaks are known. As was shown in section 6.2.5 for the atomic linear chain, knowing the positions of as little as two peaks sufficed for a reasonable approximation of the absorption spectrum. The four level recursion model presented in section 6.4 aims at calculating the position of one of the features in the absorption spectrum corresponding to a simplified Si Hamiltonian, which is used as a test case.

The absorption spectra in Fig. 6.5 were calculated for the Si Hamiltonian described in section 6.3 using the translation symmetry of the diamond structure through Bloch's theorem. Using the same Hamiltonian, approximate expressions for the centre of weight and the full width of these absorption spectra were derived in section 6.4 using the nearest neighbour coordination of the Si atoms only.

Comparing Table 6.1 with Fig. 6.5 shows that the centres of weight for all three values of p_σ are in very good agreement. This indicates that the centre of weight of the absorption spectrum is determined by the first nearest neighbour coordination only. Thus, the absorption spectra of two different structures with the same nearest neighbour coordination are expected to have the same centre of weight, irrespective of the second and higher order nearest neighbour co-ordinations.

Eq (6.48b) predicts that the width of the absorption spectrum is zero for $p_\sigma = 3$. The fact that the corresponding absorption spectrum in Fig. 6.5 has finite width is due to the finite step size used for the partition of the energy scale and is thus a numerical inaccuracy and not a physical effect. For $p_\sigma = 1.5$ and $p_\sigma = 2.0$, eq (6.48b), it seems that the values for Γ calculated from eq (6.48b) and shown in Table 1 slightly overestimate the width of the spectra in Fig. 6.5. The discrepancy is probably due to the fact that the way Γ was calculated from the width of the valence and conduction bands in the DOS is a bit arbitrary. For example, the two delta functions that describe the position and width of the valence band could have been replaced with a Gaussian of the same width and position, and similarly for the conduction band. It is not so difficult to show that the resulting absorption spectrum is again a Gaussian with a position corresponding to the distance between the centres of weight of the valence and the conduction band, but with a width that is $\sqrt{2}$ times the width of the individual bands, and *not* twice the width, as was found using delta functions throughout. Instead of eq (6.48b), the expression for the width would have been $\Gamma = 2\, g_\sigma \,|\, h_\sigma \,|\, \sqrt{3}$, leading to an *under*estimate of the widths of the absorption spectra pictured in Fig. 6.5. Due to this uncertainty in Γ, it may not be concluded that second nearest neighbours must be considered to correctly describe the width of the absorption spectrum.

In calculating the absorption spectra in sections 6.3 and 6.4, it was assumed that (ppπ) = 0. This simplifying assumption resulted in a description of the DOS in terms of a single hopping integral between σ hybrids and an absorption spectrum effectively due to a photon being absorbed by an electron in the σ bonding state, exciting the electron to the σ anti-bonding state. Similarly, a finite value for (ppπ) is expected to give rise to a *second* absorption peak, corresponding to an electronic transition from the π bonding state to the π anti-bonding state. Unequal on-site energies of atomic states on neighbouring atoms may give rise to another peak in the absorption spectrum, as was the case for the example of the linear chain discussed in section 5.4.4. Absorption spectra of binary A_xB_{1-x} materials containing A-A, A-B and B-B nearest neighbour bonds are expected to have contributions of all three nearest neighbour types. Thus, ignoring the widths of *individual* peaks such as eq (6.48b), the width of the absorption spectrum for more realistic materials can be hoped to be calculated from eq (6.16), i.e. from the *spectrum* of delta functions that arises from the σ and π bonds between the different types of nearest neighbours.

Calculating the absorption spectrum of a realistic material has proved to be too ambitious within the scope of this work. However, this is the first time analytic expressions have been derived that relate the absorption spectrum to the local atomic environment, which is a very important result in its own right. Furthermore, the fact that taking into account only the *first* nearest neighbours already seems to give an adequate description of the centre of weight and the width of the absorption spectrum is very promising for the treatment of realistic systems.

Developing a model that relates the position and width of the absorption spectrum to the nearest neighbour co-ordination is only one of the four necessary ingredients for

understanding the reason why the reflectivity changes when amorphous $Ge_2Sb_2Te_5$ is crystallised. The relation between the absorption spectrum and the reflectivity needs to be known; this was treated in chapter V. In the next chapter, the Δ and Γ are determined for $Ge_2Sb_2Te_5$ before and after crystallisation. Finally, in chapter VIII, changes in the nearest neighbour co-ordination are investigated.

References

[1] H.R. Phillipp and H. Ehrenreich, *Phys. Rev.* **129** nr. 4 (1963) p. 1550.

[2] P.Y. Yu and M. Cardona, *Fundamentals of Semiconductors*, 2nd ed., Springer Verlag, Berlin (1999).

[3] Q. Guo-Xin and D.J. Chadi, *Phys. Rev. B* **35** (1987) p. 1288.

[4] A.P. Sutton, *Electronic Structure of Materials*, Oxford University Press, Oxford (1994).

[5] E. Tsymbal, *private communication.*

[6] R. Haydock, *Solid State Physics* **35** (1980) p. 216.

[7] D.G. Pettifor and I. Oleinik, *Phys. Rev. B* **59** (1999) p. 8487.

[8] D.G. Pettifor, *Springer Proc. Phys.* **48** (1990) p. 64.

[9] D.G. Pettifor and M. Aoki, in *Structural and Phase Stability of Alloys*, J.L. Morán-López, F. Mejía-Lira and J.M. Sanchez, Plenum Press, New York (1992) p. 119.

CHAPTER VII

Determining the Optical Properties of $Ge_2Sb_2Te_5$

7.1 Introduction

In the first part of this chapter, experiments to measure the optical constants of a thin $Ge_2Sb_2Te_5$ layer on a thick glass substrate are described. These were measured before and after crystallisation for photon energies in the range 0.5 - 3.5 eV. To do this, the transmittivity and the reflectivity from both sides of the film/substrate ensemble was measured with a spectrophotometer. A new method is then derived to obtain the optical constants from these quantities and the film thickness. For comparison, the optical constants were determined using ellipsometry at a single wavelength.

In the second part of this chapter, the optical constants are used to calculate the *optical contrast* of a semi-infinite film as a function of energy. The parameters Δ and Γ, the position and the width of the absorption peak, are found for both phases by fitting to the optical contrast. The plasma energy for both phases is determined independently from an EELS measurement to reduce the number of fit parameters.

The samples used for the measurements described in this chapter were grown using DC co-sputtering from GeTe and Sb_2Te_3 targets. This yields alloys of composition

$(GeTe)_x(Sb_2Te_3)_{1-x}$. For the current studies, the alloy aimed for was $Ge_2Sb_2Te_5$, which corresponds to $x = 0.67$. The background pressure used was 3×10^{-6} mbar and the argon pressure used was 5×10^{-3} mbar. The films were all grown to have a thickness of approximately 25 nm. The samples for the PIXE and the IR-VIS-UV Spectrophotometer experiments were grown on 1.0 mm thick glass substrates. The samples used for the GIXR and ellipsometry experiments were grown on silicon, and the films examined using EELS were grown on carbon-coated mica.

7.2 Determining the film composition

The composition of the Ge-Sb-Te films was checked using PIXE analysis. The area irradiated by the proton beam is 45 by 45 μm^2. The time during which the electron count is taken is of the order of a minute. A PIXE spectrum is shown in Fig. 7.1. The electron count (arb. u.) is plotted logarithmically as a function of the energy of the electron in KeV.

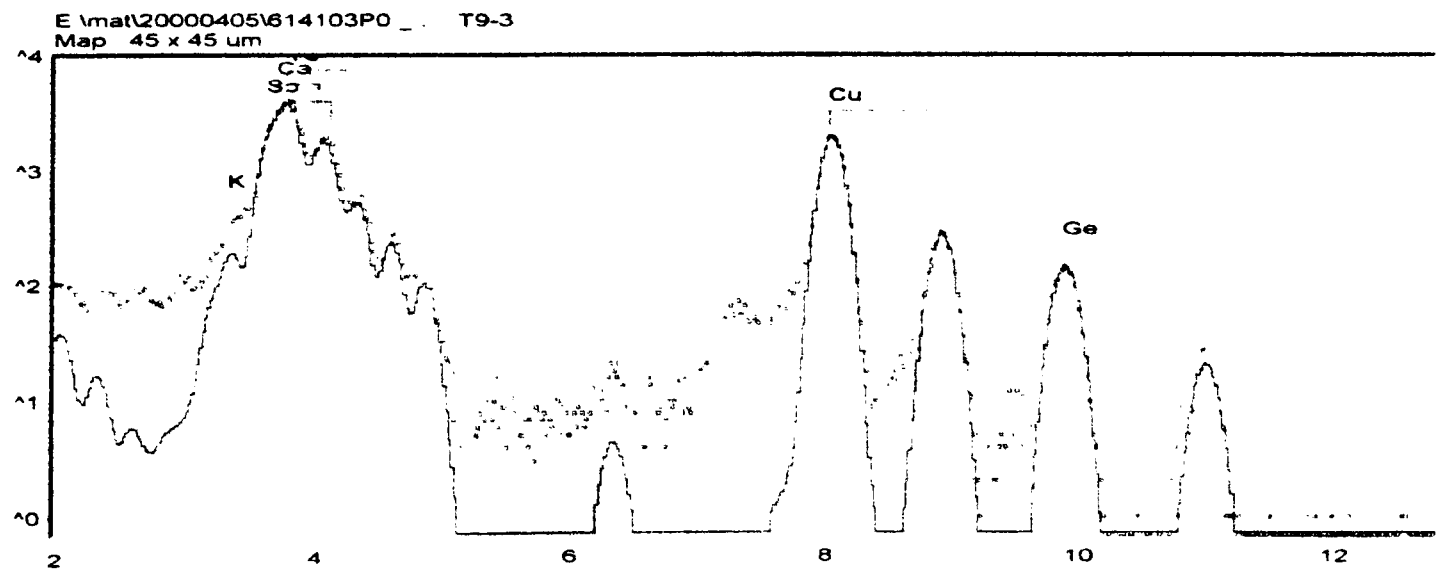


Figure 7.1 PIXE spectrum of the Ge-Sb-Te sample. The electron count (arb. u.) is plotted logarithmically as a function of the electron energy in keV. The empty squares are data points; the continuous line is a fit.

The two Cu peaks indicated and the Fe peak around 6.3 keV are instrumental artefacts, caused by stray scattering from copper and iron components of the apparatus. The K and Ca peaks indicated originate from the potassium and calcium in the glass substrate. The Ge, Sb and Te peaks are identified from the respective atomic spectra. The surface under the peaks is determined from the fit and yields values of the counts of 5620, 8698 and 21677 for Ge, Sb and Te, respectively. The number of counts is proportional to the atomic mass of the atoms, i.e. M_{Ge} = 72.61 g/mol, M_{Sb} = 121.8 g/mol and M_{Te} = 127.6 g/mol [1]. Thus dividing the number of counts by the atomic masses gives a measure of the relative amounts of each element. Assuming there are no other elements present in the alloy, rescaling these numbers so that they add up to 100 % gives the atomic percentage of the elements. This yields $Ge_{24}Sb_{22}Te_{53}$, with an estimated error of 2 %. This is fairly close to the intended stoichiometric composition $Ge_2Sb_2Te_5$, or $Ge_{22}Sb_{22}Te_{56}$.

7.3 Measuring film thickness and density

X-ray reflectivity traces were measured on $Ge_2Sb_2Te_5$ samples, deposited on Si, before and after crystallisation. The samples were crystallised by heating them in a tube furnace at 623 K for 60 minutes under an argon atmosphere. Figure 7.2 shows the GIXR curve for the crystalline sample.

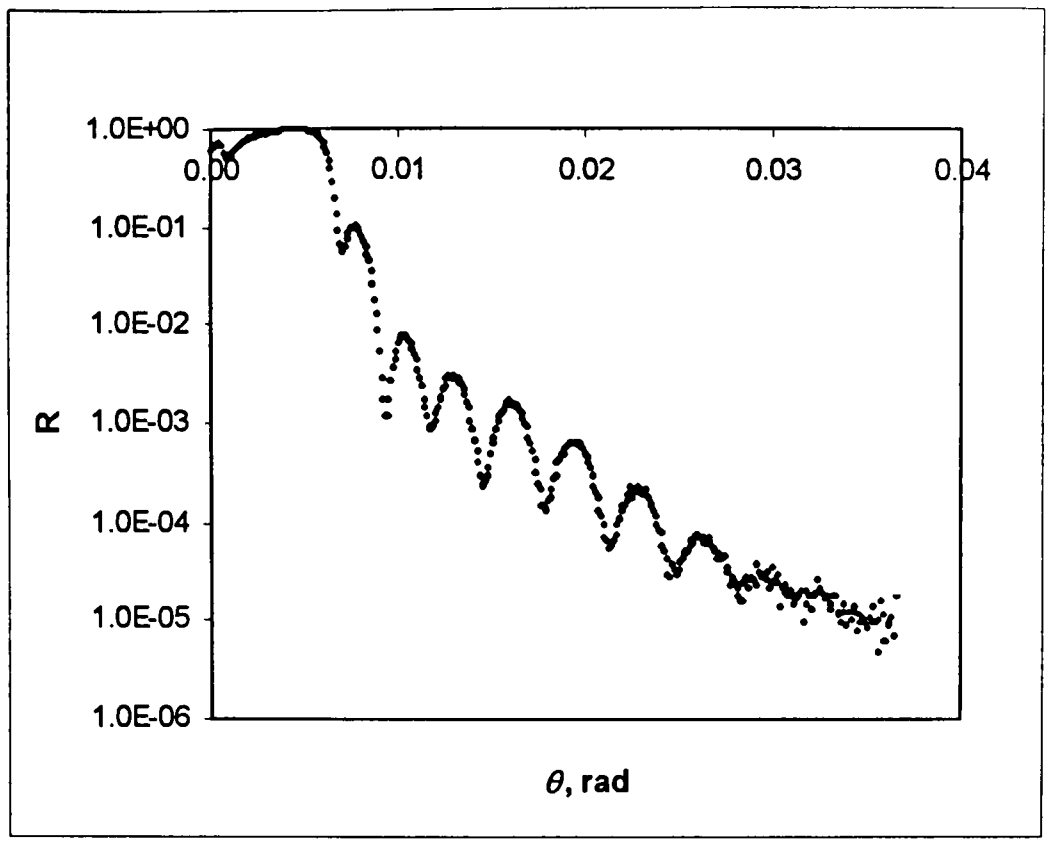


Figure 7.2 Reflectivity of the X-ray beam, R, as a function of angle of incidence, θ, for crystalline $Ge_2Sb_2Te_5$.

The density of the $Ge_2Sb_2Te_5$ film is expected to be of the order of 6 g/cm^3 [2], which is higher than the density of the glass substrate, $\rho_s = 2.5$ g/cm^3. As the photon energy of the X-rays is very large compared to the plasma energy, eqs (5.25), (5.34) and (5.35) imply that the real part of the dielectric function is expected to be lower for the sample than for the substrate whilst absorption is negligible. Eqn (5.20a) then indicates that the sample has a lower refractive index than the substrate. The thickness of the film can thus be obtained from eq (2.1b) by plotting θ_m^2 versus $(m+\frac{1}{2})^2$; the plot is shown in Fig. 7.3.

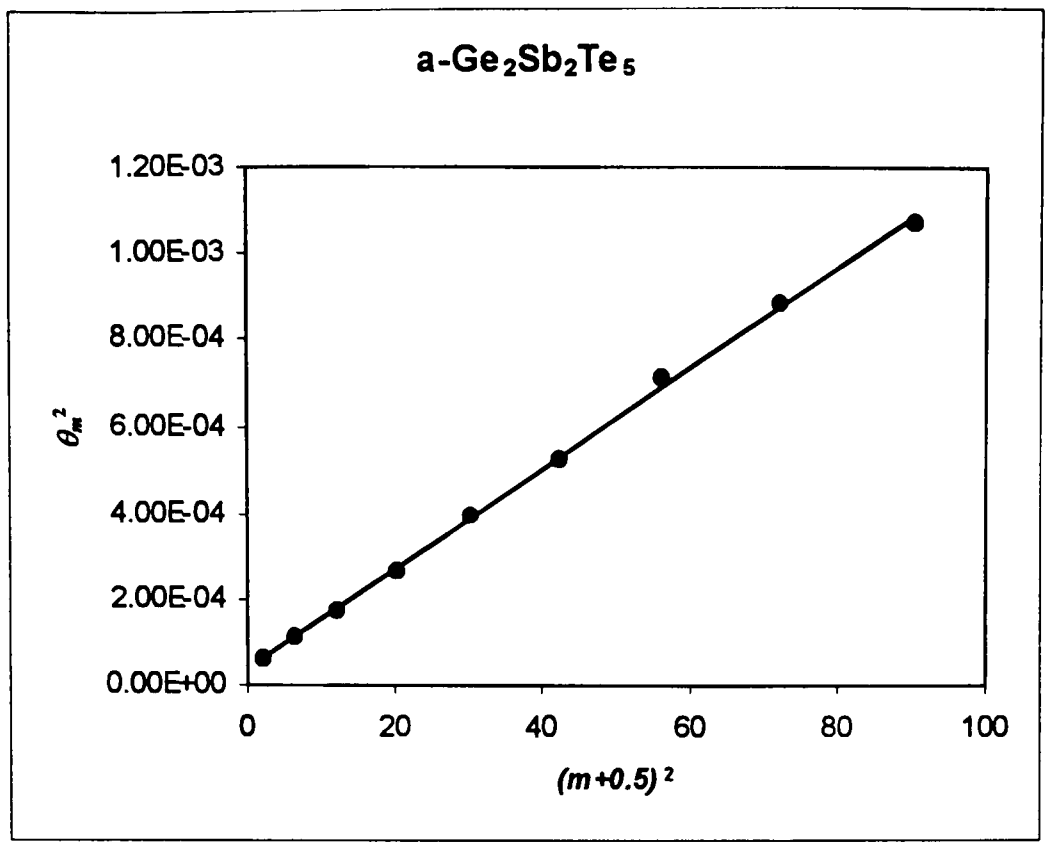


Figure 7.3 Plot of θ_m^2 vs. $(m+\frac{1}{2})^2$ for the $R(\theta)$ trace in Fig. 7.2; θ_m is the position of the m^{th} order maximum (dots). The least square fit (line) has slope 1.17×10^{-5}.

The plot clearly yields a straight line; the slope of the least square fit is equal to $\alpha = 1.17 \times 10^{-5}$. The thickness of the crystalline film then follows from $t_f^X = \lambda/(2\sqrt{\alpha}) = (22.5 \pm 0.5)$ nm, as explained in section 2.4.2. The thickness of the amorphous film was determined in the same way and yielded $t_f^A = (25.0 \pm 0.5)$ nm.

Having obtained the thickness, the density of the film, the roughness of the air/film interface, σ_f, and of the film/substrate interface, σ_s, are obtained by the fitting routine described in section 2.4.3. The fit for the crystalline film is shown in Fig. 7.4.

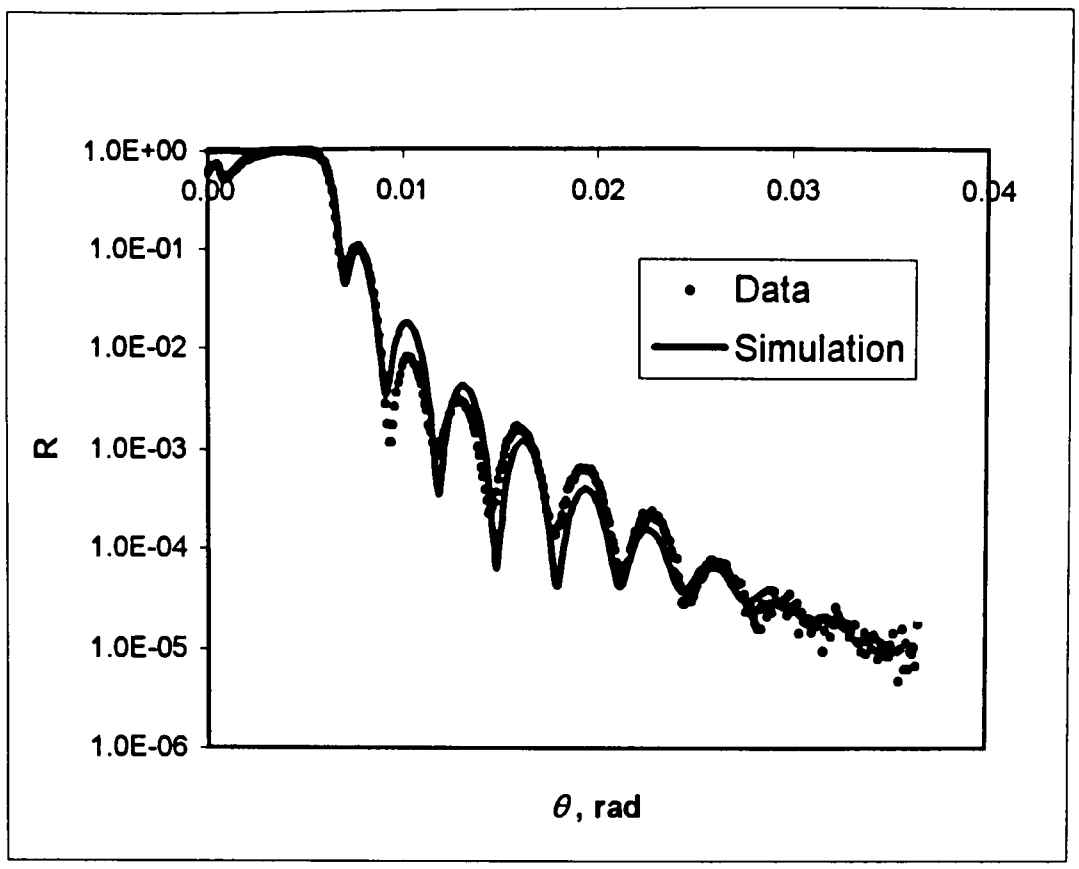


Figure 7.4 Comparison of the experimental GIXR curve (dots) and the fit (line) for the reflectivity trace in Fig. 7.2

Before and after crystallisation, the rms roughness of the air/film interface was found to be σ_f = 1.0 nm and the roughness of the film/substrate σ_s = 0.3 nm. The error in the roughness of these interfaces is estimated at 20 %. The fit parameters for both the amorphous and the crystalline film are shown in Table 7.1. The mass densities of the amorphous and the crystalline films were found to be $\rho_A = (6.0 \pm 0.3)$ g/cm^3 and $\rho_X = (6.7 \pm 0.3)$ g/cm^3, respectively.

Note that

1) the reduction on the film thickness upon crystallisation agrees well with the increase in the density of the film, and

2) the densities found in this work agree well with those quoted by Yokota (section 5.5.2).

7.4 Determining the optical constants *n* and *k*

In this section, the optical constants of a thin $Ge_2Sb_2Te_5$ film on a thick glass substrate are determined as a function of photon energy before and after crystallisation. The reflectivity of the film/substrate ensemble at the film side, R_t, and the substrate side, R_t', as well as the transmittivity, T_t, all depend on the optical constants of the film. Section 7.4.1 describes the exact functional dependence. It is explained in section 7.4.2 how R_t, R_t' and T_t were measured as a function of photon energy. In section 7.4.3 an iterative procedure is described for calculating the optical constants n and k. Based on this procedure, novel iteration equations F_1 and F_2 are derived in sections 7.4.4 and 7.4.5 such that

$$n_{i+1} = F_1(R_t, R_t', T_t, n_i, k_i)$$

and $$k_{i+1} = F_2(R_t, R_t', T_t, n_{i+1}, k_i),$$

which can be used to compute the optical constants of the $Ge_2Sb_2Te_5$ film from R_t, R_t' and T_t. Section 7.4.6 summarises the novel procedure developed during this study. The values for the optical constants are given in section 7.4.7, as a function of photon energy, before and after crystallisation.

7.4.1 Reflection, refraction and transmission

Consider a beam of light, travelling in medium 1, towards a planar interface with a second medium, as shown in Fig. 7.5.

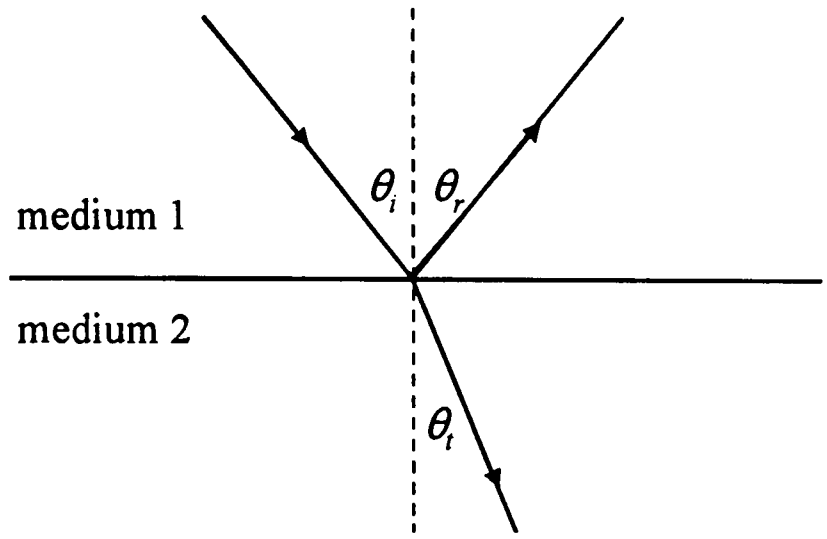


Figure 7.5 Reflection and refraction at an interface between two media.

The angle between the normal of the interface and the incident light beam is θ_i, the angle of incidence. The beam will be partly *reflected* at the interface, at an angle $\theta_r = \theta_i$ with the normal, and partly *refracted* at the interface into the second medium, at an angle θ_t with the normal. Solving the wave equation (see section 5.2.2) with the appropriate boundary conditions yields the angle of refraction through Snell's law

$$n_1 \sin\theta_i = n_2 \sin\theta_t, \tag{7.1}$$

as well as the fractions of the amplitude reflected, r, and transmitted, t, at the interface. In general, r and t are a function of the angle of incidence. For *normal* incidence, i.e. $\theta_i = 0$, they are equal to

$$r_{1,2} = \frac{\tilde{n}_2 - \tilde{n}_1}{\tilde{n}_1 + \tilde{n}_2} \tag{7.2a}$$

and

$$t_{1,2} = \frac{2\tilde{n}_1}{\tilde{n}_1 + \tilde{n}_2}, \tag{7.2b}$$

where $\tilde{n}_j = n_j + ik_j$ is the complex refractive index in medium j. These fractions are called the *Fresnel coefficients*. The reflectivity, R, of the interface, i.e. the ratio of the *intensities* of the reflected and incoming beams is then

$$R = |r_{1,2}|^2 \tag{7.3a}$$

and, similarly, the transmittivity, T, of the interface is equal to

$$T = |t_{1,2}|^2 . \tag{7.3b}$$

The reflectivity of a *semi-infinite medium* in air ($\tilde{n}_1 = 1$) is given by the reflectivity of the air-film interface so that from eqs (7.2a) and (7.3a)

$$R_f = \left|\frac{\tilde{n}_f - 1}{\tilde{n}_f + 1}\right|^2 = \frac{(n_f - 1)^2 + k_f^2}{(n_f + 1)^2 + k_f^2} . \tag{7.4}$$

Now consider a *substrate* of finite thickness in air. The reflectivities and transmittivities of the interfaces follow from eqs (7.2) and yield

$$R_{a,s} = R_{s,a} = \frac{(n_s - 1)^2 + k_s^2}{(n_s + 1)^2 + k_s^2} \tag{7.5a}$$

$$T_{a,s} = \frac{4}{(n_s + 1)^2 + k_s^2} \tag{7.5b}$$

and $$T_{s,a} = \frac{4(n_s^2 + k_s^2)}{(n_s + 1)^2 + k_s^2} . \tag{7.5c}$$

The overall reflectance of the substrate contains a second order contribution from the light that is transmitted through the air/substrate interface, then travels through the substrate, is reflected at the bottom of the substrate (substrate/air interface) and travels back through the substrate to be transmitted by the air/substrate interface. Similarly, R_s contains an infinite number of higher order contributions due to light that is reflected back and forth between the two interfaces. Summing over these contributions yields [3–5]

$$R_s = R_{a,s} + \frac{T_{a,s} T_{s,a} R_{a,s} \exp(-2\alpha_s)}{1 - R_{a,s}^2 \exp(-2\alpha_s)} . \tag{7.6a}$$

The transmittivity of the substrate can be shown to be given by

$$T_s = \frac{T_{a,s} T_{s,a} R_{a,s} \exp(-\alpha_s)}{1 - R_{a,s}^2 \exp(-2\alpha_s)}. \qquad (7.6b)$$

where $\alpha_s \equiv 2\frac{E}{\hbar c} k_s t_s$; (7.6c)

E is the photon energy, c the velocity of light and t_s the thickness of the substrate.

Now consider a *thick film*. A film can be called thick when its thickness is large enough for the film to be non-transparent. From the attenuation of a wave in an absorbing medium, eq (5.22), this gives the criterion

$$t_f >> \frac{\hbar c}{2Ek_f}, \qquad (7.7a)$$

where t_f and k_f are the thickness and the absorption coefficient of the film, respectively. When the inequality in eq (7.7a) is obeyed, the reflectivity of the film is equal to that of a semi-infinite medium, while the transmittivity is effectively zero. Another criterion used in the literature to define a thick film is

$$t_f >> L, \qquad (7.7b)$$

where L is the coherence length of the incident light. When eq (7.7b) is satisfied, the reflectivity and transmittivity are given by eqs (7.6) with the index s replaced with f.

For a *thin film* with $t_f << L$, interference between the waves further complicates the picture. Summing the amplitudes of the reflected and transmitted waves taking this interference into account, it can be shown that a thin film in air has effective Fresnel coefficients [3]

$$r_f = r_{a,f} \frac{1 - \exp(i\tilde{n}_f \alpha)}{1 - r_{a,f}^2 \exp(i\tilde{n}_f \alpha)} \qquad (7.8a)$$

and $$t_f = \frac{t_{a,f} t_{f,a} \exp(i\tilde{n}_f \alpha)}{1 - r_{a,f}^2 \exp(i\tilde{n}_f \alpha)}, \tag{7.8b}$$

where $$\alpha \equiv 2\frac{E}{\hbar c} t_f . \tag{7.8c}$$

The reflectivity and transmittivity of the film are again given by the square modulus of the effective Fresnel coefficients in eqs (7.8a) and (7.8b).

A *thin film on a semi-infinite substrate* is asymmetric; it can be thought of as a film sandwiched between two different semi-infinite media (i.e. air and the substrate). This a-symmetry results in the reflectivity of the film being dependent on whether the light is *substrate-incident* (primed) or *air-incident* (not primed) [6]:

$$R_f = |r_f|^2 \tag{7.9a}$$

$$R_f' = |r_f'|^2, \tag{7.9b}$$

and $$T_f = T_f' = n_s |t_f|^2, \tag{7.9c}$$

where $$r_f = \frac{r_{a,f} + r_{f,s} \exp(i\tilde{n}_f \alpha)}{1 + r_{a,f} r_{f,s} \exp(i\tilde{n}_f \alpha)}, \tag{7.10a}$$

$$r_f' = \frac{r_{s,f} + r_{f,a} \exp(i\tilde{n}_f \alpha)}{1 + r_{a,f} r_{f,s} \exp(i\tilde{n}_f \alpha)}, \tag{7.10b}$$

and $$t_f = \frac{t_{a,f} t_{f,s} \exp(\frac{1}{2} i\tilde{n}_f \alpha)}{1 + r_{a,f} r_{f,s} \exp(i\tilde{n}_f \alpha)}. \tag{7.10c}$$

The transmittivity is, surprisingly, independent of the direction of the incident light.

Finally, a *thin film on a thick (but finite) substrate in air* is considered. The ensemble can be considered as a substrate with air on one side and on the other side an interface with transmittivity T_f, air-incidence reflectivity R_f and substrate-incidence reflectivity R_f'. The total reflectivities and transmittivity (i.e. of the ensemble) then become [4, 5]

$$R_t = R_f + \frac{T_f^2 R_{s,a} \exp(-2\alpha_s)}{1 - R_{s,a} R_f' \exp(-2\alpha_s)}, \qquad (7.11a)$$

$$R_t' = R_{s,a} + \frac{T_{a,s} T_{s,a} R_f' \exp(-2\alpha_s)}{1 - R_{s,a} R_f' \exp(-2\alpha_s)}, \qquad (7.11b)$$

and $$T_t = \frac{T_{s,a} T_f \exp(-\alpha_s)}{1 - R_{s,a} R_f' \exp(-2\alpha_s)}, \qquad (7.11c)$$

where $R_{s,a}$, $T_{s,a}$ and $T_{a,s}$ are given by eqs (7.5) and R_f, R_f' and T_f by eqs (7.9). Thus, R_t, R_t' and T_t are complicated functions of the optical constants and thickness of the substrate, n_s, k_s and t_s, and of the film, n_f, k_f and t_f, respectively. As the optical constants of the substrate are known from the literature and the thickness of substrate and film can be measured independently, the optical constants of the film can be obtained from a measurement of R_t, R_t' and T_t by inverting eqs (7.11).

7.4.2 Measuring R_t, R_t' and T_t

The air-incident reflectivity, R_t, the substrate-incident reflectivity R_t' and the transmittivity T_t of a thin $Ge_2Sb_2Te_5$ film on a thick glass substrate were measured as a function of photon energy before and after crystallisation. The range of photon energies over which these quantities were measured was 0.6 - 6.0 eV, corresponding to the maximum range of wavelength accessible by the spectrophotometer used, *viz.* 200 - 2000 nm. The raw (i.e. not corrected for the reflectivity of Al; see section 2.6.3) data are shown in Fig. 7.6.

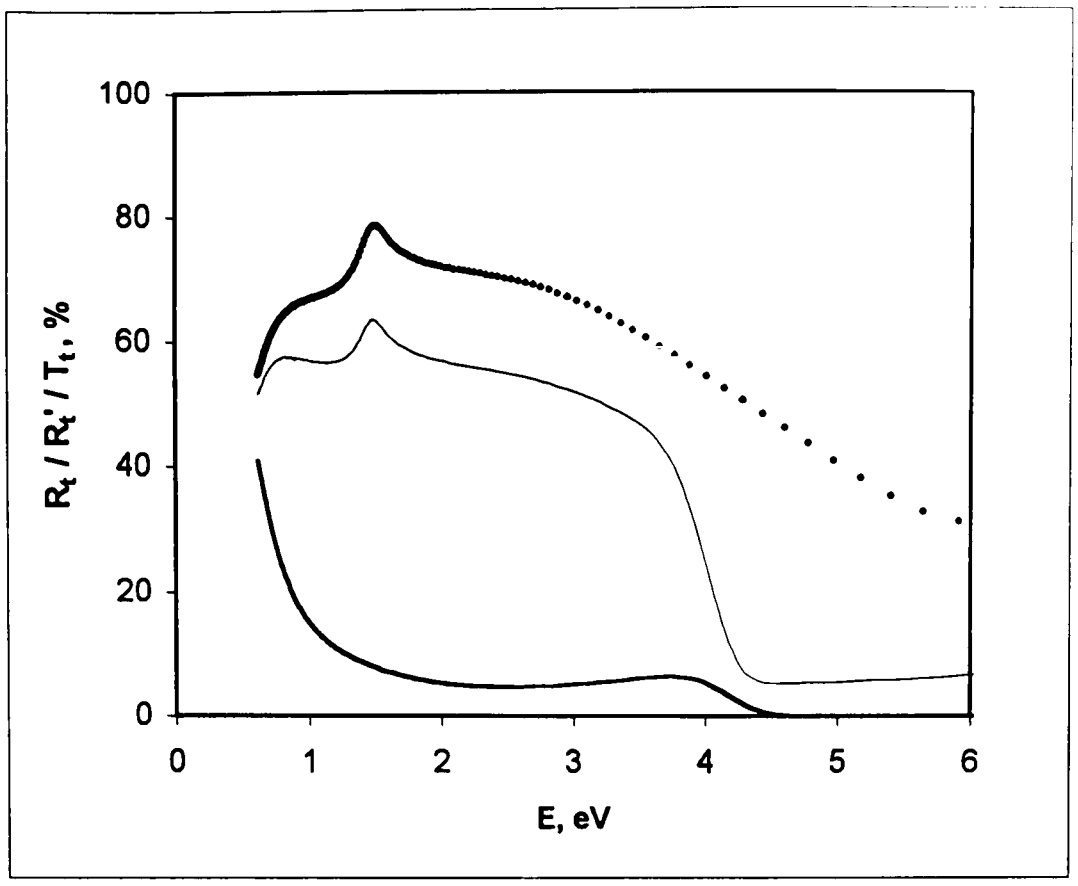


Figure 7.6 Raw spectrometry data of R_t (dotted line), R_t' (thin line) and T_t (thick line) for a crystalline $Ge_2Sb_2Te_5$ film on a glass substrate, as a function of photon energy.

The peaks in R_t and R_t' at 1.5 eV are due to a dip in the reflectivity of Al, which is shown in Fig. 7.7.

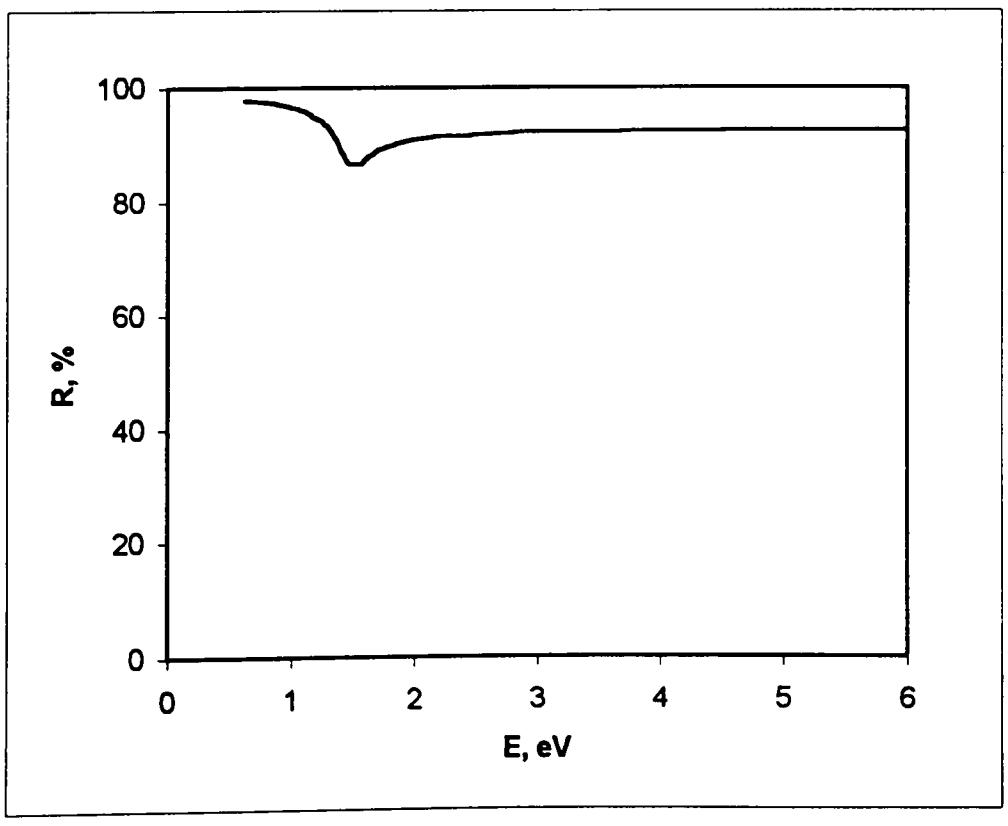


Figure 7.7 Reflectivity of Al, taken from [13], versus photon energy.

The fact that there is no dip in T_t confirms that the peaks in both reflectivities are not due to the optical properties of the film/substrate ensemble. The corrected values for R_t and R_t', as well as T_t, are shown in Fig. 7.8.

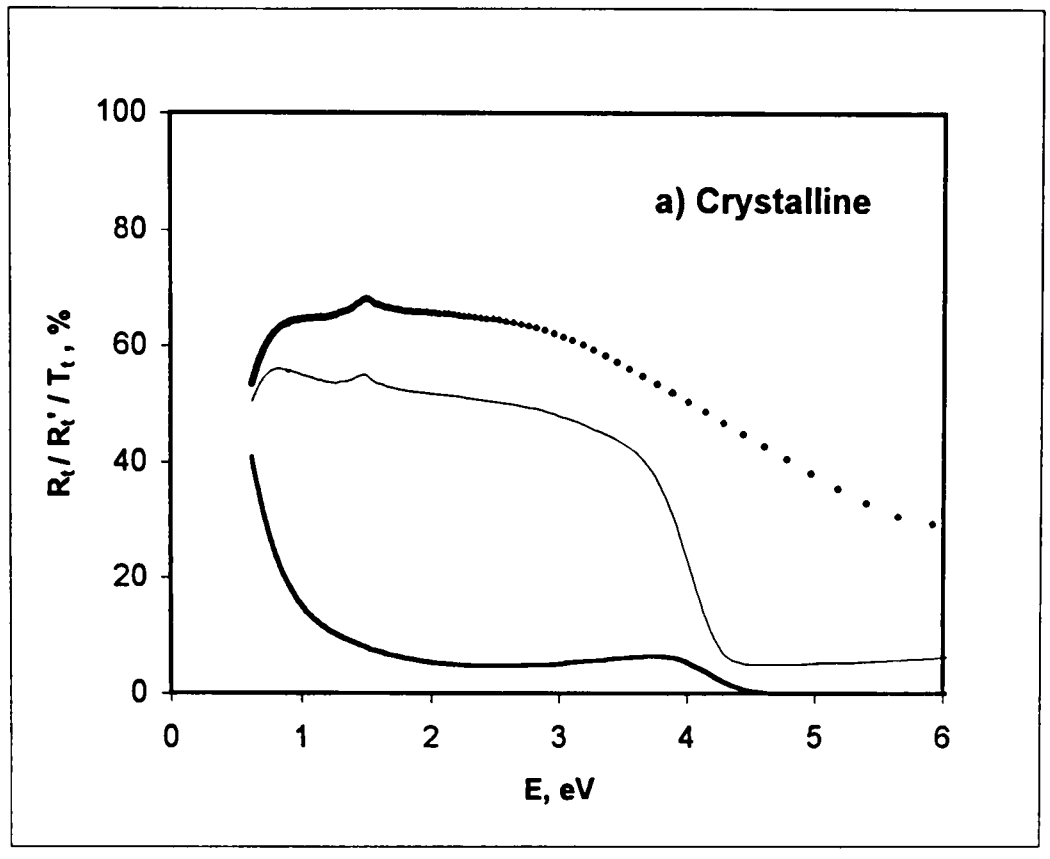


Figure 7.8 R_t (dotted line) and R_t' (thin line), corrected for the reflectivity of Al, and T_t (thick line) for a) the data in Fig. 7.6 and b) values for the amorphous film.

The fact that there are still two small peaks in the reflectivities indicate that the correction is not perfect. This may be due to the fact that the reflectivity of Al shown in Fig. 7.7 was

obtained by measuring a clean de-oxidized Al surface in vacuum, whilst the reference measurement in the current experiments were carried out using an Al mirror coated with a thin passivating Al_2O_3 oxide layer.

The fact that T_t falls to zero around 4.6 eV is due to absorption by the glass substrate. The optical constants of the film will be calculated for energies up to 3.5 eV, where the absorption of the substrate is small.

7.4.3 Obtaining n and k from R_f, T_f and $R_{a,f}$

Consider the thin film on a semi-infinite substrate discussed in section 7.4.1. There are two main difficulties in obtaining the optical constants of the film from eqs (7.9) and from measured values for R_f, R_f' and T_f. Firstly, it is impossible to invert eqs (7.9) to obtain analytical expressions for n and k in terms of R_f, R_f' and T_f only. Secondly, there are many different combinations of n and k that yield the *same* values for R_f, R_f' and T_f. However, it is possible to derive analytically a set of functions F_1 and F_2 for which

$$n = F_1(R_f, R_{a,f}, T_f, n, k) \tag{7.12a}$$

and

$$k = F_2(R_f, R_{a,f}, T_f, n, k), \tag{7.12b}$$

where $R_{a,f}$ is the reflectivity of the air/film interface. Provided that the expressions *converge*, eqs (7.12) can be used to find n and k iteratively. The task remains to find expressions for F_1 and F_2 that converge both rapidly and to the correct physical solution. This is done in the remainder of the section. The derivation follows Vriens and Rippens [6], who were the first to solve this problem for a weakly absorbing substrate.

It can be shown [7–10] that whilst many sets of n and k yield the same values for R_f and T_f, this is not true for the functions $(1 \pm R_f)/T_f$. From eqs (7.9) and (7.10) it can be shown that [6]

$$\frac{1 \pm R_f}{T_f} = \frac{(1 \pm R_{a,f})[1 \pm R_{a,f} \exp(-2k\alpha)]}{T_{a,f} T_{f,a} \exp(-k\alpha)}$$

$$- \frac{(r_{a,f} \pm r^*_{a,f})[r_{a,f} \exp(i\tilde{n}\alpha) \pm r^*_{a,f} \exp(-i\tilde{n}^*\alpha)}{T_{a,f} T_{f,a} \exp(-k\alpha)} \qquad (7.13)$$

where $r_{a,f}$ is given by eq (7.2a); $r^*_{a,f}$ is its complex conjugate; $R_{a,f}$, $T_{a,f}$ and $T_{f,a}$ follow from the square moduli of eqs (7.2) and it is defined for convenience that

$$\alpha \equiv 2 \frac{E}{\hbar c} t_f . \qquad (7.14)$$

The two eqs (7.13) can be re-written as [6]

$$R_{a,f} \exp(-2k\alpha) + (x - q) \exp(-k\alpha) - 1 = 0 \qquad (7.15a)$$

and $$R_{a,f} \exp(-2k\alpha) + (p - y) \exp(-k\alpha) + 1 = 0 , \qquad (7.15b)$$

where the following abbreviations have been defined

$$x \equiv (1 - R_{a,f}) \left(\frac{1 - R_f}{T_f} \right) \qquad (7.16a)$$

$$y \equiv \left(\frac{T_{a,f} \cdot T_{f,a}}{1 + R_{a,f}} \right) \left(\frac{1 + R_f}{T_f} \right) \qquad (7.16b)$$

$$q \equiv \frac{k}{n} \left[\left(1 - \frac{1}{n} \right) + R_{a,f} \left(1 + \frac{1}{n} \right) \right] \sin(n\alpha) + \left(\frac{k}{n} \right)^2 (1 - R_{a,f}) \cos(n\alpha) \qquad (7.16c)$$

and $$p \equiv \left[\frac{1}{n} \left(\frac{1 - R_{a,f}}{1 + R_{af}} \right) - 1 \right]$$

$$* \left[\left(1 - \frac{1}{n} \right) \cos(n\alpha) + R_{a,f} \left(1 + \frac{1}{n} \right) \cos(n\alpha) - \frac{k}{n} (1 - R_{a,f}) \sin(n\alpha) \right] . \qquad (7.16d)$$

Eqs (7.15) should now be solved simultaneously for n and k, from experimentally determined values for R_f and T_f.

Eqs (7.15) are quadratic equations in $\exp(-k\alpha)$ which can be solved to give

$$\exp(-k\alpha) = \frac{x-q}{2R_{a,f}}\left[-1+\sqrt{1+\frac{4R_{a,f}}{(x-q)^2}}\right] \qquad (7.17a)$$

$$\exp(-k\alpha) = \frac{y-p}{2R_{a,f}}\left[1-\sqrt{1-\frac{4R_{a,f}}{(y-p)^2}}\right]. \qquad (7.17b)$$

Vriens and Rippens now rewrite eq (7.17a) as

$$k = -\frac{1}{\alpha}\ln\left[\frac{x-q}{2R_{a,f}}\left(-1+\sqrt{1+\frac{4R_{a,f}}{(x-q)^2}}\right)\right]. \qquad (7.18a)$$

They then *measure* $R_{a,f}$ from the reflectivity of a very thick film (so that $R_{a,f} = R_f = R_t$), set $q = 0$ in eq (7.18a) and thus obtain a first estimate for k in terms of R_f, T_f, and $R_{a,f}$. A first iterative value for n is found by inverting the expression for $R_{a,f}$, i.e. eq (7.4), to give

$$n = \left(\frac{1+R_{a,f}}{1-R_{a,f}}\right)+\sqrt{\left(\frac{1+R_{a,f}}{1-R_{a,f}}\right)^2-(1+k^2)}\,. \qquad (7.18b)$$

With this value of n, q in eq (7.18a) can be calculated from eq (7.16c). The procedure is repeated until the input values for n and k differ from the output values calculated with eqs (7.18) by less than 0.01, which typically takes four iterations [6].

For technical reasons, however, it was not possible with the DC sputtering set-up used in this study to grow films thick enough to measure $R_{a,f}$. For this reason, eq (7.18b) can not be used as an iteration equation for n. In the next section, an iteration equation for n is derived that does *not* require knowledge of $R_{a,f}$. The derivation is original work.

7.4.4 Calculating n and k from R_f and T_f only

Note that eqs (7.17) are solutions of eqs (7.15). As one of these solutions, *viz.* eq (7.17a), is used to derive an iteration equation for k, the obvious thing to try is to derive an iteration equation for n from the other solution, *viz.* eq (7.17b). This was attempted first, but, unfortunately, the resulting pair of iteration equations does not converge. The reason for this is the presence of the $\exp(-k\alpha)$ term in the iteration equation for n; for a certain error in k (i.e. the difference between the exact solution and the value for k used in a particular iteration), the error in $\exp(-k\alpha)$ is increased exponentially and gives rise to a value for n that is further away from the exact solution than the input value of k, which means that the iteration equation for n diverges. Thus, an iteration equation for n needs to be derived that does not include the $\exp(-k\alpha)$ term.

Whilst eqs (7.15a) and (7.15b) are second order equations in $\exp(-k\alpha)$, adding and subtracting the two yields two *first* order equations in $\exp(-k\alpha)$, which can be solved to give [6]

$$\exp(-k\alpha) = \frac{2}{x+y-q-p} \tag{7.19a}$$

and $$\exp(-k\alpha) = \frac{y+q-x-p}{2R_{a,f}}. \tag{7.19b}$$

By equating eqs (7.19a) and (7.19b) it easily follows that

$$y = p + \sqrt{(x-q)^2 + 4R_{a,f}}\ . \tag{7.20}$$

Eq (7.16b) can be rearranged to give

$$T_{a,f} \cdot T_{f,a} = y(1+R_{a,f})\left(\frac{1+R_f}{T_f}\right)^{-1} \tag{7.21}$$

whilst from eqs (7.5b) and (7.5c) it follows that

$$T_{a,f}T_{f,a} = 16\frac{n^2+k^2}{[(n+1)^2+k^2]^2}. \tag{7.22}$$

Equating eqs (7.21) and (7.22) yields

$$(n+1)^2+k^2 = 4\sqrt{\frac{n^2+k^2}{y(1+R_{a,f})}\left(\frac{1+R_f}{T_f}\right)}. \tag{7.23}$$

Defining, for convenience of notation,

$$\kappa \equiv \sqrt{\frac{n^2+k^2}{y(1+R_{a,f})}\left(\frac{1+R_f}{T_f}\right)}, \tag{7.24}$$

eq (7.23) can be rewritten as

$$n = -1+\sqrt{4\kappa-k^2}\ . \tag{7.25}$$

As the term $\exp(-k\alpha)$ has been eliminated from y in eq (7.20), which enters into eq (7.25) through κ, this equation is suitable as an iteration equation for n.

Finding n and k iteratively from eqs (7.18a) and (7.25) yields the simultaneous solutions of eqs (7.15), as eq (7.18a) is derived from eq (7.15a) whilst eq (7.25) is derived from a linear combination of eqs (7.15a) and (7.15b).

7.4.5 Obtaining n and k from R_t, R_t' and T_t

In the previous section, iteration equations for n and k were derived in terms of $(1 + R_f)/T_f$ and $(1 - R_f)/T_f$. In this section, it will be shown how these quantities can be derived from R_t, R_t' and T_t. First, eqs (7.11) can be inverted to give [6]

$$R_f = R_t - \frac{T_t^2 R_{s,a}}{R_{s,a}R_t'+T_{s,a}-R_{s,a}}, \tag{7.26a}$$

$$R_f' = \frac{(R_t'-R_{s,a})\exp(2\alpha_s)}{R_{s,a}R_t'+T_{s,a}-R_{s,a}}, \tag{7.26b}$$

and $$T_f = \frac{T_t T_{s,a} \exp(\alpha_s)}{R_{s,a} R_t' + T_{s,a} - R_{s,a}}. \qquad (7.26c)$$

From eqs (7.26a) and (7.26c) it can then be shown that

$$\frac{1 \pm R_f}{T_f} = \left\{ \left(\frac{1 \pm R_t}{T_t} \right) \left[1 - \frac{R_{s,a}}{1 - R_{s,a}} (1 - R_t') \right] \mp T_t \frac{R_{s,a}}{1 - R_{s,a}} \right\} \exp(-\alpha_s), \quad (7.27)$$

which, unlike the similar equation used by Vriens and Rippens, is exact. This completes the procedure of how to obtain the optical constants from experimentally determined values of the air-incident and substrate incident reflectivities and the transmittivity of a thin film on a thick substrate.

7.4.6 Recap of the iteration procedure

Now that the necessary equations have been derived, the equations used for the actual iteration procedure are summarised in this section. Formally, the iteration equations for n and k are given by eqs (7.12):

$$n_{i+1} = F_1(R_t, R_t', T_t, n_i, k_i) \qquad (7.28a)$$

and $$k_{i+1} = F_2(R_t, R_t', T_t, n_{i+1}, k_i). \qquad (7.28b)$$

The iteration equation used for k is (7.18a):

$$k = -\frac{1}{\alpha} \ln \left[\frac{x - q}{2R_{a,f}} \left(-1 + \sqrt{1 + \frac{4R_{a,f}}{(x - q)^2}} \right) \right]. \qquad (7.29)$$

where α is given by eq (7.8c):

$$\alpha \equiv 2 \frac{E}{\hbar c} t_f, \qquad (7.30)$$

with E the photon energy, $\hbar$ Planck's constant, c the velocity of light in vacuum and t_f the thickness of the film. $R_{a,f}$, the reflectivity of the air/film interface is taken from eq (7.4)

$$R_{a,f} = \frac{(n-1)^2 + k^2}{(n+1)^2 + k^2}. \tag{7.31}$$

The abbreviations x and q in eq (7.29) are given in eqs (7.16a) and (7.16c):

$$x \equiv (1 - R_{a,f})\left(\frac{1 - R_f}{T_f}\right) \tag{7.32}$$

and $$q \equiv \frac{k}{n}\left[\left(1 - \frac{1}{n}\right) + R_{a,f}\left(1 + \frac{1}{n}\right)\right]\sin(n\alpha) + \left(\frac{k}{n}\right)^2 (1 - R_{a,f})\cos(n\alpha), \tag{7.33}$$

Values for $(1-R_f)/T_f$ are obtained from eq (7.27):

$$\frac{1 \pm R_f}{T_f} = \left\{\left(\frac{1 \pm R_t}{T_t}\right)\left[1 - \frac{R_{s,a}}{1 - R_{s,a}}(1 - R_t')\right] \mp T_t \frac{R_{s,a}}{1 - R_{s,a}}\right\}\exp(-\alpha_s), \tag{7.34}$$

where $R_{s,a}$ is the reflectivity of the substrate/air interface as in eq (7.5a):

$$R_{s,a} = \frac{(n_s - 1)^2 + k_s^2}{(n_s + 1)^2 + k_s^2} \tag{7.35}$$

and $$\alpha_s \equiv 2\frac{E}{\hbar c} k_s t_s, \tag{7.36}$$

which was previously given by eq (7.6c).

The optical constants for the glass substrate, n_s and k_s, are taken from literature; the substrate thickness, t_s, is measured. The values for R_t, R_t' and T_t that enter eq (7.34) are taken from experiment.

The iteration equation used for n is

$$n = -1 + \sqrt{4\kappa - k^2}. \tag{7.37}$$

where κ is defined as

$$\kappa \equiv \sqrt{\frac{n^2 + k^2}{y(1 + R_{a,f})}\left(\frac{1 + R_f}{T_f}\right)}, \tag{7.38}$$

as in eq (7.24) and the abbreviation y is calculated from eq (7.20):

$$y = p + \sqrt{(x-q)^2 + 4R_{a,f}}\ , \tag{7.39}$$

where $$p \equiv \left[\frac{1}{n}\left(\frac{1-R_{a,f}}{1+R_{af}}\right)-1\right]$$

$$*\left[\left(1-\frac{1}{n}\right)\cos(n\alpha)+R_{a,f}\left(1+\frac{1}{n}\right)\cos(n\alpha)-\frac{k}{n}(1-R_{a,f})\sin(n\alpha)\right], \tag{7.40}$$

which was previously given in eq (7.16d).

It is emphasised that, be it at the cost of algebraic tedium, all equations presented in this chapter are exact, straight from Maxwell's theory.

7.4.7 Spectrometry results for n and k

The parameters needed to calculate n and k are:

1) the thickness of the $Ge_2Sb_2Te_5$ film before and after crystallisation. This was determined in section 7.3 and found to be $t_f^A = (25.0 \pm 0.5)$ nm and $t_f^X = (22.5 \pm 0.5)$ nm.

2) the thickness of the substrate was measured with a vernier calliper and found to be $t_s = (1.00 \pm 0.05)$ mm.

3) the optical constants of the substrate (standard microscope glass) were taken from [6]: $n_s = 1.50 \pm 0.05$ and k_s given in Fig. 7.9.

4) The experimental values for R_t, R_t' and T_t were taken from section 7.4.2.

Using these input parameters, the optical constants are determined by the iteration procedure described in section 7.4.6.

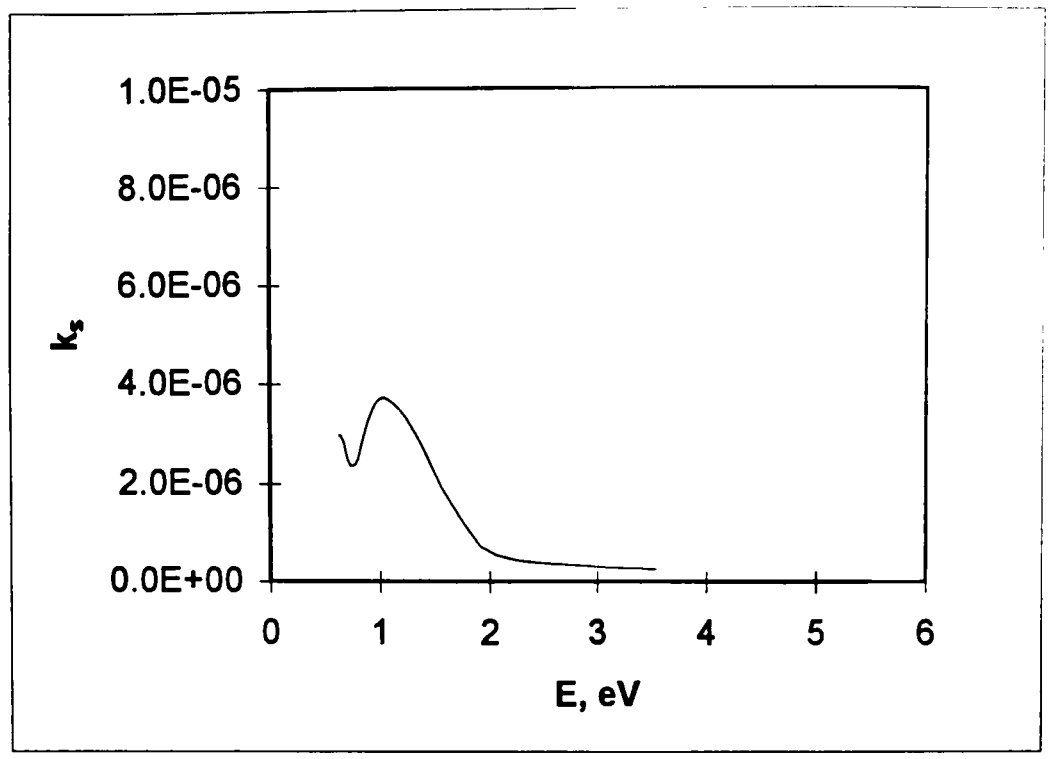
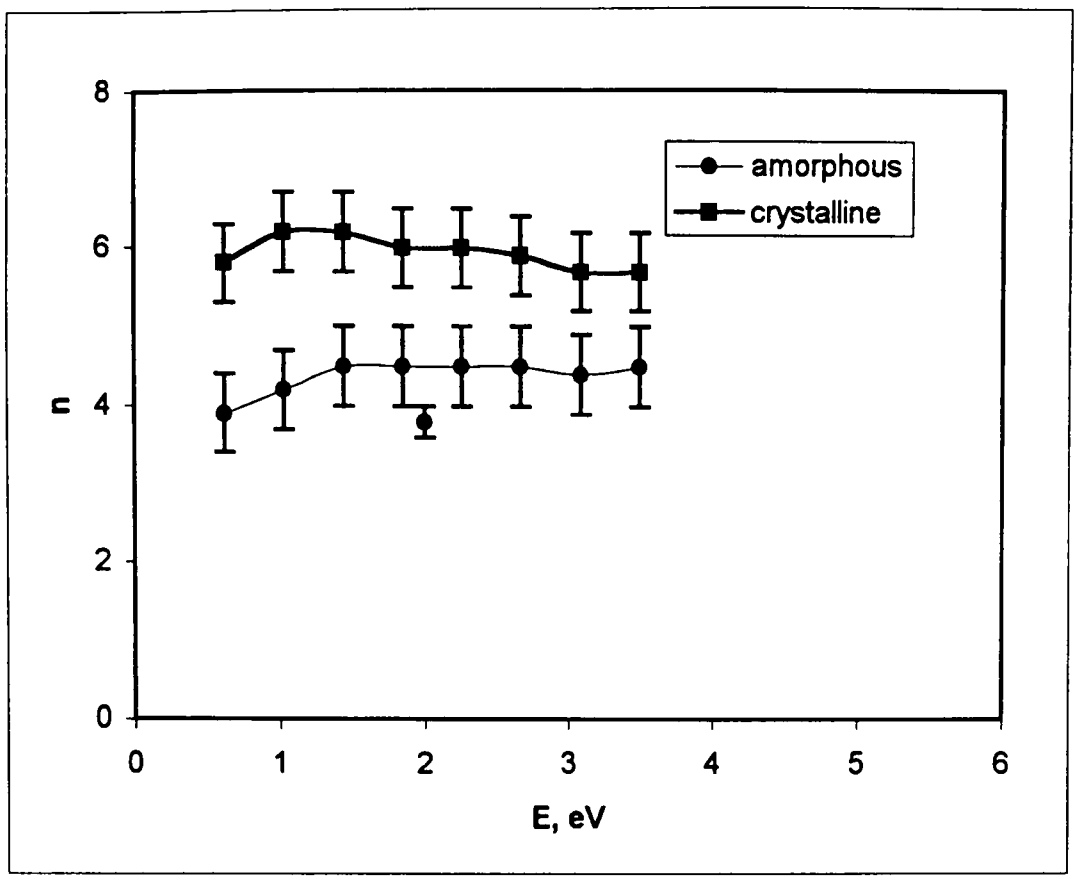


Figure 7.9 Absorption coefficient of the glass substrate, taken from [Vriens].

7.4.8 Ellipsometry results for *n* and *k*

To check the values found for the optical constants using spectrophotometry, the optical constants of an amorphous $Ge_2Sb_2Te_5$ film were determined with ellipsometry, using a laser with a photon energy of 2.0 eV. The sample was deposited on a silicon substrate and sputtered during the same run as the sample deposited on glass that was used for the spectrophotometry experiments. The procedure described in section 2.7 yielded $n_A(2.0) = 3.8 \pm 0.2$ and $k_A(2.0) = 1.9 \pm 0.1$; both values are shown in Fig. 7.10.



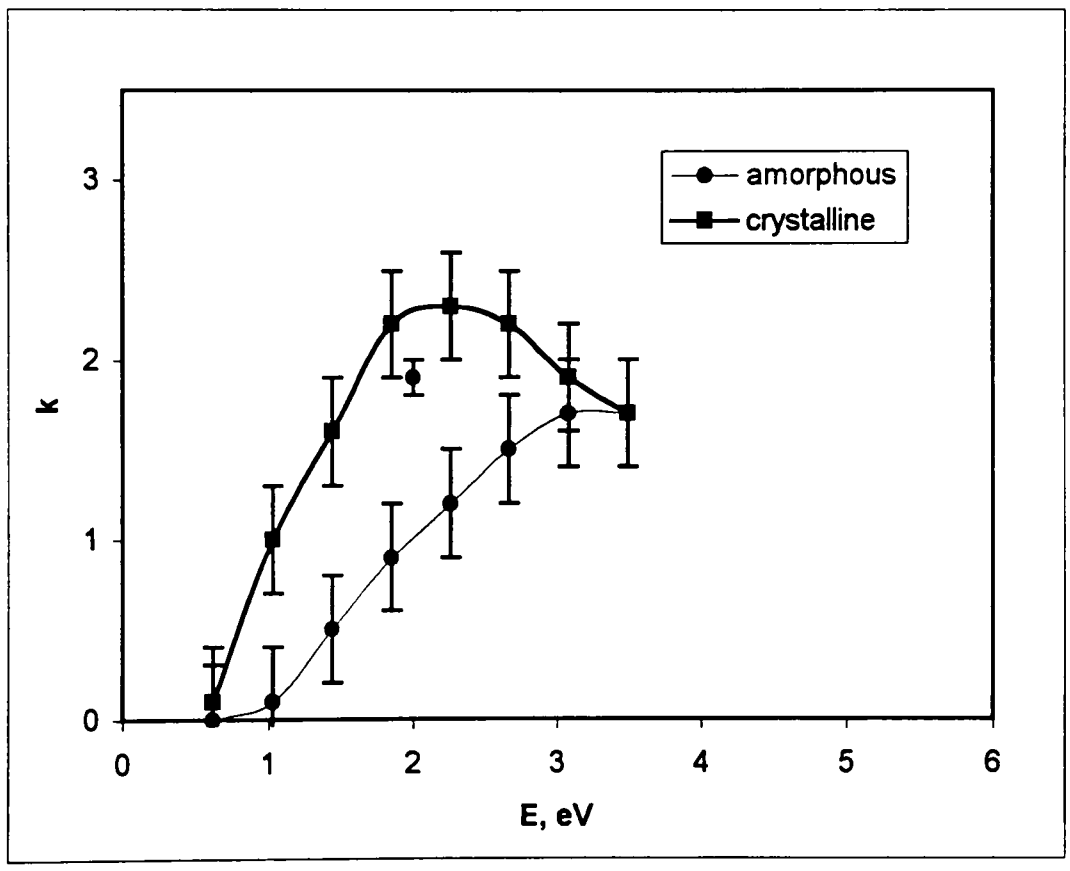


Figure 7.10 Refractive index and absorption coefficient of amorphous and crystalline $Ge_2Sb_2Te_5$ versus photon energy (the solid line merely connects data of the same series). The data point at 2.0 eV is the ellipsometry result for amorphous $Ge_2Sb_2Te_5$.

7.4.9 Comparison with *n* and *k* from the literature

Qualitatively, the spectrometry data show that, in the photon range 0.5 - 3.5 eV:

1) the crystalline values for *n* and *k* are higher than the amorphous values

2) the refractive index does not vary much with photon energy

3) The absorption coefficient seems to increase from zero at small photon energy to a maximum; the amorphous phase has a maximum in k that occurs at a higher photon energy than the crystalline phase.

These trends were also found by Vriens and Rippens [6] for a Te-based alloy. The ellipsometry result for $n_A(2.0)$ also agrees well with the spectrometry value, as can be seen in Fig. 7.10. However, the value for $k_A(2.0)$ determined with ellipsometry can be seen to be significantly higher than the value determined from the spectrometry experiment. The zero-energy limits for n estimated by Yokota [2] for $Ge_2Sb_2Te_5$: $n_A(0) = 4.2$ and $n_X(0) = 6.2$, compare well with extrapolating the values for n_A and n_X in Fig. 7.10 to zero energy. Using a 1.5 eV laser, Yamada *et al.* [11] found $n_A(1.5) = 4.7$ and $n_X(1.5) = 6.9$, which compares well with Fig. 7.10. Their values for the absorption coefficient, $k_A(1.5) = 1.3$ and $k_X(1.5) = 2.6$, however, are higher than the values in Fig 7.10 by about a factor of two. Yamanaka *et al.* [12] report a measurement of the optical constants of crystalline $Ge_2Sb_2Te_5$ over the photon range 0.5 - 3.5 eV. They find the absorption coefficient to be equal to zero up to 0.6 eV, it then rises to a maximum at 2.0 eV to then fall off smoothly to 70 % of its maximum at 3.5 eV, in agreement to the experimental $k_X(E)$ shown in Fig. 7.10. The value of the maximum, however, is $k_X(2.0) = 4.7$, which is about a factor two higher than the maximum in the absorption coefficient shown in Fig. 7.10, i.e. $k_X(2.2) = 2.3$. The refractive index reported by Yamanaka *et al.* shows a clear dependence of photon energy, unlike $n_X(E)$ in Fig. 7.10. The result at the low-energy end of the spectrum, $n_X(0.5) = 6.8$ agrees fairly well with the present work, but Yamanaka *et al.* find $n_X(E)$ to rise to a maximum $n_X(1.0) = 7.1$ to then smoothly decrease to $n_X(3.5) = 1.7$ at the high-energy end of the spectrum. The authors give no error bars and do not mention how the experimental data were obtained.

7.5 Determining the plasma energy

The plasma energy was given in section 5.3.1 to be

$$E_p = \sqrt{\frac{\hbar^2 e^2}{\varepsilon_o m_e}\frac{N_e}{V}}. \tag{7.41}$$

The electron density can be related to the mass density ρ through

$$\frac{N_e}{V} = \rho\, \overline{N}_{e/a}\left(\overline{M}_a\right)^{-1}, \tag{7.42}$$

where $\overline{N}_{e/a}$ is the average number of valence electrons per atom and $\overline{M}_a$ is the average atomic mass. The electronic configurations of Ge, is [Ar] $3d^{10}$, $4s^2$, $4p^2$, that of Sb: [Kr] $4d^{10}$, $5s^2$, $5p^3$ and that of Te: [Kr] $4d^{10}$, $5s^2$, $5p^4$. The average number of *outer* shell electrons per atom in $Ge_2Sb_2Te_5$ is:

$$\overline{N}_{e/a} = \frac{2}{9}(2+2)+\frac{2}{9}(2+3)+\frac{5}{9}(2+4) = 5.33. \tag{7.43}$$

Similarly, the average atomic mass in $Ge_2Sb_2Te_5$ is equal to the weighted average of the elemental atomic masses $M_{Ge} = 72.6$, $M_{Sb} = 121.8$ and $M_{Te} = 127.6$:

$$\overline{M}_a = 114.1 m_p, \tag{7.44}$$

where m_p is the mass of a proton (or neutron). With the mass densities of the amorphous and crystalline films taken from section 7.3, the corresponding plasma energies are calculated from eqs (7.41–7.42) to be $E_p^A = 15.2 \pm 0.4$ eV and $E_p^X = 16.1 \pm 0.4$ eV.

An EELS spectrum was measured in a FEGTEM for an amorphous $Ge_2Sb_2Te_5$ film. The film was deposited on carbon-coated mica, floated off the mica as described in section 2.5.8 and plasma cleaned for five minutes in a Fischione 1020 plasma cleaner to remove the carbon release layer. The result of the EELS measurement is shown in Fig. 7.11.

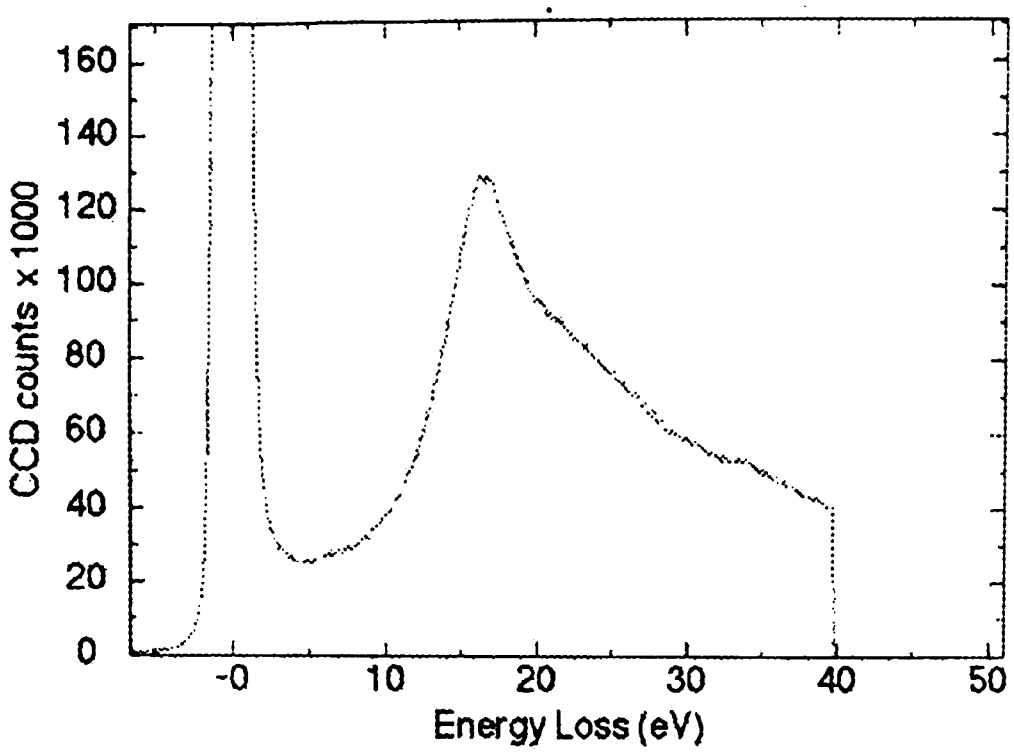


Figure 7.11 EELS spectrum for amorphous $Ge_2Sb_2Te_5$.

The peak at $E = 0$ eV, the zero energy loss peak, is due to electrons that do not experience inelastic scattering when passing through the sample. The peak at $E = 16.5 \pm 0.5$ eV is the plasmon peak, which occurs at $E = \sqrt{E_p^2 + \Delta^2}$ (see section 5.3.1). Using Yokota's value of $\Delta_A = 3.7$ eV for the effective transition energy in the amorphous material, this yields for the plasma energy for amorphous $Ge_2Sb_2Te_5$: $E_p^A = 16.0 \pm 0.5$. This value agrees with the calculated value $E_p^A = 15.2 \pm 0.4$. The calculated values for the plasma energy will be used in the next section because they do not require an estimate of Δ and because of their slightly higher accuracy.

7.6 Fitting Δ and Γ for both phases to the absorption spectra

The imaginary part of the dielectric function (i.e. the absorption spectrum) of amorphous and crystalline $Ge_2Sb_2Te_5$ can be calculated from eq (5.20d) and the experimentally determined values for the optical constants (shown in Fig 7.10). The resulting absorption spectra, effectively determined from the spectrometry data, are shown in Fig. 7.12.

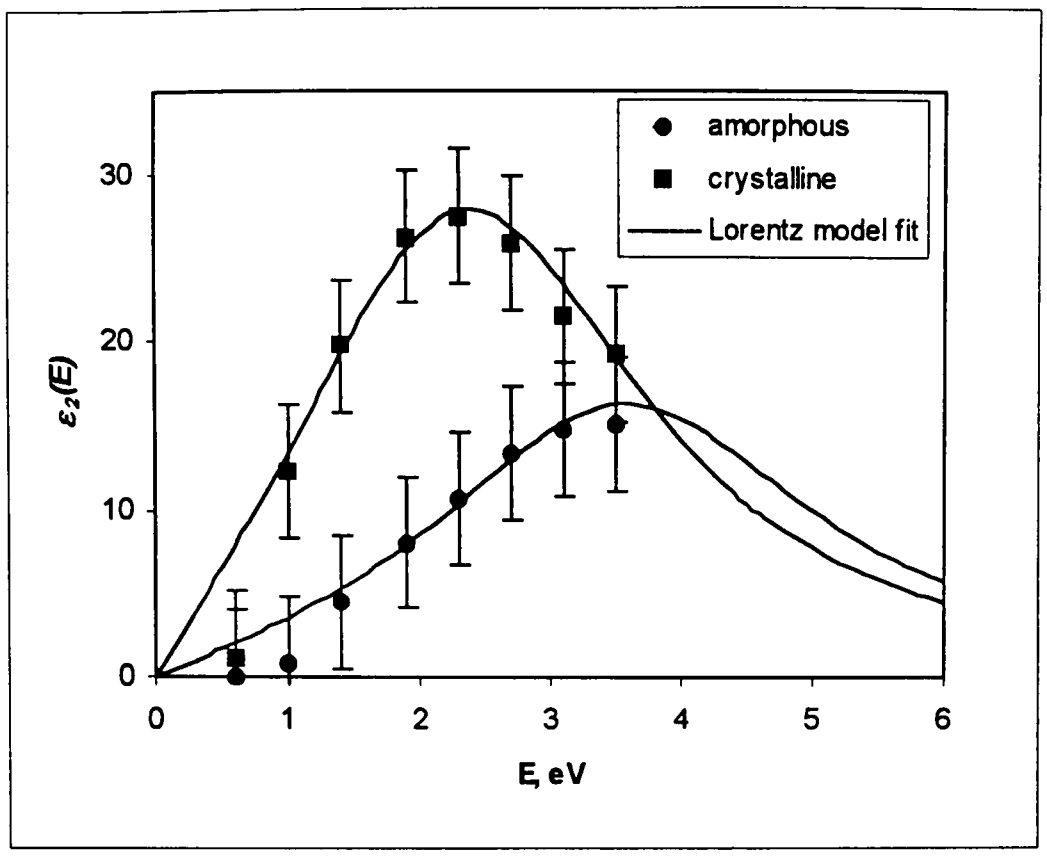


Figure 7.12 Least square fit of ε_2 (E) from eq (6.2) (straight line) to the values of ε_2 (E) calculated from eq (5.20d) and the experimentally determined optical constants. The fit yields Δ_A = 4.0 eV and Γ_A = 3.7 eV for the amorphous film (full dots) and Δ_X = 2.9 eV and Γ_X = 3.5 eV for the crystalline film (full squares).

The data are fitted to ε_2 (E) in eq (6.2), using the position of the absorption peak, Δ, and its width, Γ, as fit parameters; the values for the plasma energies are taken from the previous section. The fit describes the experimental data very well, apart from the point at $\varepsilon_2(0.6)$ for the crystalline material. This is due to the fact that the Lorentz model used is too simple to describe an absorption *threshold*; the model dielectric function, eq (6.2), gives $\varepsilon_2(0) = 0$, but non-zero values for small photon energies. The presence of an absorption threshold, however, is not important here; when $\varepsilon_2(E)$ is small, the reflectivity is governed by $\varepsilon_1(E)$, which *is* accurately described by the Lorentz model used. The fit yields Δ_A = 4.0 eV and Γ_A = 3.7 eV for the amorphous material and Δ_X = 2.9 eV and Γ_X = 3.5 eV for the crystalline material. To estimate the uncertainty in these values, small changes were made to the optical

constants and the Lorentz model was fitted to the new "experimental" data. It was found that changes in n of 10 % and changes of k of 20 %, corresponding to typical errors in the optical constants shown in Fig. 7.10, yielded values for Δ and Γ that differed by about 0.5 eV from the values found for Δ and Γ quoted above.

The values for Δ are fairly close to those reported by Yokota [2]: $\Delta_A = 3.7$ eV and $\Delta_X = 2.6$ eV. The error in the data of Yokota is not indicated, but an error in $R(0)$ of a few percent and an error in E_p of 0.5 eV would lead to an uncertainty in Δ of 0.3 eV. Thus, the values found for Δ for amorphous and the crystalline $Ge_2Sb_2Te_5$ agree with Yokota. This means that the absorption spectrum of $Ge_2Sb_2Te_5$ can indeed be described by a single peak and that there are no more significant peaks in the absorption spectrum at energies higher than 3.5 eV, which were not accessible experimentally. Thus, the simple model for the absorption spectrum, given by eq (6.2), describes the experimental absorption spectrum well. Note that this was a requirement for the moments based method for calculating Δ and Γ to work well.

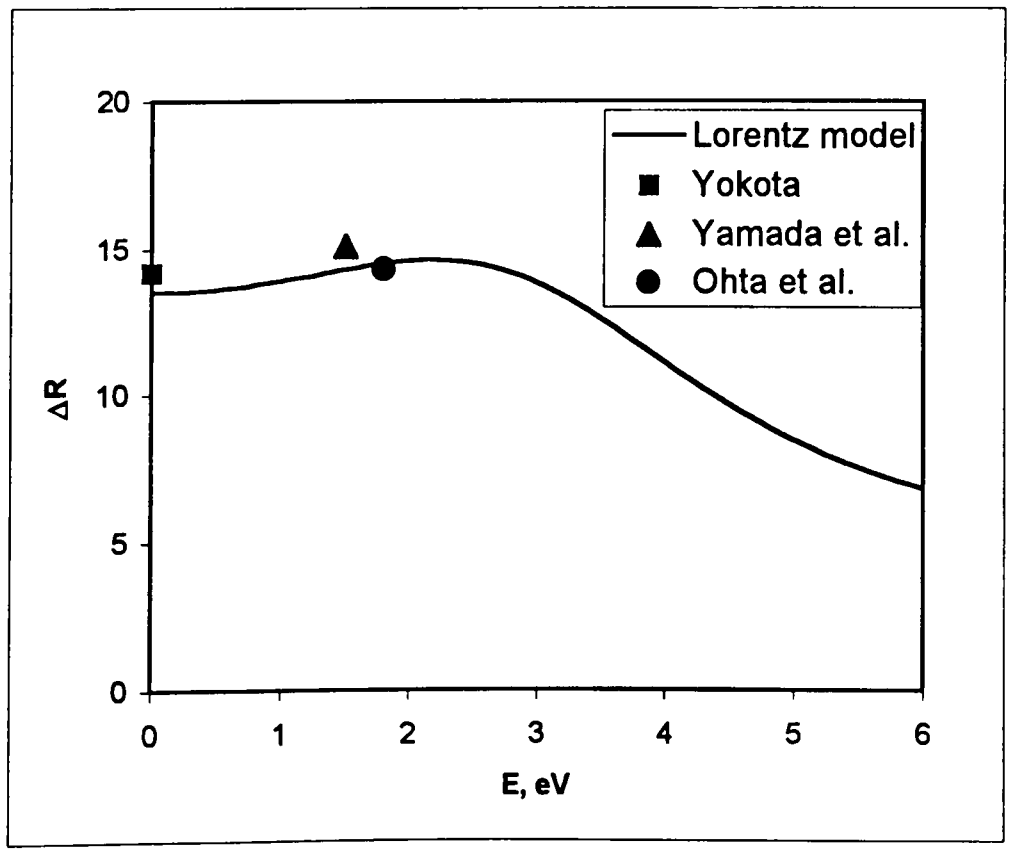


Figure 7.13 Plot of the optical contrast of a semi-infinite $G_eSb_2Te_5$ film, calculated from the Lorentz model (full line). The data points are calculated from the optical constants reported by Yokota [2], Yamada *et al.* [11] and Ohta *et al.* [14].

Using the parameters stated above for E_p, Δ and Γ, the optical contrast of a semi-infinite film is calculated and plotted as a function of energy in Fig. 7.13; the error in $\Delta R(E)$ is estimated to be a few percent. The data compare very well with values for ΔR from the literature. This confirms that the optical contrast between the amorphous and crystalline $Ge_2Sb_2Te_5$ phases can be accurately described using the model dielectric function in eq (6.2).

7.7 Summary and conclusions

1) The composition of the Ge-Sb-Te film was measured and found to be close to the intended stoichiometric composition $Ge_2Sb_2Te_5$.

2) The mass density of the amorphous and crystalline $Ge_2Sb_2Te_5$ films were found to be $\rho_A = (6.0 \pm 0.3)$ g/cm^3 and $\rho_X = (6.7 \pm 0.3)$ g/cm^3, respectively, in agreement with the literature.

3) The plasma energy was calculated from the density, yielding $E_p^A = 15.2 \pm 0.4$ eV and $E_p^X = 16.1 \pm 0.4$ eV.

4) Having derived a novel iteration method for obtaining the optical constants from spectrometry data, the optical constants of $Ge_2Sb_2Te_5$ were determined before and after crystallisation as a function of photon energy in the range 0.5 - 3.5 eV.

5) The optical constants were also determined at 2.0 eV using ellipsometry.

6) The values found for $n(E)$ found with spectrometry compare well with the ellipsometry data and fairly well with the literature.

7) The values for $k(E)$ found with spectrometry, however, seem to be too low, roughly by a factor of two. The reason for this discrepancy is unclear.

8) The absorption spectrum was calculated from the experimentally obtained optical constants for the amorphous and the crystalline phases. Both spectra can be fitted very well

to a damped harmonic oscillator model for $\varepsilon_2(E)$. The fit yields $\Delta_A = 4.0 \pm 0.5$ eV and $\Gamma_A = 3.7 \pm 0.5$ eV for the amorphous material and $\Delta_X = 2.9 \pm 0.5$ eV and $\Gamma_X = 3.5 \pm 0.5$ eV for the crystalline material. Together with the plasma energies from 3), these values for Δ and Γ determine the absorption spectra and thus the optical response of $Ge_2Sb_2Te_5$ before and after crystallisation.

9) The values for Δ, obtained from the dependence of the complex part of the dielectric function on photon energy, agree well with those reported by Yokota [2]: $\Delta_A = 3.7 \pm 0.3$ eV and $\Delta_X = 2.6 \pm 0.3$ eV, obtained from the static limit of the real part of the dielectric function.

10) The fact that the values for Δ obtained from $\varepsilon_2(E)$ and $\varepsilon_1(0)$, respectively, agree, means that the absorption spectra for crystalline and amorphous $Ge_2Sb_2Te_5$ can indeed be described by a single peak. This means that using eq (6.2), which has the shape of a single peak, as a model absorption spectrum gives a good description of the optical response.

11) The relative changes upon crystallisation in E_p, Δ and Γ are 6 %, 32 % and 6 %, respectively. Thus, the optical contrast is mainly due to a change in the effective transition energy, Δ, and is not so much a consequence of the change in density (resulting in the change in E_p). Also, the common wisdom that "disorder increases peak broadening" does not explain the observed optical contrast.

References

[1] http://www.webelements.com/webelements/index.html

[2] R. Yokota, *Jpn. J. Appl. Phys.* **28** (1989), p. 1407.

[3] O.S. Heavens, *Optical Properties of Thin Films*, Butterworth, London (1969).

[4] H. Wolter, *Z. Physik* **105** (1937) p. 269.

[5] H.E. Bennett and J.M. Bennett, *Physics of Thin Films*, G. Hass and R.E. Thun (eds.), Academic Press, New York (1967).

[6] L. Vriens and W. Rippens, *Appl. Opt.* **22** (1983) p. 4105.

[7] S.G. Tomlin, *J. Phys. D* **1** (1968) p. 1667.

[8] S.G. Tomlin, *J. Phys. D* **5** (1972) p. 847.

[9] R.E. Denton, R.D. Campbell, and S.G. Tomlin, *J. Phys. D* **5** (1972) p. 852.

[10] K. Truszkowska, T. Borowicz and C. Wesolowska, *Appl. Opt.* **17** (1978) p. 1579.

[11] Yamada, E. Ohno, N. Akahira, K. Nishiuchi, K. Nagata and M. Takao, *Jpn. J. Appl. Phys.* **26** (1987) p. 61.

[12] S. Yamanaka, S. Ogawa, I. Morimoto and Y. Ueshima, *Jpn. J. Appl. Phys.* **37** (1998) p. 3327.

[13] H. Ehrenreich, H.R. Phillipp and B. Segall, *Phys. Rev.* **132** (1963) p. 1918.

[14] T. Ohta, M. Uchida, K. Yoshioka, S. Furukawa and K. Kotera, *Proc. Soc. Photo-Opt. Instr. Eng., Techn. Digest Ser.* **1** (1989) p. 14.

CHAPTER VIII

Determining the local structure of $Ge_2Sb_2Te_5$

8.1 Introduction

When amorphous $Ge_2Sb_2Te_5$ is heated up to around 440 K, the material crystallises into a cubic NaCl-like crystalline phase. At higher temperatures, a crystalline-to-crystalline phase change occurs, changing the phase of the material from the cubic phase into a hexagonal phase. The amorphous to cubic NaCl-like crystalline phase transition is accompanied by a change in the reflectivity, while there is no significant change in reflectivity when the phase changes from the cubic to the hexagonal phase [1]. In chapter VII, the absorption spectrum of $Ge_2Sb_2Te_5$ was measured for the amorphous and the cubic crystalline phases. It was found that this phase change shifted the centre of weight of the absorption peak, Δ, to lower energies. In chapter VI, a simple model was developed that relates the nearest neighbour co-ordination of a material to its optical properties. In this chapter, it is attempted to resolve the nearest neighbour co-ordination in the three phases of $Ge_2Sb_2Te_5$.

The hexagonal phase of $Ge_2Sb_2Te_5$ was resolved by Petrov *et al.* [2]; the co-ordination of nearest neighbours in this phase was determined from the hexagonal unit cell using their data. The co-ordination of nearest neighbours in the cubic crystalline phase was resolved with the help of the radial distribution function (RDF) determined in the present work and

with a model of this structure proposed by Yamada [3]. Using the RDF measured for the amorphous $Ge_2Sb_2Te_5$ structure, the nearest neighbour co-ordination was proposed for this phase.

8.2 Obtaining the radial distribution functions from experiment

In this section, the way in which electron diffraction was used to experimentally determine the radial distribution functions of $Ge_2Sb_2Te_5$ is described. The RDFs were measured before and after crystallising the as-deposited amorphous samples at 420 K. The structure factors were calculated from the diffraction patterns (DPs), and the radial distribution functions (RDFs) were then obtained by taking the Fourier transform of the structure factor.

8.2.1 Sample preparation

The samples used for these diffraction experiments were grown using DC magnetron sputtering on a carbon-coated mica substrate. The scattering theory used in this chapter assumes single scattering of electrons; to make sure that multiple scattering is kept to a minimum, $Ge_2Sb_2Te_5$ films with a thickness of approximately 15 nm were used, which is thinner than the films used for the crystallisation experiments (chapter IV) and the experiments related to the optical properties (chapter VII), which were approximately 25 nm thick. The films were floated off their mica substrates and picked up on 200 mesh copper TEM grids. Some of the samples were heated using *in-situ* heating in a JEOL 4000 TEM to 420 K until they were seen to crystallise. All samples were then put in a Fischione 1020 plasma cleaner for 5 minutes, to remove the carbon release layer (approximately 30 nm thick). Attempts to prepare samples crystallised at 570 K were made, but failed. Although the actual crystallisation proved no problem, the $Ge_2Sb_2Te_5$ films crystallised at this temperature did not support themselves once the carbon release layer had been removed. Not

removing the carbon layer would result in undesirable scattering by the carbon atoms while growing thicker films does not guarantee single scattering.

8.2.2 Measuring the diffraction pattern

Electron diffraction patterns were recorded using a JEOL 3000F FEGTEM, using the smallest condenser aperture and with no objective aperture. To keep the distance between the sample and the screen the same for all experiments, the "lenses" of the microscope were cycled to avoid hysteresis effects and the image on the screen was focused by changing the sample height, all other parameters being kept constant. As the diffraction theory assumes elastic scattering, the diffracted electrons were energy filtered to exclude electrons that had lost energy during the scattering process. The diffraction patterns were imaged using a CCD camera. One quarter of the DP was recorded, making it possible to measure the scattered intensity further out into reciprocal space. The DPs were saved as Digital Micrograph files and then transferred to SEMPER, an image processing package.

8.2.3 Obtaining the scattered intensity *vs.* reciprocal space distance

The DP gives the intensity of the scattered electrons, I, as a function of the reciprocal space distance, i.e. the distance away from the centre of the pattern, s, and the azimuthal angle, φ. The centre of the DP was found by fitting a circle to the smallest ring in the pattern. Averaging $I(s, \varphi)$ over the azimuthal angle gives $I(s)$, the scattered intensity as a function of the reciprocal distance measured in pixel counts of the CCD array. The RDF is calculated from the scattered intensity as a function of the magnitude of the scattering vector, q. How the scattering vector relates to the reciprocal space distance is illustrated in Fig. 8.1.

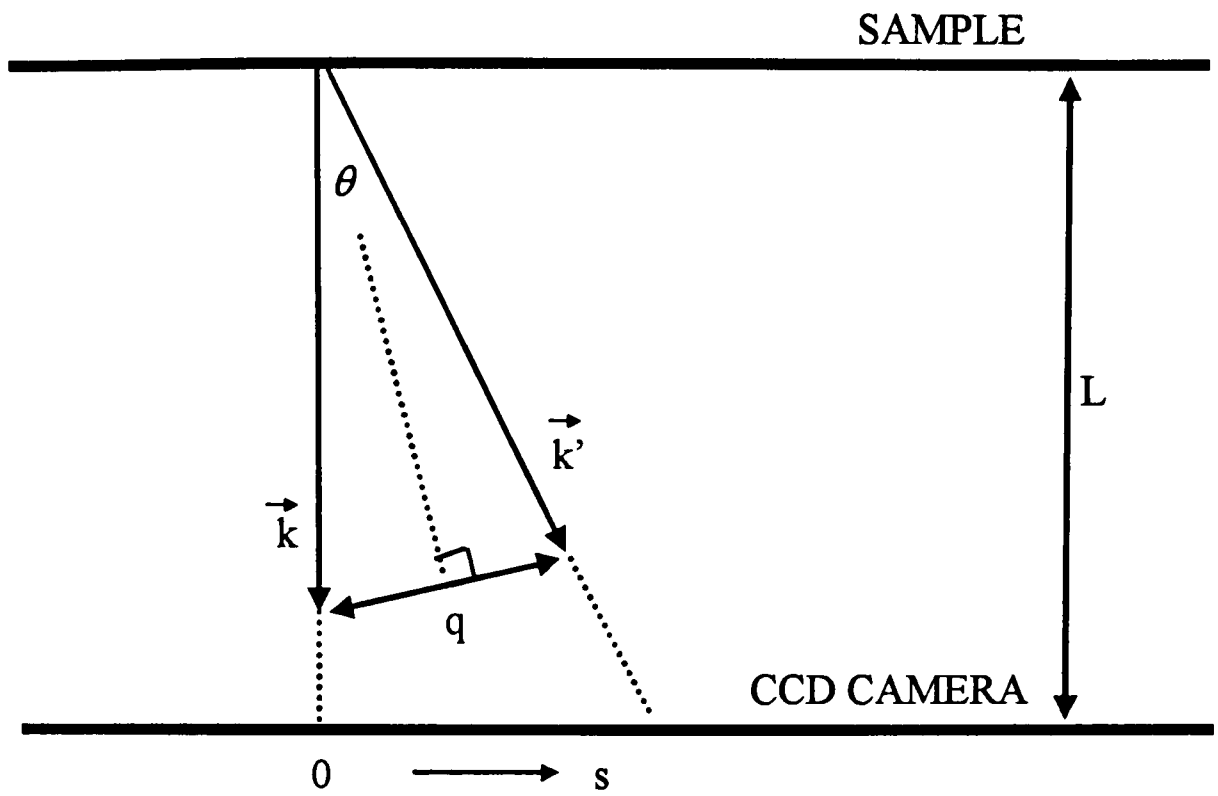


Figure 8.1 Relation between the scattering angle, θ, the magnitude of the scattering vector, q, and the reciprocal space distance, s, where $\vec{k}$ is the incoming wave vector, $\vec{k}'$ the scattered wave vector and L the distance between the sample and the camera.

8.2.4 Calibrating the reciprocal space distance

It is clear from Fig. 8.1 that, for small scattering angle, the scattering vector is proportional to the reciprocal space distance:

$$q = \alpha s \qquad (8.1)$$

and that, knowing L, the distance between the sample and the CCD camera, $|\vec{k}|$, the magnitude of the incoming wave vector (determined by the wavelength of the electrons), and s, the reciprocal space distance (in metres, not in pixel counts), the constant of proportionality, α, can be calculated. In practice, however, not all of these parameters are accurately known and a calibration is made, using a known structure. A Si sample, viewed along the [100] orientation, was used as an external calibration. A DP was taken of this

sample; it showed a square lattice with a periodicity of 284 pixels. As the (110) and (200) reflections in Si are forbidden, the spots in the DP that are closest to the centre correspond to the (220) reflection. Thus, $s_{(220)}$ is equal to the spacing of the reciprocal lattice, i.e.

$$s_{(220)} = 284 \text{ pixels.} \tag{8.2}$$

The remaining task is now to find $q_{(220)}$, the magnitude of the scattering vector for the (220) planes in Si. From Fig. 8.1, it is clear that

$$\tfrac{1}{2} q = |\vec{k}| \sin\theta = \frac{2\pi}{\lambda} \sin\theta, \tag{8.3}$$

where λ is the wavelength of the electrons. Bragg's law states

$$2d \sin\theta = m\lambda, \tag{8.4}$$

where d is the distance between two crystalline planes and m is the order of the reflection. Eliminating $\sin(\theta)$ from eqs (8.3) and (8.4), it follows that

$$q = 2\pi \frac{m}{d}, \tag{8.5}$$

so that for the first order (220) reflection

$$q_{(220)} = \frac{2\pi}{d_{(220)}}. \tag{8.6}$$

Si has the diamond structure with $a = 0.54309$ nm [4], so that

$$d_{(220)} = \frac{a}{\sqrt{2^2 + 2^2 + 0^2}} = 0.1620 \text{ nm}, \tag{8.7}$$

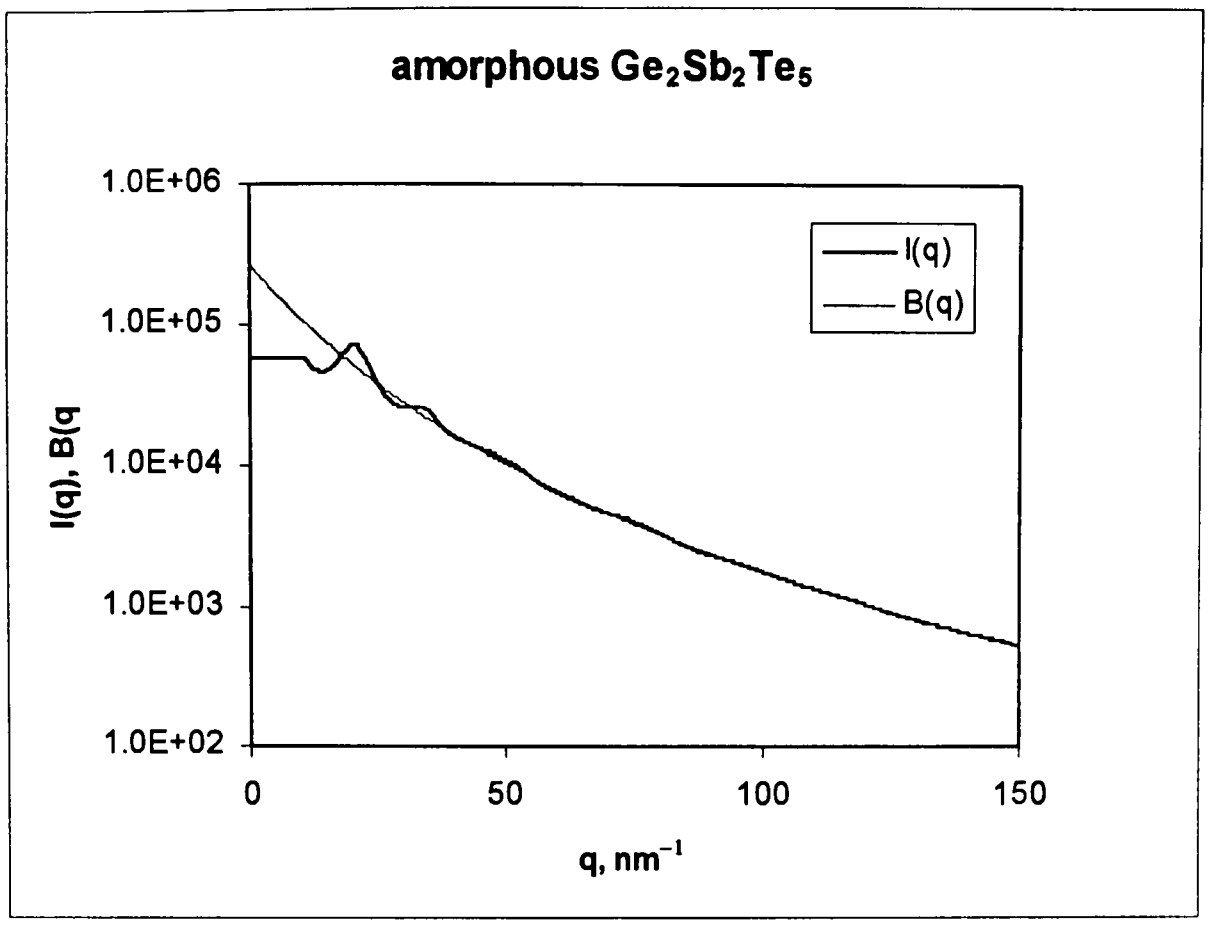
which, together with eq (8.6), gives

$$q_{(220)} = 32.72 \text{ nm}^{-1}. \tag{8.8}$$

Putting eqs (8.8) and (8.2) into eq (8.1) finally gives

$$\alpha = 0.1152 \text{ nm}^{-1}/\text{pixel}, \tag{8.9}$$

completing the calibration. The scattered intensity is plotted as a function of scattering vector in Fig. 8.2 for $Ge_2Sb_2Te_5$ with the amorphous and NaCl-like structures, respectively.



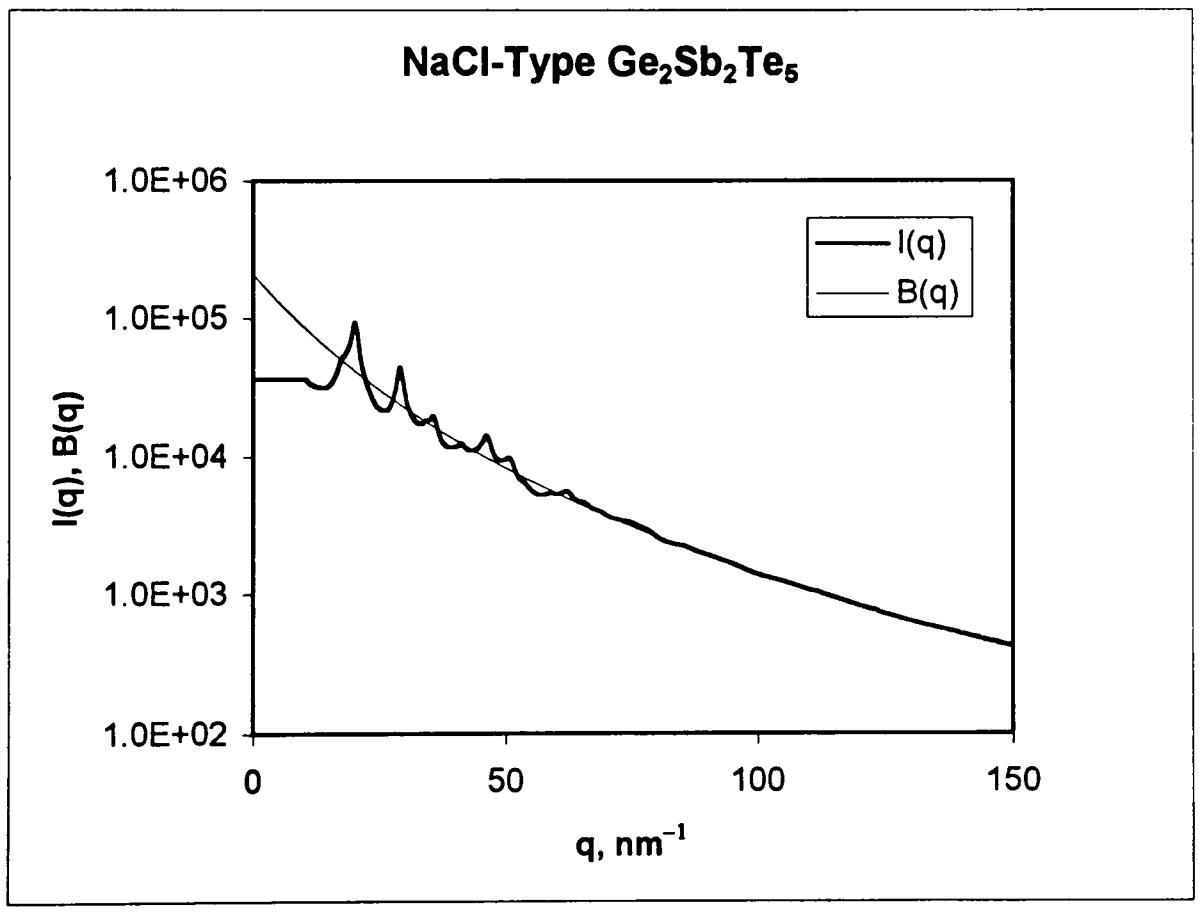


Figure 8.2 Scattered intensity, $I(q)$, and the background intensity, $B(q)$, as a function of the scattering vector, q, for amorphous and NaCl-type crystalline $Ge_2Sb_2Te_5$.

In the absence of any order, the total scattered intensity is simply given by the sum of the contributions of the individual atoms:

$$\sum_i f_i(q), \tag{8.10}$$

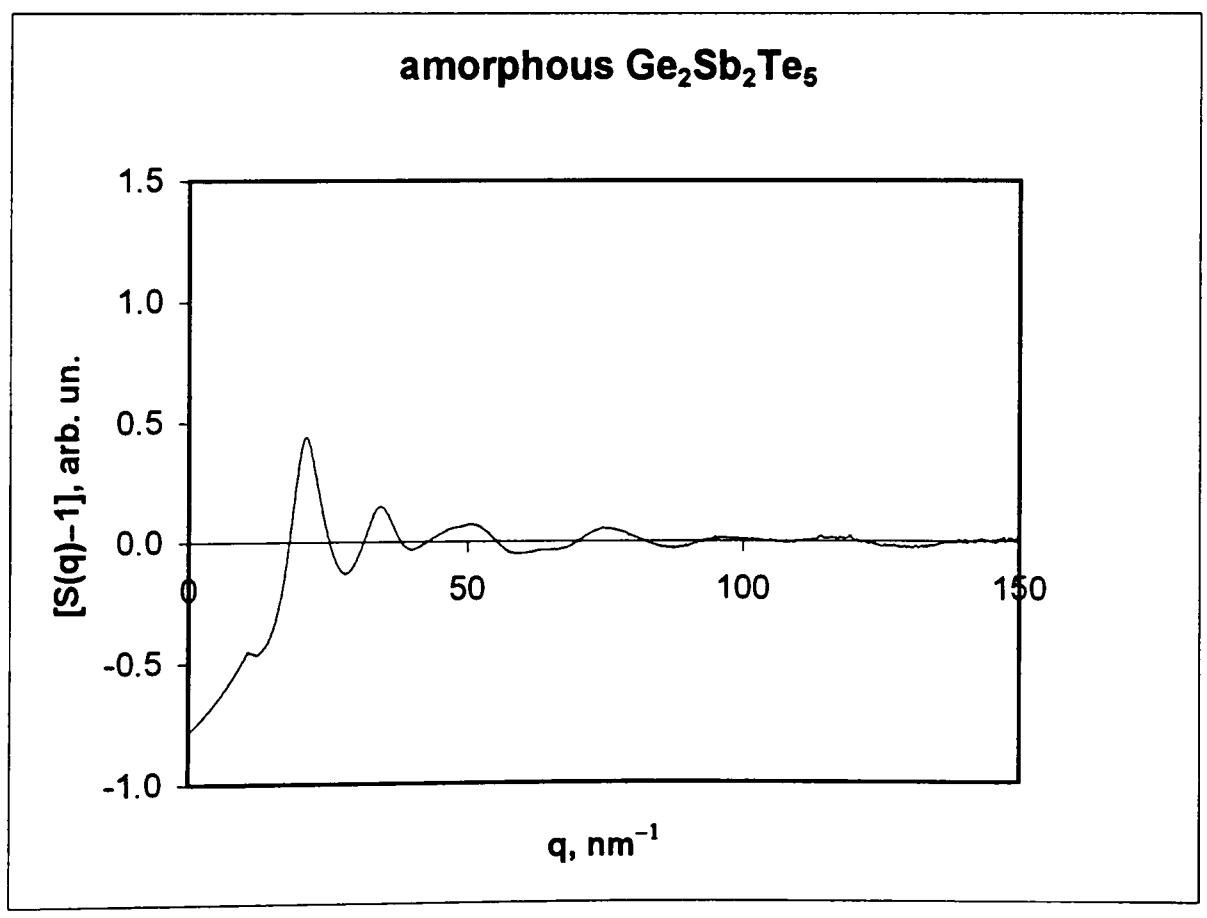
where f_i is called the *scattering factor* of atom i. This contribution of scattering from the individual atoms gives rise to the background signal, $B(q)$, visible in Fig. 8.2. The structure in $I(q)$ on top of this background is due to interference between waves scattered from different atoms. The *structure factor* of the atomic structure is equal to [5]

$$S(q) = \frac{I(q)}{B(q)}, \tag{8.10}$$

i.e. the scattered intensity normalised by its background. The background was assumed to have the functional form

$$B(q) = \frac{C}{(q+q_o)^p} \tag{8.11}$$

and fitted to $S(q)$ by trial and error. The fits are shown in Fig. 8.2. The structure factors, calculated from eq (8.10), are shown in Fig. 8.3.



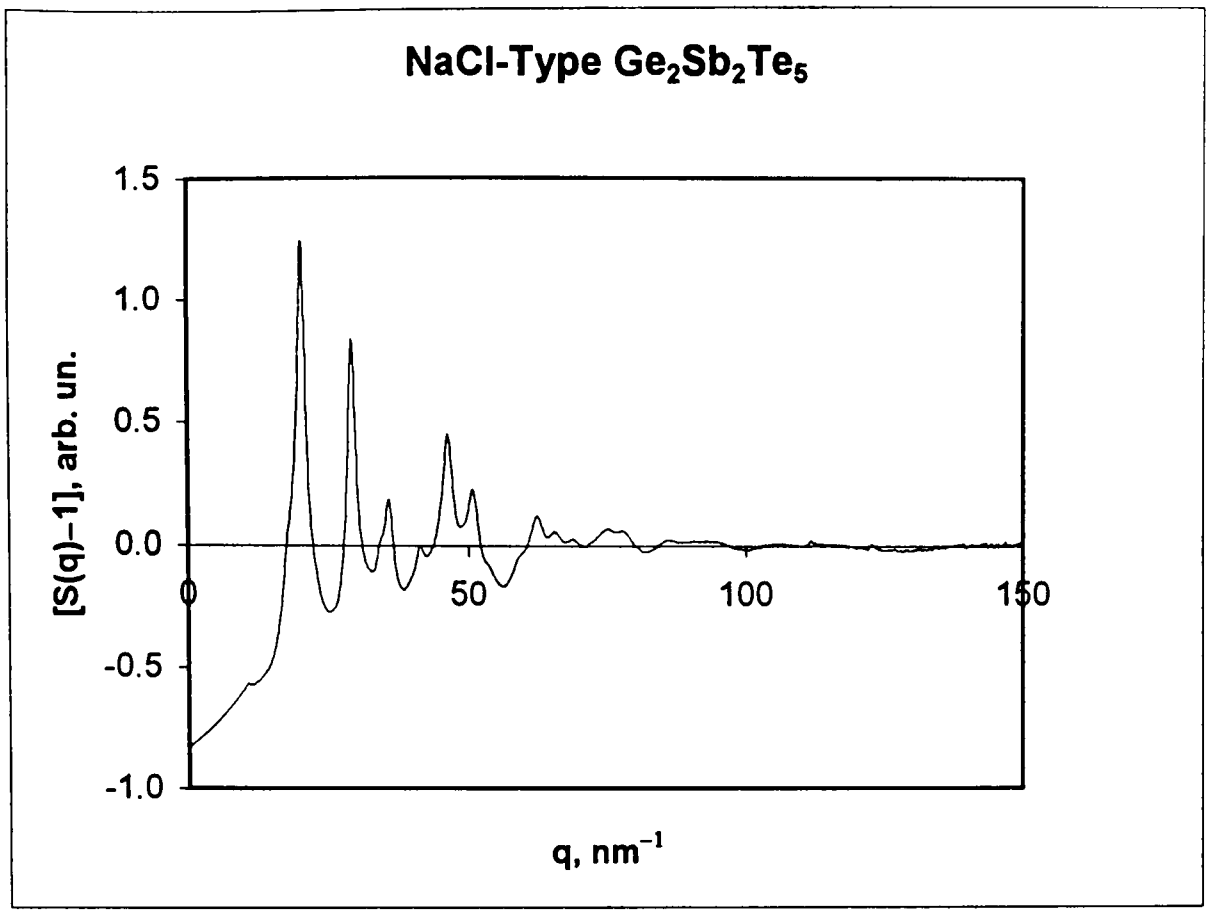


Figure 8.3 Structure factor, $S(q)$, as a function of the scattering wave vector, q, for amorphous and NaCl-crystalline $Ge_2Sb_2Te_5$.

8.2.5 Calculating the radial distribution function

The radial distribution function (sometimes called pair correlation function) is defined as

$$g(r) = \frac{\rho(r)}{\rho_o}, \tag{8.12}$$

where $\rho(r)$ is the concentration of atoms a distance r away from an "average atom" and ρ_o is the overall number density of atoms. For a monatomic material, $g(r)$ is related to the structure factor through [5]

$$[g(r)-1] = \frac{1}{2\pi^2 \rho_o r} \int_{q=0}^{\infty} [S(q)-1] q \sin(qr) \mathrm{d}q \,. \tag{8.13}$$

Eq (8.13) can be shown to be valid for alloys too, provided that the scattering factors are proportional over the entire range of the scattering vector [6]. A plot of the scattering factors for Ge, Sb and Te is shown in Fig. 8.4, showing that they are indeed proportional over the entire range of q.

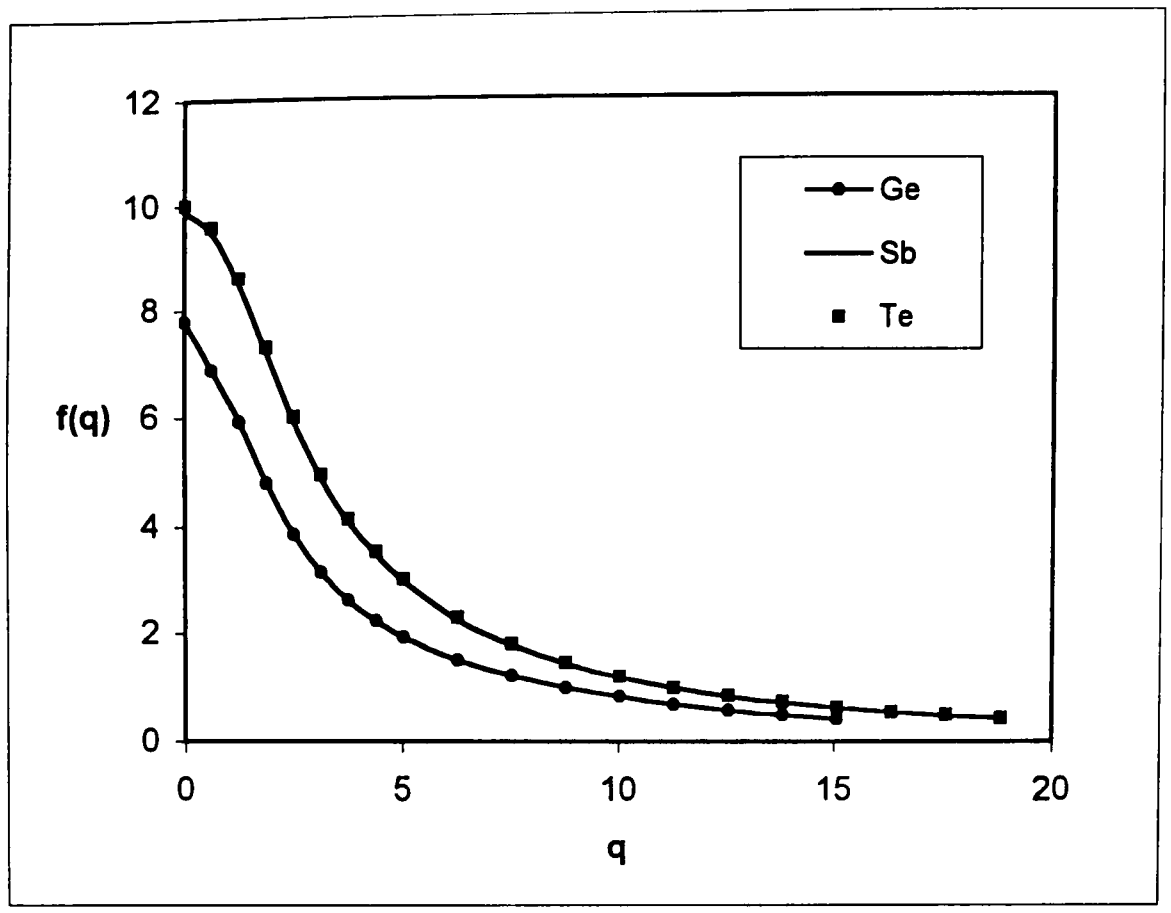


Figure 8.4 Scattering factors of Ge, Sb and Te as a function of the scattering wave vector, taken from Hirsch *et al.* [7]. Note that the scattering factors of Sb and Te are both plotted, but lie almost on the same line.

The integral in eq (8.13) is approximated by a summation (with step size $dq = \alpha\, ds = \alpha$, as the pixel count s is an integer, so that $ds = 1$):

$$g(r) - 1 = \frac{\alpha}{2\pi^2 \rho_o r} \sum_i [S(q_i) - 1] q_i \sin(q_i r) . \qquad (8.14)$$

Fig. 8.3 shows that the structure factor tends to unity for $q > 100$. This means that the range of q over which the structure factor is measured is large enough so that the $[S(q) - 1]$ term in eq (8.14) tends to zero and the summation converges. However, eq (8.14) does not converge due to the noise in $S(q)$; the *trend* in $[S(q) - 1]$ may go to zero, but, because of the noise in the signal, the actual value is never quite zero. The noise is fairly constant over the entire range of q, so that the term $[S(q) - 1]q$ in eq (8.14) gets larger as q gets larger, causing the

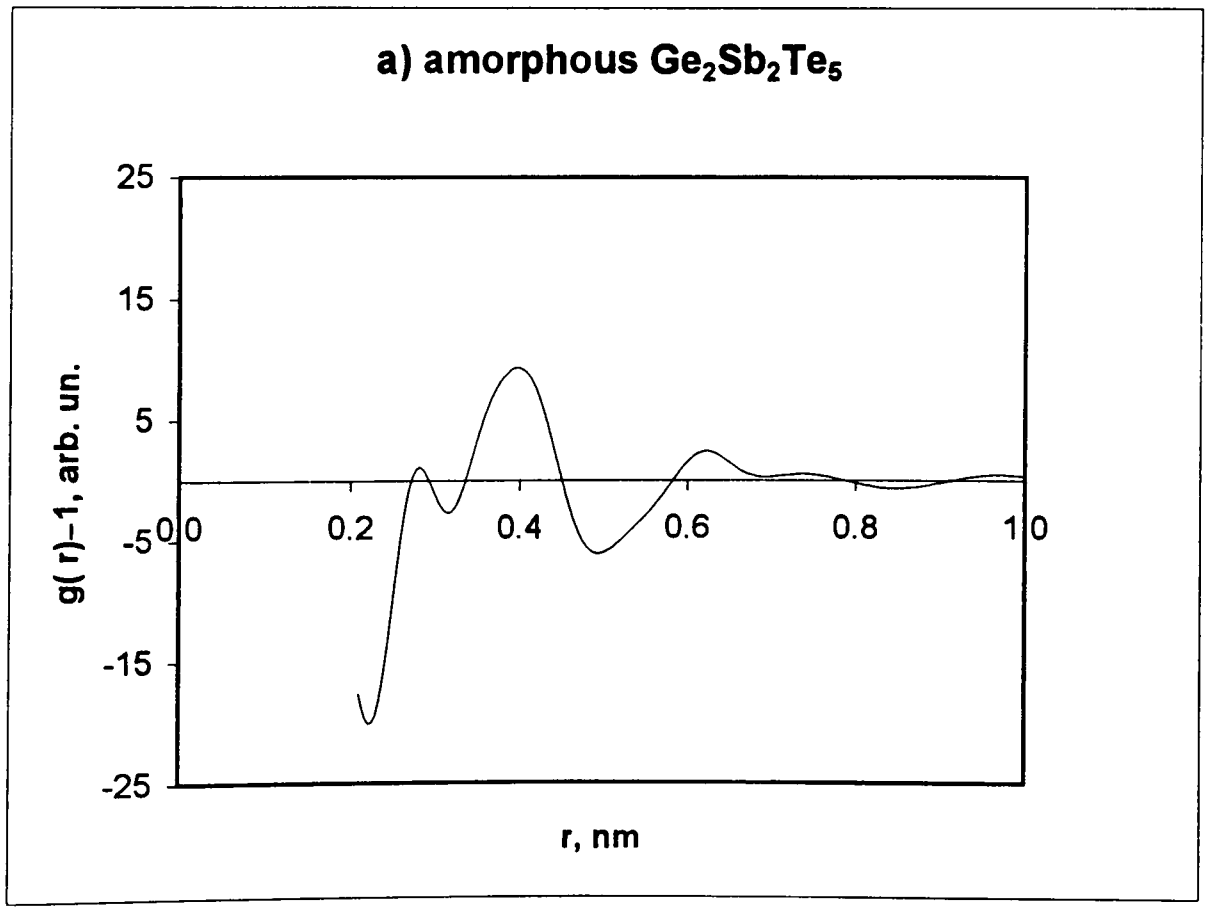
summation to diverge. To remedy this, the $S(q) - 1$ term is multiplied by a smoothed unit step function:

$$U(q) \equiv \exp\left[-(q/Q)^4\right]. \qquad (8.15)$$

Note that eq (8.15) is close to unity when $0 < q < Q$ and close to zero when $q > Q$. The value of Q is chosen such that $[S(q) - 1]$ shows appreciable structure for $0 < q < Q$ but is merely noise in the range $q > Q$. This way, the noise is suppressed in the appropriate range of q and the summation converges. The summation thus becomes

$$g(r) - 1 = \frac{1}{r}\sum_i U(q_i)[S(q_i) - 1] q_i \sin(q_i r), \qquad (8.16)$$

where the constant $\alpha/(2\pi^2\rho_o)$ has been set to unity for simplicity, so that $[g(r) - 1]$ is now given in arbitrary units. Fig. 8.5 shows the radial distribution functions calculated using eq (8.16) from the structure factors of Fig. 8.3.



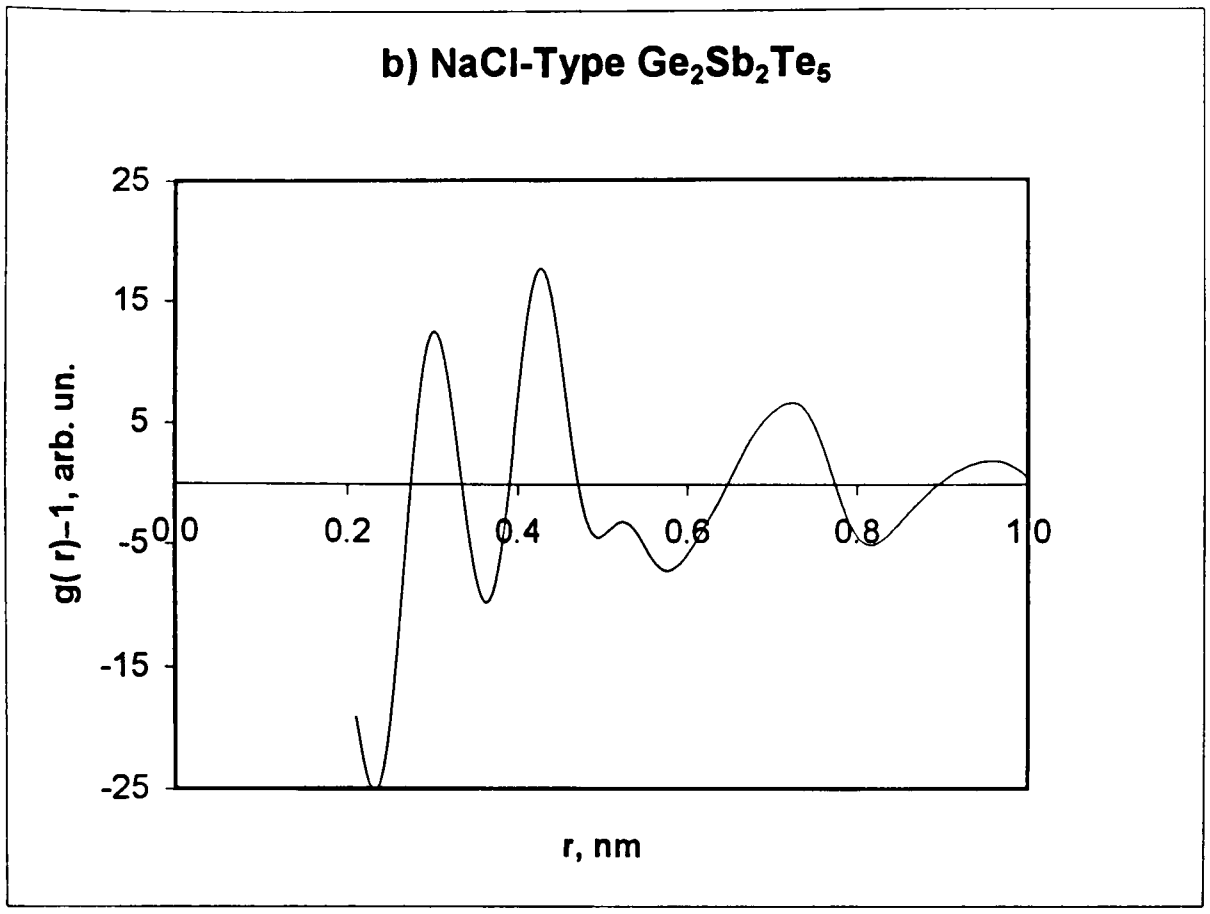


Figure 8.5 Experimentally determined RDFs for a) amorphous and b) NaCl-type crystalline $Ge_2Sb_2Te_5$, calculated from the structure factors in Fig. 8.3.

Both figures clearly show the first, second and third nearest neighbour peaks; the position of these peaks gives the first, second and third nearest neighbour distances, respectively. Calibration of the reciprocal space distance has yielded a calibrated real space distance, resulting in absolute values of the nearest neighbour distances. As the radial distribution function is related to the probability of finding an atom a distance *r* away from an average atom, a calibrated vertical scale would have allowed the nearest neighbour *numbers* to be calculated, in principle. In practice, however, such a calculation is very inaccurate. To determine the nearest neighbour numbers, a different route will be followed: a model of the structure is proposed *a priori* and the corresponding RDF is calculated. If a good match is found between the RDF of the proposed structure and the experimentally determined RDF, this indicates that the material indeed has the proposed atomic structure. The nearest neighbour coordination then follows from the model. This is done in the next section.

8.3 Determining the nearest neighbour coordination

8.3.1 NaCl-type crystalline $Ge_2Sb_2Te_5$

The first crystalline phase of $Ge_2Sb_2Te_5$ is reported to be have an Na-Cl type structure, with lattice constant 0.6 nm. [3], with the Na positions mainly occupied by Te atoms whilst the Cl positions are mainly occupied by the Ge and Sb atoms. As $Ge_2Sb_2Te_5$ contains 56 % Te, some of the Cl positions are also occupied by Te atoms. The unit cell of the NaCl structure is given in Fig. 8.6.

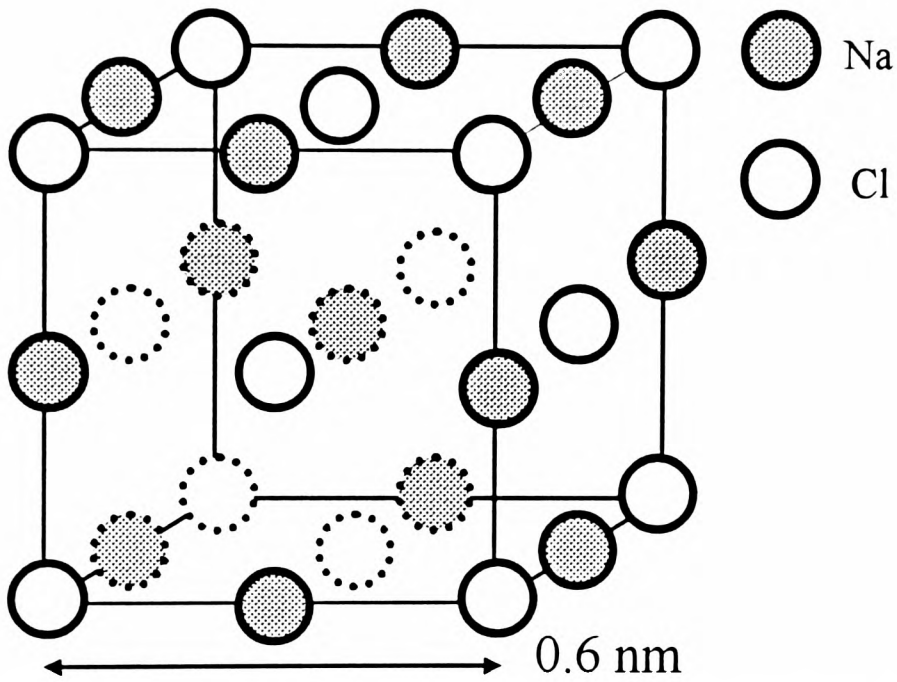


Figure 8.6 Unit cell of the NaCl structure; the Na atoms and the Cl atoms each occupy an FCC lattice. Atoms with a full line contour are in the top, front and right faces of the cube.

Note that, if the atomic species is ignored, the atoms in the NaCl structure form a simple cubic (SC) lattice with lattice constant 0.3 nm. The RDF corresponding to the SC lattice will now be calculated.

In an SC lattice, there are atoms at positions

$$(x, y, z) = a(i, j, k), \tag{8.17}$$

where a is the lattice constant and i, j and k are integers. The distance d from the atom at the origin to an atom at (x, y, z) is

$$d = a\sqrt{i^2 + j^2 + k^2}\ . \tag{8.18}$$

As the atom at the origin has the same coordination as any other atom, the first nearest neighbours are at $d_1 = a$, the second nearest neighbours are at $d_2 = a\sqrt{2}$ etc. The corresponding nearest neighbour numbers then follows from the number of combinations of i, j and k's that give rise to a particular distance. The first seven nearest neighbour numbers and distances determined in this way are given in Table 8.1.

Table 8.1 Nearest neighbour numbers and distances up to the 7th nearest neighbour for the SC crystal lattice.

i	1	2	3	4	5	6	7
n_i	6	12	8	6	24	24	12
d_i/a	1	$\sqrt{2}$	$\sqrt{3}$	2	$\sqrt{5}$	$\sqrt{6}$	$\sqrt{8}$

When there are n_i nearest neighbours at a distance d_i away from the atom at the origin, the atomic number density is

$$\rho(r) = \frac{1}{4\pi r^2}\sum_i n_i \delta(r - d_i), \tag{8.19}$$

where δ is the Dirac delta function and $4\pi r^2$ is the surface of a sphere of radius r. As the SC unit cell is a cube of size a^3 containing a single atom, the average number density is $\rho_o = a^{-3}$. Putting this, together with eq (8.19), into eq (8.12) gives

$$g(r) = \frac{a^3}{4\pi r^2} \sum_i n_i \delta(r - d_i) . \qquad (8.20)$$

In practice, the delta function peaks are broadened by several types of disorder whilst instrumental limitations lead to experimental RDFs with nearest neighbour peaks that are broadened further. These broadening effects are taken into account by replacing the delta functions by Gaussians with a standard deviation σ_i :

$$g(r) = \frac{a^3}{4\pi r^2} \sum_i \frac{n_i}{\sigma_i \sqrt{2}} \exp\left[-\frac{1}{2} \left(\frac{r - d_i}{\sigma_i} \right)^2 \right] . \qquad (8.21)$$

For simplicity, a single broadening parameter β is defined by assuming that the width of the i^{th} nearest neighbour peak is proportional to its position:

$$\sigma_i = \frac{\beta}{100} d_i . \qquad (8.22)$$

As a consequence of this assumption, higher order nearest neighbour peaks are less well resolved, which is what is found experimentally.

In Fig. 8.7 a), eq (8.21) is plotted for the SC lattice, using the nearest neighbour numbers and distances of the first seven peaks as given in Table 8.1. The lattice constant and the broadening parameter were chosen to be $a = 0.3$ nm and $\beta = 6$ %, respectively, so that the position and the width of the first nearest neighbour peak agrees with experiment (see Fig. 8.5). As some of the higher order peaks merge due to the broadening, only four peaks are resolved in $g(r)$, not all seven. RDFs calculated in the same way are also shown in Fig. 8.7 for the body centred cubic (BCC), face centred cubic (FCC) and hexagonal close packed (HCP) structures.

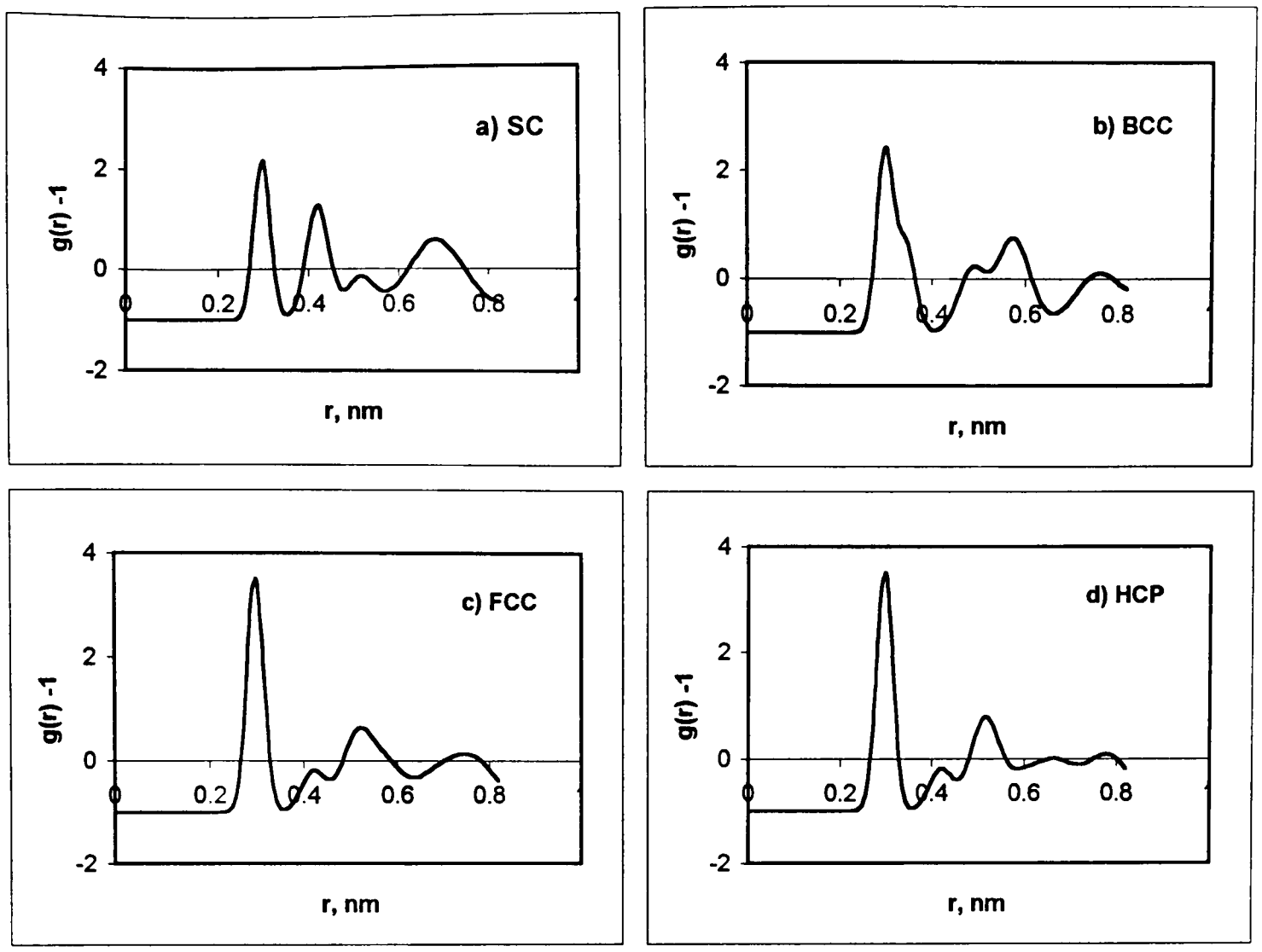


Figure 8.7 Radial distribution functions calculated from eq (8.21) for the following structures: a) SC, b) BCC, c) FCC and d) HCP.

The first nearest neighbour peaks for all four structures shown in Fig. 8.7 have the same position and width as they are fitted to the experimental RDF. Comparison between the higher order peaks in Figs. 8.5 b) and 8.7, however, shows that the experimentally determined RDF agrees best with $g(r)$ calculated for the SC structure. Most notably, the position and width of the second nearest neighbour peak in Fig. 8.5 b) agrees with the RDF calculated for the SC structure, as does the relative size of the two peaks. This indicates that the atoms in the first crystalline $Ge_2Sb_2Te_5$ phase sit on an SC lattice with lattice constant 0.3 nm, in agreement with Yamada *et al.* [3]. Each atom is thus six-fold coordinated by its nearest neighbours, a distance 0.3 nm away. The local coordination polyhedron, i.e. the

polyhedron formed by the nearest neighbours around each atom is therefore an octahedron, as shown in Fig. 8.8.

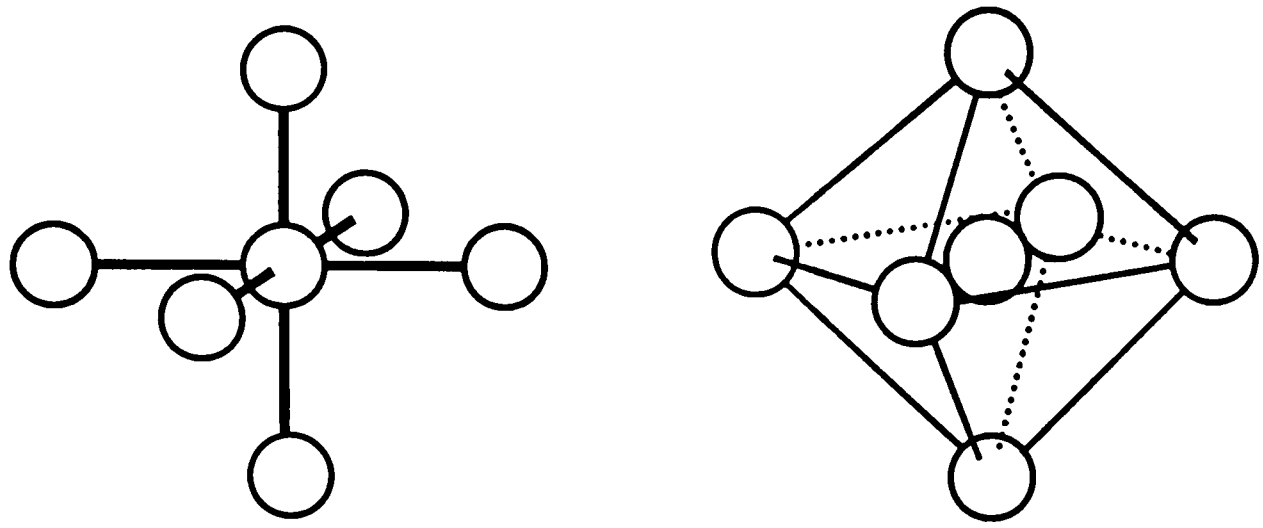


Figure 8.8 Nearest neighbour coordination of atoms in the SC lattice, showing a) the six equivalent nearest neighbour bonds with 90° bond angles and that b) the local co-ordination polyhedron is an octahedron.

In terms of the nearest neighbour coordination, the chemical ordering proposed by Yamada *et al.* implies that: 1) all the Ge atoms and all the Sb atoms have six Te nearest neighbours (i.e. there are no Ge-Ge or Sb-Sb nearest neighbours), and 2) Te atoms are most frequently coordinated by three Ge atoms and three Sb atoms (but there are some Te-Te nearest neighbours). However, which atomic species make up which nearest neighbour peaks can, in practice, not be extracted from the RDF in Fig. 8.5 b), because the scattering factors of the three elements are so similar. The chemical ordering proposed by Yamada could therefore not be checked.

8.3.2 Amorphous $Ge_2Sb_2Te_5$

Compared to the case for crystalline lattices, it is difficult to characterise an amorphous structure. Probably for this reason, no models for the structure of amorphous $Ge_2Sb_2Te_5$ can be found in the literature. Instead of adopting a model from the literature, an atomic model of

the structure of amorphous $Ge_2Sb_2Te_5$ is proposed and compared to the experimental diffraction data. The first and second nearest neighbour peaks in the experimentally determined RDF of the amorphous phase (see Fig. 8.5a) resemble those in Fig. 8.7 a) more than any of the other RDFs in Fig. 8.7. This suggests that amorphous $Ge_2Sb_2Te_5$ may consist of a continuous random network (CRN) of atoms that are six-fold coordinated, just like the atoms in the NaCl-type crystalline structure. Using a "ball and stick" model, a CRN was built with fifty six-fold coordinated atoms. The network is pictured in Fig. 8.9; the sticks indicate the nearest neighbour bonds. Compared to the perfect coordination in Fig. 8.8, the bond lengths and bond angles are only slightly distorted, making the local coordination polyhedron a distorted octahedron.

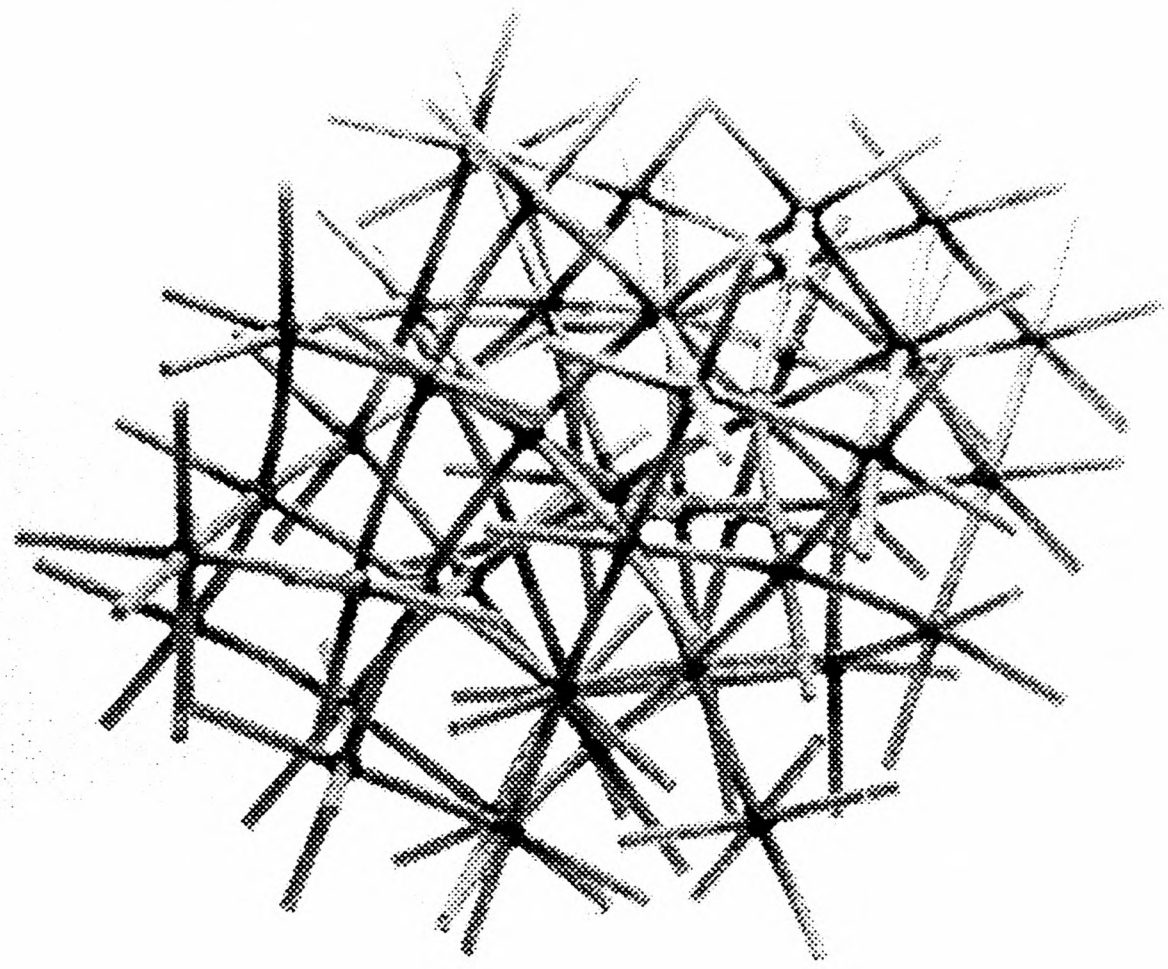


Figure 8.9 CRN of fifty six-fold coordinated atoms. The sticks indicate nearest neighbour bonds; the local coordination polyhedron is a slightly distorted octahedron.

If the CRN in Fig. 8.9 is indeed the structure of amorphous $Ge_2Sb_2Te_5$, its RDF must agree with the experimentally determined RDF in Fig. 8.5 a). To test if this is indeed the case, the

distance between the central atom and the remaining 49 atoms in the structure was measured and the radial distribution corresponding to the central atom calculated from eqs (8.21) and (8.22), with $a = 0.29$ nm and $\beta = 6$ %, just as for the NaCl-type crystalline case (but with $n_i = 1$ for all i, where i runs from 1 to 49). The result is shown in Fig. 8.10.

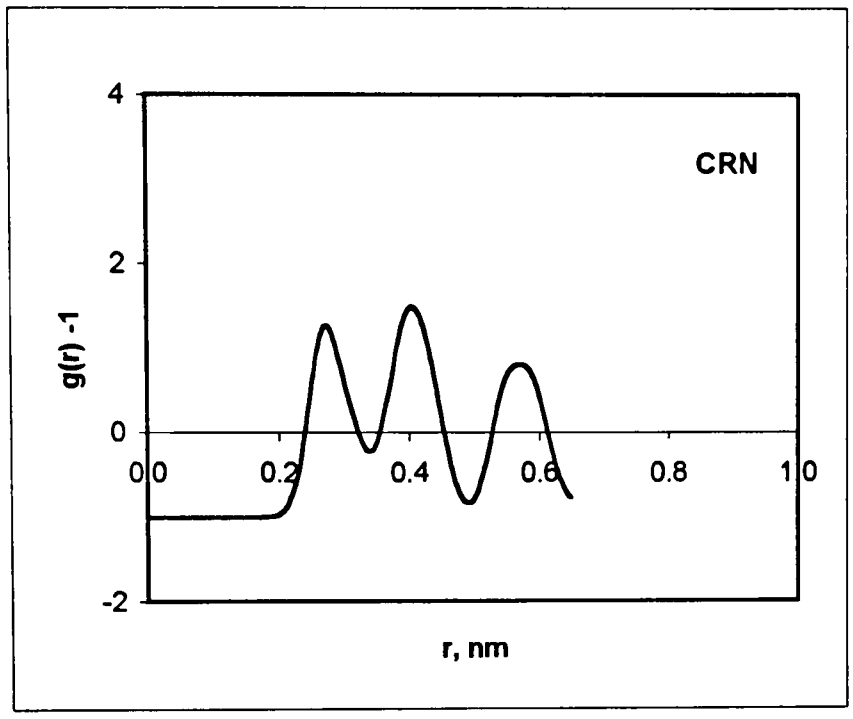


Figure 8.10 Plot of the radial distribution of atoms around the central atom of the CRN pictured in Fig. 8.9.

The RDF of a structure, however, corresponds to the average of all the radial distribution functions of the individual atoms, which are not necessarily the same element. Apart from the central atom, however, no other atom in the CRN has an RDF with three nearest neighbour peaks that are unaffected by the finite size of the ball and stick model. For this reason, only the RDF of the central atom was calculated. Comparing the RDFs in Fig. 8.10 with the experimentally determined RDF for the amorphous state in Fig. 8.5 a) shows that:

1) the first nearest neighbour peaks are both at $d_1 = 0.29$ nm. This is because the r-axis in Fig. 8.10 was scaled so that the first nearest neighbour distance corresponds with experiment.

2) the second nearest neighbours are at $d_2 = (0.42 \pm 0.02)$ nm for the CRN and at $d_2 = (0.43 \pm 0.01)$ nm for the experimental RDF; the difference is negligible. In both cases d_2 / d_1

is close to $\sqrt{2}$. This is what one would expect when the atoms are six-fold co-ordinated with 90° bond angles. It is clear from Fig. 8.8 that whilst the central atom has six nearest neighbours at distance d_1, the nearest neighbours themselves have, within the cluster, four second nearest neighbours at distance $d_2 = d_1\sqrt{2}$.

3) the third nearest neighbour peaks are at d_3 = 0.58 nm for the CRN model and at d_3 = 0.63 nm for the experimental RDF. The cluster in Fig. 8.8 shows that assuming a six-fold co-ordination with 90° bond angles gives rise to third nearest neighbours at 2 d_1 = 0.6 nm, which is close to the position of the third nearest neighbour peaks in Figs 8.4 and 8.10.

Thus, the results suggest that amorphous $Ge_2Sb_2Te_5$ may have a continuous random network structure of six-fold co-ordinated atoms.

8.3.3 hexagonal $Ge_2Sb_2Te_5$

The structure of hexagonal $Ge_2Sb_2Te_5$ was determined by Petrov *et al.* [2]; the hexagonal unit cell, shown in Fig. 8.11, was found to have lattice parameters a = 0.420 nm and c = 1.696 nm.

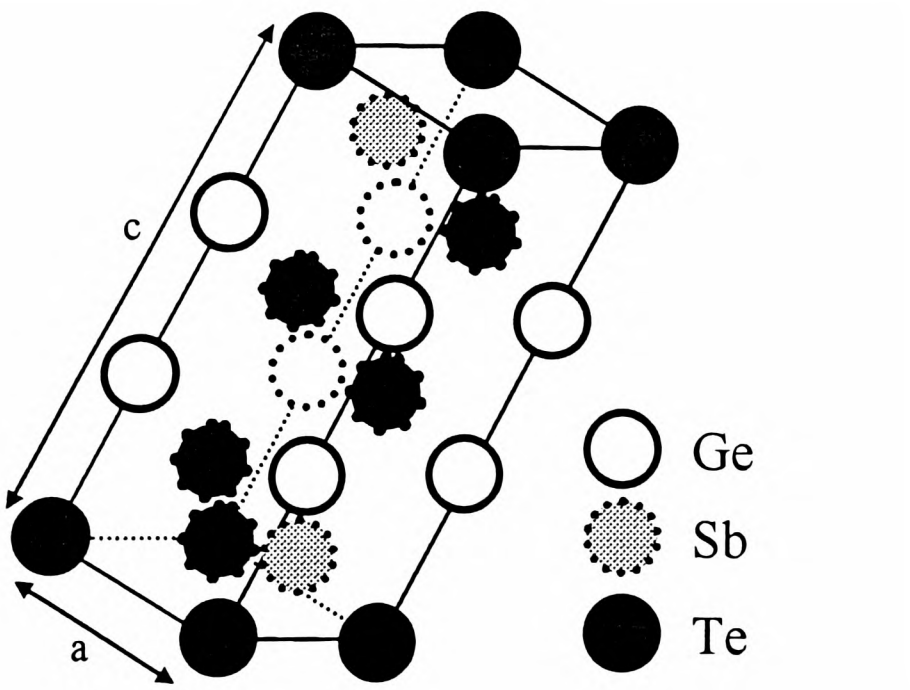


Figure 8.11 Unit cell of hexagonal $Ge_2Sb_2Te_5$; a dashed line around an atom indicates that it does not lie in the front left/right or top plane of the polyhedron.

Note that the unit cell contains $\frac{1}{4}\cdot 8 = 2$ Ge atoms, 2 Sb atoms and $\frac{1}{8}\cdot 8 + 4 = 5$ Te atoms, i.e. one $Ge_2Sb_2Te_5$ unit. The nearest neighbour distances were reported to be 0.300 nm (Ge-Te), 0.302 nm (Sb-Te) and 0.361 nm (Te-Te). The unit cell shows that $Ge_2Sb_2Te_5$ is built up from a repeating unit of nine hexagonally packed layers: (-Te-Sb-Te-Ge-Te-Te-Ge-Te-Sb-). The distance between the Te atoms in the bottom Te layer depicted in Fig. 8.11 is seen to be equal to $a = 0.420$, which is larger than the reported Te-Te nearest neighbour distance. Thus, the hexagonal layers are *not* close packed; Te-Te nearest neighbours only occur between the two adjacent Te layers (layers five and six in the sequence).

To see by how many nearest neighbours each atom is surrounded, three adjacent layers (layers two, three and four in the sequence) are drawn in projection along the *c* axis in Fig. 8.12; the lower layer consists of Sb atoms, the middle layer of Te atoms and the upper layer consists of Ge atoms.

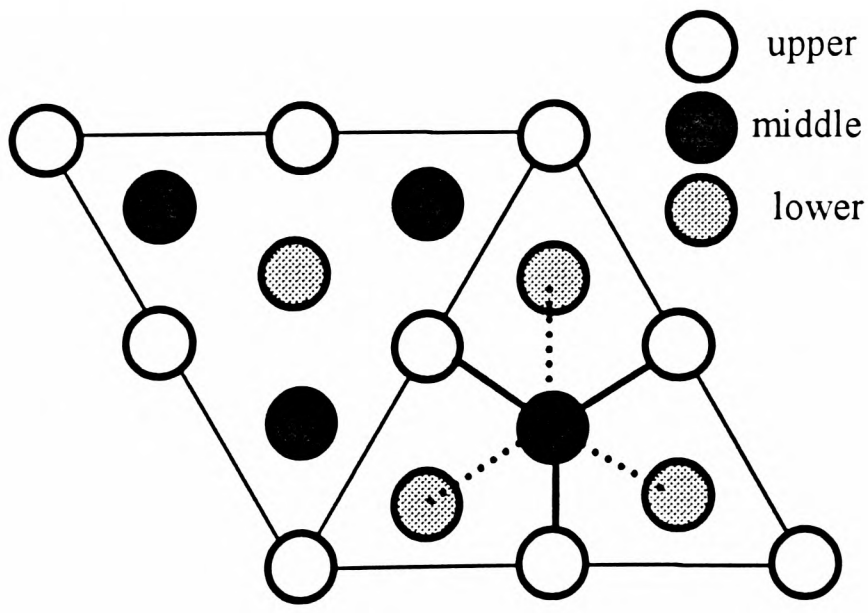


Figure 8.12 Three hexagonally packed layers, shown in projection along the *c* axis. The bold lines indicate nearest neighbour bonds between a Te atom in the middle layer and the Sb atoms in the lower layer (dashed line) and Ge atoms in the upper layer (full line), respectively.

An arbitrary Te atom in the middle layer is seen to have three Sb nearest neighbours in the lower layer and three Ge nearest neighbours in the upper layer. Thus, the Te atoms are six-fold coordinated, just as in the NaCl-type structure.

The bond angles, however, are not quite 90°. Fig. 8.13 pictures the Te atom from Fig 8.12, one of its Te neighbours from the same hexagonal plane and two Ge atoms from the upper plane in Fig. 8.12.

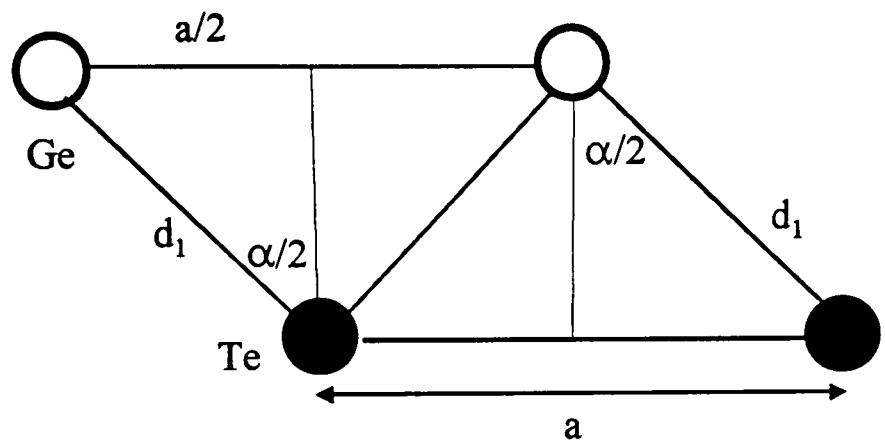


Figure 8.13 Ge-Te-Ge bond angle, α, for the Ge-Te

The bond angle, α, follows from $\sin(\frac{1}{2}\alpha) = \frac{1}{2}a/d_1$ and is thus equal to

$$\alpha = 2\sin^{-1}\left(\frac{a}{2d_1}\right), \tag{8.23}$$

which yields 88.9° for the Ge-Te-Ge (or Te-Ge-Te) bond, as a = 0.42 nm and d_1 = 0.30 nm for Ge-Te. The remaining bond angles of the type X-Y-X *where the X atoms are in the same plane* are 88.1° for Sb-Te-Sb (or Te-Sb-Te) and 71.1° for Te-Te-Te. Note that, as there are no adjacent Ge-Ge, Ge-Sb or Sb-Sb planes in the (-Te-Sb-Te-Ge-Te-Te-Ge-Te-Sb-) sequence, there are also no Ge-Ge, Ge-Sb or Sb-Sb nearest neighbours, so that Ge-Sb-Ge (or Sb-Ge-Sb), Ge-Ge-Ge or Sb-Sb-Sb bond angles are *not* nearest neighbour bond angles.

Denoting the coordination of an atom X by six Y atoms as X: Y(6), it is clear from the stacking sequence that the two Ge atoms in the unit cell have coordination Ge: Te(6), the two Sb atoms have coordination Sb: Te(6) whilst of the five Te atoms, two are Te: Ge(3)Te(3) coordinated, two Te: Ge(3)Sb(3) and one Te: Sb(6).

The characterisation of the hexagonal structure reported by Petrov *et al.* in terms of nearest neighbour coordination is now complete; the five different types of coordination are pictured in Fig. 8.14 and their relative occurrence is indicated.

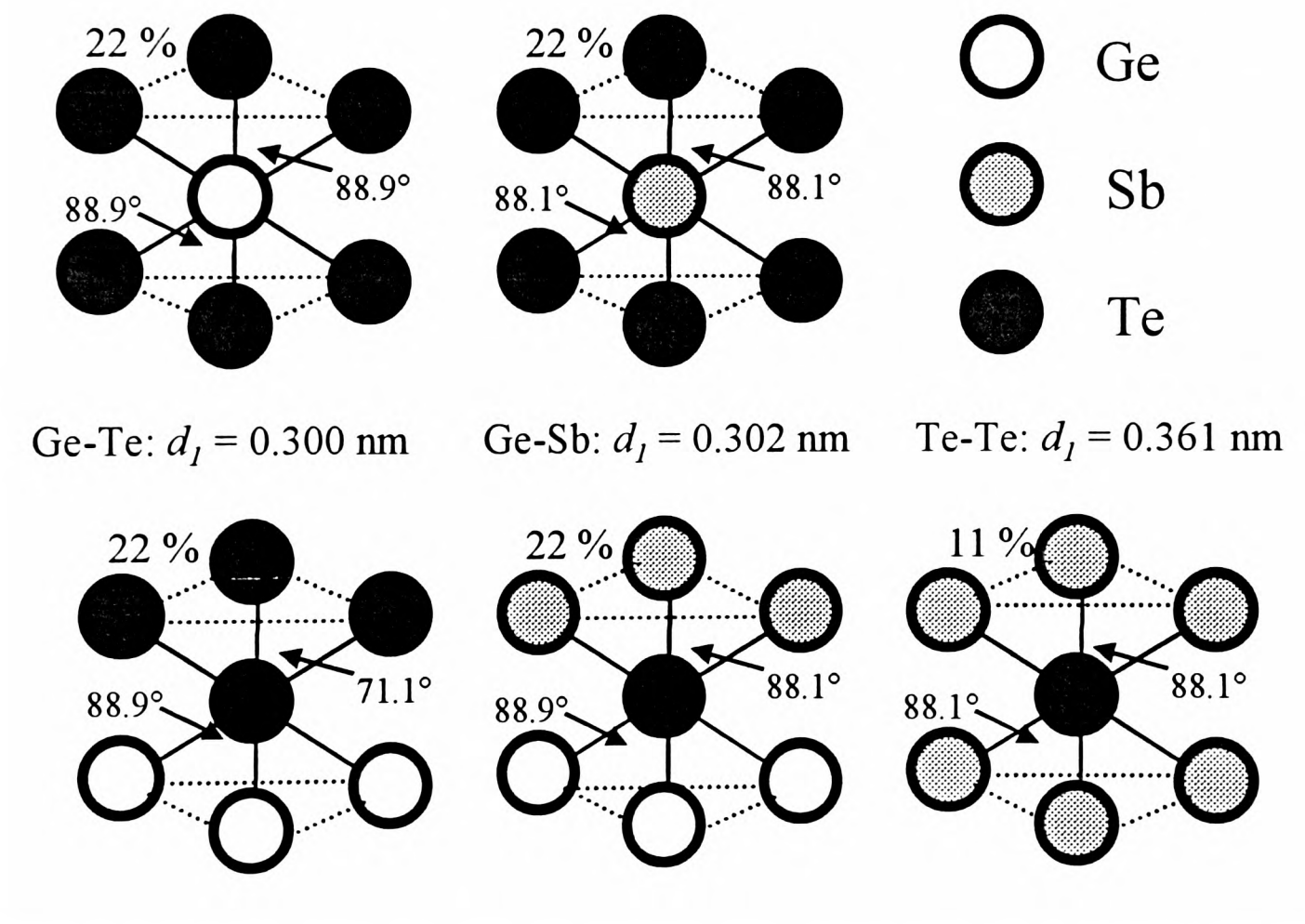


Figure 8.14 The five different types of nearest neighbour coordination found in hexagonal $Ge_2Sb_2Te_5$. Nearest neighbour bonds are represented by a solid line; the broken line connects atoms in the same hexagonal plane. The percentages indicate the occurrence of the coordination.

8.4 Discussion and conclusions

Phillips' spectroscopic theory (see section 5.5) was used by Yokota [8] to calculate the optical contrast between amorphous and hexagonal $Ge_2Sb_2Te_5$ from the nearest neighbour bonding. For the nearest neighbour distance in the hexagonal phase, $d_1 = 0.30$ nm was used, taken from Petrov *et al.* To obtain the nearest neighbour distance for amorphous $Ge_2Sb_2Te_5$, Yokota assumes that this distance can be estimated from the weighted average of amorphous GeTe and amorphous Sb_2Te_3 and finds $d_1 = 0.27$ nm. Although these values for d_1 lead to an estimate of the optical contrast that agrees with experiment, it is hard to see how the nearest neighbour distances can *increase* upon crystallisation by over 10 %, whilst the density *also* increases, roughly by the same percentage. The radial distribution functions measured in this work (see section 8.2.4) for amorphous $Ge_2Sb_2Te_5$ shows that the nearest neighbour distance in the amorphous phase is $d_1 = 0.29$ nm, indicating that Yokota's assumption does not produce an accurate estimate of the nearest neighbour distance in the amorphous phase. The RDF for the NaCl-type phase of $Ge_2Sb_2Te_5$ measured in this work shows that the nearest neighbour distance in this phase is also $d_1 = 0.30$ nm, in agreement with the model of Yamada [3]. Thus, electron diffraction studies indicate that the nearest neighbour distances in amorphous, cubic and hexagonal $Ge_2Sb_2Te_5$ are all close to $d_1 = 0.30$ nm.

Regarding the nearest neighbour *numbers*, Yamada's model of the NaCl-type crystalline structure claims that each atom in this structure is coordinated by six nearest neighbours. The RDF measured in this work supports this. The CRN model proposed in this work assumes that the atoms in the amorphous phase also have six nearest neighbours. The RDF calculated for the central atom has marked similarities with the RDF determined experimentally in this work. Analysing the unit cell of the hexagonal crystalline structure resolved by Petrov *et al.* shows that this phase too has six-fold nearest neighbour coordination.

The nearest neighbour *angles* for the NaCl-type crystalline phase are all 90°. For this to be true, the second nearest neighbour peak must be positioned at $d_2 = d_1\sqrt{2}$. Both RDFs in Fig. 8.5 show this ratio, which means that not only the NaCl-type crystalline phase has 90° bond angles, but the amorphous phase does, too. Analysing the hexagonal unit cell shows that the nearest neighbour bond angles are slightly distorted, but average out to 90°.

Thus, perhaps rather surprisingly considering the crucial changes in the symmetry of the structures, the topological arrangement of the nearest neighbours is very similar in all three structures. However, the *chemical order* in the three phases may still be different. For the hexagonal phase, the chemical order uniquely follows from the unit cell; the relative occurrences of the five types of nearest neighbour co-ordinations are given in Table 8.2.

Table 8.2 Comparison of the relative occurrences of different nearest neighbour co-ordinations in the hexagonal phase and the ordered NaCl-type phase.

	hexagonal	ordered NaCl-type
Ge: Te(6)	22 %	22 %
Sb: Te(6)	22 %	22 %
Te: Ge(3)Sb(3)	22 %	17 %
Te: Ge(3)Te(3)	22 %	0 %
Te: Sb(6)	11 %	0 %
Te: Te(6)	0 %	6 %
Te: Ge(3)Sb(2)Te	0 %	17 %
Te: Ge(2)Sb(3)Te	0 %	17 %

To discuss the chemical ordering in the NaCl-type structure proposed by Yamada, it is convenient to consider *two* $Ge_2Sb_2Te_5$ units, containing eighteen atoms, which may be written as $Ge_4Sb_4Te_{10}$. According to the model, *all* Na positions are occupied by Te atoms. Thus nine out of ten Te atoms occupy Na positions whilst the remaining nine atoms (four Ge atoms, four Sb atoms and the remaining Te atom) occupy the Cl positions. As all Cl positions are six-fold coordinated by Na positions, it immediately follows that Ge: Te(6) and Sb: Te(6) both have a relative occurrence of (4/18)×100 % = 22 %, and that Te: Te(6) has a relative occurrence of (1/18) ×100 % = 6 %. How the Te atoms occupying the Na positions are surrounded by the Ge, Sb and Te on the Cl positions depends on the chemical ordering of the atoms on the Cl positions.

Yamada's model, however, does not mention any such order/disorder. Let's first consider the case of a completely random occupancy. As there are four Ge atoms, four Sb atoms and only one Te atom available, the Te: Ge(3)Sb(3) coordination will occur frequently. It will be more common than more unequal distributions like Te: Ge(2)Sb(4) or Te: Ge(4)Sb(2), as the number of Ge and Sb nearest neighbours available for the coordination is equal. Of the co-ordinations of the Na positions that *do* have Te-Te nearest neighbours, the co-ordinations Te: Ge(3)Sb(2)Te and Te: Ge(2)Sb(3)Te are equally common. They are more common than co-ordinations that have a more unequal distribution of Ge and Sb neighbours like Te: Ge(4)Sb(1)Te etc. They are also more common than Na positions that have two or more Te nearest neighbours as there are relatively few Te atoms available for the Cl positions. Thus, in the case the Cl occupancy is completely random, the *most likely* co-ordinations of the Te atoms occupying the Cl positions are Te: Ge(3)Sb(3), Te: Ge(3)Sb(2)Te and Te: Ge(2) Sb(3)Te.

Now consider the case in which the Cl occupancy is *ordered* such that these three co-ordinations are the *only* ones that occur. In that case, it is easy to see that all three co-ordinations are equally probable. Added together, the number of atoms on the Cl positions of the three co-ordinations mentioned are 3 + 3 + 2 = 8 for Ge, 3 + 2 + 3 = 8 for Sb and 0 + 1 + 1 = 2 for Te, so that the relative Ge:Sb:Te ratio of the atoms occupying Cl positions is 8:8:2 = 4:4:1, which is the *same* ratio as for the Ge, Sb and Te atoms available for the Cl positions, so that the three different co-ordinations of the Na positions are equally probably. As half of all the sites in the NaCl structure are Na sites, the relative occurrence of each of these three co-ordinations is (1/2) × (1/3) × 100 % = 17 %. The relative occurrences of the six different types of nearest neighbour coordination in the ordered NaCl type crystalline phase are given in Table 8.2. Assuming a random distribution of the Cl sites would, in addition to the three most likely co-ordinations, have yielded a large number of less likely co-ordinations for the Te atoms on the Na sites. The essential differences in the occurrences of the nearest neighbour co-ordinations in the hexagonal and the NaCl-type structure, however, are quantitatively the same, regardless of the assumed chemical ordering of the Cl sites.

There are a few important conclusions that can be drawn from the discussion above. Regardless of the absence or presence of chemical ordering of the atoms on the Cl sites:

1) the co-ordinations Ge: Te (6) and Sb: Te(6) will occur with a probability of 22 %, just as in the hexagonal structure.

2) the co-ordination Te: Ge(3)Sb(3) is one of the most likely Te co-ordinations in both the cubic and the hexagonal structure.

The remaining Te co-ordinations may be quite different, but nevertheless the chemical ordering in the cubic and hexagonal phases is remarkably similar.

The fact that the topological and the chemical ordering in the cubic and hexagonal phases is similar is probably the reason why these structures have such similar optical properties. The fact that the topological ordering in amorphous and cubic crystalline $Ge_2Sb_2Te_5$ seem to be similar while the optical properties are markedly different, suggest that the chemical ordering in the two phases is very different. However, as the scattering factors are so similar, chemically specific information could not be obtained from the RDF and no model could be made and tested for the chemical ordering in the amorphous phase.

References

[1] J. González-Hernández, E. López-Cruz, M. Yáñez-Limón, D. Strand, B.B. Chao and S. R. Ovshinsky, *Sol. State Comm.* **95** nr. 9 (1995) p. 593.

[2] I.I. Petrov, R.M. Imamov and Z.G. Pinsker, *Sov. Phys. Cryst.* **13** nr. 3 (1968) p. 339.

[3] N. Yamada, *MRS Bulletin*, September (1996) p. 48.

[4] http://www.webelements.com/webelements/index.html

[5] C. Kittel, *Introduction to Solid State Physics* 6th ed. , Wiley & Son, New York (1986).

[6] D.J.H. Cockayne and D.R. McKenzie, *Acta Cryst.* **A44** (1988) p. 870.

[7] P.B. Hirsh, A. Howie, R.B. Nicholson, D.W. Pashley and M.J. Whelan, *Electron Microscopy of Thin Crystals*, Butterworths (1965).

[8] R. Yokota, *Jpn. J. Appl. Phys.* **28** nr. 8 (1989) p. 1407.

CHAPTER IX

Conclusions and Suggestions for Further Work

9.1 Introduction

This chapter outlines the conclusions drawn from the work carried out by the author and discussed in chapters III, IV and VI–VIII. Chapter III deals with JMAK theory while in chapter IV the kinetics of the crystallisation of thin $Ge_2Sb_2Te_5$ films is investigated. In chapter VI, a simple theoretical model is presented for calculating the optical properties from the nearest neighbour co-ordination of the atoms in a material; the optical properties of $Ge_2Sb_2Te_5$ are characterised in chapter VII, while the nearest neighbour co-ordination in the different phases of $Ge_2Sb_2Te_5$ is investigated in chapter VIII.

9.2 Conclusions

The isothermal JMAK equations have been derived in the literature for various nucleation mechanisms and for interface- and diffusion-controlled growth. Whether or not the JMAK parameters are valid under non-isothermal conditions, however, is not obvious. In chapter III it was shown that the linear heating JMAK equations can be derived for the same nucleation and growth mechanisms for which the isothermal JMAK equations have been derived, if it is assumed that the activation energies for nucleation and growth are much larger than the thermal energy of the system. This had already been done for interface-controlled growth,

but not for diffusion-controlled growth. It was then pointed out that the assumption regarding the activation energies was also made implicitly in the derivation of the isothermal JMAK equations, which had not been pointed out in the literature before. It is therefore concluded that JMAK kinetics is equally valid under linear heating conditions as under isothermal conditions.

From the derivations of the JMAK equations, it was also concluded that the Avrami exponent that appears in the linear heating JMAK equation is exactly twice the value of the Avrami exponent in the isothermal JMAK equation. It was then shown that peak shift methods for determining the JMAK parameters are valid under the exact same conditions as the JMAK equations themselves. Furthermore, it was concluded that Kissinger analysis and other peak shift methods are formally equivalent. Measurements of the JMAK parameters found in the literature that were determined using peak shift methods can therefore be compared to the results found in isothermal experiments.

A derivation found in the literature for determining the JMAK parameters from a linear heating experiment was concluded to be at fault. The error arises from an approximation that is assumed to be valid during the entire transformation. However, it is shown in section 3.4.4 that the approximation only holds when the fraction of transformed material is still small. It was also concluded that when the rate of nucleation and growth of particles of the transformed phase are both thermally activated, the grain size in the transformed phase is a function of temperature; depending on the numerical values of the nucleation and growth parameters, the grain size is found to either increase or decrease as a function of the isothermal annealing temperature.

The isothermal crystallisation kinetics of RF sputtered amorphous $Ge_2Sb_2Te_5$ films, with a thickness of 25.0 ± 0.5 nm and sandwiched between two Si_3N_4 dielectric layers, were examined using *in-situ* TEM. The crystallisation was found to be preceded by an incubation time. It was concluded that *in-situ* TEM is the only technique available with which the incubation times, as well as the starting point of the crystallisation process, can be accurately determined as the individual nuclei can be seen to form in real time. The crystallisation of the amorphous films was found to follow JMAK kinetics. The JMAK parameters determined were in good agreement with the parameters that describe the nucleation and the growth processes, which were determined independently. Determining the starting point of the transformation accurately was found to be of crucial importance to the accuracy with which the Avrami exponent can be determined, as a small uncertainty in the starting point of the crystallisation process leads to a large uncertainty in the Avrami exponent. The nuclei were found to form primarily at the $Ge_2Sb_2Te_5/Si_3N_4$ interfaces. The average grain size in the crystallised phase was approximately 50 nm and was found to have no significant dependence on the annealing temperature, in agreement with the nucleation and growth parameters.

The dimensionality of the growth of the nuclei is initially three (they grow as hemispheres) but will eventually become two for thin films (after the crystallites reach the opposite $Ge_2Sb_2Te_5/Si_3N_4$ interface and before they impinge) or one for thick films (the crystallites impinge first and then only keep growing in one direction, towards the opposite interface). Thus, when the film thickness is of the order of the grain size, the dimensionality of the growth, and with it the Avrami exponent, are largest, leading to short crystallisation times at the erase temperature. It is for this reason that the erase times of the bits show a minimum as a function of the film thickness. A higher dimensionality of the growth does not, however,

reduce the stability of the amorphous phase at room temperature, as this is determined by the nucleation process.

The absorption spectrum of a material consists of a large number of very closely spaced Dirac delta function peaks which, for many materials, blend into a single absorption peak. When this is the case, the optical response of the material can be treated as a single damped harmonic oscillator, characterised by only three parameters: the plasma energy, E_p, an effective transition energy, Δ, and an effective damping constant, Γ. Simple analytical expressions were derived for Δ and Γ, in terms of the positions of the delta function peaks. It was concluded that these expressions give a good first order approximation of the delta function spectrum.

A theoretical model was developed aimed at calculating the absorption spectrum from the nearest neighbour co-ordination of the atoms in a material. Silicon was used as a case study as its structure, optical properties and the tight binding parameters needed for the model are all well-known. Several simplifying assumptions were made regarding the tight binding parameters to simplify the maths. It is concluded that, at least for this simplified model, the exact absorption spectrum can be approximated by a small number of delta function peaks and that the positions of these peaks can be calculated from the nearest neighbour co-ordination of the atoms only. It is also concluded that it seems likely that the model can be extended to describe more realistic materials. As all optical properties of a material can be calculated from its absorption spectrum, it was concluded that the reflectivity of a material is, to first order, determined by Δ, Γ and E_p only and that these parameters can be calculated from the nearest neighbour co-ordination of the atoms in the material.

The density of $Ge_2Sb_2Te_5$ was measured before and after crystallisation using GIXR. From the density and the valency of the atoms, the plasma energy was calculated for the amorphous and the crystalline phase. The absorption spectrum was determined for both phases using spectrometry and found to have the form of a single absorption peak. Δ and Γ were determined by fitting the absorption spectrum to the damped harmonic oscillator model. From the values of E_p, Δ and Γ, it was concluded that the main change in the absorption spectrum upon crystallisation is due to a change in the effective transition energy. Thus, the optical contrast of $Ge_2Sb_2Te_5$ is also predominantly caused by this change in Δ.

When amorphous $Ge_2Sb_2Te_5$ samples are heated, they crystallise into a cubic NaCl-type structure. From the electron diffraction studies carried out it was found that the nearest neighbour distances in the amorphous and cubic crystalline phases did not differ significantly. It was concluded that the change in reflectivity upon crystallisation does not arise due to a change in the nearest neighbour distance, contrary to a report in the literature. The radial distribution functions that were calculated from the diffraction patterns suggest that the atoms in both the amorphous and the cubic crystalline structures are co-ordinated by six nearest neighbours and that the bond angles are approximately 90°.

At higher temperatures, the cubic crystalline phase changes into a hexagonal crystalline phase; both crystalline phases have similar optical properties. From the unit cells reported in the literature for the cubic and hexagonal crystalline phases it was concluded that the topological co-ordination of nearest neighbours was virtually identical. The chemical order of the nearest neighbours was also found to be similar in the two structures. On this ground, it was concluded that the change in reflectivity upon crystallisation is probably not due to the change in topological order but to a change in the chemical order of the nearest neighbours.

Also, the fact that the two crystalline phases have such similar optical properties is probably a result of the fact that the topological nearest neighbour co-ordination is virtually identical, while the chemical order is similar.

9.3 Suggestions for further work

The *in-situ* TEM investigation of the crystallisation kinetics of amorphous $Ge_2Sb_2Te_5$ films has yielded fairly accurate values of the nucleation and growth parameters, which determine the speed of crystallisation. However, the erase time of an amorphous bit is equal to the sum of the incubation time and the crystallisation time, and equally dependent on the parameters that determine the incubation time. To complement this study, it would be interesting to investigate the temperature dependence of the incubation time over a large temperature range, ideally all the way up to the melting point. The most remarkable and interesting feature of the transformation kinetics of amorphous $Ge_2Sb_2Te_5$ is the fact that nucleation is suppressed for so long during the incubation period, but once the nuclei do start forming, the nucleation rate increases almost with the square of time. Perhaps a Monte Carlo simulation of the formation of a single nucleus at an $Ge_2Sb_2Te_5/Si_3N_4$ interface could be done, ideally including the influence of stress as the change in density during crystallisation will cause stress in the film which may influence the nucleation rate.

The four level recursion model for calculating the contribution of the nearest neighbour bonds to the absorption spectrum needs to be developed further. The contribution of the π bonds needs to be included; the accuracy of the geometric mean approximation needs to be investigated and finite on-site energies need to be considered. Although none of these further developments are trivial, they do all look feasible. Having done the diamond structure, the same path should be followed for the nearest neighbour co-ordination of interest. As each

nearest neighbour bond gives its own contribution, extending the model to multi-component systems such as $Ge_2Sb_2Te_5$ should not be difficult.

The topological order in amorphous $Ge_2Sb_2Te_5$ needs to be studied in more detail. An EXAFS (extended X-ray absorption fine structure) study would be ideal, as this technique potentially yields nearest neighbour distances, bond angles and nearest neighbour numbers of each of the atomic species in the structure. However, as Sb and Te are next to each other in the periodic system, it will be difficult to tell them apart.